

Quasi-free cross section measurements for the $\pi^+\pi^-$
electroproduction off the proton in deuterium with
CLAS and a 2.039 GeV beam

Iuliia A. Skorodumina^{1,a}, Gleb V. Fedotov², Ralf W. Gothe¹

¹*Department of Physics and Astronomy, University of South Carolina, Columbia, SC*

²*National Research Centre “Kurchatov Institute” B. P. Konstantinov Petersburg Nuclear Physics Institute,
Gatchina, St. Petersburg, Russia*

E-mail: ^a*skorodumina@gmail.com*

¹ Contents

² 1	Introduction	4
³ 2	Event selection	7
⁴ 2.1	Particle identification	8
⁵ 2.1.1	Electron identification	9
⁶ 2.1.2	Hadron identification	21
⁷ 2.2	Momentum corrections	26
⁸ 2.2.1	Proton momentum correction (energy loss)	26
⁹ 2.2.2	Electron momentum correction	27
¹⁰ 2.3	Other cuts	30
¹¹ 2.3.1	Fiducial cuts	30
¹² 2.3.2	Data quality check	39
¹³ 2.3.3	Vertex cut	40
¹⁴ 2.4	Exclusivity cut in the presence of Fermi smearing and FSI	45
¹⁵ 2.4.1	Fully exclusive topology	50
¹⁶ 2.4.2	π^- missing topology	54
¹⁷ 3	Cross section calculation	57
¹⁸ 3.1	W -smearing and boundary blurring of the Q^2 versus W distribution	57
¹⁹ 3.2	Lab to CMS transformation	60
²⁰ 3.3	Kinematic variables	62
²¹ 3.4	Binning and kinematic coverage	67
²² 3.5	Cross section formulae	70

23	3.5.1 Electron scattering cross section	70
24	3.5.2 Virtual photoproduction cross section	71
25	3.6 Efficiency evaluation	73
26	4 Corrections to the cross sections	76
27	4.1 Filling kinematic cells with zero acceptance	76
28	4.2 Radiative correction	81
29	4.3 Unfolding the effects of the target motion	83
30	4.4 Correction for binning effects	87
31	5 Other issues	92
32	5.1 The cross section dependence on the beam energy	92
33	5.2 Off-shell effects	93
34	6 Normalization verification	94
35	7 Cross section uncertainties	101
36	7.1 Statistical uncertainties	101
37	7.2 Model dependent uncertainties	103
38	7.3 Systematic uncertainties	104
39	7.4 Summary for the cross section uncertainties	107
40	8 Results and conclusion	109
41	Appendices	114
42	A: Features of missing mass distributions	114
43	B: Lab to CMS transformation for the case of proton at rest	120
44	C: The reaction phase-space	122
45	D: Uncertainties for indirect measurements	123
46	E: Analysis procedure and code availability	124
47	F: Measured single-differential cross sections	126
48	Bibliography	177

⁴⁹ **Chapter 1**

⁵⁰ **Introduction**

⁵¹ Exclusive meson photo- and electroproduction reactions off protons are intensively studied
⁵² in laboratories all over the world as a very powerful tool for the investigation of nucleon
⁵³ structure and the principles of the strong interaction. These studies include the extraction
⁵⁴ of various observables through the analysis of the experimental data and the consequent
⁵⁵ theoretical and phenomenological interpretations of these observables [1–3].

⁵⁶ By now exclusive reactions off the free proton have been studied in considerable de-
⁵⁷ tail, and a lot of information on differential cross sections and different single and double-
⁵⁸ polarization asymmetries with almost complete coverage of the final hadron phase-space is
⁵⁹ available. A large part of this information came from the analysis of data collected in Hall
⁶⁰ B at Jefferson Lab with the CLAS detector [4] and stored in the CLAS physics database [5].

⁶¹ Meanwhile, reactions occurring in photon and electron scattering off nuclei are less ex-
⁶² tensively investigated, i.e. the experimental information on these processes is scarce and
⁶³ mostly limited to the inclusive measurements of total nuclear photoproduction cross sec-
⁶⁴ tions [6–8] and nucleon structure function F_2 [9–11]. The available inclusive data, however,
⁶⁵ exhibit some surprising peculiar features not fully elucidated over the years, which are now
⁶⁶ attracting significant scientific attention. Specifically, the nuclear photoproduction cross sec-
⁶⁷ tion (per nucleon) turns out to be less pronounced and damped in strength compared with
⁶⁸ the cross section off the free proton. This effect manifests itself differently depending on the
⁶⁹ invariant mass range, i.e. the $\Delta(1232)$ -resonance peak is damped, but still evident for all nu-
⁷⁰ clei, however, the second resonance region becomes somewhat less pronounced and damped
⁷¹ for the deuteron and strongly suppressed and structureless for all heavier nuclei. A similar
⁷² effect is observed in the behavior of the nucleon structure function F_2 , which in the case of
⁷³ the deuteron shows moderate damping and flattening [10] and completely loses its structure,
⁷⁴ when measured off carbon [11] (compared with the free proton structure function [12]). A
⁷⁵ fact of particular interest is that the intensity of this effect increases as Q^2 grows, i.e. as $Q^2 =$
⁷⁶ 3 GeV^2 is reached, the structure function F_2 becomes almost flat even for the deuteron [11].
⁷⁷ These peculiar features can not be explained by the Fermi motion of nucleons in the nucleus

78 and are thought to be an indication that nucleons and their excited states, bound inside the
79 nuclear medium, may be subject to some modifications of their properties [6–8, 13, 14].

80 This phenomenon, which is still not fully understood, generates lots of debates among
81 scientists, triggering efforts to describe the processes that happen in reactions off bound
82 nucleons. These studies rely heavily on the experimental data, which at the moment are
83 mostly limited to inclusive measurements [6–11] and lack information on exclusive reactions.
84 This information, however, is crucial, since various exclusive channels have different energy
85 dependencies and different sensitivity to reaction mechanisms. This situation creates a strong
86 demand for exclusive measurements off bound nucleons, and the deuteron, being the lightest
87 and weakly-bound nucleus, is the best target for initiating these efforts.

88 This study provides the first results of cross section measurements for the exclusive
89 process of charged double-pion electroproduction off the proton bound in the deuteron. The
90 results are obtained through the analysis of experimental data on electron scattering off the
91 deuteron target, collected with the CLAS detector. The measurements are performed in
92 the second resonance region, where the double-pion production plays an important role, i.e.
93 the channel opens at the double-pion production threshold at $W \approx 1.22$ GeV, contributes
94 significantly to the total inclusive cross section for $W \lesssim 1.6$ GeV, and starts to dominate all
95 other exclusive channels for $W \gtrsim 1.6$ GeV .

96 The experimental identification of exclusive multi-particle final states is a rather sophisti-
97 cated task, which requires certain analysis techniques to be elaborated and established. This
98 was carried out over the last twenty years as the different studies of double-pion production
99 off the free proton were being performed [15–23], and currently a solid framework for such
100 studies is in place. For this particular study, focused on the $N\pi\pi$ final state, this framework
101 laid the foundation. However, the deuteron as a target introduces some specific issues, which
102 are external to the free proton data analysis and originate from (a) the motion of the target
103 proton in the deuteron and (b) complex effects of the final state interactions due to the
104 presence of the additional nucleon. This caused some difficulties that were encountered and
105 needed to be overcome during the analysis and, therefore, in this report special attention is
106 paid to a detailed description of these issues.

107 Specifically, the report presents the integrated and single-differential cross sections of the
108 reaction $\gamma_vp(n) \rightarrow p'(n')\pi^+\pi^-$ in the kinematic region of invariant mass W from 1.3 GeV
109 to 1.825 GeV and photon virtuality Q^2 from 0.4 GeV 2 to 1 GeV 2 . Sufficient experimental
110 statistics allows narrow binning, e.g. 25 MeV in W and 0.05 GeV 2 in Q^2 , while maintaining
111 an adequate statistical uncertainty. Cross sections are extracted in the quasi-free regime,
112 which implies that only events not affected by final state interactions were selected.

113 This study benefits from the fact that the corresponding cross sections of the same exclu-
114 sive reaction off the free proton have been recently extracted from CLAS data [22, 23]. These
115 free proton measurements were performed under the same experimental conditions as the
116 cross sections of this study, including the beam energy value and the target setup. For the
117 majority of (W, Q^2) points, the statistical uncertainty combined with the model dependent

¹¹⁸ uncertainty ($\delta_{\text{stat, mod}}^{\text{tot}}$) is on a level of $\sim 1\%-3\%$ for the free proton integral cross sections and
¹¹⁹ on a level of $\sim 4\%-6\%$ for the quasi-free integral cross sections obtained in this study. Being
¹²⁰ performed in the same experimental configuration, both measurements have identical bin-
¹²¹ ning in all kinematic variables and similar inherent systematic inaccuracies. Therefore, the
¹²² direct comparison of these two sets of cross sections provides experimentally the best possi-
¹²³ ble opportunity to investigate the differences and alterations (including possible in-medium
¹²⁴ modifications) that occur in the exclusive reaction off the bound proton in comparison with
¹²⁵ that off the free proton. This comparison also allows us to better understand the influence
¹²⁶ of Fermi motion and final state interactions on the cross sections.

¹²⁷ A few example plots, which demonstrate the difference between integral cross sections
¹²⁸ obtained in this analysis and their free proton analogue from Ref. [22, 23] are given in Sect. 8
¹²⁹ of this report. Meanwhile, the complete compilation of this comparison as well as the full
¹³⁰ physical discussion of the results and their physical interpretation will be presented in the
¹³¹ PhD thesis (which is in preparation) and a future publication on the subject.

¹³² **Chapter 2**

¹³³ **Event selection**

¹³⁴ This report presents the analysis of experimental data that were collected at JLab Hall B
¹³⁵ with the CLAS detector [4]. The measurements were part of the “e1e” run period that
¹³⁶ lasted from November 2002 until January 2003 and included several parts with different
¹³⁷ beam energies (1 GeV and 2.039 GeV) and different target cell content (liquid hydrogen and
¹³⁸ liquid deuterium). The torus current was 2250 A and the mini torus current 5995 A. This
¹³⁹ particular analysis concentrates on the dataset obtained with the 2-cm-long liquid deuterium
¹⁴⁰ target and a 2.039 GeV polarized electron beam. The range of run numbers is 36516 - 36615.

¹⁴¹ All data collected with the CLAS detector is stored in a specific format, which is BOS
¹⁴² format [24, 25]. The information on the detector response to particles passing through is
¹⁴³ recorded for each event and sorted into the set of BOS banks. The original BOS files store the
¹⁴⁴ data in terms of “raw” signals (like TDC, ADC). These “raw” files are then “cooked” with
¹⁴⁵ the reconstruction software (reccsis), which converts the detector response to the variables
¹⁴⁶ that characterize the events directly, i.e. the particle momentum, the track coordinates,
¹⁴⁷ timing, etc. This information is also stored in BOS banks. However, since the cooking
¹⁴⁸ process introduces new variables, the structure of the “cooked” BOS files is different from
¹⁴⁹ that for the “raw” files. The “cooked” data is stored in various formats including BOS files
¹⁵⁰ and ROOT ntuples. In this analysis the latter were used¹.

¹⁵¹ Events corresponding to the investigated reaction $ep(n) \rightarrow e'p'(n')\pi^+\pi^-$ are distinguished
¹⁵² among all other registered events through the event selection procedure, described in detail
¹⁵³ in this Section. The selected exclusive events, however, represent only a part of the total
¹⁵⁴ number of events produced in the reaction, while the remainder were not registered due to
¹⁵⁵ (i) geometrical holes in the detector acceptance and (ii) less than 100% efficiency of particle
¹⁵⁶ detection within the detector acceptance. Therefore, to extract the reaction cross section,
¹⁵⁷ the experimental event yield should be adjusted for the geometric and detection efficiency,
¹⁵⁸ thus accounting for the lost events.

¹ The location of the data files is provided in App. E. The link to the scripts, which were used in the simulation/reconstruction sequence for this analysis is also given there.

159 In order to determine the detector efficiency, a Monte Carlo simulation is typically per-
160 formed. In this analysis, double-pion events are generated with TWOPEG-D, which is an
161 event generator for the double-pion electroproduction off a moving proton [26]. These events
162 are hereinafter called “generated” events.

163 The generated events are passed through a standard multi-stage procedure of simulating
164 the detector response [4]. At the first stage the interaction of the generated events with the
165 CLAS detector is simulated. For this purpose, the GSIM package (GEANT SIMulation) is
166 used. GSIM incorporates information about the detector geometry and materials with their
167 electromagnetic properties, magnetic fields, target material and geometry, etc. It propagates
168 all the particles through the CLAS detector from the vertex produced by the event generator
169 and provides the detector response in terms of the same “raw” signals as the actual CLAS
170 detector does.

171 Although the GSIM package includes all the detector geometry and properties, it still
172 does not properly reproduce the resolution of the drift chambers and the TOF system. So
173 the GSIM Post Processor (GPP) is used to better match the resolution as well as to include
174 the effects of less-than-perfect detector response (due to broken drift wires, problematic
175 phototubes, etc.). The latter effects are unique for a particular run period, and therefore the
176 information on the detector imperfections is usually provided along with the data files to be
177 then used in the GPP. Meanwhile, the GPP parameters intended to adjust the resolution
178 (DC and TOF smearing factors) are typically determined individually during a particular
179 analysis as the resolution depends on kinematics and hence on experimental conditions.
180 This analysis uses the same resolution related GPP parameters as those determined in the
181 study [22, 23], which reports the cross section measurements off the free proton performed
182 under the same experimental conditions (as they were also a part of the “e1e” run period).

183 At the final stage the GPP output files are “cooked” using the same reconstruction
184 software that was used for the real data (recois). Events that survive after the “cooking”
185 process are hereinafter called “reconstructed” Monte Carlo events. They are analyzed in the
186 same way as real experimental events.

187 2.1 Particle identification

188 The CLAS detector consists of six sectors that are operated as independent detectors [4].
189 Each sector includes four sub-detectors: Drift Chambers (DC), Čerenkov Counters (CC),
190 Time-of-Flight System (TOF), and Electromagnetic Calorimeters (EC).

191 In the initial analysis step, all collected events are subject to a standard event preselec-
192 tion², which is performed using specific variables from the BOS banks [24, 25]. Firstly, to

²In this analysis this preselection is performed when converting the “h10” ROOT ntuples to the “t21” ROOT ntuples. See more details in App. E

193 ensure that particles within an event were properly reconstructed, the number of geometri-
194 cally reconstructed particles (*gpart*) is required to be greater than zero for each event. The
195 *gpart* variable is extracted from the variable *NPGP* in the HEVT bank according to the
196 following relation,

$$NPGP = (\text{Number of final reconstructed particles}) \times 100 + gpart. \quad (2.1.1)$$

197 Then, to exclude from consideration out-of-time particles, the status word *stat* (which
198 corresponds to the variable *Status* in the EVNT bank) is required to be greater than zero
199 for each particle candidate.

200 For each event the electron candidate is defined as the first in time particle that gives
201 signals in all four parts of the CLAS detector (DC, CC, TOF, and EC), which means that the
202 variables *DCStat*, *CCStat*, *SCStat*, and *ECStat* from the EVNT bank should be greater
203 than zero. To select hadron candidates, signals only in two sub-detectors (DC and TOF)
204 are required, i.e. the variables *DCStat* and *SCStat* from the EVNT bank should be greater
205 than zero.

206 Finally, all particle candidates should have an appropriate charge, i.e. the variable
207 *Charge* from the EVNT bank is required to be ± 1 depending on the candidate type.

208 The particle candidates that survive this event preselection are then subject to further
209 detailed selection, which is described below.

210 2.1.1 Electron identification

211 Firstly, the electromagnetic calorimeter (EC) and Čerenkov counter (CC) responses need to
212 be examined, to reveal good electrons among all electron candidates and to separate them
213 from electronic noise, accidentals and the contamination from negative pions.

214 EC cuts

215 According to [27], the overall EC resolution as well as uncertainties from the EC output
216 summing electronics lead to fluctuations of the EC response near the hardware threshold.
217 Therefore, to select only reliable EC signals, a minimal cut on the scattered electron mo-
218 mentum $P_{e'}$ should be applied in the software. The value of this cut is chosen according to
219 the relation (2.1.2) suggested in [27],

$$P_{e'}^{min} \text{ (in MeV)} = 214 + 2.47 \cdot V_{th} \text{ (in mV)}, \quad (2.1.2)$$

220 where V_{th} is the calorimeter threshold voltage.

221 For “e1e” run $V_{th} = 100$ mV, which results in $P_{e'}^{min} = 461$ MeV.

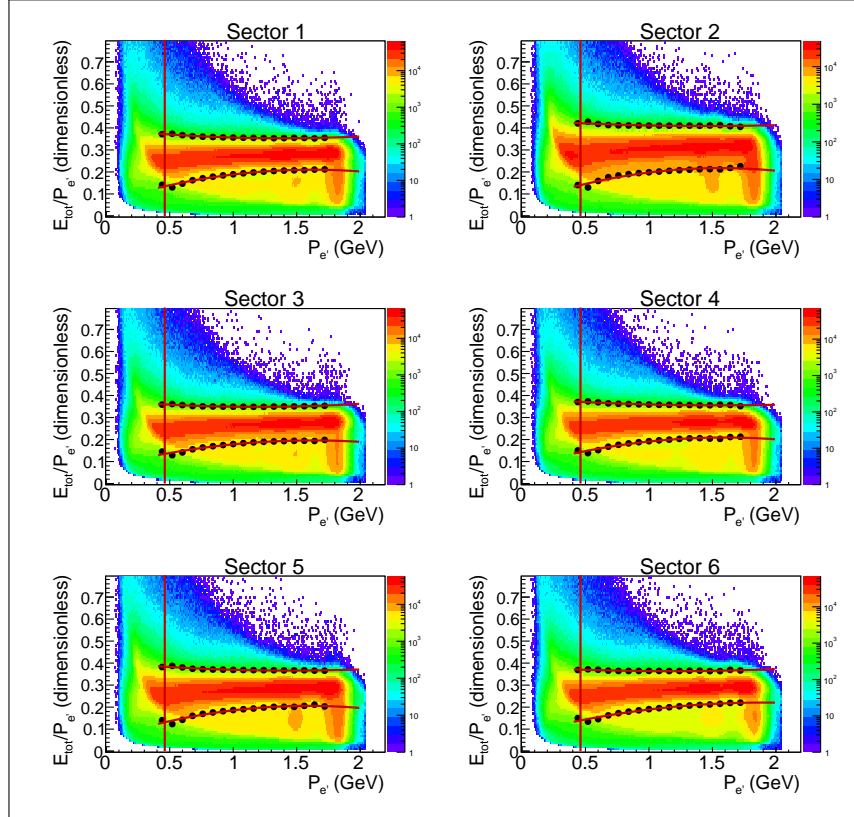


Figure 2.1: Sampling fraction distributions for the data. The six plots correspond to the six CLAS sectors. The vertical red line at $P_{e'} = 0.461$ GeV shows the EC threshold cut. Black points correspond to the positions of Gaussian fit maxima $\pm 3\sigma$ for different X -slices of the 2D histograms. These points are fit by a second order polynomial, the resulting functions are shown by the red curves. Events between the red curves are selected for further analysis.

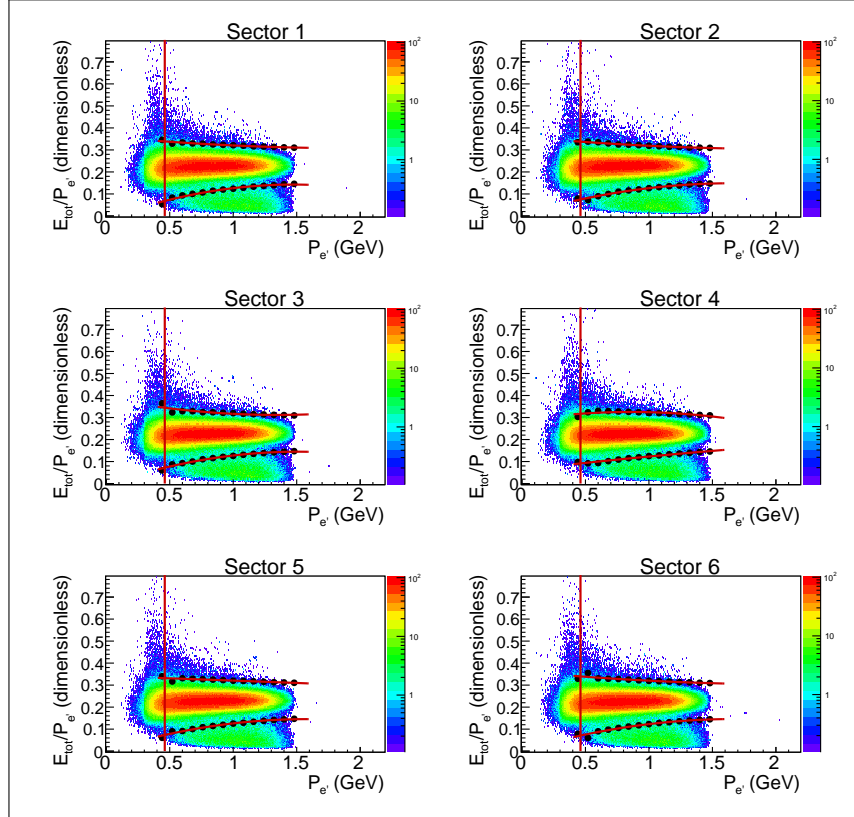


Figure 2.2: Sampling fraction distributions for the reconstructed Monte Carlo events. The six plots correspond to the six CLAS sectors. The vertical red line at $P_{e'} = 0.461$ GeV shows the EC threshold cut. Black points correspond to the positions of Gaussian fit maxima $\pm 3\sigma$ for different X -slices of the 2D histograms. These points are fit by a second order polynomial, the resulting functions are shown by the red curves. Events between red curves are selected for further analysis.

Then, the so-called sampling fraction cut is applied to eliminate part of the pion contamination. To develop this cut, the fact that electrons and pions have different energy deposition patterns in the EC is used. An electron produces an electromagnetic shower, where the deposited energy E_{tot} is proportional to the scattered electron momentum $P_{e'}$, while a π^- loses a constant amount of energy per scintillator (~ 2 MeV/cm) independently of its momentum. Therefore, for electrons the quantity $E_{tot}/P_{e'}$ plotted as a function of $P_{e'}$ should follow the straight line that is parallel to the x -axis and located around the value $1/3$ on the y -axis, since electrons lose about $2/3$ of their energy in lead sheets (in reality this line has a slight slope).

In Fig. 2.1 the total energy deposited in the EC divided by the particle momentum is shown as a function of particle momentum. The six plots correspond to the six CLAS sectors. Events between the red curves are selected as good electron candidates for further analysis. The vertical red line at $P_{e'} = 0.461$ GeV shows the EC threshold cut. The upper and lower red curves are obtained in the following way: X -slices of the 2D histograms are fit by Gaussians. In this way points that correspond to the positions of the fit maxima $\pm 3\sigma$ are obtained. These points are shown by black circles in Fig. 2.1. They determine the upper and lower boundaries for the cut. Finally, to obtain smooth curves, all points are fit by a second order polynomial.

Cuts on the minimal electron momentum and on sampling fraction are applied both to the experimental and reconstructed Monte Carlo events. Since the Monte Carlo simulation does not reproduce electromagnetic showers well enough, the sampling fraction distributions for the simulation are slightly lower than for the data. EC cuts for the simulation, obtained using the same procedure as for the data, are shown in Fig. 2.2. These plots contain no events with $P_{e'} > 1.5$ GeV since only double-pion events were generated, while for the data events with $P_{e'} > 1.5$ GeV exist since Figure 2.1 was plotted for inclusive electrons.

CC cuts

To improve the quality of the electron candidate selection and π^-/e^- separation, a Čerenkov counter is used [28]. As shown in [29], there is a contamination in the measured CC spectra that manifests itself as a so-called single-photoelectron peak, which is actually located at a few photoelectrons (see the distributions shown in black in Fig. 2.5). The main source of this contamination are accidental coincidences of PMT noise signals with measured pion tracks [29]. The goal of CC cuts is to separate the spectrum of good electron candidates (it corresponds to the main maximum of the photoelectron distribution) from the single-photoelectron peak, but at the same time to minimize the loss of good events. As seen in Fig. 2.5 (black curves), where photoelectron distributions are plotted, the single-photoelectron peak is rather pronounced and it significantly overlaps with the spectrum of good electron candidates. Thus the elimination of this contamination is not a straightforward task and a special procedure has been developed for this purpose.

260 The following set of CC cuts was applied:

- 261 • fiducial cut,
262 • φ_{cc} matching cut,
263 • θ_{cc} matching cut,
264 • geometrical cut that removes inefficient zones, and
265 • standard procedure of dealing with the single-photoelectron peak contamination based
266 on the fit of the photoelectron distributions by the modified Poisson function.

267 All these cuts, except the last one, are defined in the so-called “CC projective plane” [29].
268 This is an imaginary plane behind the CC where the Čerenkov radiation would arrive if its
269 polygonal (due to reflections in the mirror system) path from the emission point to the PMT
270 was substituted by a straight line preserving the initial propagation direction and the total
271 distance traveled [28, 29]. The polar and azimuthal angles ($\theta_{cc}, \varphi_{cc}$), which are defined in
272 this projective plane, are not directly available in the BOS banks [24]. Therefore, some
273 calculations are made to derive these angles from the variables available in the DCPB bank.
274 Figure 2.3 illustrates these calculations.

275 The CC projective plane is defined in the sector reference coordinate system, i.e. the
276 sector is bisected in the middle by the xz -plane with the z -axis directed along the beam line.
277 In this reference system the equation of the projective plane is the following (according to
278 Ref. [29]),

$$\begin{aligned} Ax + By + Cz + D &= 0, \\ A &= -0.000785, \quad B = 0, \\ C &= -0.00168, \quad D = 1, \\ \vec{S} &= (A, B, C), \end{aligned} \tag{2.1.3}$$

279 where \vec{S} is a vector perpendicular to the projective plane.

280 In Fig. 2.3 the particle track in the DC is shown by the thin dashed curve. Since the
281 particle moves through a magnetic field in the DC, the track is curved. Having left the
282 magnetic field region of the DC, the particle moves further along a straight line, tangential
283 to a curved DC track in the point of its intersection with the CC. The unit vector that
284 defines the direction of this tangent is known from the DCPB bank $\vec{n} = (n_x, n_y, n_z) =$
285 $(\text{CX_SC}, \text{CY_SC}, \text{CZ_SC})$. In Fig. 2.3 the vector \vec{t} is pointing this direction and goes from
286 the SC hit point to the CC projective plane.

287 The $(\theta_{cc}, \varphi_{cc})$ angles in the projective plane are determined by the vector $\vec{P} = \vec{P}_0 + \vec{t}$,
288 where \vec{P}_0 is a vector that goes from the vertex to the point of the track intersection with the
289 SC. Its components are known from the DCPB bank $\vec{P}_0 = (p_x^0, p_y^0, p_z^0) = (\text{x_SC}, \text{y_SC}, \text{z_SC})$ ³.

³ In the DCPB bank both \vec{n} and \vec{P}_0 are defined in the sector reference frame.

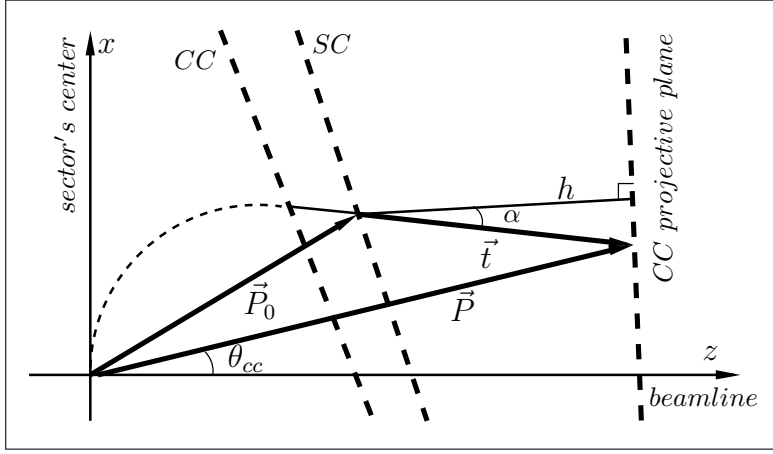


Figure 2.3: Illustration for the calculation of the polar θ_{cc} and azimuthal φ_{cc} angles in the CC projective plane (see text for details).

²⁹⁰ The vector \vec{t} can be defined as

$$\vec{t} = |\vec{t}| \cdot \vec{n} = \frac{h}{\cos \alpha} \cdot \vec{n}, \quad (2.1.4)$$

²⁹¹ where \vec{n} is the unit vector in the \vec{t} -direction defined above, while h is the distance from
²⁹² the SC hit point to the CC projective plane, which is given by⁴

$$h = \frac{|(\vec{S} \cdot \vec{P}_0) + D|}{|\vec{S}|}, \quad (2.1.5)$$

²⁹³ where \vec{S} is the vector normal to the CC projective plane defined by Eq. (2.1.3).

²⁹⁴ In turn $\cos \alpha$ can be calculated as

$$\cos \alpha = \frac{|(\vec{S} \cdot \vec{n})|}{|\vec{S}|}, \quad (2.1.6)$$

²⁹⁵ since \vec{S} is directed along h and \vec{n} is directed along \vec{t} .

²⁹⁶ This leads to the following expression for the vector \vec{t} ,

$$\vec{t} = |\vec{t}| \cdot \vec{n} = \left| \frac{(\vec{S} \cdot \vec{P}_0) + D}{(\vec{S} \cdot \vec{n})} \right| \cdot \vec{n} = \left| \frac{A \cdot p_x^0 + B \cdot p_y^0 + C \cdot p_z^0 + D}{A \cdot n_x + B \cdot n_y + C \cdot n_z} \right| \cdot \vec{n}. \quad (2.1.7)$$

⁴This is a standard relation for the distance from the point (given here by the vector \vec{P}_0) to the plane $Ax + By + Cz + D = 0$.

297 Then, obtaining the required vector \vec{P} as the sum of \vec{P}_0 and \vec{t} , one can finally calculate
 298 the angles θ_{cc} and φ_{cc} as

$$\begin{aligned}\theta_{cc} &= \arccos\left(\frac{P_z}{|\vec{P}|}\right), \\ \varphi_{cc} &= \arctan\left(\frac{P_y}{P_x}\right).\end{aligned}\tag{2.1.8}$$

299 The angle φ_{cc} defined by Eq. (2.1.8) is determined with respect to the center of each
 300 sector. This means that $\varphi_{cc} = 0$ is the middle of the sector, $\varphi_{cc} < 0$ is on the left side of the
 301 sector, and $\varphi_{cc} > 0$ is on its right side.

302 One should also define the variables *CC segment number* (that indicates which segment
 303 has been hit) and *index* (that indicates which PMT has fired). They are taken from the
 304 CCPB bank *Status* variable according to the following relation,

$$Status = 10 \times (\text{CC segment number}) + 1000 \times (1 + \text{index}),\tag{2.1.9}$$

305 where *index* is 1 for right PMTs, -1 for left PMTs, and 0 when both PMTs have fired.

306 After all needed variables have been defined, all the cuts from the list specified above
 307 can be implemented.

308 First of all the fiducial cut in the CC plane is applied. The shape of this cut is taken
 309 from [30] and is given by

$$\begin{aligned}\theta_{cc} &> 7.0 + 0.0032 \cdot \varphi_{cc} + 0.0499 \cdot \varphi_{cc}^2, \\ \left(\frac{\theta_{cc} - 45.5^\circ}{34.5^\circ}\right)^2 + \left(\frac{\varphi_{cc}}{21^\circ}\right)^2 &\leq 1, \\ \left(\frac{\theta_{cc} - 45.5^\circ}{1.75^\circ}\right)^2 + \left(\frac{\varphi_{cc}}{21^\circ}\right)^2 &> 1, \text{ and} \\ \theta_{cc} &< 45^\circ.\end{aligned}\tag{2.1.10}$$

310 Then the so-called φ_{cc} and θ_{cc} matching procedures (based on the studies [29] and [31]) are
 311 performed. The idea of this matching is quite simple: there must be one-to-one correspon-
 312 dence between the angles in the CC plane (which are calculated based on the information
 313 from the DC) and PMT signals in the CC for real events, while background noise and
 314 accidentals should not show such correlation.

315 The principle of the φ_{cc} matching cut is the following: when the track is on the right side
 316 of the CC segment, the right PMT should be fired, and vice versa. Therefore, if $\varphi_{cc} < 0$,
 317 the *index* defined in Eq. (2.1.9) is required to be -1 and if $\varphi_{cc} > 0$, the *index* is required
 318 to be 1. Events that do not satisfy these conditions are removed. All events with *index* = 0
 319 are kept.

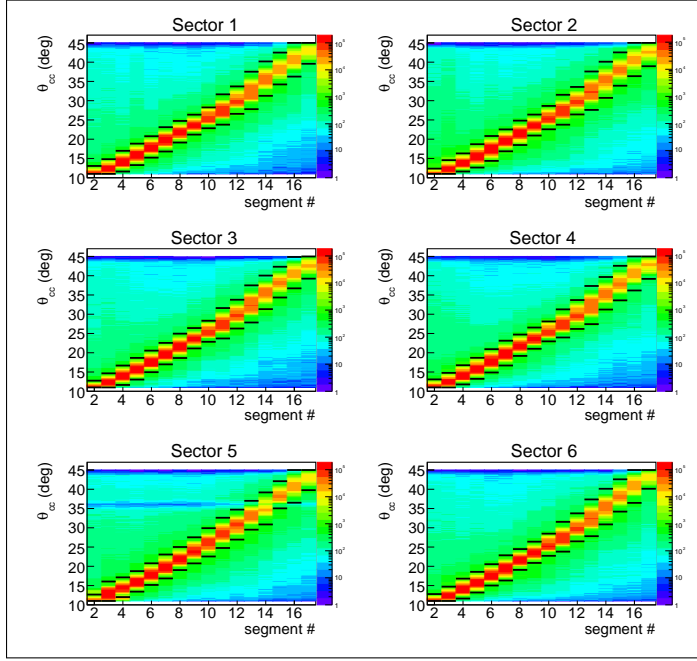


Figure 2.4: θ_{cc} versus segment distributions for six CLAS sectors. Events between the horizontal black lines are treated as good electron candidates.

321 In order to perform θ_{cc} matching, the θ_{cc} versus segment number cut should be done.
 322 Figure 2.4 shows θ_{cc} versus segment distributions for the six CLAS sectors. Event distri-
 323 butions in each segment have been plotted as a function of θ_{cc} and fit by Gaussians. The
 324 horizontal black lines correspond to the positions of the fit maxima $\pm 4\sigma$. Events between
 325 these black lines are treated as good electron candidates.

326 The influence of φ_{cc} and θ_{cc} matching cuts on the photoelectron distributions is demon-
 327 strated in Fig. 2.5, where the distributions before matching cuts are plotted in black, distri-
 328 butions after the φ_{cc} matching are plotted in red, and after the subsequent θ_{cc} versus segment
 329 cut are plotted in blue. As seen in Fig. 2.5 both these cuts reduce the single-photoelectron
 330 peak, but leave the main part of the spectrum unchanged. The same φ_{cc} and θ_{cc} matching
 331 cuts are also applied to the reconstructed Monte Carlo events.

322 The accidental noise and pion background are not the only source of the single-
 323 photoelectron peak contamination. The peak also partially corresponds to electrons that
 324 hit some specific geometrical zones with low CC efficiency. When an electron hits such a
 325 zone the number of detected photoelectrons turns out to be significantly less than expected.
 326 This leads to the fact that the region of the photoelectron spectrum, which corresponds to the
 327 low number of photoelectrons, appears to be overpopulated by events. Since low efficiency
 328 zones are distributed inhomogeneously in the CC plane and the Monte Carlo simulation do
 329 not reproduce them properly, it is better to remove them from the consideration completely.

340 For this purpose a special geometrical cut is established.

341 This geometrical cut is done in the following way. Distributions φ_{cc} versus θ_{cc} are plotted
342 for each CLAS sector (see Fig. 2.6, upper frame) with the quantity (2.1.11) as a color code.

$$\frac{\text{number of events inside } (\theta_{cc}, \varphi_{cc}) \text{ bin with more than five photoelectrons}}{\text{total number of events inside } (\theta_{cc}, \varphi_{cc}) \text{ bin}} \quad (2.1.11)$$

343 This quantity varies from zero to one and shows the proportion of electron candidates with
344 number of photoelectrons greater than five inside a $(\theta_{cc}, \varphi_{cc})$ bin. The value for this criterion
345 (five photoelectrons) was chosen rather arbitrarily, since its only purpose is to facilitate the
346 separation of inefficient zones (which correspond mostly to low numbers of photoelectrons)
347 from the regular zones (which correspond to the full photoelectron spectrum).

348 The curved vertical stripe in sector five in Fig. 2.6 corresponds to an inefficient zone that
349 will be discussed further in Sec. 2.3.1.

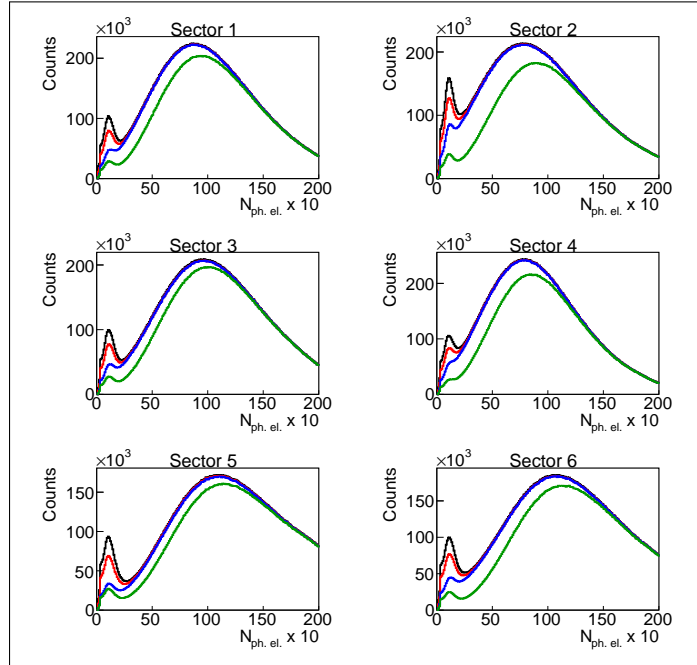


Figure 2.5: Influence of different CC cuts on the distributions of the number of photoelectrons multiplied by ten for the six CLAS sectors. Black curve – only fiducial cut in the CC plane is applied, red curve – the φ_{cc} matching cut is added, blue curve – the θ_{cc} matching cut is added, and green curve – the geometrical cut in the CC plane that removes inefficient zones is finally added.

350 For further analysis only fiducial areas with a ratio (2.1.11) greater than the certain
351 threshold value are selected. This threshold value was chosen to be 0.7, 0.65, 0.7, 0.65,
352 0.8, and 0.8 for sectors 1, 2, 3, 4, 5, and 6, respectively. Since inefficient zones are not

353 identical for various CLAS sectors (see Fig. 2.6), different threshold values are needed for
 354 them. Geometrical zones, which are selected for further analysis, are shown in black in the
 355 lower plots of Fig. 2.6. All zones shown in white are treated as inefficient and are removed
 356 from the analysis. As seen in Fig. 2.6, there is an inefficient zone in the middle of each sector.
 357 This is expected since two CC mirrors are joined here.

358 The threshold values for the ratio (2.1.11) were chosen in order to keep the balance be-
 359 tween the intention to reduce the amount of low efficient zones as much as possible and the
 360 desire to preserve most of the statistics. The influence of this geometrical cut on the photo-
 361 electron distributions in different sectors is demonstrated in Fig. 2.5, where the distributions
 362 after the cut are plotted in green. As was expected, this cut leads to some reduction in the
 363 low lying part of the photoelectron spectrum, including the region of the single-photoelectron
 364 peak, and leaves the high lying part of the spectrum unchanged.

365 This geometrical cut is fully based on the experimental data. It acts as a fiducial cut,
 366 because it simply removes certain geometrical regions in the CC plane. This means that
 367 it can be safely applied to the Monte Carlo simulation, too. Thus, the same geometrical
 368 regions (shown in white in the lower plots in Fig. 2.6) are removed both for the experimental
 369 and reconstructed Monte Carlo events.

370 After the geometrical cut discussed above is applied, the single-photoelectron peak ap-
 371 pears to be significantly smaller and better separated from the main spectrum, but still
 372 remains (see Fig. 2.5). Therefore, in order to completely get rid of this contamination, the
 373 standard procedure should then be applied [17].

374 To apply the standard procedure of dealing with the single-photoelectron peak contami-
 375 nation, the photoelectron distributions are plotted for each PMT on the left and right sides
 376 of each CC segment and for each CLAS sector (see Fig. 2.7).

377 In Fig. 2.7 the red lines show the cuts that are made in order to eliminate events under
 378 the single-photoelectron peak. The cut position is individually optimized for each PMT in
 379 each sector. The distributions of events, for which both right and left PMTs have fired
 380 (*index* = 0) are not subject to this cut, since their contamination caused by the single-
 381 photoelectron peak is assumed negligible.

382 Since the Monte Carlo does not reproduce photoelectron distributions well enough, the
 383 cut shown by the red lines in Fig. 2.7 is applied only to the data. To recover the good electrons
 384 that were cut off in this way, a special procedure is applied. The part of the distributions
 385 on the right side of the red line is fit by the function (2.1.12), which is a slightly modified
 386 Poisson distribution.

$$y = P_1 \left(\frac{P_3^{\frac{x}{P_2}}}{\Gamma \left(\frac{x}{P_2} + 1 \right)} \right) e^{-P_3}, \quad (2.1.12)$$

387 where P_1 , P_2 , and P_3 are free fit parameters.

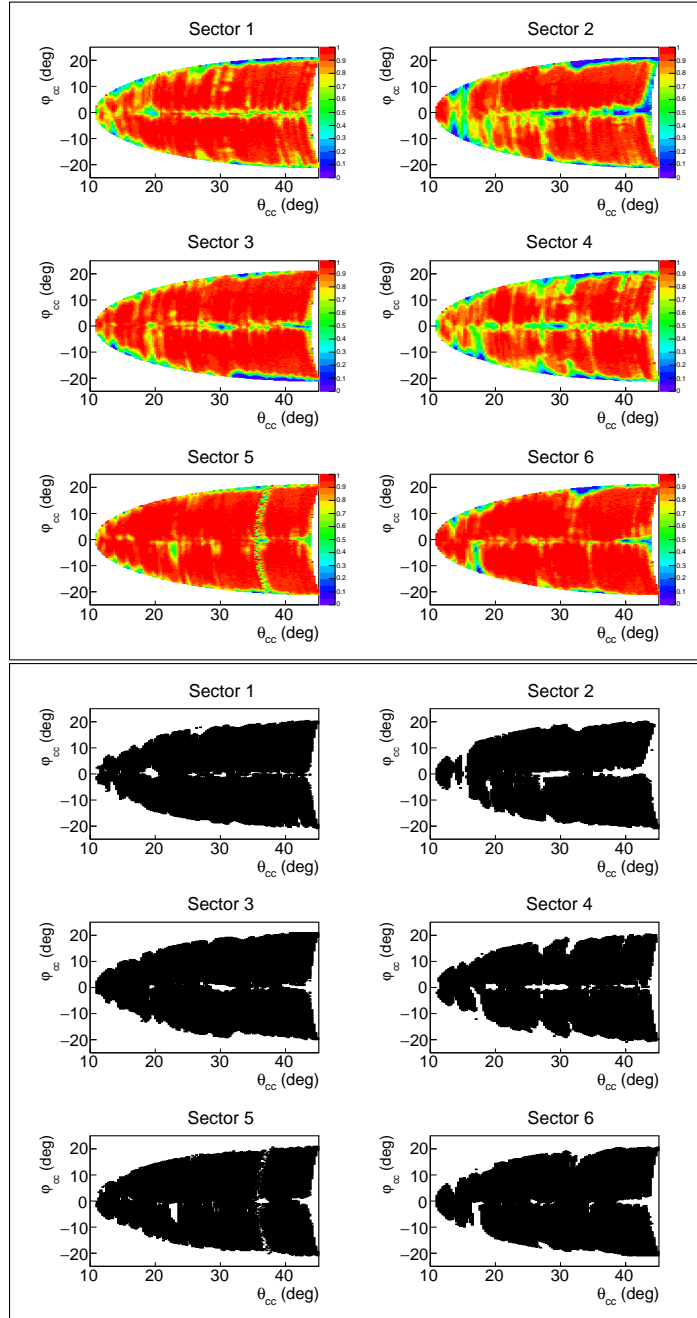


Figure 2.6: Upper frame: Distributions of the quantity (2.1.11) as a function of the polar θ_{cc} and azimuthal φ_{cc} angles in the CC plane for the six CLAS sectors. This quantity varies from zero to one and shows the proportion of electron candidates with number of photoelectrons greater than five inside a $(\theta_{cc}, \varphi_{cc})$ bin. Lower frame: Black zones correspond to the fiducial areas with the ratio (2.1.11) greater than 0.7, 0.65, 0.7, 0.65, 0.8, and 0.8 for sectors 1, 2, 3, 4, 5, and 6, respectively. These zones are selected for further analysis. All zones shown in white are treated as inefficient and removed from the analysis.

388 The fitting function is then continued into the region on the left side of the red line.
 389 In this way the two regions, shown in blue and green in Fig. 2.7, are determined. Finally
 390 the correction factors are defined by (2.1.13) and applied as a weight for each event, which
 391 goes to the particular PMT. These correction factors depend on the PMT number and are
 392 typically on a level of a few percent.

$$F_{ph. el.} = \frac{\text{green area} + \text{blue area}}{\text{green area}} \quad (2.1.13)$$

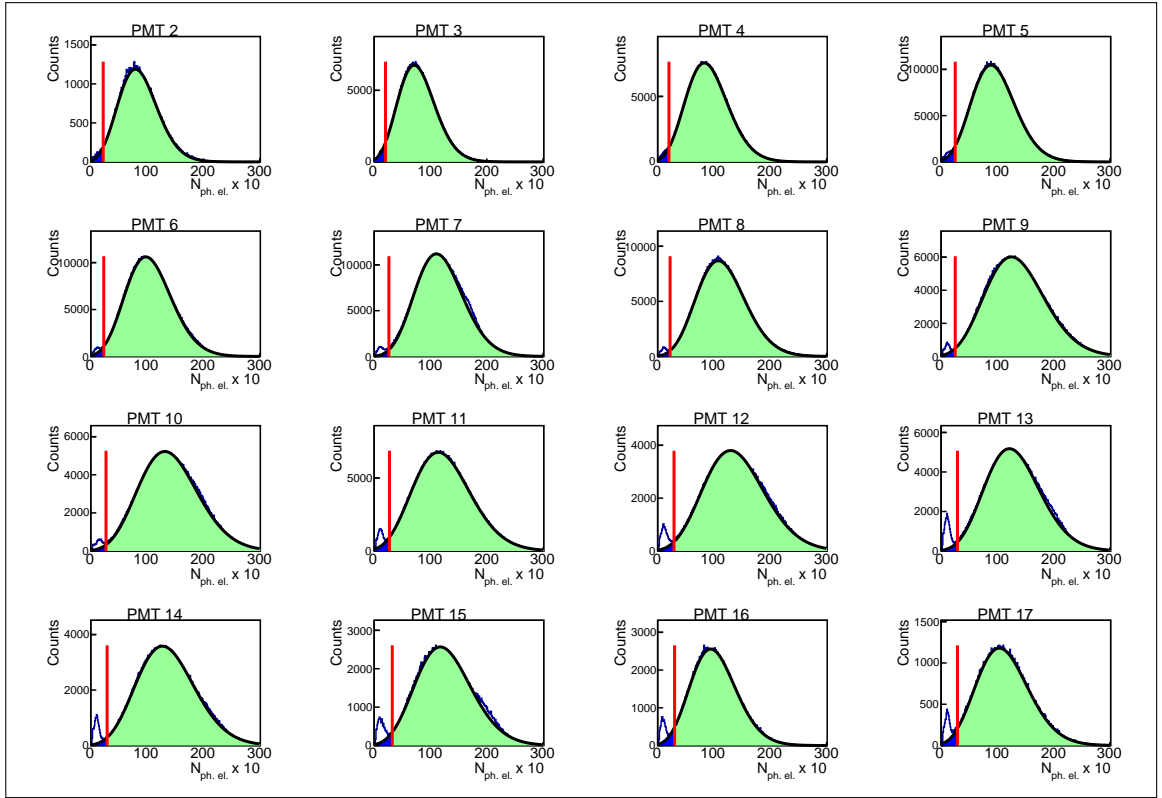


Figure 2.7: Distributions of number of photoelectrons multiplied by ten for the left side of sector one of the CC. Various plots correspond to various CC segments. Black curves show the fit by the function (2.1.12). Red vertical lines show the applied cut. Regions that are needed to calculate the correction ratio (2.1.13) are shown in blue and green.

393 Note that segments #1 and #18 are removed from the analysis completely (both in data
 394 and Monte Carlo), since they are dominated by events from the single-photoelectron peak.

395

³⁹⁶ **2.1.2 Hadron identification**

³⁹⁷ The CLAS TOF system provides information, based on which the particle velocity can be
³⁹⁸ determined. In this analysis for this purpose the following calculations were done.

$$\beta_h = \frac{v_h}{c} = \frac{l_h}{t_h \cdot c}, \quad (2.1.14)$$

³⁹⁹ where v_h is the hadron velocity, c the speed of light, l_h the hadron path length from the
⁴⁰⁰ vertex to the SC-plane (variable *Path* in the SCPB bank), and t_h the time that it took
⁴⁰¹ the hadron to travel from the vertex to the SC-plane. This time can be calculated in the
⁴⁰² following way.

$$t_h = t_e + (t_h^{t\text{of}} - t_e^{t\text{of}}) = \frac{l_e}{c} + (t_h^{t\text{of}} - t_e^{t\text{of}}), \quad (2.1.15)$$

⁴⁰³ where $t_e = \frac{l_e}{c}$ is the time that the electron spent on traveling from the vertex to the SC-plane
⁴⁰⁴ and l_e the electron path length. $t_e^{t\text{of}}$ and $t_h^{t\text{of}}$ are the times, when the electron and hadron
⁴⁰⁵ hit the SC-plane, respectively (the variable *Time* in the SCPB bank).

⁴⁰⁶ Equation (2.1.15) assumes that the hadron and electron departed from the vertex at the
⁴⁰⁷ same time, but the electron traveling with the speed of light reached the SC-plane earlier
⁴⁰⁸ than the hadron. The difference $t_h^{t\text{of}} - t_e^{t\text{of}}$ indicates the hadron delay time, which is the
⁴⁰⁹ consequence of traveling with the velocity $v_h < c$. Thus Eq. (2.1.15) makes the hadron time
⁴¹⁰ related to that of electron for each event⁵.

⁴¹¹ The charged hadron can be identified by the comparison of β_h determined from TOF
⁴¹² according to Eqs. (2.1.14) and (2.1.15) with β_n given by

$$\beta_n = \frac{p_h}{\sqrt{p_h^2 + m_h^2}}. \quad (2.1.16)$$

⁴¹³ In Eq. (2.1.16) β_n is a so-called nominal value that is calculated using the particle mo-
⁴¹⁴ mentum (p_h) known from the DC and the exact particle mass assumption (m_h).

⁴¹⁵ The usual way to develop hadron id cuts is to investigate β versus momentum distribu-
⁴¹⁶ tions for different TOF paddles for each hadron type separately. This investigation reveals
⁴¹⁷ three types of problematic paddles, i.e.

⁴¹⁸ A Paddles which signals are completely unreliable (bad paddles). These are paddles #16
⁴¹⁹ in sector 2, #44 in sector 3, #17 in sector 5, and #48 in each sector. They are excluded
⁴²⁰ from this analysis both for experimental data and reconstructed Monte Carlo events.

⁵ It worth noting that usually one uses the value of β directly defined in the EVNT bank (variable *Betta*), but it turned out that this quantity shows noticeable inaccuracies in electron bunch determination, which were made during the cooking. The value of β calculated by Eqs. (2.1.14) and (2.1.15) do not show these inaccuracies because in this method the timing of the hadron is related to that of electron for each event.

421 B Paddles in which the distributions are shifted from their expected positions. The reason
 422 for this is most likely mistakes during data cooking/calibration. Typical examples of
 423 such paddles are shown in Fig. 2.8.

424 C Paddles for which the distributions for a given hadron have double band structure. This
 425 problem appears for most of the paddles with number ≥ 40 and originates from the
 426 fact that (along with the mistakes during cooking/calibration) for these paddles two
 427 scintillation bars were connected to one TDC [32]. Typical examples of such paddles
 428 are shown in Fig. 2.9.

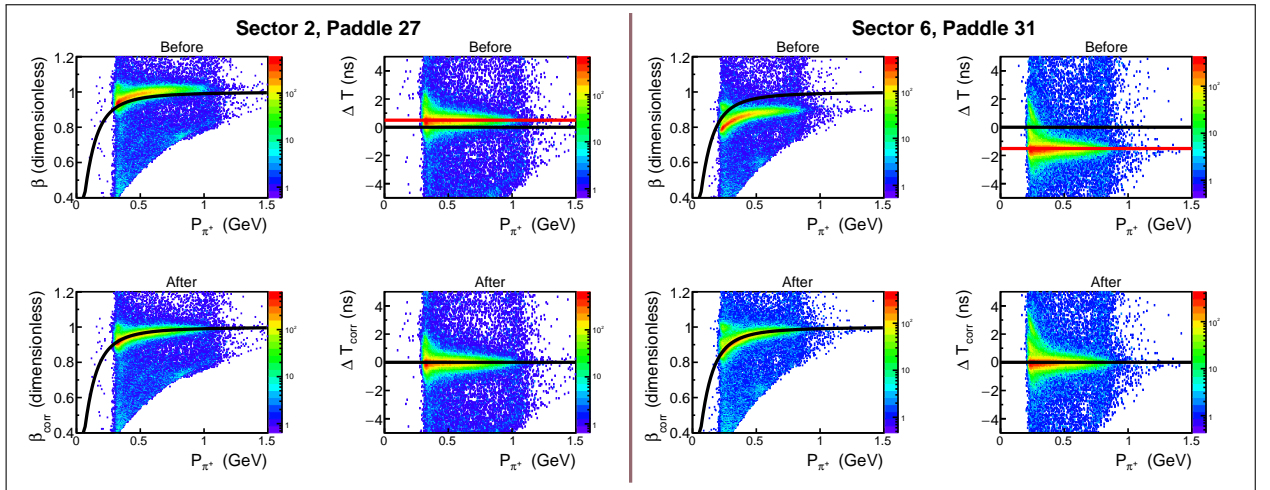


Figure 2.8: Timing correction for type B problematic paddles #27 in sector 2 (left side) and #31 in sector 6 (right side) for π^+ candidates. The first column in each side shows the β_h versus momentum distributions with the black curve corresponding to the nominal β_n defined by Eq. (2.1.16). The second column in each side corresponds to the ΔT versus momentum distributions, where the black horizontal line shows the position of zero and the red line shows the position of shifted ΔT -band. The uncorrected distributions are given in the first row, while the influence of the correction is shown in the second row.

429 To cure the latter two types of problems, a so-called timing correction is developed.
 430 To perform this correction, the quantity ΔT is calculated, which corresponds to the time
 431 difference between the real TOF signal and the expected one.

$$\Delta T = \frac{l_h}{c} \left(\frac{1}{\beta_n} - \frac{1}{\beta_h} \right). \quad (2.1.17)$$

432 Figure 2.8 illustrates the timing correction for type B problematic paddles #27 in sector
 433 2 (left side) and #31 in sector 6 (right side) for π^+ candidates. The plots in the first row
 434 correspond to the β_h versus momentum and ΔT versus momentum distributions before the

435 correction. It is seen that β_h versus momentum bands are shifted from their expected position
 436 shown by the black curve, which corresponds to the nominal β_n defined by Eq. (2.1.16). These
 437 shifts of β_h versus momentum bands are caused by the corresponding shifts of the ΔT versus
 438 momentum bands from zero position shown by the black horizontal lines. The idea of the
 439 timing correction is to move ΔT bands back to the position around zero, as shown in the
 440 corrected ΔT versus momentum plots in the second row. The corrected value of β is then
 441 calculated as

$$\beta_{corr} = \frac{1}{\frac{1}{\beta_n} - \frac{(\Delta T - t_{shift}) \cdot c}{l_h}}, \quad (2.1.18)$$

442 where t_{shift} is the position of shifted ΔT -band shown by the corresponding red horizontal
 443 line in Fig. 2.8.

444 The β_{corr} versus momentum distributions are shown in second row in Fig. 2.8. As seen in
 445 these plots, β_{corr} versus momentum bands demonstrate no shift from the black curves after
 446 the timing correction is applied.

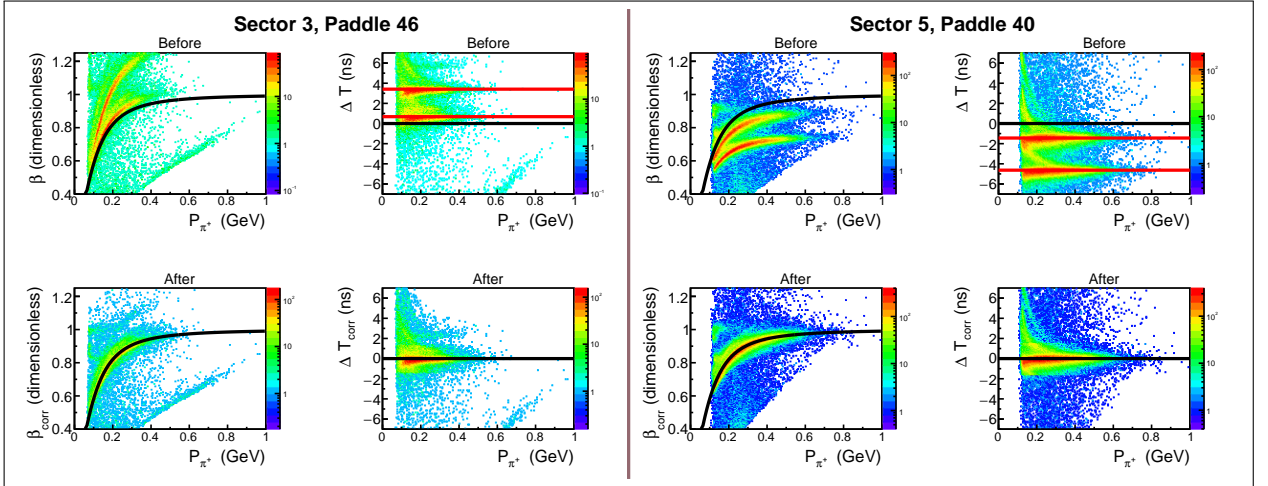


Figure 2.9: Timing correction for type C problematic paddles #46 in sector 3 (left side) and #40 in sector 5 (right side) for π^+ candidates. The first column in each side shows the β_h versus momentum distributions with the black curve corresponding to the nominal β_n defined by Eq. (2.1.16). The second column in each side corresponds to the ΔT versus momentum distributions, where the black horizontal line shows the position of zero and the red lines show the position of shifted ΔT -bands. The uncorrected distributions are given in the first row, while the influence of the correction is shown in the second row.

447 Figure 2.9 illustrates the timing correction for type C problematic paddles #46 in sector
 448 3 (left side) and #40 in sector 5 (right side) for π^+ candidates. The plots in the first row
 449 clearly show the double band structures in β_h versus momentum and ΔT versus momentum
 450 distributions. To perform timing correction for this type of paddles, one needs to determine
 451 the position t_{shift} of each incorrect ΔT -band (see horizontal red lines in Fig. 2.9) and then

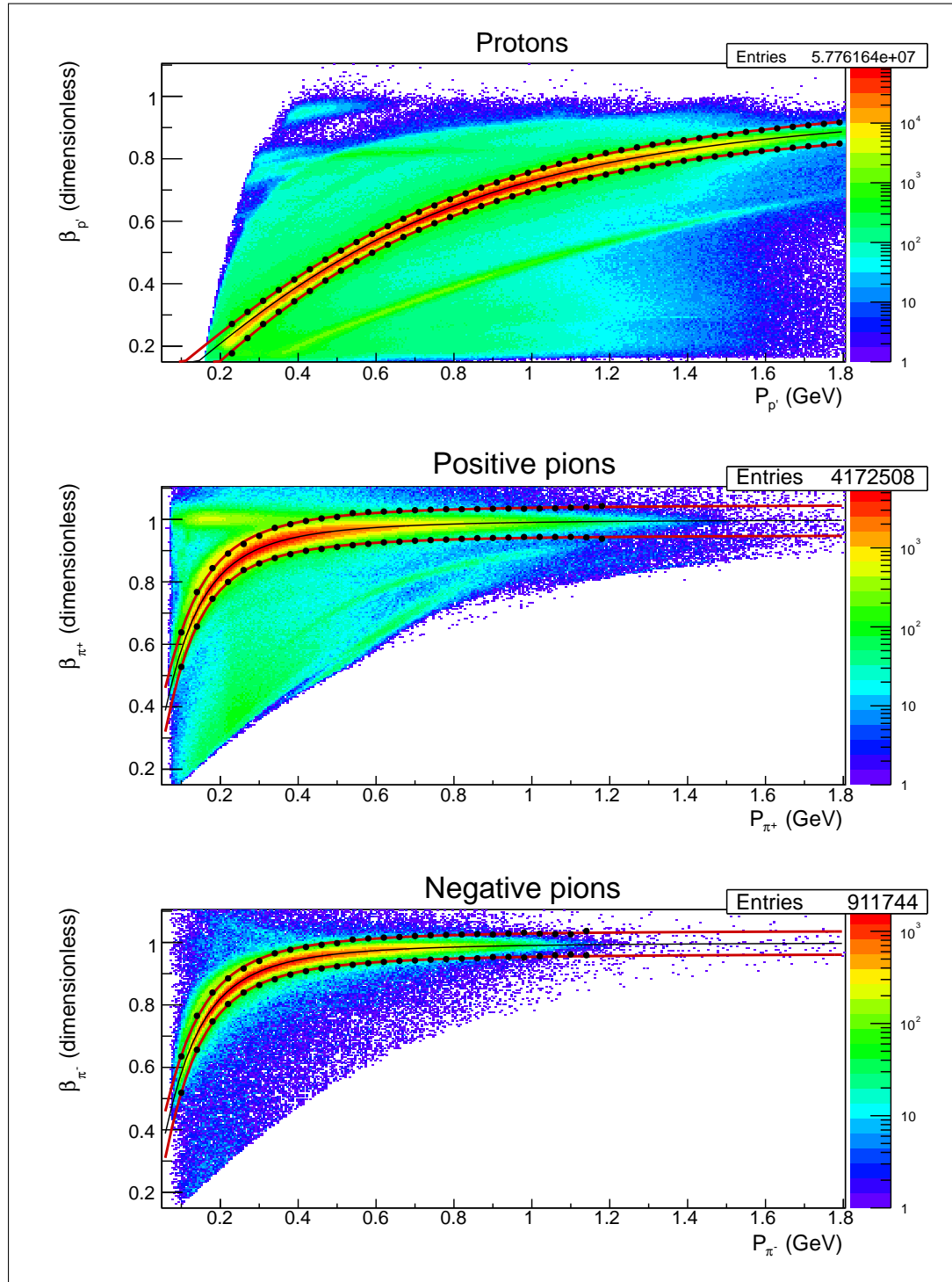


Figure 2.10: β_{corr} versus momentum distributions for proton (upper plot), positive pion (middle plot), and negative pion (bottom plot) candidates. Thin black solid curves in the middle of each band correspond to the nominal β_n given by Eq. (2.1.16). Black points correspond to the positions of Gaussian fit maxima $\pm 3\sigma$ for individual x-slices of the 2D histograms. These points are fit by the function Eq. (2.1.19), the resulting functions are shown by the red curves. Events between the red curves are selected for further analysis.

452 to move both of them to the correct position around zero, as demonstrated in the second
 453 row. The corrected value of β is again calculated according to Eq. (2.1.18) with the only
 454 distinction, that events from different ΔT -bands are treated separately and different t_{shift}
 455 values are used for them.

456 The β_{corr} versus momentum distributions are shown in the second row in Fig. 2.9. As
 457 seen in these plots, after the timing correction is applied β_{corr} versus momentum bands
 458 demonstrate neither double band structures nor shifts from the black curves.

459 Figures 2.8 and 2.9 give examples of the timing correction for π^+ candidates. Similar
 460 corrections have also been performed for proton and π^- candidates.

461 After the timing problems are eliminated in each TOF paddle, the hadron identification
 462 can be made. For the hadron identification, only events with good electron candidates that
 463 have been selected in the previous step are used. Figure 2.10 shows β_{corr} versus momentum
 464 distributions for each type of hadron candidate: protons (upper plot), positive pions (middle
 465 plot), and negative pions (bottom plot). These distributions include all sectors and all TOF
 466 paddles (with the exclusion of bad ones). The red curves show the corresponding hadron id
 467 cuts. These curves were obtained in the following way. Firstly, x-slices of the 2D histograms
 468 are fit by Gaussians. In this way points that correspond to the positions of the fit maxima
 469 $\pm 3\sigma$ are obtained⁶. These points are shown by black bullets in Fig. 2.10. They determine
 470 the upper and lower boundaries for the cut. Finally, to obtain smooth curves, all points are
 471 fit by the following function,

$$f(p_h) = \frac{a_0 \cdot p_h}{\sqrt{a_1 \cdot p_h^2 + m_h^2 + a_2}} + a_3, \quad (2.1.19)$$

472 where p_h is the hadron momentum, m_h hadron mass, and a_0, a_1, a_2, a_3 are fit parameters.

473 Events which are located between the red curves in Fig. 2.10 are selected for further
 474 analysis and treated as good corresponding hadron candidates. It also needs to be mentioned
 475 that the distribution for positive pions was plotted only for events that already have a good
 476 proton candidate, and the distribution for negative pions was plotted only for events with
 477 good proton and positive pion candidates. Furthermore, in order to simplify the analysis
 478 process, all hadrons were preselected on an initial analysis step. The consequence of this
 479 preselection is the fact that distributions shown in Fig. 2.10 contain areas that are not
 480 populated with events.

481 These established hadron id cuts are also applied to the reconstructed Monte Carlo events.

⁶Note that to establish the upper cut boundary for pions, the 3σ value was used only for $p_\pi > 0.54$ GeV. For $p_\pi < 0.54$ GeV different smaller values were used. This was done in order to better separate good pion candidates from the small upper band that is located very close to the pion band and most likely corresponds to muons.

482 2.2 Momentum corrections

483 2.2.1 Proton momentum correction (energy loss)

484 While traveling through the detector and the target, the final state particles lose a part
 485 of their energy due to the interactions with the medium. Therefore, the measured particle
 486 momentum appears to be lower than the actual value. GSIM simulation of the CLAS detector
 487 correctly propagates particles through the media and, therefore, the effect of the energy loss
 488 is included into the efficiency and does not impact the extracted cross sections. However, in
 489 order to avoid shifts in the distributions of some kinematic quantities (e.g. missing masses)
 490 from their expected values, an energy loss correction is applied to the proton momentum
 491 magnitude, since the low-energy protons are affected the most by energy loss in the materials.
 492 This correction is based on the GSIM simulation of the CLAS detector and is performed for
 493 both experimental and reconstructed Monte Carlo events.

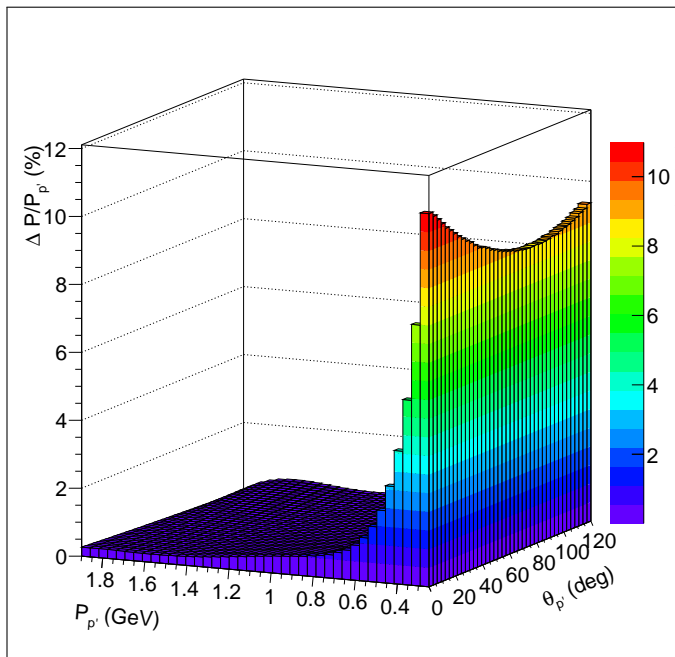


Figure 2.11: Percentage of momentum that protons lose when they move through the detector and target media as a function of the momentum $P_{p'}$ and scattered angle $\theta_{p'}$ of the final proton.

494 To obtain the correction function, the quantity ΔP that is the difference between the
 495 generated and reconstructed proton momenta was considered. This quantity was binned in
 496 the reconstructed proton momentum $P_{p'}$ and polar angle $\theta_{p'}$ and fit by a Gaussian in each
 497 $(P_{p'}, \theta_{p'})$ bin. The obtained mean values were further fit by a fifth order polynomial as a
 498 function of $P_{p'}$ in each $\theta_{p'}$ bin. Then the parameters of the resulting fit functions were fit as
 499 a function of $\theta_{p'}$ by a second order polynomial.

500 The resulting energy loss correction function is shown in Fig. 2.11. It gives the percentage
501 of the momentum that protons lose when they move through the detector and target media.

502 Note that if one wants to isolate the pure effect of the energy loss, the difference between
503 proton momenta for events reconstructed with and without detector and target materials
504 must be considered. Since in the applied procedure the difference between generated and
505 reconstructed proton momenta is analyzed, the correction function shown in Fig. 2.11 can
506 also include other effects that lead to improper proton momentum reconstruction.

507 2.2.2 Electron momentum correction

508 Due to slight misalignments in the DC position, small inaccuracies in the description of
509 the torus magnetic field, and other possible reasons the momentum and angle of particles
510 may have some small systematic deviations from their real values. These effects being of
511 undefined origin cannot be simulated in GSIM, therefore a special momentum correction
512 procedure is needed for the experimental data. According to [33], the evidence of the need
513 for such corrections is most directly seen in the dependence of the elastic peak position on the
514 azimuthal angle of the scattered electrons. It is shown in [33] that the elastic peak position
515 is shifted from the true value (0.938 GeV) and this shift is sector dependent.

516 The significance of this effect depends on the beam energy. In the analysis [22] it is
517 shown that a beam energy of 2.039 GeV leads to the small shift (~ 3 MeV) in elastic peak
518 position, while the study [33] demonstrates that in case of 5.754 GeV beam energy this shift
519 reaches 20 MeV. Moreover, the study [33] also shows that this effect becomes discernible
520 only if the particle momentum is sufficiently high (e.g. for pions the correction is needed
521 only if their momentum is higher than 2 GeV). Thus, the small beam energy of this analyzed
522 dataset and the fact that in double-pion kinematics hadrons carry only a small portion of
523 the total momentum allows us to come to the conclusion that the correction is needed only
524 for electrons, while deviation in hadron momenta can be neglected.

525 Since this analysis suffers from additional complications as binding and motion of the
526 target proton inside the deuteron, it was considered sensible to use the electron momentum
527 corrections that have previously been developed and tested in the analysis of the free proton
528 part of “e1e” dataset at the same beam energy [22]. To establish them, the approach [33],
529 which is based on elastic kinematics, was used. These corrections include electron momentum
530 magnitude correction as well as electron polar angle correction, which were developed for
531 each CLAS sector individually.

532 Figure 2.12, which was taken from the analysis [22], demonstrates that after the electron
533 momentum corrections the elastic peak position for all CLAS sectors gets closer to the proton
534 mass, shown by the red horizontal line.

535 The correction discussed above is applied only for experimental data. As for the Monte
536 Carlo simulation, it turns out that due to unknown reasons (most likely because electrons

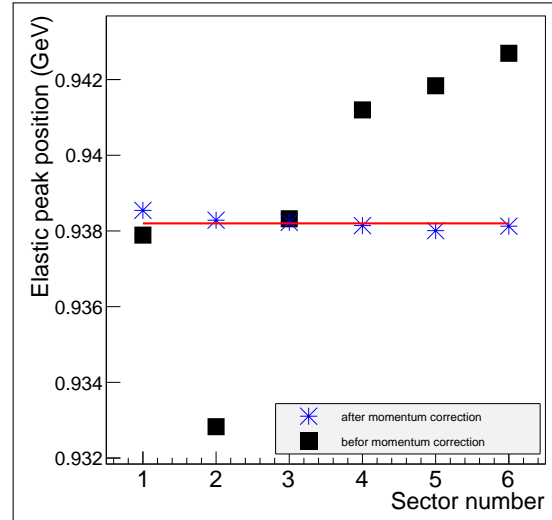


Figure 2.12: Elastic peak position for the six CLAS sectors before (black squares) and after (blue stars) electron momentum correction for the proton part of “e1e” dataset. The horizontal red line shows the proton mass. This figure is taken from the analysis [22].

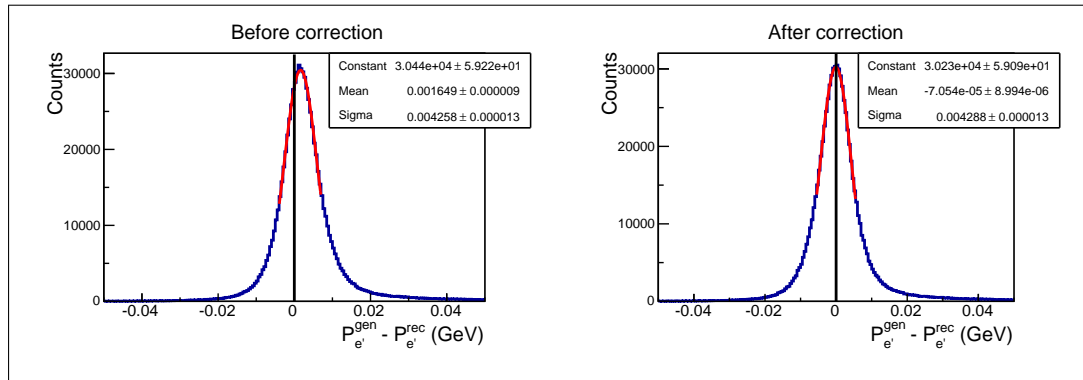


Figure 2.13: Difference between generated and reconstructed electron momenta before (left plot) and after (right plot) the correction of the momentum magnitude, which has been applied to the reconstructed electrons. The vertical black line shows the position of zero.

537 lose some energy when they travel through the detector and target media) the reconstructed
538 electron momentum appears to be slightly lower than the generated one. This effect is
539 demonstrated in the left plot of Fig. 2.13, where the event distribution of the quantity ΔP
540 (which is the difference between generated and reconstructed electron momenta) is presented.
541 Therefore, an adapted procedure of correcting the electron momentum magnitude is also
542 applied to the reconstructed Monte Carlo events. This procedure is similar to that used
543 for the proton energy loss (see Sect. 2.2.1). The correction depends only on the scattered
544 electron momentum and polar angle, but not on the CLAS sector. The typical value of this
545 correction is 0.2%. The right plot in Fig. 2.13 shows the result of the correction. As seen
546 in this plot, the mean value of the quantity ΔP demonstrates no shift from zero when the
547 momentum magnitude for reconstructed electron is corrected.

548 **2.3 Other cuts**

549 **2.3.1 Fiducial cuts**

550 The active detection solid angle of the CLAS detector is smaller than 4π [4]. This is in
551 part due to the space filled with the torus field coils: the angles covered by the coils are
552 not equipped with any detection system and therefore form a “dead” area for detection.
553 Additionally, the detection area is also limited in polar angle from 8° up to 45° for electrons
554 and up to 140° for other charged particles [4]. Moreover, different studies and analyses
555 have shown that also the edges of the active area do not provide a safe region for the
556 particle reconstruction, being affected by rescattering from the coil, field distortions, and
557 similar effects. Therefore, it is now common practice to accept for the analysis only events
558 inside specific fiducial cuts, i.e. cuts on the kinematic variables (momentum and angles)
559 of each particle. This method guarantees that events accepted in the analysis include only
560 particles detected in “safe” areas of the detector, where the acceptance is thought to be
561 well understood. These cuts are applied to both real events and reconstructed Monte Carlo
562 events.

563 **Fiducial cuts for negatively charged particles**

564 In CLAS experiments with normal direction of the torus magnetic field, like in the “e1e”
565 experiment, negatively charged particles are inbending, which means that their trajectories
566 are bent in the forward direction. For these particles sector independent, symmetrical, and
567 momentum dependent cuts are applied.

568 For electron and negative pion candidates the analytical shapes of fiducial cuts are given
569 by Eq. (2.3.1) and Eq. (2.3.2), respectively. The shapes of these cuts were taken from the
570 similar analysis [22] of the “e1e” dataset (but off proton target) and carefully adjusted to
571 the data.

572 In Eq. (2.3.1) and Eq. (2.3.2) polar and azimuthal angles of electrons ($\theta_{e'}$, $\varphi_{e'}$) and
573 negative pions (θ_π , φ_π) are assumed to be in degrees, while their momenta ($p_{e'}$, p_π) are in
574 GeV, respectively. The angles are taken at the interaction vertex. Events that satisfy the
575 criteria $\theta^{min} < \theta < \theta^{max}$ and $\varphi^{min} < \varphi < \varphi^{max}$ are selected for the analysis.

$$\begin{aligned}
\theta_{e'}^{min}(p_{e'}) &= 11.7398 + \frac{8.21504}{0.433327 \cdot p_{e'} + 0.158076} \\
\theta_{e'}^{max}(p_{e'}) &= 76.8617 - 76.537 \cdot p_{e'} + 77.9387 \cdot p_{e'}^2 - 28.389 \cdot p_{e'}^3 \\
\varphi_{e'}^{min}(\theta_{e'}) &= -41.3 \cdot \sin [a_3 \cdot (\theta_{e'} - \theta_{e'}^{min})]^{[a_1 + a_2 / \theta_{e'} + 1485 / \theta_{e'}^2]} - 1 \\
\varphi_{e'}^{max}(\theta_{e'}) &= +41.3 \cdot \sin [a_3 \cdot (\theta_{e'} - \theta_{e'}^{min})]^{[a_1 + a_2 / \theta_{e'} + 1485 / \theta_{e'}^2]} + 1. \\
a_1(p_{e'}) &= 0.85 + 1.1 \cdot p_{e'} \\
a_2(p_{e'}) &= -62.8 - 30 \cdot p_{e'} \\
a_3(p_{e'}) &= 0.0047 \cdot p_{e'} + 0.0079.
\end{aligned} \tag{2.3.1}$$

$$\begin{aligned}
\theta_\pi^{min}(p_\pi) &= 11.09 + \frac{8}{0.472 \cdot (p_\pi - 0.03) + 0.117}, \text{ if } p_\pi > 0.3. \\
\theta_\pi^{min2}(p_\pi) &= 33 + \frac{5.24894 \cdot 10^{-5}}{5.71075 \cdot 10^{-5} \cdot (p_\pi + 0.004)^2}, \text{ if } p_\pi < 0.3. \\
\theta_\pi^{max} &= 140. \\
\varphi_\pi^{min}(\theta_\pi) &= \begin{cases} -23.5 \cdot \sin [0.015 \cdot (\theta_\pi - \theta_\pi^{min})]^{[a_1 + a_2 / \theta_\pi + 1400 / \theta_\pi^2]} - a_3, & \text{if } \theta_\pi < \theta_\pi^* \\ \varphi_\pi^{min}(\theta_\pi^*), & \text{if } \theta_\pi > \theta_\pi^* \end{cases} \\
\varphi_\pi^{max}(\theta_\pi) &= \begin{cases} +23.5 \cdot \sin [0.015 \cdot (\theta_\pi - \theta_\pi^{min})]^{[a_1 + a_2 / \theta_\pi + 1400 / \theta_\pi^2]} + a_3, & \text{if } \theta_\pi < \theta_\pi^* \\ \varphi_\pi^{max}(\theta_\pi^*), & \text{if } \theta_\pi > \theta_\pi^* \end{cases} \\
a_1(p_\pi) &= 0.61 + 1.18 \cdot p_\pi. \\
a_2(p_\pi) &= -59.2 - 35.3 \cdot p_\pi. \\
a_3(p_\pi) &= 17.2 \cdot p_\pi - 11.9 \cdot p_\pi^2 - 2.5. \\
\theta_\pi^* &= \theta_\pi^{max} - \frac{13}{15} \cdot (\theta_\pi^{max} - \theta_\pi^{min}).
\end{aligned} \tag{2.3.2}$$

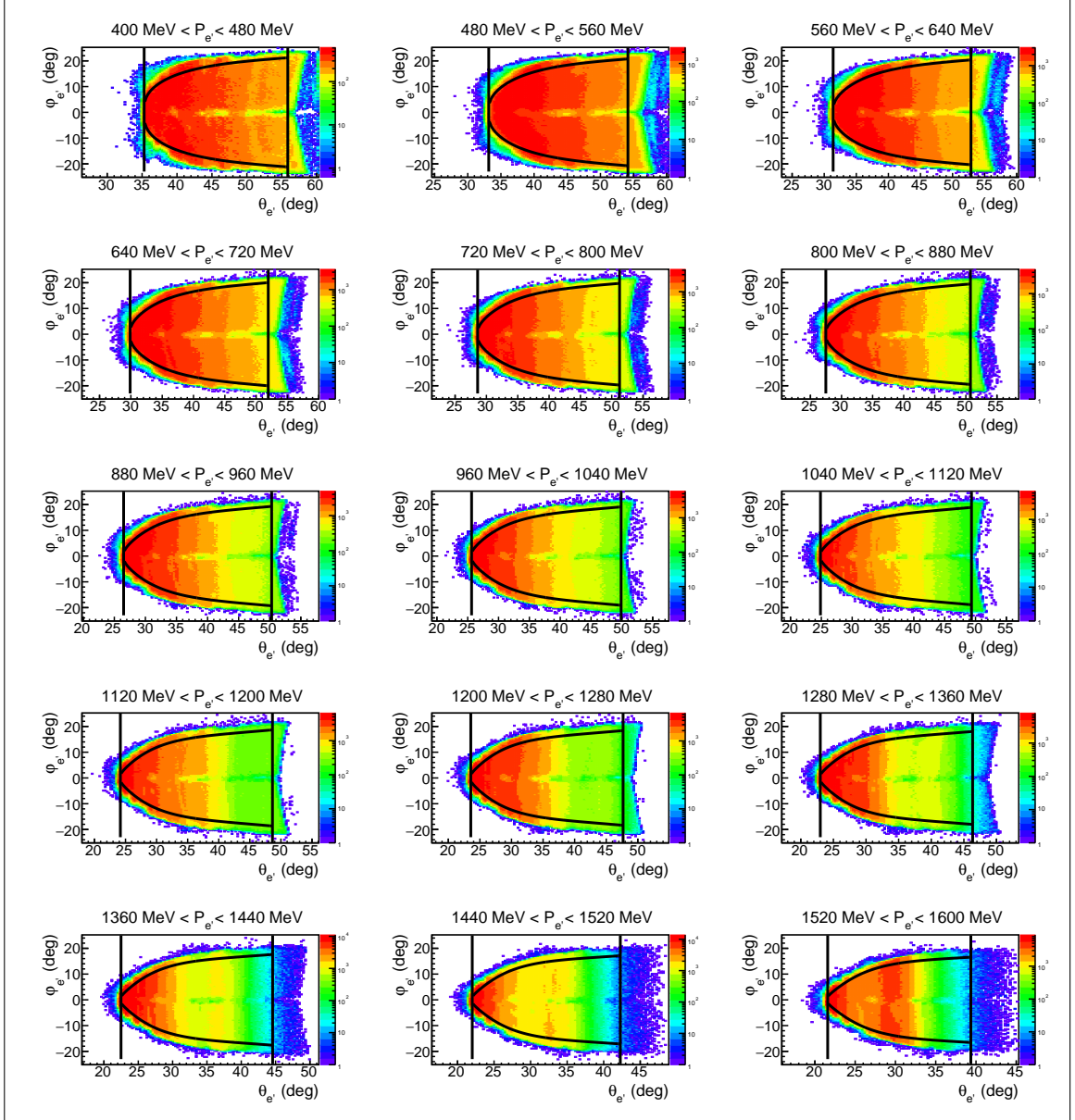


Figure 2.14: φ versus θ distributions for electron candidates for different 80-MeV-wide momentum slices plotted for events from all CLAS sectors. Curves show the applied fiducial cuts given by Eq. (2.3.1), vertical lines stand for $\theta_{e'}^{\min}$ and $\theta_{e'}^{\max}$. The angles are taken at the interaction vertex. For each momentum slice the shape of the fiducial cut was calculated for the value of the electron momentum taken in the center of the momentum bin.

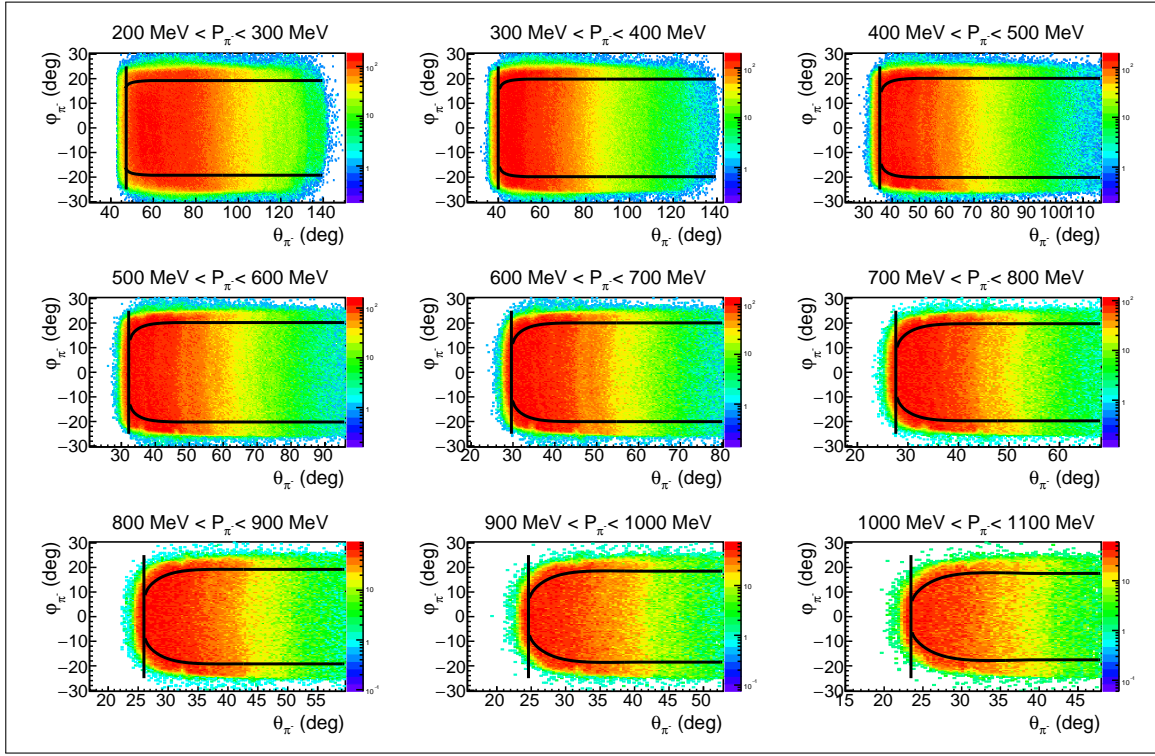


Figure 2.15: φ versus θ distributions for negative pion candidates for different 100-MeV-wide momentum slices plotted for events from all CLAS sectors. Curves show the applied fiducial cuts given by Eq. (2.3.2), vertical lines stand for θ_{π}^{min} and θ_{π}^{max} . The angles are taken at the interaction vertex. For each momentum slice the shape of the fiducial cut was calculated for the value of the pion momentum taken in the center of the momentum bin.

The fiducial cut for electron candidates is illustrated in Fig. 2.14, where the curves given by Eq. (2.3.1) are superimposed on the φ versus θ distributions for different 80-MeV-wide momentum slices. Vertical lines correspond to $\theta_{e'}^{min}$ and $\theta_{e'}^{max}$. For each momentum slice the shape of the fiducial cut was calculated for the value of the electron momentum taken in the center of the momentum bin. The depleted area around $\varphi_{e'} = 0$ corresponds to the inefficient region in CC and was discussed above in Sect. 2.1.1.

The fiducial cut for negative pion candidates is illustrated in Fig. 2.15, where the curves given by Eq. (2.3.2) are superimposed on the φ versus θ distributions for different 100-MeV-wide momentum slices. Vertical lines correspond to θ_{π}^{min} and θ_{π}^{max} . For each momentum slice the shape of the fiducial cut was calculated for the value of the pion momentum taken in the center of the momentum bin.

The same fiducial cuts for negatively charged particles are also applied to the reconstructed Monte Carlo events.

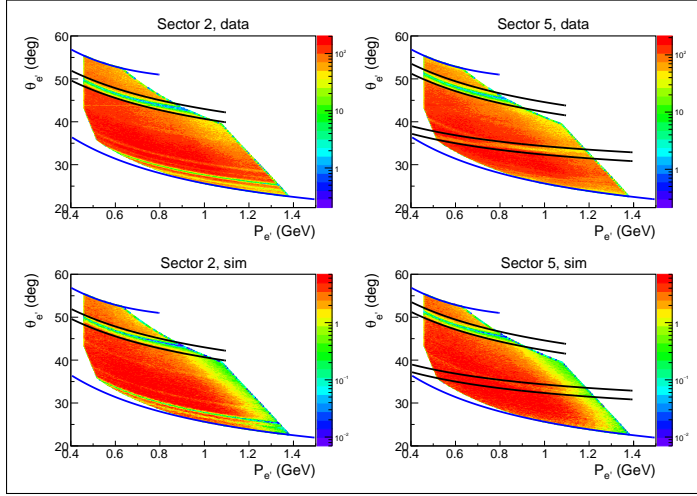


Figure 2.16: θ versus momentum distributions for electron candidates for CLAS sectors two (left side) and five (right side). The angle θ is taken at the interaction vertex. Top row corresponds to the data, bottom row corresponds to the reconstructed Monte Carlo events. Blue curves correspond to $\theta_{e'}^{min}$ and $\theta_{e'}^{max}$ in Eq. (2.3.1). Black curves correspond to additional fiducial θ versus momentum cuts. These distributions are plotted under the conditions $1.3 \text{ GeV} < W < 1.825 \text{ GeV}$ and $0.4 \text{ GeV}^2 < Q^2 < 1.0 \text{ GeV}^2$ which account for the extra cuts of the distribution edges. Other small inefficiencies that are seen in these plots are due to the geometrical cut in the CC plane (see Sect. 2.1.1).

589 There are some additional dead areas in CLAS acceptance that are not related to the
 590 gaps between the sectors and limitations on the detection polar angle. They are typically
 591 caused by some inefficiencies in the Drift Chambers and Time-of-Flight system (dead wires
 592 or PMTs). Some of them are well reproduced in the Monte Carlo simulation, while others
 593 are not. To exclude the latter from the analysis and to eliminate events near the acceptance
 594 edges, additional fiducial cuts on θ versus momentum distributions are applied. These cuts
 595 are individual for each CLAS sector. They are shown by the black curves for real and Monte
 596 Carlo events in Fig. 2.16 for electron candidates and in Fig. 2.17 for negative pion candidates.

597 For the electron distributions shown in Fig. 2.16 inefficient areas in sectors two and five
 598 correspond to bad TOF paddles #16 and #17, respectively. Other small inefficiencies that
 599 are seen in these plots are due to the geometrical cut in the CC plane (see Sect. 2.1.1), they
 600 are almost identical for data and Monte Carlo events and, therefore, no additional fiducial
 601 cuts are needed for them. θ versus momentum distributions for electron candidates in other
 602 sectors do not show significant inefficiencies.

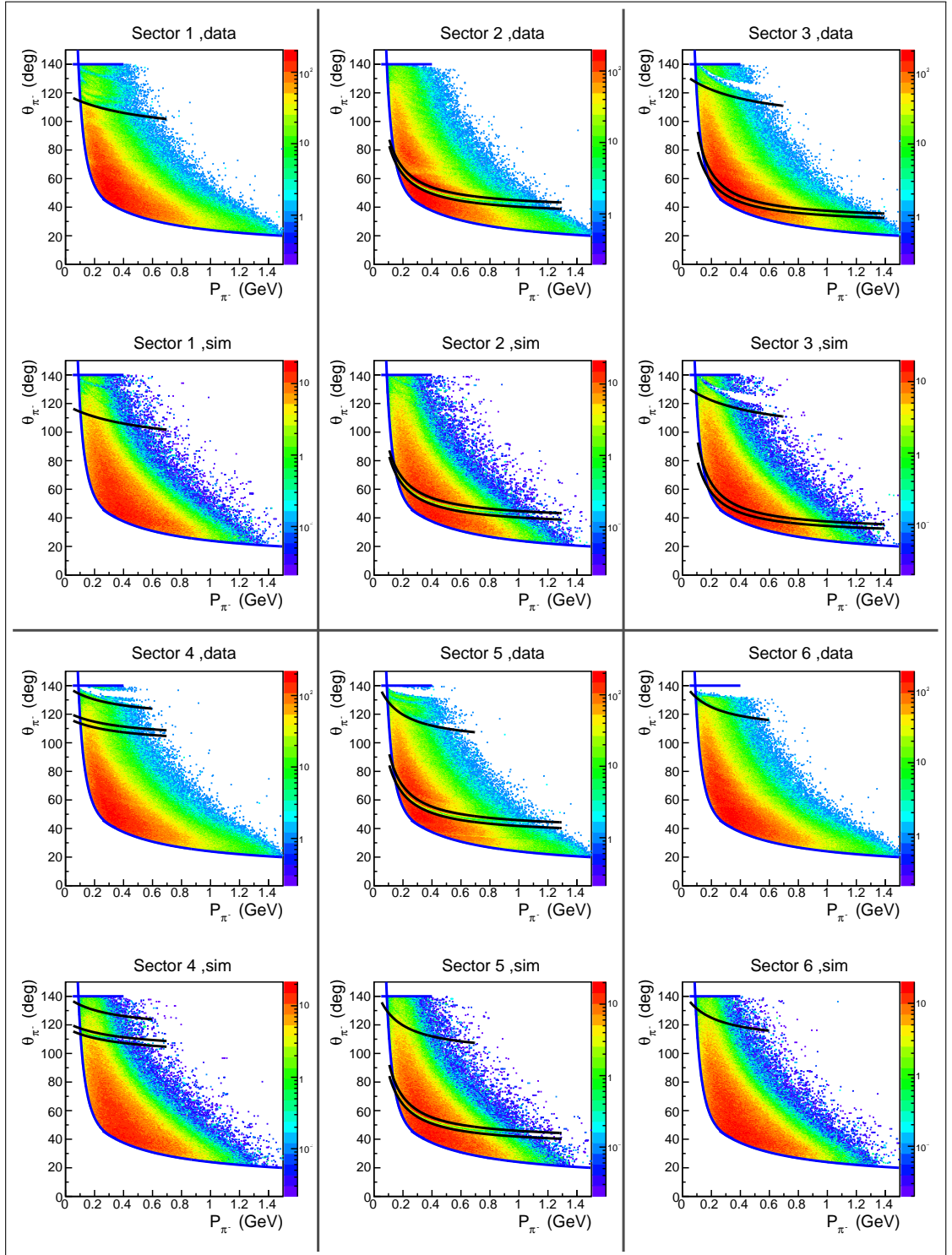


Figure 2.17: θ versus momentum distributions for negative pion candidates for different CLAS sectors. The angle θ is taken at the interaction vertex. Plots are given both for real data and reconstructed Monte Carlo events. Blue curves correspond to θ_{π}^{\min} and θ_{π}^{\max} in Eq. (2.3.2). Black curves correspond to additional fiducial θ versus momentum cuts.

603 **Fiducial cuts for positively charged particles**

604 For positively charged particles, which are outbending in the “e1e” experiment, momentum
 605 independent and symmetrical fiducial cuts suit our purpose best. The analytical shape of
 606 these cuts is given by Eq. (2.3.3), which was also taken from the analysis [22] and carefully
 607 adjusted to the data. All angles in Eq. (2.3.3) are taken at the interaction vertex and assumed
 608 to be in degrees. Events that satisfy the criteria $\theta^{min} < \theta < \theta^{max}$ and $\varphi^{min} < \varphi < \varphi^{max}$ are
 609 selected for the analysis.

$$\theta^{min} = 12.$$

$$\begin{aligned} \theta^{max} &= \begin{cases} 60 & \text{for protons} \\ 120 & \text{for pions} \end{cases} \\ \varphi^{min}(\theta) &= -25 \cdot [1 - e^{-[0.12 \cdot (\theta - 10)]}] + 3. \\ \varphi^{max}(\theta) &= +25 \cdot [1 - e^{-[0.12 \cdot (\theta - 10)]}] - 3. \end{aligned} \quad (2.3.3)$$

610 Fiducial cuts for positive hadron candidates are illustrated in Fig. 2.18, where the curves
 611 given by Eq. (2.3.3) are superimposed on the φ versus θ distributions for protons (left plot)
 612 and pions (right plot). Vertical lines correspond to θ^{min} and θ^{max} . The same fiducial cuts
 613 for positively charged particles are also applied to the reconstructed Monte Carlo events.

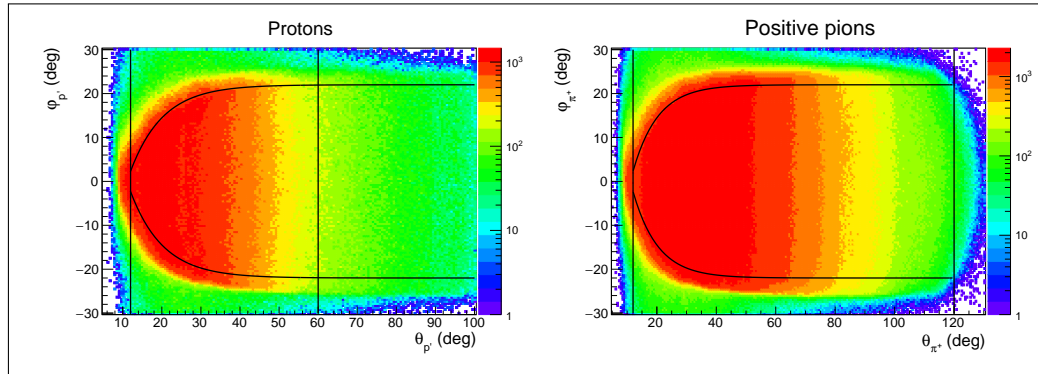


Figure 2.18: φ versus θ distributions for positive hadron candidates: left plot – for protons, right plot – for positive pions. The distributions are plotted for events from all CLAS sectors. Curves show the applied fiducial cuts given by Eq. (2.3.3), vertical lines stand for θ^{min} and θ^{max} . The angles are taken at the interaction vertex.

614 Additional fiducial cuts in θ versus momentum coordinates are shown by the black curves
 615 for the data and reconstructed Monte Carlo events in Fig. 2.19 for protons and in Fig. 2.20
 616 for π^+ .

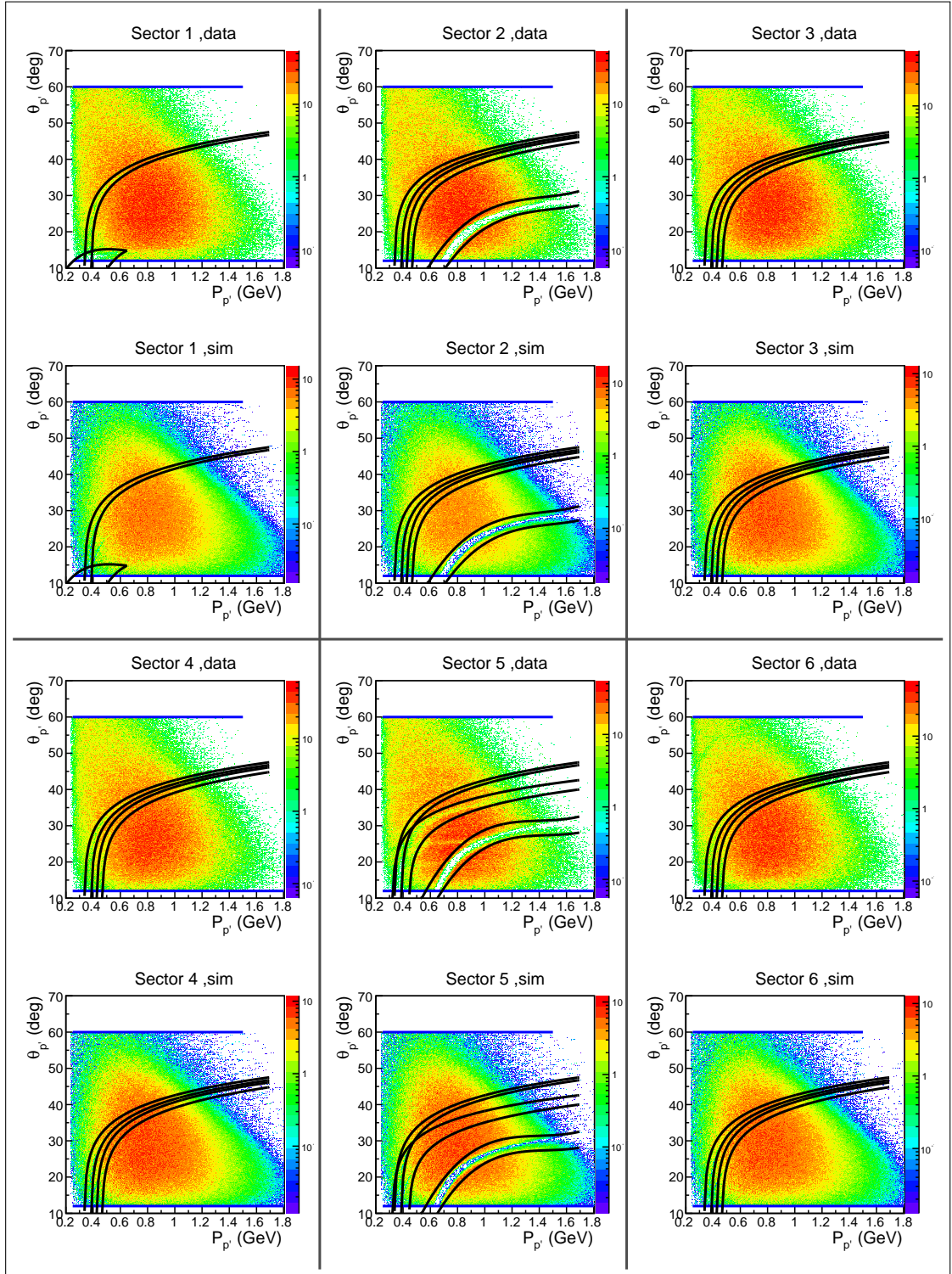


Figure 2.19: θ versus momentum distributions for proton candidates for different CLAS sectors. The angle θ is taken at the interaction vertex. Plots are given both for the real data and reconstructed Monte Carlo events. Blue lines correspond to $\theta_{\min}^{\text{real}}$ and $\theta_{\max}^{\text{real}}$ in Eq. (2.3.3). Black curves correspond to additional fiducial θ versus momentum cuts.

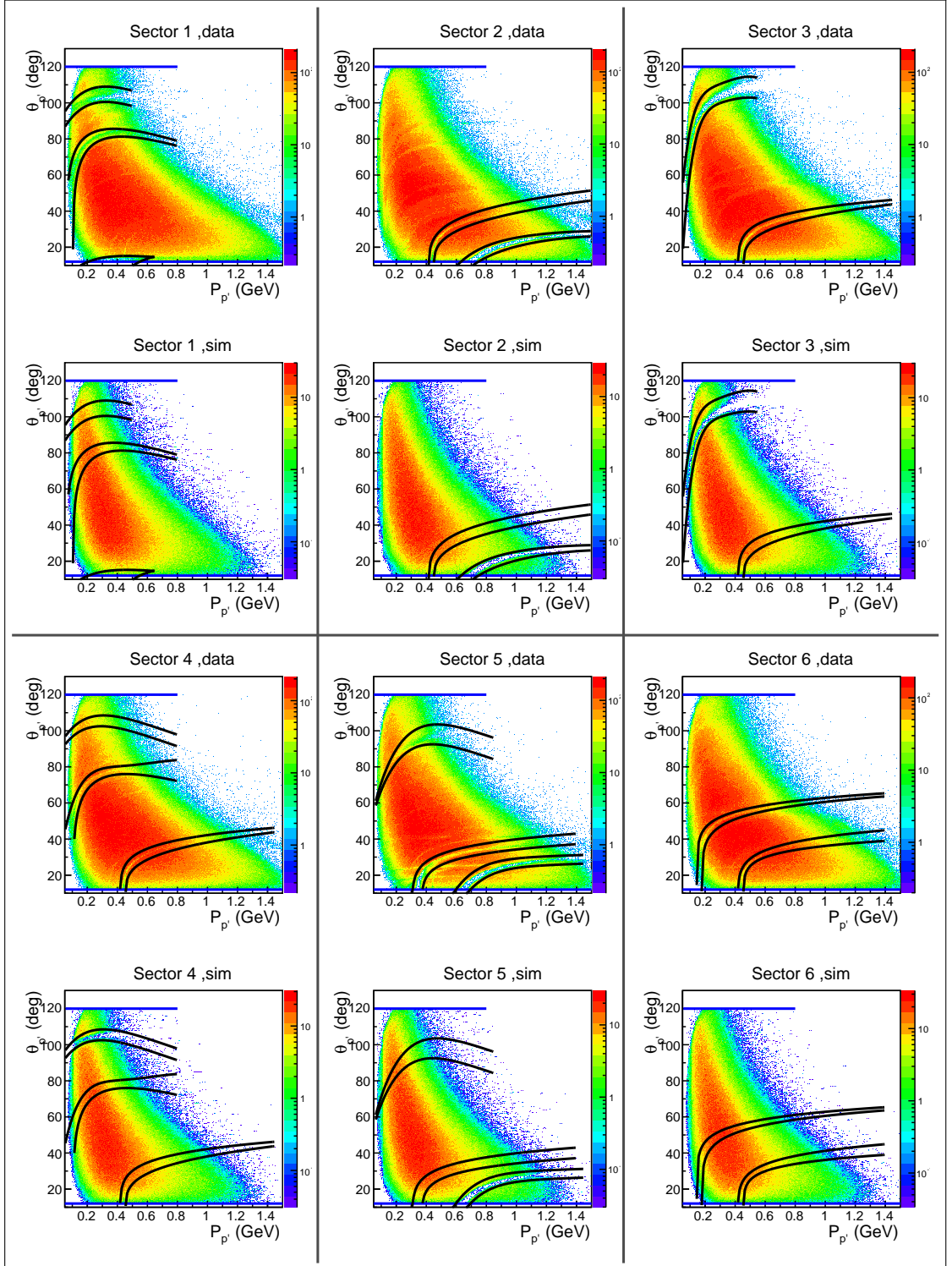


Figure 2.20: θ versus momentum distributions for positive pion candidates for different CLAS sectors. The angle θ is taken at the interaction vertex. Plots are given both for the real data and reconstructed Monte Carlo events. Blue lines correspond to θ^{min} and θ^{max} in Eq. (2.3.3). Black curves correspond to additional fiducial θ versus momentum cuts.

617 2.3.2 Data quality check

618 During a long experimental run, variations of the experimental conditions, e.g. fluctuations
 619 in the target density, deviations of the beam current and position as well as changes in the
 620 response of parts of the detector, can lead to fluctuations in event yields. Only the parts of
 621 the run with relatively stable event rates are selected for the analysis. Therefore, cuts on
 622 Data Acquisition (DAQ) live time and number of events per Faraday cup (FC) charge need
 623 to be established.

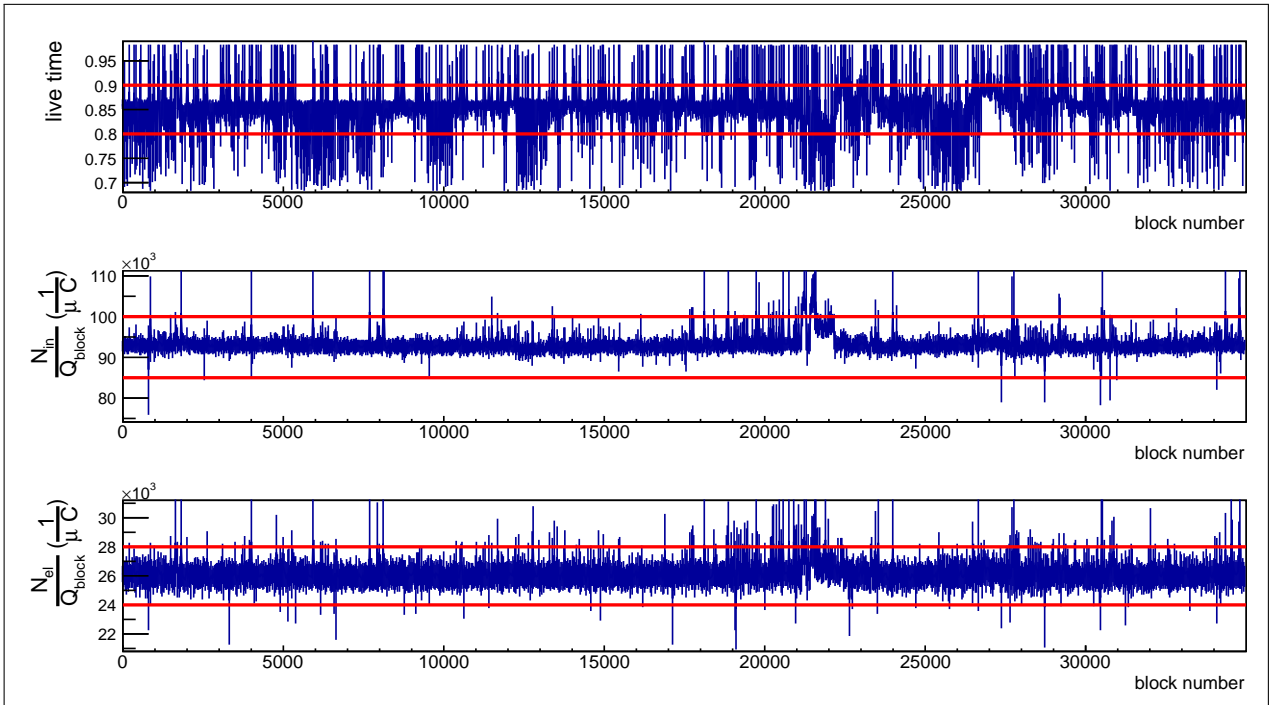


Figure 2.21: In the top plot DAQ live time is shown as a function of *block* number. Each *block* corresponds to the portion of events that is accumulated during a single Faraday cup charge reading cycle. *Block* numbers range from one to the maximum number and represent the run duration in the units of Faraday cup readouts. In the middle plot the number of inclusive events accumulated within each *block* divided by FC charge accumulated during the *block* is plotted versus *block* number. The bottom plot shows the number of elastic events accumulated within each *block* divided by FC charge accumulated during the *block* as a function of *block* number. Horizontal red lines show the applied cuts.

624 The FC charge updates with a given frequency, so the whole run time can be divided
 625 into so-called *blocks*. Each *block* corresponds to the portion of time between two FC charge
 626 readouts. FC charge readouts happen approximately once every ten seconds. The *block*
 627 number ranges over the run time from one to a certain maximum number. The first and last
 628 *blocks* in each run file are excluded from the analysis, since FC readout is not synchronized
 629 in time with the start/stop of writing to the file.

630 The DAQ live time is the portion of time within the *block* during which the DAQ system
 631 is able to accumulate events. A significant deviation of the live time from the average value
 632 indicates event rate alteration. For instance, if the live time is close to one, then the event
 633 rate is too low and vice versa. In Fig. 2.21 the DAQ live time (top plot) as well as the
 634 yields of inclusive (middle plot) and elastic (bottom plot) events normalized to FC charge
 635 are shown as a function of *block* number. *Blocks* between the horizontal red lines in Fig. 2.21
 636 are selected for the analysis. Due to the enormous amount of *blocks* all of them cannot
 637 be made visible in two-dimensional histograms, therefore, to have a general feeling of what
 638 amount of blocks are removed, the *y*-axis projections of the histograms in Fig. 2.21 are given
 639 in Fig. 2.22. The horizontal red cut lines in Fig. 2.21 correspond to the vertical red cut lines
 640 in Fig. 2.22.

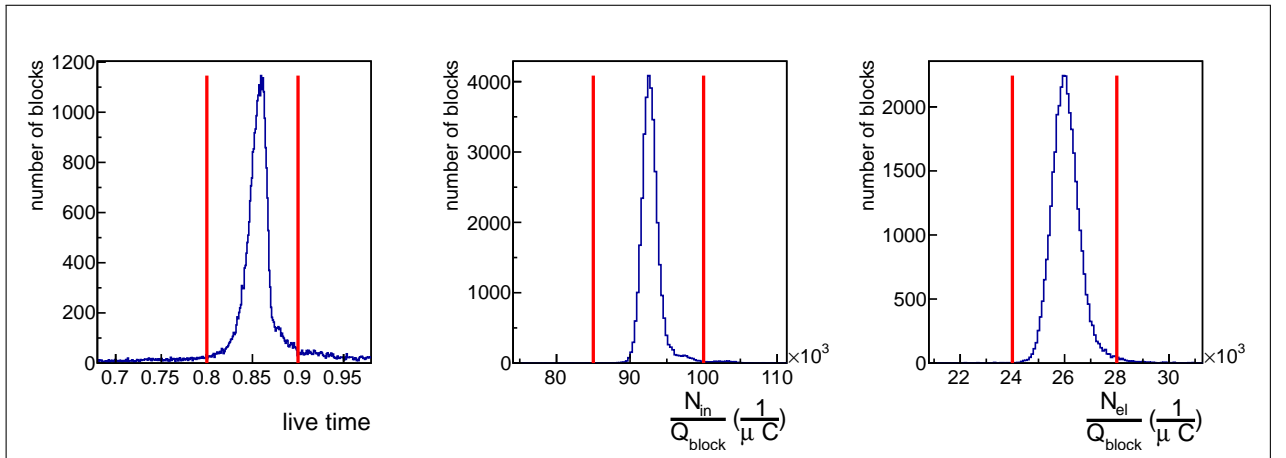


Figure 2.22: Number of *block* occurrences (see explanation in the text) as a function of DAQ live time (left plot), inclusive event yield normalized to FC charge (middle plot), and elastic event yield normalized to FC charge (right plot). The vertical red cut lines correspond to the horizontal red cut lines in Fig. 2.21.

641 2.3.3 Vertex cut

642 The “e1e” experiment employed a specific target [34] with the same assembly for the hydro-
 643 gen and the deuterium parts of the run period. The target setup is presented in Fig. 2.23.
 644 The conical shape of the target (with the diameter varying from 0.35 to 0.6 cm) serves the
 645 purpose of effective extraction of gas bubbles, which are formed in the liquid target content
 646 due to the heat that either originates from the beam and/or comes from outside through
 647 the target walls. Due to the conical shape, the bubbles are drained upwards and into a
 648 wider area of the target thus clearing the beam interaction region and allowing the boiled
 649 deuterium to be effectively delivered back to the cooling system to be condensed.

650 The target cell had 15- μm -thick aluminum entrance and exit windows. In addition, an
 651 aluminum foil was located 2.0 cm downstream of the target. This foil was made exactly the
 652 same as the entry/exit windows of the target cell and served for both the estimation of the
 653 number of events that originated in the target windows and the precise determination of the
 654 target z -position along the beamline.

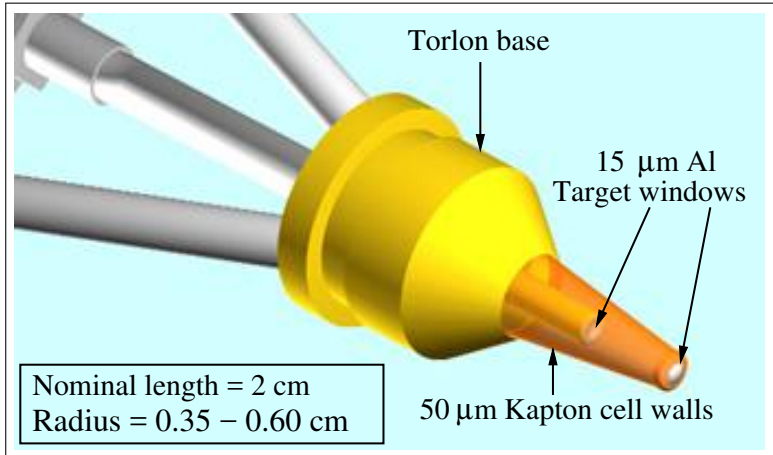


Figure 2.23: LH₂/LD₂ target cell and its support structure used during “e1e” run period [34].

655 In Fig. 2.24 distributions of electron z -coordinate at the interaction vertex are shown for
 656 events from both empty and full target runs for all six CLAS sectors. The vertical red lines
 657 show the cut that is applied in addition to the empty target event subtraction. The vertical
 658 dashed line marks the position $z = -0.4$ cm, where the center of the target is expected to
 659 be. However, as seen in Fig. 2.24, the $z_{e'}$ distributions demonstrate small sector dependent
 660 deviations from their expected position. The source of these deviations is an offset of the
 661 beam position from the CLAS central line $(x, y) = (0, 0)$.

662 To estimate the beam offset, the $y_{e'}^{dc}$ versus $x_{e'}^{dc}$ distribution was investigated, where $x_{e'}^{dc}$
 663 and $y_{e'}^{dc}$ are the corresponding coordinates of an electron at the point of interaction, which
 664 are taken from the DCPB bank (variables X_v and Y_v, respectively). This distribution is
 665 shown in Fig. 2.25, where the intersections of black dashed and solid red lines indicate the
 666 nominal and actual beam positions, respectively. The actual beam position was found to
 667 be $(x, y) = (0.057 \text{ cm}, -0.182 \text{ cm})$. The generated Monte Carlo events were reconstructed
 668 taking into account the determined beam offset to improve resemblance to the real data⁷.

669 In Fig. 2.26 event distributions after the subtraction of the empty target contribution are
 670 shown in comparison with Monte Carlo events reconstructed taking into account the beam
 671 offset. As can be seen in this figure the simulation matches the data well enough and almost
 672 completely reproduces the sector dependent deviation of the distributions from the nominal
 673 position marked by the black dashed lines.

⁷ The following option was used in the *ffread card*: POSBEAM 0.057 -0.182.

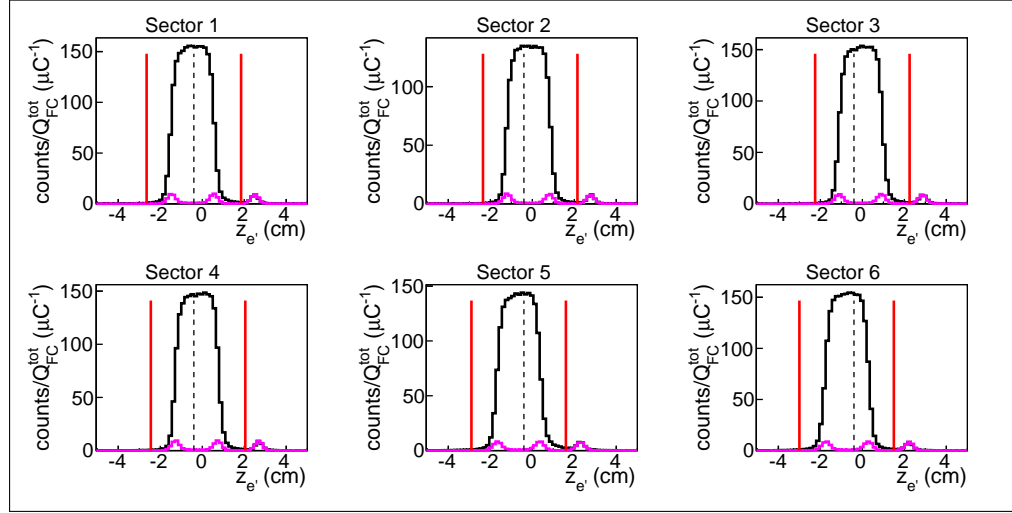


Figure 2.24: Distributions of the electron z -coordinate at the vertex for full (black curves) and empty (magenta curves) target runs for the six CLAS sectors. Vertical dashed lines mark the position $z = -0.4$ cm, where the center of the target is expected to be. Vertical red lines show the applied cuts. Both full and empty target distributions are normalized to the corresponding FC charge.

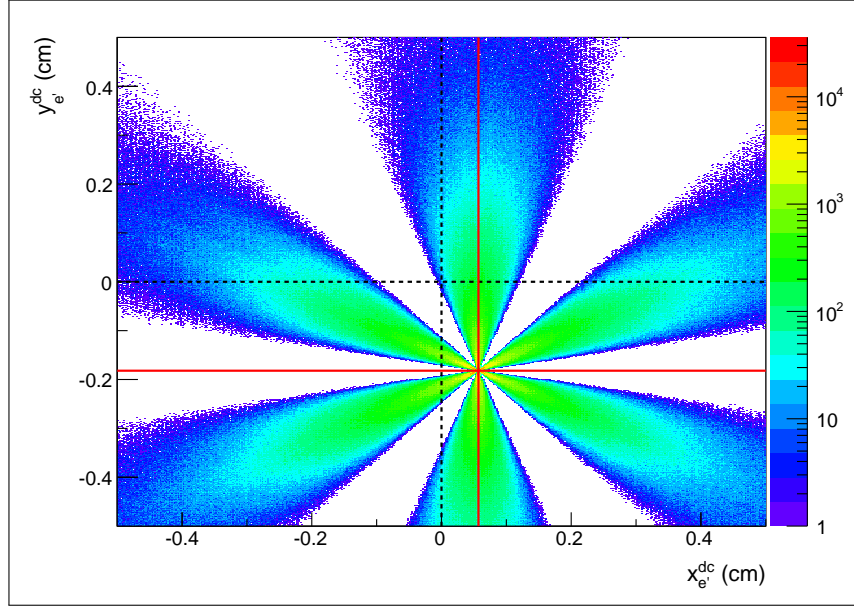


Figure 2.25: $y_{e'}^{dc}$ versus $x_{e'}^{dc}$ distribution that demonstrates the beam offset. Black dashed lines mark the position $(x, y) = (0, 0)$, where the beam is expected to be. Red lines demonstrate the actual beam position at $(x, y) = (0.057 \text{ cm}, -0.182 \text{ cm})$.

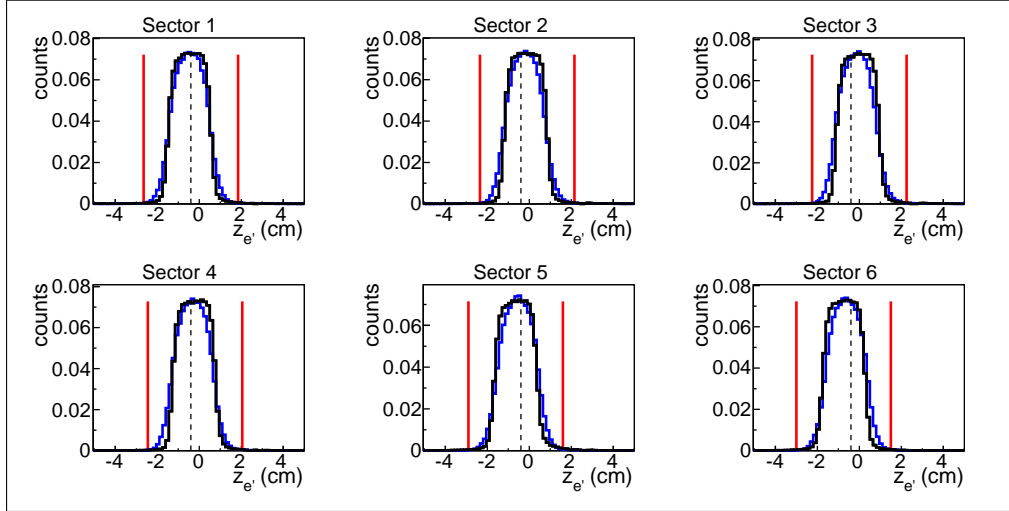


Figure 2.26: Distributions of the electron z -coordinate at the vertex for the experimental data (black curves) and the Monte Carlo events reconstructed taking into account the beam offset (blue curves) for the six CLAS sectors. For the data empty target contributions are subtracted. Vertical dashed lines mark the position $z = -0.4$ cm, where the center of the target is expected to be. Vertical red lines show the applied cuts. All distributions are normalized to the integral.

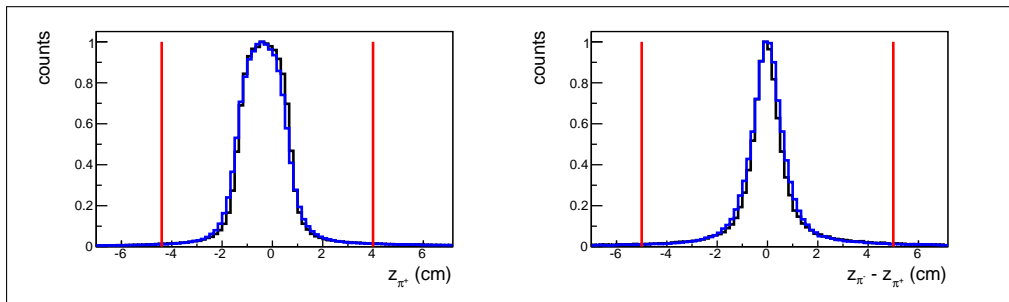


Figure 2.27: Left plot: an example of the cut on the hadron z -coordinate, $|z_{\pi^+} + 0.4| < 4.4$ cm. Right plot: an example of the cut on the difference of the vertex z -coordinates of the final particles, $|z_{\pi^-} - z_{\pi^+}| < 5$ cm. The black curves correspond to the data, while the blue ones correspond to the reconstructed Monte Carlo events. All histograms are normalized to their maxima.

674 To reduce the number of events in which the final state particles came from different
675 events and/or took part in final state interactions, the following two additional cuts on the
676 particle z -coordinates at the vertex are applied. The first cut is $|z_h + 0.4| < 4.4$ cm, where the
677 index h corresponds to the final hadron type (proton, π^+ , and π^-). The left side of Fig. 2.27
678 shows an example of this cut for the case $h = \pi^+$. The second cut is $|z_i - z_j| < 5$ cm, where
679 the indices i and j ($i \neq j$) correspond to the final particle type (electron, proton, π^+ , and
680 π^-). The right side of Fig. 2.27 shows an example of this cut for the case $i = \pi^-$, $j = \pi^+$.
681 These additional cuts are made rather loose in order to avoid unjustified loss of good events.

682 2.4 Exclusivity cut in the presence of Fermi smearing 683 and FSI

684 For picking out certain exclusive reactions one needs to register the scattered electron and
685 either all final hadrons or all except one. In the latter case the four-momentum of the unreg-
686 istered hadron can be restored using energy-momentum conservation (a so-called “missing
687 mass technique”). Thus for the reaction $ep \rightarrow e'p'\pi^+\pi^-$ one can in general distinguish be-
688 tween four so-called “topologies” depending on the specific combination of registered final
689 hadrons. In this particular analysis the following two topologies are analyzed,

- 690 • the fully exclusive topology (all final particles are registered) $ep \rightarrow e'p'\pi^+\pi^-X$, and
691 • the π^- missing topology $ep \rightarrow e'p'\pi^+X$.

692 Due to the experimental conditions the statistics of the fully exclusive topology is very
693 limited. This happens mainly because CLAS does not cover the polar angle range $0^\circ < \theta_{lab} <$
694 8° [4]. The presence of this forward acceptance hole does not affect much the registration of
695 the positive particles (p and π^+), since their trajectories are bent by the magnetic field away
696 from the hole. Meanwhile, the negative particles (e and π^-) are inbending, which means that
697 their trajectories are bent into the forward direction. Electrons being very light and rapid
698 undergo small track curvature, and the presence of the forward hole leads for them only to
699 a constraint on the minimum achievable Q^2 . However, for negative pions the situation is
700 dramatic: being heavier and slower they are bent dominantly into the forward detector hole
701 and, therefore, most of them cannot be registered. This leads to the fact that the π^- missing
702 topology contains the dominant part of the statistics. The contribution of the fully exclusive
703 topology to the total analyzed statistics⁸ varies from $\sim 5\%$ near the reaction threshold to
704 $\sim 25\%$ at $W \sim 1.7 - 1.8$ GeV.

705 For reactions with multi-particle final states the problem of limited acceptance is an
706 essential issue. Specifically, in the case of the $p\pi^+\pi^-$ final state the cross section depends
707 on five final hadron variables and hence is multi-dimensional, but the limited statistics only
708 allows the extraction of a set of one-fold differential cross sections (see Sects. 3.3 and 3.5).
709 This leads to the necessity to fill kinematic cells with zero acceptance (so-called “empty
710 cells”) based on some model assumptions, which leads to model dependent results (see
711 Sect. 4.1). The fully exclusive topology suffers from the problem of limited acceptance (and
712 therefore large amount of empty cells) that along with the problem of limited statistics does
713 not allow any sensible cross section information to be obtained from this topology alone. The
714 π^- missing topology, having significantly fewer empty cells, serves the purpose of the cross
715 section extraction best. The use of both topologies combined allows the model dependence
716 of the cross section (that originates from empty cells filling) to be reduced as well as slightly
717 increasing the statistics.

⁸The combined statistics of both the π^- missing and the fully exclusive topologies.

718 The aforementioned features of the two topologies are caused by the experimental con-
719 ditions and valid either for an experiment off the free proton or for one off the proton bound
720 in the deuteron. Meanwhile, there are also some features that appear only in bound proton
721 experiments. Those that are crucial for exclusive event selection are addressed later in this
722 Section, while others are discussed later in the report.

723 Actually, two more topologies can be distinguished, i.e. the proton missing topology
724 and the π^+ missing topology. Both require registration of the π^- in the final state and as a
725 consequence suffer from the similar problems of suppressed statistics⁹ and limited acceptance
726 as in the case of the fully exclusive topology. Therefore, these two topologies are usually
727 ignored in analyses of the reaction $ep \rightarrow e'p'\pi^+\pi^-$ [15–19]. Nevertheless, as demonstrated
728 in the sophisticated analysis of this reaction off the free proton target [22, 23], they can
729 be used as complimentary topologies to the main π^- missing topology, that allows a slight
730 increase in the statistics and a reduction in the amount of empty cells as much as possible,
731 therefore minimizing the model dependence of the extracted cross sections. However, if
732 the pion pair is produced off the proton bound in the deuteron, additional complications
733 appear: these topologies turn out to be polluted with events from other reaction channels.
734 In the proton missing topology the missing mass technique fails to distinguish whether the
735 pion pair was produced off the proton or off the neutron, because their masses are almost
736 identical. A similar situation occurs for the π^+ missing topology, where the same reason
737 prevents distinguishing between the production of $\pi^+\pi^-$ pair off the proton and $\pi^0\pi^-$ pair
738 off the neutron, if only the proton and the π^- in the final state are registered. Moreover,
739 the event sample in the π^+ missing topology demonstrates strong admixture of events from
740 the reaction $en(p) \rightarrow e'p'(p')\pi^-$, which was found to be not very easy to remove.

741 Taking into account all the above arguments, the following topology ranking takes place
742 in this particular analysis: the π^- topology is the main one and the fully exclusive topology
743 is treated as the complimentary one, which gives a slight increase in statistics as well as
744 some reduction in the amount of empty cells, while the proton missing and the π^+ missing
745 topologies are not used at all.

746 Meanwhile, an experiment on bound nucleons has some specific features, which are ex-
747 trinsic to the free proton experiments. Those of them that are related to the problem of the
748 channel identification are listed below.

- 749 • The Fermi motion of the target proton.
- 750 • Complex effects of Final State Interactions (FSI) due to the presence of the neutron
751 and the multi-particle final state.

752 The manifestations of these effects in the π^- missing and fully exclusive topologies differ.

⁹ Each of them contains about 10% of the full statistics of all four topologies combined.

753 The movement that the target proton undergoes in the deuterium nucleus is concealed
754 from the observer and is not measured¹⁰. However, if all particles in the final state are
755 registered, one can restore the information about the momentum distribution of the target
756 proton via energy-momentum conservation (see Sect. 2.4.1 for details). This is not the
757 case for the π^- missing topology, where incomplete knowledge about the final state leads
758 to the fact that information about the motion of the initial proton turns out to be totally
759 lost. Therefore, one is forced to work under a so-called “target-at-rest-assumption” that
760 considers the target proton to have no motion and as a consequence inevitably leads to
761 the smearing of various kinematic quantities, such as missing mass, reaction invariant mass
762 (W), etc [35]. Although the fully exclusive topology has the advantage of the possibility
763 of avoiding the smearing¹¹, all kinematic quantities are nevertheless calculated under the
764 target-at-rest-assumption in order to treat this complimentary topology in the same way as
765 the main one.

766 In order to reliably identify the exclusive channel and correctly calculate the detector ef-
767 ficiency, the distributions of the reconstructed Monte Carlo events must match experimental
768 ones as well as possible. As mentioned above, the necessity to work under the target-at-
769 rest-assumption smears the experimental distributions, which in turn demands the simulated
770 distributions reproduce this smearing. Therefore, the effects of the target motion must be
771 properly included in the Monte Carlo simulation.

772 That is why the event generator TWOPEG-D [26] was used to perform the Monte Carlo
773 simulation. It is a version of the TWOPEG (event generator for double-pion electroproduction
774 off the free proton [36]) that was developed for this analysis in order to simulate the
775 effects of the target motion. In this version of the event generator the Fermi motion of the
776 initial proton is generated according to Bonn potential [37] and then naturally merged into
777 the specific kinematics of double-pion electroproduction.

778 The second intrinsic feature of a bound nucleon experiment is the complex effects of FSI.
779 This phenomenon is driven by the strong interaction and consists in the fact that after the
780 production of the final state hadrons and before their registration they manage to interact
781 with each other and/or the recoil nucleon. These interactions include (but are not limited
782 to) the simple momentum exchange between the hadrons as well as the process of exciting
783 nucleon resonances with their subsequent decay that may lead to the production of new
784 particles.

785 Final hadrons produced off the free proton are also subject to the FSI, but in the absence
786 of the recoil neutron these interactions are not substantial. The arguments for that are the
787 following. The probability to interact in the final state depends on the distance between

¹⁰In general it can be measured by detecting the recoil nucleon (neutron in this case), but it was not an option in this experiment.

¹¹For example, in the fully exclusive topology the value of W , being calculated using the four-momenta of the registered final hadrons, turns out to be determined within the detector resolution and not affected by the effects of the target motion.

hadrons and their relative velocity, i.e. for slower and closer travelling hadrons the chance to interact is higher than for distant and rapid hadrons. Final state hadrons are produced in one vertex, which means that in the beginning they are very close to each other and therefore have a high chance to interact. However, immediately after the production they start to fly apart from the vertex in radial directions increasing the distance between each other, which causes the interaction probability drop.

The presence of an additional recoil nucleon changes the situation drastically. The neutron, which initially was not involved into the reaction of hadron production, is located slightly aside of the interaction vertex but at the same time very close to it, so that the flying-off final hadrons can impact the neutron. In addition to that, the neutron also moves with Fermi momentum, thus the FSI are brought to the usual hadron-hadron collisions, which may result in the resonance excitation and/or particle production. Direct hadron-hadron collisions, which are unlikely to occur in the reaction off the free proton, since the final hadrons fly apart from one point, start to play a role in the reaction off the bound proton in the presence of the neutron. Therefore, FSI effects in the bound nucleon experiment are rather strong in contrast to those in the free proton one.

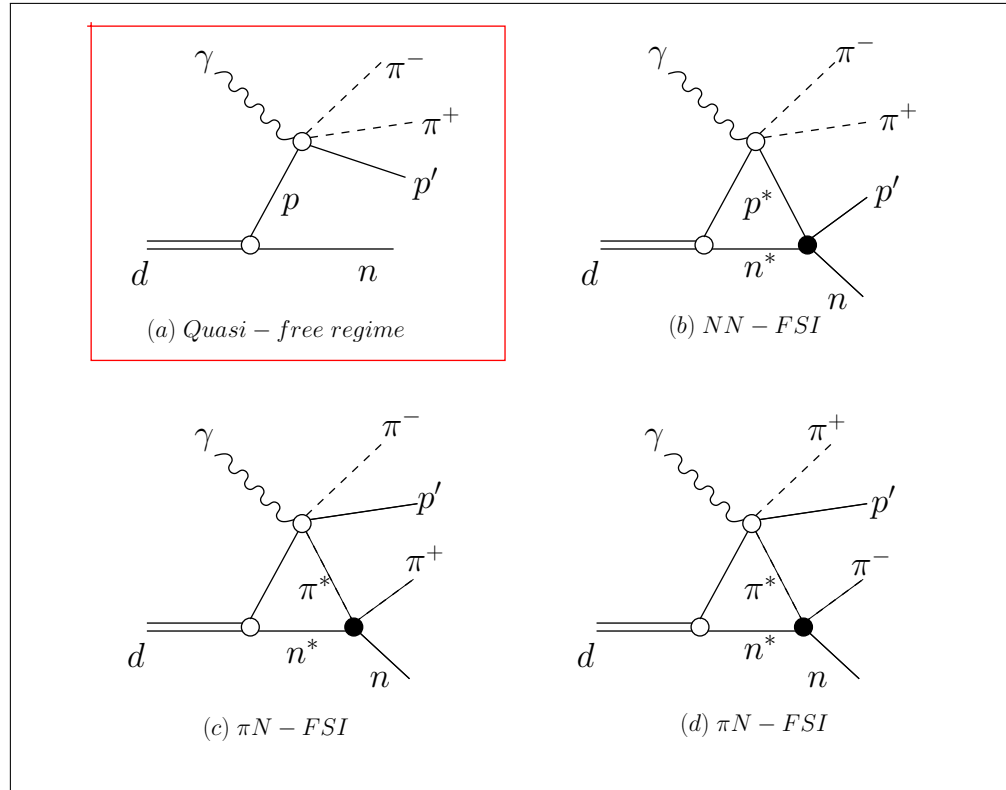


Figure 2.28: Illustration of the leading contributors to the process of the double-pion production off the proton bound in deuteron. (a) Quasi-free regime, (b) NN-FSI, and (c-d) πN -FSI.

804 FSI affect the final hadron momenta, making them either distorted by rescattering ef-
805 fects or leak away via the production of extra particles in hadron-hadron collisions. This
806 leads to the distortion of various kinematic quantities, such as missing masses. If the final
807 hadrons manage to avoid any interaction with the neutron, then the neutron is treated as
808 a spectator and the reaction is considered to occur in a so-called “quasi-free regime”. Fig-
809 ure 2.28 schematically illustrates the production of the pion pair off the bound proton in
810 the quasi-free regime (a) as well as the leading components for FSI of the final hadrons with
811 the neutron (b-d), which result in so-called “FSI-disturbed kinematics”. The goal of this
812 study is to extract the cross sections of the process (a), which implies the need to select
813 for the analysis only events in quasi-free kinematics. This in turn means removing from
814 consideration those events in which final hadrons have undergone FSI.

815 In contrast to the effects of the target motion, which can be simulated fairly easy, the
816 effects of FSI can hardly be taken into account in the simulation because they are of very
817 complex nature and hence not yet fully understood. Therefore, the Monte Carlo simulation
818 is not able to reproduce the distortions due to FSI that occur in some experimental distribu-
819 tions, but this is not a problem if events in quasi-free kinematics are properly separated from
820 those in FSI-disturbed kinematics. This leads to the necessity to develop special procedures
821 of selecting quasi-free events as well as correcting for the remaining admixture of undesired
822 events, if they cannot be fully eliminated.

823 The yield of events in FSI-disturbed kinematics turned out to strongly depend on (i) the
824 reaction invariant mass (W) and (ii) on the hadron scattering angles. The latter issue causes
825 FSI effects to manifest themselves differently depending on the reaction topology, since the
826 topologies have non-identical geometrical acceptance.

827 As follows from the above, the two analyzed topologies differ from each other both in
828 treating of the Fermi motion of the initial proton and in FSI manifestations. Therefore, the
829 channel identification in the quasi-free regime was performed in each topology individually
830 (see subsequent subsections).

831 The problem of background channels is also an issue that deserves special attention for
832 the bound proton experiment. For the reaction of double-pion production off the free proton
833 the main background channel is $ep \rightarrow e'p'\pi^+\pi^-\pi^0$. In the analysis [22] that was carried out
834 for the same beam energy $E_{beam} = 2.039$ GeV, it is shown that although the admixture of
835 the events from this background channel becomes discernible at $W \gtrsim 1.6$ GeV, it remains
836 negligible and well separated from the double-pion events via the exclusivity cuts. For the
837 experiments with the deuteron target the reaction $en(p) \rightarrow e'p'(p')\pi^+\pi^-\pi^-$ can also act as
838 a background channel for the investigated $ep(n) \rightarrow e'p'(n')\pi^+\pi^-$ reaction, however it is also
839 expected to give an insignificant and well separated admixture. Here and hereinafter the term
840 “background channel” is used to denote the reaction that happened in electron scattering
841 off the target nucleon along with the investigated double-pion reaction. Any reaction that
842 might occur during the FSI is not treated as the contribution from “background channels”,
843 but is attributed to the FSI-background.

844 2.4.1 Fully exclusive topology

845 In the fully exclusive topology for the selection of double-pion events in quasi-free kinematics
 846 the distributions of the following quantities were investigated: the missing momentum P_X
 847 and the missing mass squared $M_{X[0]}^2$ for the reaction $ep(n) \rightarrow e'p'(n')\pi^+\pi^-X$ as well as the
 848 missing mass squared $M_{X[\pi^-]}^2$ for the reaction $ep(n) \rightarrow e'p'(n')\pi^+X$. These quantities are
 849 defined by

$$\begin{aligned} P_X &= |\vec{P}_e - \vec{P}_{e'} - \vec{P}_{p'} - \vec{P}_{\pi^+} - \vec{P}_{\pi^-}|, \\ M_{X[0]}^2 &= [P_e^\mu + P_p^\mu - P_{e'}^\mu - P_{p'}^\mu - P_{\pi^+}^\mu - P_{\pi^-}^\mu]^2, \\ M_{X[\pi^-]}^2 &= [P_{\pi^- \text{ miss}}^\mu]^2 = [P_e^\mu + P_p^\mu - P_{e'}^\mu - P_{p'}^\mu - P_{\pi^+}^\mu]^2, \end{aligned} \quad (2.4.1)$$

850 where P_i^μ are the four-momenta and \vec{P}_i the three-momenta of the particle i . All three quanti-
 851 ties are calculated under the target-at-rest-assumption, i.e. considering $P_p^\mu = (0, 0, 0, m_p)$,
 852 where m_p is the proton mass.

853 The quantities P_X and $M_{X[0]}^2$ are unique for the fully exclusive topology, they can be
 854 calculated only if all final hadrons are registered. Although adding the missing mass squared
 855 $M_{X[\pi^-]}^2$ to this set seems not to provide any additional information, it is investigated in order
 856 to observe consistency with the π^- missing topology, where the distribution of this quantity
 857 is the only source for developing a criterion for channel identification. See App. A for details
 858 on features of missing mass distributions.

859 Distributions of the quantities P_X (first column), $M_{X[0]}^2$ (second column), and $M_{X[\pi^-]}^2$
 860 (third column) for five 100-MeV-wide bins¹² in W are shown in Fig. 2.29 both for the
 861 experimental data (black curves) and reconstructed Monte Carlo events (blue curves).

862 The quantity P_X (first column in Fig. 2.29) is the missing momentum of the initial
 863 proton calculated under the target-at-rest-assumption, therefore the blue curves stand for
 864 the Fermi momentum (simulated according to Bonn potential [37]) convoluted with the
 865 detector resolution, whereas the black ones correspond to the experimental momentum of
 866 initial proton, mixed with the FSI effects, contributions from background channels, and the
 867 detector resolution. As seen in the left column of Fig. 2.29, the simulated distributions
 868 perfectly match the experimental ones for $P_x < 0.2$ GeV, while for $P_x > 0.2$ GeV the
 869 simulation underestimates data. Such behavior is mostly related to the fact that relative
 870 contributions from FSI, which were not included into the Monte Carlo simulation, turn out
 871 to be the most significant outside of the peak region. The background channels, being not
 872 included into the Monte Carlo as well, also contribute to this mismatch, but as mentioned
 873 above their contribution is minor. The value $P_x = 0.2$ GeV (marked by the red dashed lines
 874 in each plot in the left column) was chosen as a criterion for the selection of events in quasi-

¹²The value of W is calculated for the initial state under the target-at-rest-assumption by $W = \sqrt{(P_e^\mu + P_p^\mu - P_{e'}^\mu)^2}$.

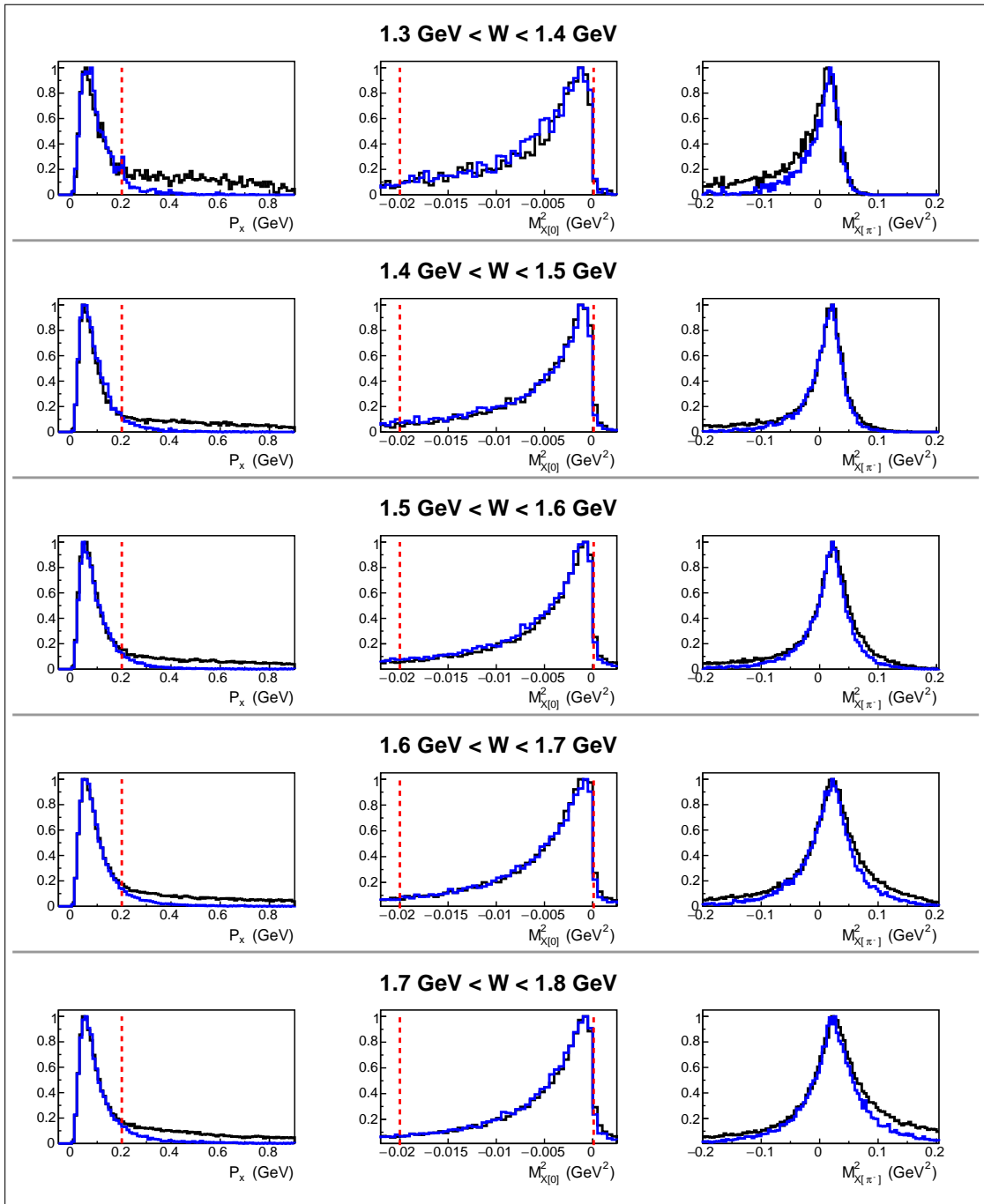


Figure 2.29: Distributions of the quantities P_X (left column), $M_{X[0]}^2$ (middle column), and $M_{X[\pi^-]}^2$ (right column) defined in Eq. (2.4.1) for experimental data (black curves) and Monte Carlo simulation (blue curves) for different 100-MeV-wide W bins. Vertical red lines indicate the cuts applied for the selection of exclusive quasi-free events. All plotted quantities as well as the values of W are calculated under the target-at-rest-assumption. All distributions are normalized to their maxima.

875 free kinematics. Thus, experimental events located at the left side of this line correspond
 876 to the reaction in the quasi-free regime, while events at the right side correspond mostly to
 877 “disturbed” kinematics with great impact of FSI.

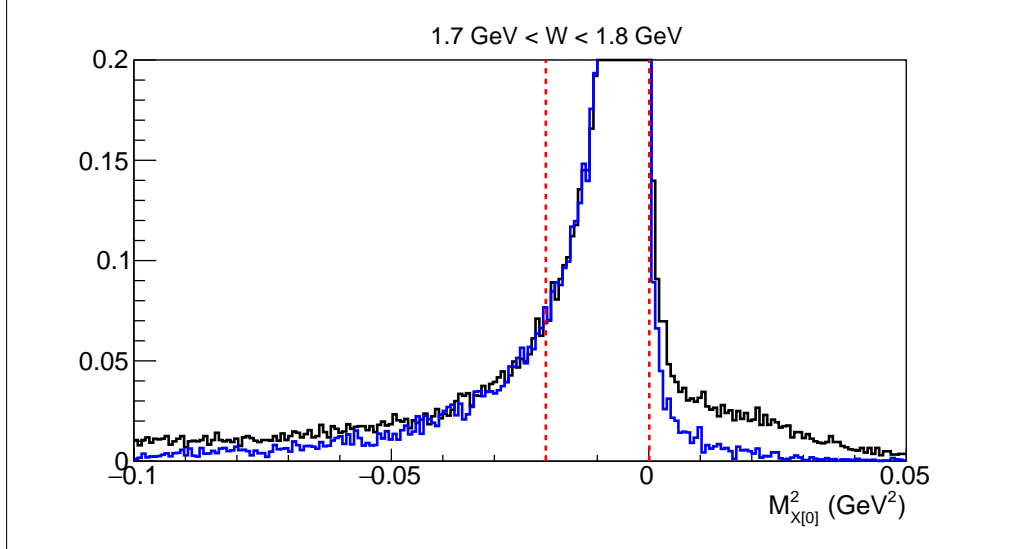


Figure 2.30: Distributions of the missing mass squared $M_{X[0]}^2$ for experimental data (black curves) and Monte Carlo simulation (blue curves) zoomed at the foot. Vertical red lines indicate the applied cut. The mismatch between data and simulation originates from FSI effects at the left and three-pion background at the right. The example is given for $1.7 \text{ GeV} < W < 1.8 \text{ GeV}$, where the latter is greatest over the whole W range. The agreement between data and simulation within the cut boundaries is better shown in Fig. 2.29 (middle column).

878 The distributions of the quantity $M_{X[0]}^2$ shown in the middle column in Fig. 2.29 deserve
 879 more attention. As demonstrated in Refs. [22, 23] and here in App. A, in free proton
 880 experiments this quantity forms a very narrow peak at zero position barely affected either
 881 by radiative effects or by detector resolution. An admixture from the three-pion background,
 882 if present in the analyzed event sample, forms then an additional peaked structure at m_π^2
 883 well-separated from the main distribution peak. Meanwhile, in this analysis $M_{X[0]}^2$, being
 884 calculated under the target-at-rest-assumption, loses its thinness and acquires the smearing
 885 (mostly left-sided), which is well-reproduced by the Monte Carlo simulation.

886 In order to clean up the sample of exclusive events, the cut on the missing mass squared
 887 $M_{X[0]}^2$ was also applied as complimentary to the cut on the missing momentum. This cut is
 888 shown in Fig. 2.29 (middle column) by the vertical red dashed lines. The plots in the middle
 889 column are zoomed near the peak to demonstrate good agreement between the data and the
 890 simulation within the cut limits. The behavior of $M_{X[0]}^2$ in a wider range is shown in Fig. 2.30,
 891 where the distributions are zoomed at the foot. As seen, outside the cut boundaries there is
 892 a mismatch between the data and simulation, which originates from FSI effects at the left

893 and the contribution from the three-pion background at the right. The latter forms a peaked
 894 structure around m_π^2 ($\sim 0.02 \text{ GeV}^2$), which is more smeared compared to the free proton case
 895 due to the target-at-rest-assumption and FSI disturbances. The example is given for high
 896 W to observe the greatest background admixture over the investigated W range.

897 The three-pion background in this topology is considered to be fully eliminated by the
 898 described above cuts on the missing momentum P_X and the missing mass squared $M_{X[0]}^2$.

899 The right column in Fig. 2.29 stands for the missing mass squared $M_{X[\pi^-]}^2$ defined by
 900 Eq. (2.4.1) under the target-at-rest-assumption, thus being Fermi smeared. The observed
 901 mismatch between the measured and simulated distributions is W -dependent and caused
 mostly by the FSI effects.

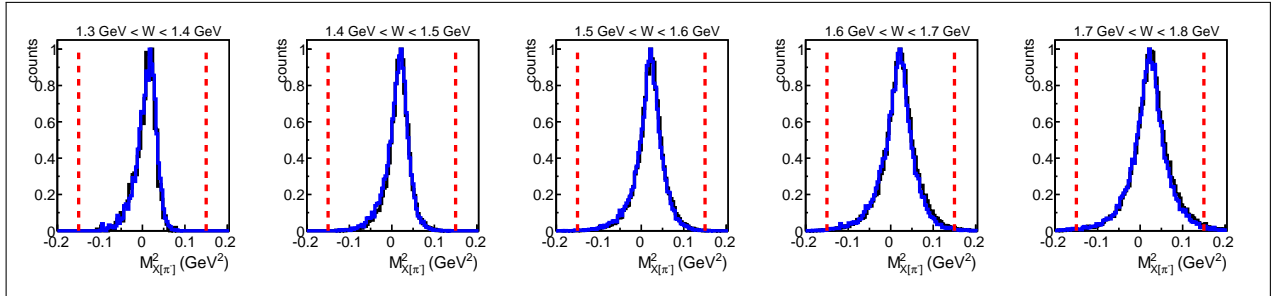


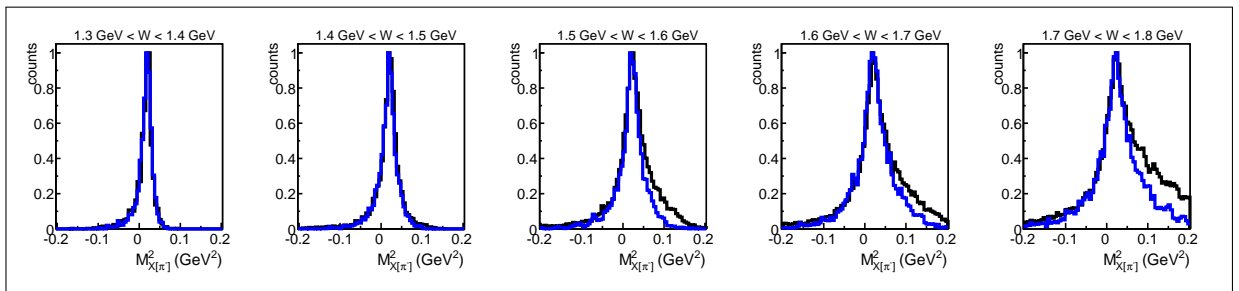
Figure 2.31: Distributions of the missing mass squared $M_{X[\pi^-]}^2$ defined in Eq. (2.4.1) for the fully exclusive topology plotted for selected quasi-free exclusive events for experimental data (black curves) and Monte Carlo simulation (blue curves). The comparison is shown for different 100-MeV-wide W bins. The quantity $M_{X[\pi^-]}^2$ as well as the values of W are calculated under the target-at-rest-assumption. The vertical red lines show the applied cuts. All distributions are normalized to their maxima. See text for details.

902
 903 Figure 2.31 shows the distributions of the missing mass squared $M_{X[\pi^-]}^2$ plotted for quasi-
 904 free exclusive events selected by the cuts on missing momentum P_x and missing mass squared
 905 $M_{X[0]}^2$. The distributions for the experimental (black curves) and reconstructed Monte Carlo
 906 (blue curves) events perfectly match each other in all W subranges, which demonstrates the
 907 reliability of quasi-free exclusive event selection as well as the fact that effects of the target
 908 motion are correctly implemented into the simulation. The vertical red lines in Fig. 2.31
 909 correspond to the additional cut that was applied on the missing mass squared $M_{X[\pi^-]}^2$.

910 Although in the fully exclusive topology the four-momentum of the π^- is measured pre-
 911 cisely within the detector resolution, it is not used in the subsequent calculation of kinematic
 912 variables for the cross section extraction. The measured four-momentum is instead replaced
 913 by the one that is calculated as missing ($P_{\pi^- \text{ miss}}^\mu$ in Eq. (2.4.1)) and thus is Fermi smeared.
 914 This is done to imitate the event selection in the main π^- missing topology in order to treat
 915 events in both topologies identically.

916 2.4.2 π^- missing topology

917 In the π^- missing topology the quantities P_X and $M_{X[0]}^2$ defined in Eq. (2.4.1) are not avail-
 918 able due to the incomplete knowledge about the final state, and $M_{X[\pi^-]}^2$ is the only remaining
 919 quantity suitable for the selection of exclusive events in quasi-free kinematics. The distri-
 920 butions of this quantity are shown in Fig. 2.32 for five 100-MeV-wide bins in W for the
 921 experimental data (black curves) and the Monte Carlo simulation (blue curves). The com-
 922 parison shown in this figure demonstrates again the W -dependent mismatch between data
 923 and simulation, which is different from that seen in the fully exclusive topology. The mis-
 924 match is mostly observed at the right side of the distribution peak and becomes discernible
 only for $W \gtrsim 1.5$ GeV.



925 Figure 2.32: Distributions of the missing mass squared $M_{X[\pi^-]}^2$ defined in Eq. (2.4.1) for the π^-
 missing topology plotted before the selection of quasi-free exclusive events for experimental data
 (black curves) and Monte Carlo simulation (blue curves). The comparison is shown for different
 100-MeV-wide W bins. The quantity $M_{X[\pi^-]}^2$ as well as the values of W are calculated under the
 target-at-rest-assumption. All distributions are normalized to their maxima. See text for details.

926 The similar analysis [22] carried out for the same beam energy but off a free proton
 927 target did not reveal any substantial discrepancies between the experimental and simulated
 928 distributions of the quantity $M_{X[\pi^-]}^2$; they are shown to be in a very good agreement for all
 929 W values. Figure 2.31 plotted for selected exclusive quasi-free events in the fully exclusive
 930 topology in turn proves that the Monte Carlo simulation incorporates effects of the tar-
 931 get motion correctly. Therefore, the discrepancy between data and simulation observed in
 932 Fig. 2.32 is attributed mainly to the FSI effects, which are not included into the simulation.

933 This mismatch between data and simulation together with the fact that in the π^- missing
 934 topology the quantity $M_{X[\pi^-]}^2$ is the only one available for the channel identification makes
 935 the task of selecting events in quasi-free kinematic rather challenging. To accomplish this
 936 goal, a special procedure was developed. This procedure is described below.

937 To select events in quasi-free kinematics properly, the following quantity is analyzed.

$$M_{X[\pi^-]} = \sqrt{|M_{X[\pi^-]}^2|} = \sqrt{|[P_{\pi^- \text{ miss}}^\mu]^2|} = \sqrt{|[P_e^\mu + P_p^\mu - P_{e'}^\mu - P_{p'}^\mu - P_{\pi^+}^\mu]^2|}. \quad (2.4.2)$$

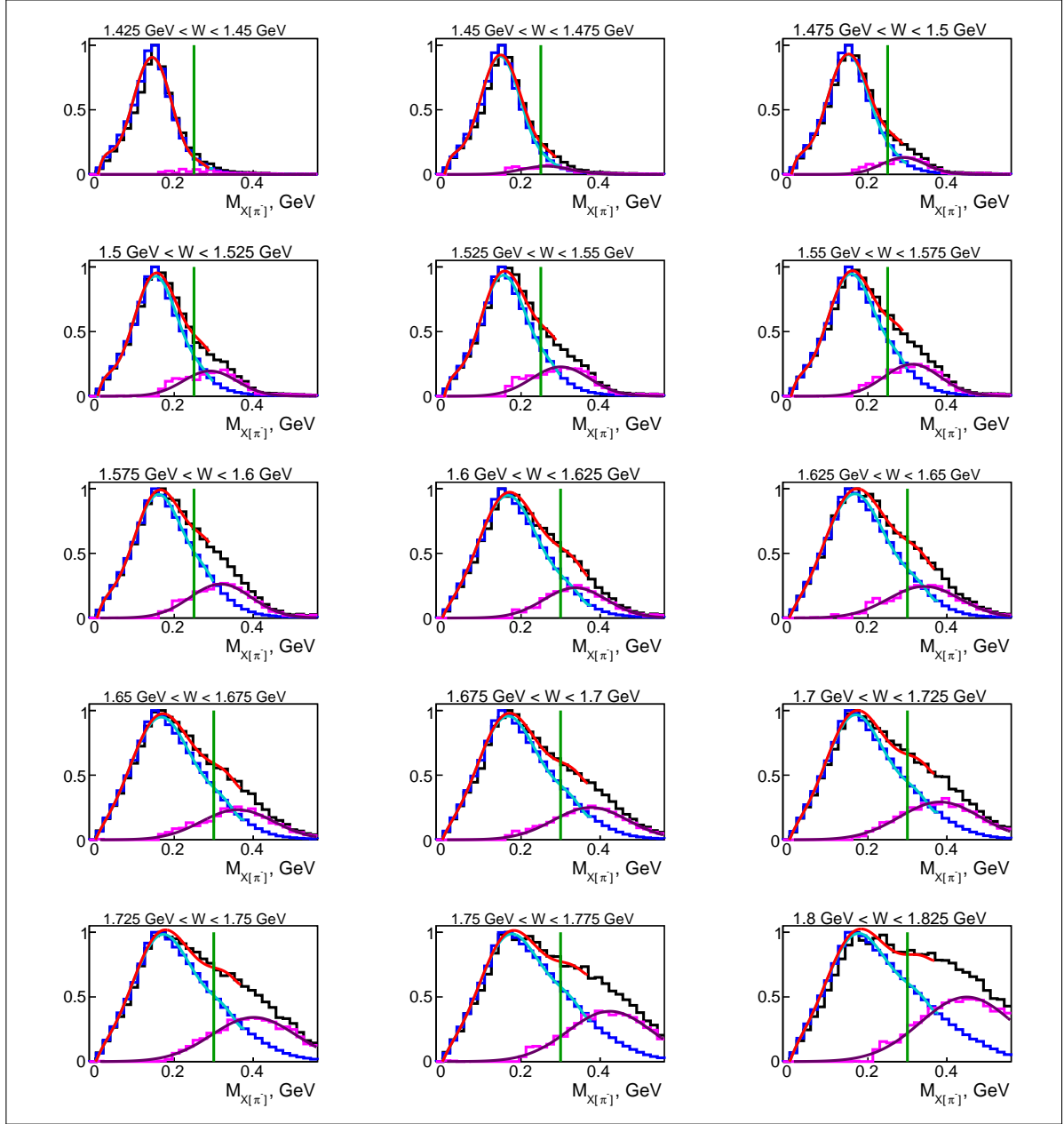


Figure 2.33: Distributions of the quantity $M_{X[\pi^-]}$ (defined by Eq. (2.4.2)) in different 25-MeV-wide W bins for experimental data (black histograms), Monte Carlo simulation (blue histograms), and their difference (magenta histograms). The explanation of the fit curves is given in the text. Green vertical lines correspond to the position of the cut that is intended to select quasi-free events. This cut is applied to the reconstructed Monte Carlo events as well.

939 The distributions of the quantity $M_{X[\pi^-]}$ in different 25-MeV-wide W bins are shown in
 940 Fig. 2.33 for experimental data (black histograms) and for Monte Carlo simulation (blue
 941 histograms). Both are normalized to their maxima. The mismatch between data and sim-
 942 ulation becomes discernible at $W \approx 1.5$ GeV, increases as W grows and becomes large at
 943 $W \approx 1.8$ GeV. The magenta histogram stands for the difference between the black and blue
 944 histograms and thus represents the distribution of background events originated mainly from
 945 FSI effects. The green vertical lines correspond to the position of the cut that is intended
 946 to select quasi-free events. This cut is applied to the reconstructed Monte Carlo events as
 947 well. However, as seen in Fig. 2.33, one can hardly completely separate the quasi-free event
 948 sample from the FSI-background by tightening the cut: in this way the statistics of quasi-
 949 free events will be subject to significant reduction, while the background admixture will still
 950 not be completely eliminated. Therefore, it was decided to perform a so-called “effective
 951 correction” of the FSI-background admixture, which includes the following steps.

- 952 • The distributions of $M_{X[\pi^-]}$ for the reconstructed Monte Carlo events (blue histograms)
 953 were fit by a ninth order polynomial in a slightly wider range than marked by the green
 954 cut lines. The results of the fit are shown in Fig. 2.33 by the cyan curves.
- 955 • The magenta background distributions were fit by Gaussians. The results of the fit are
 956 shown by the dark-magenta curves.
- 957 • The cyan and dark-magenta curves were summed up to produce the red curve, which
 958 perfectly matches the black experimental histogram in each W bin.
- 959 • The following correction factor was determined in the left side of the green cut line,

$$F_{fsi}(W) = \frac{\text{area under the cyan curve}}{\text{area under the red curve}} \leq 1. \quad (2.4.3)$$

- 960 • In each W bin the experimental event yield in the π^- -missing topology is multiplied by
 961 the factor F_{fsi} , which serves as an effective correction due to the remaining admixture
 962 of the FSI-background events.

964 The factor F_{fsi} is assumed to be only W dependent as it was found that it does not
 965 demonstrate any Q^2 dependence, and the dependence on the final hadron variables is ne-
 966 glected due to the statistics limitation. The typical value of F_{fsi} varies from ~ 0.97 to ~ 0.93
 967 in the W range from 1.4875 GeV to 1.8125 GeV, while for $W < 1.4875$ GeV $F_{fsi} = 1$ as the
 968 correction there is not needed.

969 Note that the exclusivity cut shown in Fig. 2.33 accompanied by the corresponding
 970 correction cares for all other possible effects that along with the FSI effects may contribute
 971 to the mismatch between the data and the simulation in this topology (including the three-
 972 pion background).

₉₇₃ **Chapter 3**

₉₇₄ **Cross section calculation**

₉₇₅ **3.1 W -smearing and boundary blurring of the Q^2 ver-**
₉₇₆ **sus W distribution**

₉₇₇ The smearing of the invariant mass W has the same origin as the smearing of the missing
₉₇₈ mass, which is already discussed in Sect. 2.4, but since W is the variable needed to describe
₉₇₉ the reaction (and the extracted cross section is binned in W), the issue of W -smearing
₉₈₀ requires special attention and, therefore, is separately addressed here.

₉₈₁ For the process of double-pion electroproduction off the proton (as for any other exclusive
₉₈₂ process) the reaction's invariant mass can in general be determined in two ways, i.e. either
₉₈₃ from the initial particle four-momenta¹ (W_i) or from the final particle four-momenta (W_f)
₉₈₄ as Eqs. (3.1.1) and (3.1.2) demonstrate.

$$W_i = \sqrt{(P_p^\mu + P_{\gamma_v}^\mu)^2} \quad (3.1.1)$$

$$W_f = \sqrt{(P_{\pi^+}^\mu + P_{\pi^-}^\mu + P_{p'}^\mu)^2} \quad (3.1.2)$$

₉₈₅ Here $P_{\pi^+}^\mu$, $P_{\pi^-}^\mu$, and $P_{p'}^\mu$ are the four-momenta of the final state hadrons, P_p^μ is the four-
₉₈₆ momentum of the initial proton and $P_{\gamma_v}^\mu = P_e^\mu - P_{e'}^\mu$ the four-momentum of the virtual photon
₉₈₇ with P_e^μ and $P_{e'}^\mu$ the four-momenta of the incoming and scattered electrons, respectively.

₉₈₈ To determine W_f , all final hadrons should be registered, while for the calculation of W_i
₉₈₉ it is sufficient to register the scattered electron. The latter opportunity allows event samples
₉₉₀ with one unregistered final hadron, whose four-momentum is recovered via the missing mass

¹ Although the scattered electron is treated as a final particle, here it is classified as “initial”, since it defines the virtual photon, which in turn is attributed to the initial state.

991 technique, to be used. This approach allows for a significant increase of the analyzed statistics
992 (see Sect. 2.4).

993 In experiments off protons at rest W_f and W_i may differ due to the detector resolution
994 and the radiative effects, which electrons undergo. In moving proton experiments one more
995 aspect takes effect, i.e. in order to calculate W_i , one needs information about the target
996 proton momentum (P_p^μ), which is accessible only in the fully exclusive topology². Therefore,
997 the value of W_i given by Eq. (3.1.1) turns out to be ill-defined, if one of the final hadrons
998 is not registered. This brings us to the choice to either demand the registration of all final
999 hadrons to determine W_f (that reduces the flexibility of the analysis) or to work under a so-
1000 called “target-at-rest-assumption”, which assumes the initial proton to be at rest. In the last
1001 approach the value of W_i appears to be smeared. This smeared value of the invariant mass
1002 is hereinafter denoted as W_{sm} . Meanwhile, the value W_f corresponds to the true reaction
1003 invariant mass and, therefore, is denoted as W_{true} . It can be calculated only in the fully
1004 exclusive topology.

1005 If a smeared value W_{sm} is used to describe the reaction, the extracted cross sections
1006 turned out to be convoluted with a function that is determined by the Fermi motion of the
1007 initial proton [26, 35]. To retrieve the non-smeared observable, a correction that unfolds this
1008 effect should be applied to the cross sections.

1009 Beside the W -smearing, the Fermi motion of the target proton is also responsible for the
1010 boundary blurring of the Q^2 versus W distribution³. This happens because the experiment
1011 off the moving proton with fixed laboratory beam energy is equivalent to that off the proton
1012 at rest performed with altered effective beam energy [26]. The boundaries of the Q^2 versus
1013 W distribution, however, are beam energy dependent. Therefore, the distribution edges,
1014 being sharp and distinct in the proton at rest experiment, become blurred in the experiment
1015 off a moving proton.

1016 The blurring, however, affects only the edges of Q^2 versus W_{true} distribution, where W_{true}
1017 is the true reaction invariant mass given by Eq. (3.1.2), since W_{true} accounts for the target
1018 motion and, therefore, for the alteration of the effective beam energy. If the smeared value
1019 W_{sm} , calculated by Eq. (3.1.1) under the target-at-rest-assumption, is used instead, the
1020 distribution edges are not subject to the blurring because the fixed value of the laboratory
1021 beam energy is used in calculations.

1022 This situation is illustrated in Fig. 3.1, where the Q^2 versus W distributions are shown
1023 for W_{sm} (left) and W_{true} (right). These distributions are plotted for the fully exclusive
1024 topology only, since it allows for the determination of both W_{sm} and W_{true} . The distributions,
1025 therefore, contain only a small portion of the total analyzed statistics. The boundaries of
1026 the left distribution are sharp, since the W_{sm} is calculated assuming the fixed laboratory
1027 beam energy and the target at rest. The boundaries of the right distribution are blurred,

²If the spectator nucleon momentum is not directly measured in the experiment. This was not an option in the analyzed “e1e” experiment.

³This issue is addressed in more details in Ref. [26]

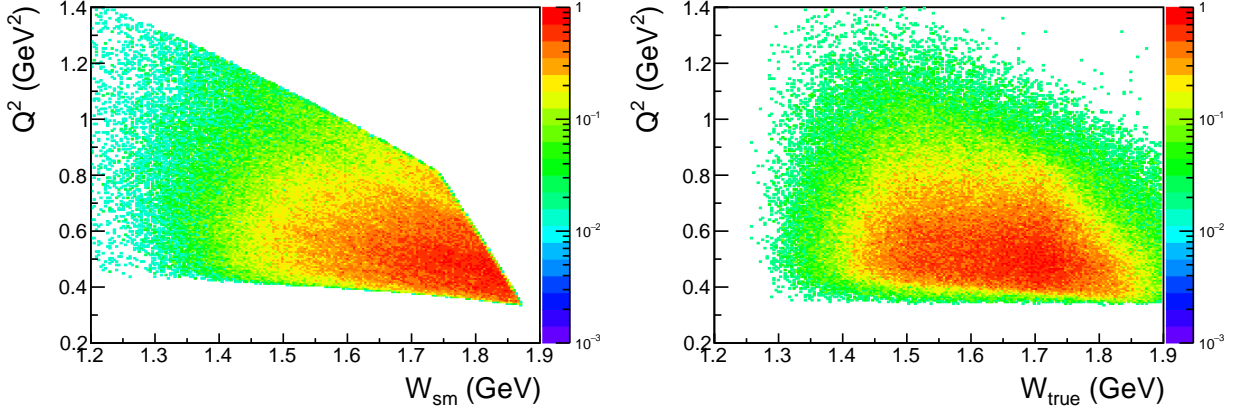


Figure 3.1: Experimental Q^2 versus W distributions for W_{sm} (left) and W_{true} (right) plotted for the fully exclusive topology. The boundaries of the left distribution are sharp, since the W_{sm} is calculated under the target-at-rest-assumption and the fixed value of the laboratory beam energy is used in calculations. The boundaries of the right distribution are blurred, since the calculation of W_{true} accounts for the target proton motion and therefore for the alteration of the effective beam energy of the experiment.

since the calculation of W_{true} accounts for the target proton motion and, therefore, for the alteration of the effective beam energy of the experiment.

The event yield in the blurred region suffers from depletion of events (compared to that for the case of fixed beam energy and sharp distribution edges). To estimate this effect, one should know the function that describes the alteration of the effective beam energy. This function is in turn determined by the target proton momentum distribution. The cross sections extracted in the blurred region need a special correction, otherwise they will suffer from the underestimation.

The situation described above offers two options, i.e. to use either W_{sm} or W_{true} to describe the reaction. The former opportunity leads to the need to apply a correction that unfolds the cross section smearing, while the latter requires the correction due to the blurring effect. The first option was chosen in this analysis because it has the advantage of using the π^- missing topology that accumulates the majority of the experimentally available statistics.

Thus, to calculate the cross section in this analysis, events are binned in W_{sm} . Note, however, that the corresponding W points on the chosen W_{sm} grid (see Sect. 3.4) are then treated as actual W -values where the cross section is eventually reported. However, the cross section values assigned to these W points is treated as distorted. The necessary correction to the cross section is based on the TWOPEG-D event generator [26], which offers a proper Monte Carlo simulation of the double-pion electroproduction off moving protons. This correction is described in Sect. 4.3.

1048 3.2 Lab to CMS transformation

1049 Once the quasi-free double-pion events are selected as described in Chapter 2, the laboratory
 1050 four-momenta of all final particles are known: they are either registered or calculated as
 1051 missing. These four-momenta are then used for the calculation of the kinematic variables,
 1052 which are introduced in Sect. 3.3. The cross sections meanwhile are extracted in the center-
 1053 of-mass frame of the *virtual photon – initial proton* system (CMS). Therefore, to calculate
 1054 the kinematic variables, the four-momenta of all particles need to be transformed from the
 1055 laboratory system (Lab) to the CMS.

1056 The CMS is uniquely defined as the system, where the initial proton and the photon
 1057 move towards each other with the z_{CMS} -axis along the photon and the net momentum equal
 1058 to zero. However, the procedure of the Lab to CMS transformation differs depending on
 1059 the specificity of the reaction initial state (real or virtual photons, at rest or moving target).
 1060 Figure 3.2 illustrates three options⁴ for the experimental specification of the reaction initial
 1061 state.

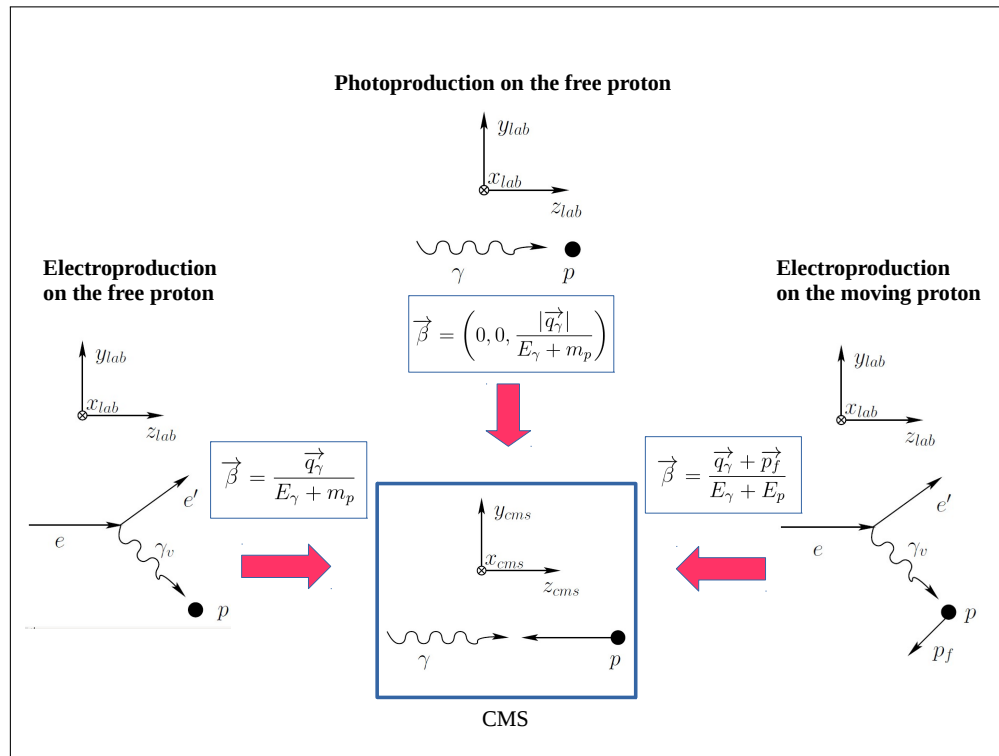


Figure 3.2: Illustration of three options for the experimental specification of the reaction initial state. Here m_p is the proton mass, \vec{q}_γ and E_γ are the three-momentum and the energy of the interacting photon, respectively, while p_f is the Fermi momentum of the target proton.

⁴The fourth option of the reaction off the moving proton induced by the real photons is not shown.

1062 The correct procedure of the Lab to CMS transformation for an electroproduction ex-
1063 periment off a moving target (bottom right illustration in Fig. 3.2) can be subdivided into
1064 two major steps.

- 1065 A. First, one needs to perform the transition to the auxiliary system, where the target
1066 proton is at rest, while the incoming electron moves along the z -axis. This system is
1067 called “quasi-Lab”, since the initial conditions of the reaction in this frame imitate
1068 those existing in the Lab system in the case of the free proton experiment. The recipe
1069 of the Lab to quasi-Lab transformations is given in detail in Ref. [26].
- 1070 B. Then, the quasi-Lab to CMS transformation should be performed by the standard
1071 method used for an electroproduction experiment off a proton at rest [22] (bottom left
1072 illustration in Fig. 3.2). Further details are given in App. B.

1073 To perform the first step of this procedure (Lab to quasi-Lab transformation), one should
1074 be aware of the initial proton momentum for each reaction event [26]. In this analysis,
1075 however, this information is available only in the fully exclusive topology, while the main
1076 π^- missing topology lacks this information. This situation brings us to the impossibility to
1077 perform the correct Lab to CMS transformation for the majority of events. Therefore, in this
1078 analysis the procedure of Lab to CMS transformation for an electroproduction experiment
1079 off a proton at rest [22] is used (bottom left illustration in Fig. 3.2). The procedure is
1080 described in App. B. This is done for both fully-exclusive and main π^- missing topologies
1081 for consistency.

1082 This approximation in the Lab to CMS transformation introduces a systematic inaccuracy
1083 to the extracted cross sections. A correction for this effect is included into the procedure of
1084 unfolding the effects of the target motion (see Sect. 4.3).

1085 3.3 Kinematic variables

1086 When the four-momenta of all particles are defined and transformed to the CMS, one can
 1087 calculate the kinematic variables that describe the reaction $ep(n) \rightarrow e'p'(n')\pi^+\pi^-$. For the
 1088 description of the reaction initial state two variables are needed. In this study they are chosen
 1089 in the following way: the invariant mass W , which is calculated according to Eq. (3.1.1),
 1090 and the photon virtuality Q^2 , which is defined as

$$Q^2 = -(P_{\gamma_v}^\mu)^2 = -(P_e^\mu - P_{e'}^\mu)^2, \quad (3.3.1)$$

1091 where $P_{\gamma_v}^\mu$ is the four-momentum of the virtual photon, while P_e^μ and $P_{e'}^\mu$ the four-momenta
 1092 of the incoming and scattered electrons, respectively.

1093 The three-body final hadron state is unambiguously determined by five kinematic vari-
 1094 ables [22], and there are several options for their choice. The following generalized set of
 1095 variables is used in this analysis⁵:

- 1096 • invariant mass of the first pair of the hadrons $M_{h_1 h_2}$,
- 1097 • invariant mass of the second pair of the hadrons $M_{h_2 h_3}$,
- 1098 • the first particle solid angle $\Omega_{h_1} = (\theta_{h_1}, \varphi_{h_1})$, and
- 1099 • the angle α_{h_1} between the two planes (i) defined by the three-momenta of the virtual
 1100 photon (or initial proton) and the first final hadron and (ii) defined by the three-
 1101 momenta of all final hadrons⁶.

1102 The cross sections in this analysis are obtained in three sets of variables depending on
 1103 various assignments for the first, second, and third final hadrons:

- 1104 1. $[p', \pi^+, \pi^-] M_{p'\pi^+}, M_{\pi^+\pi^-}, \theta_{p'}, \varphi_{p'}, \alpha_{p'} \text{ (or } \alpha_{[pp'][\pi^+\pi^-]} \text{)},$
- 1105 2. $[\pi^-, \pi^+, p'] M_{\pi^-\pi^+}, M_{\pi^+p'}, \theta_{\pi^-}, \varphi_{\pi^-}, \alpha_{\pi^-} \text{ (or } \alpha_{[p\pi^-][p'\pi^+]} \text{)},$
- 1106 3. $[\pi^+, \pi^-, p'] M_{\pi^+\pi^-}, M_{\pi^-p'}, \theta_{\pi^+}, \varphi_{\pi^+}, \alpha_{\pi^+} \text{ (or } \alpha_{[p\pi^+][p'\pi^-]} \text{)}.$

1107 Lets explain in more detail the calculation of the kinematic variables for the case of the set
 1108 number two. The invariant masses $M_{\pi^+\pi^-}$ and $M_{\pi^+p'}$ are calculated from the four-momenta
 1109 of the final particles $P_{\pi^-}^\mu, P_{\pi^+}^\mu, P_{p'}^\mu$ in the following way:

$$\begin{aligned} M_{\pi^+\pi^-} &= \sqrt{(P_{\pi^+}^\mu + P_{\pi^-}^\mu)^2} \quad \text{and} \\ M_{\pi^+p'} &= \sqrt{(P_{\pi^+}^\mu + P_{p'}^\mu)^2}. \end{aligned} \quad (3.3.2)$$

⁵ More details on the organization of the reaction phase-space can be found in App. C.

⁶ Note that the three-momenta of the π^+, π^-, p' are in the same plane, since in the CMS their total three-momentum has to be equal to zero.

1110 The polar (θ_{π^-}) and azimuthal (φ_{π^-}) angles of the π^- in the CMS are shown in Fig. 3.3.
 1111 In this figure the z -axis is directed along the virtual photon (with the unit vector \vec{n}_z), while
 1112 the x -axis is located in the electron scattering plane and follows the direction of the scattered
 1113 electron (see App. B for details). The plane A in Fig. 3.3 is defined by the three-momenta
 1114 of the π^- and initial proton.

1115 The angle θ_{π^-} varies in the range $[0, \pi]$ and is calculated as:

$$\theta_{\pi^-} = \arccos \left(\frac{(\vec{P}_{\pi^-} \cdot \vec{P}_\gamma)}{|\vec{P}_{\pi^-}| |\vec{P}_\gamma|} \right), \quad (3.3.3)$$

1116 where \vec{P}_γ is the three-momentum of the virtual photon and \vec{P}_{π^-} is the three-momentum of
 1117 the π^- (both are situated in the plane A).

1118 The angle φ_{π^-} varies in the range $[0, 2\pi]$ and is determined as:

$$\begin{aligned} \varphi_{\pi^-} &= \arctan \left(\frac{P_y}{P_x} \right), & \text{if } P_x > 0 \text{ and } P_y > 0, \\ \varphi_{\pi^-} &= \arctan \left(\frac{P_y}{P_x} \right) + 2\pi, & \text{if } P_x > 0 \text{ and } P_y < 0, \\ \varphi_{\pi^-} &= \arctan \left(\frac{P_y}{P_x} \right) + \pi, & \text{if } P_x < 0 \text{ and } P_y < 0, \\ \varphi_{\pi^-} &= \arctan \left(\frac{P_y}{P_x} \right) + \pi, & \text{if } P_x < 0 \text{ and } P_y > 0, \\ \varphi_{\pi^-} &= \frac{\pi}{2}, & \text{if } P_x = 0 \text{ and } P_y > 0, \\ \varphi_{\pi^-} &= \frac{3\pi}{2}, & \text{if } P_x = 0 \text{ and } P_y < 0, \end{aligned} \quad (3.3.4)$$

1119 where P_i is the i -component of the π^- three-momentum in the CMS ($i = x, y, z$).

1120 The calculation of the angle α_{π^-} , which is shown in Fig. 3.4, is more complicated. This
 1121 is the angle between the two planes A and B, which varies in a range $[0, 2\pi]$. The plane
 1122 A is defined by the three-momentum of the initial proton and the three-momentum of the
 1123 π^- . The plane B is defined by the three-momenta of all final hadrons. For the calculation
 1124 of the α_{π^-} , one determines first three auxiliary vectors $\vec{\gamma}$, $\vec{\beta}$, and $\vec{\delta}$, which are also shown in
 1125 Fig. 3.4.

1126 The auxiliary unit vector $\vec{\gamma}$ is situated in the plane A. This vector is perpendicular to
 1127 the three-momentum of the π^- and directed toward the vector $[-\vec{n}_z]$, where \vec{n}_z is the unit
 1128 vector directed along the z -axis. The vector $\vec{\gamma}$ can be expressed as

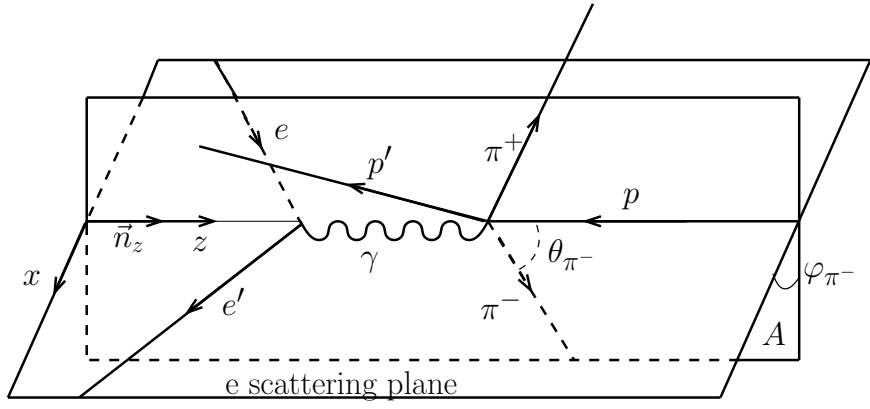


Figure 3.3: Polar (θ_{π^-}) and azimuthal (φ_{π^-}) angles of the π^- in the CMS. The z -axis is directed along the virtual photon (with the unit vector \vec{n}_z), while the x -axis is located in the electron scattering plane and follows the direction of the scattered electron. The plane A is defined by the three-momenta of the π^- and initial proton.

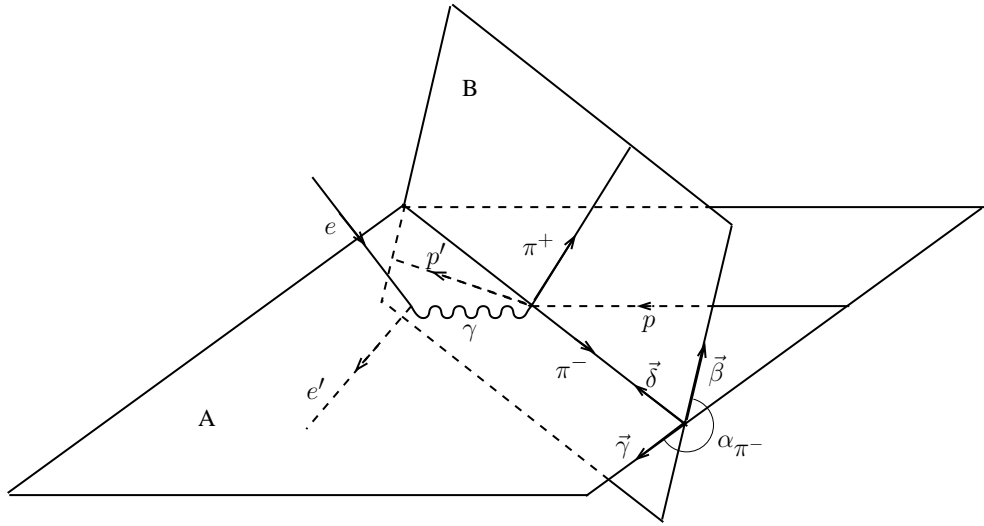


Figure 3.4: Definition of the angle α_{π^-} between the two planes: the plane A is defined by the three-momenta of the π^- and initial proton, while the plane B is defined by the three-momenta of all final hadrons. The definitions of auxiliary vectors $\vec{\beta}$, $\vec{\gamma}$, and $\vec{\delta}$ are given in the text.

$$\vec{\gamma} = a_\alpha \cdot [-\vec{n}_z] + b_\alpha \cdot \vec{n}_{\pi^-}$$

$$\text{with } a_\alpha = \sqrt{\frac{1}{1 - (\vec{n}_{\pi^-} \cdot [-\vec{n}_z])^2}} \quad \text{and} \quad b_\alpha = -a_\alpha \cdot (\vec{n}_{\pi^-} \cdot [-\vec{n}_z]) ,$$

1129 where \vec{n}_{π^-} is the unit vector directed along the three-momentum of the π^- .

The auxiliary unit vector $\vec{\beta}$ is situated in the plane B. This vector is perpendicular to the three-momentum of the π^- and directed toward the three-momentum of the π^+ . The vector $\vec{\beta}$ can be expressed as

$$\vec{\beta} = a_\beta \cdot \vec{n}_{\pi^+} + b_\beta \cdot \vec{n}_{\pi^-}$$

$$\text{with } a_\beta = \sqrt{\frac{1}{1 - (\vec{n}_{\pi^+} \cdot \vec{n}_{\pi^-})^2}} \quad \text{and} \quad b_\beta = -a_\beta \cdot (\vec{n}_{\pi^+} \cdot \vec{n}_{\pi^-}) ,$$

1130 where \vec{n}_{π^+} is the unit vector directed along the three-momentum of the π^+ .

1131 Taking the scalar products $(\vec{\gamma} \cdot \vec{\gamma})$, $(\vec{\beta} \cdot \vec{\beta})$, $(\vec{\gamma} \cdot \vec{n}_{\pi^-})$, and $(\vec{\beta} \cdot \vec{n}_{\pi^-})$, it is straightforward
1132 to verify that $\vec{\gamma}$ and $\vec{\beta}$ are the unit vectors perpendicular to the three-momentum of the π^- .

1133 The auxiliary unit vector $\vec{\delta}$ is the vector product of the auxiliary vectors $\vec{\gamma}$ and $\vec{\beta}$, i.e.

$$\vec{\delta} = [\vec{\gamma} \times \vec{\beta}] . \quad (3.3.5)$$

1134 Then the angle α_{π^-} is determined as:

$$\begin{aligned} \alpha_{\pi^-} &= \arccos(\vec{\gamma} \cdot \vec{\beta}), & \text{if } \vec{\delta} \uparrow\uparrow \vec{n}_{\pi^-}, \\ \alpha_{\pi^-} &= 2\pi - \arccos(\vec{\gamma} \cdot \vec{\beta}), & \text{if } \vec{\delta} \uparrow\downarrow \vec{n}_{\pi^-}. \end{aligned} \quad (3.3.6)$$

1135 The kinematic variables for the first and third sets are calculated in a similar way. The
1136 angles $\alpha_{p'}$ and α_{π^+} are shown for the convenience in Figs. 3.5 and 3.6. Further information
1137 on the kinematic of reactions with multi-particle final states can be found in Ref. [38].

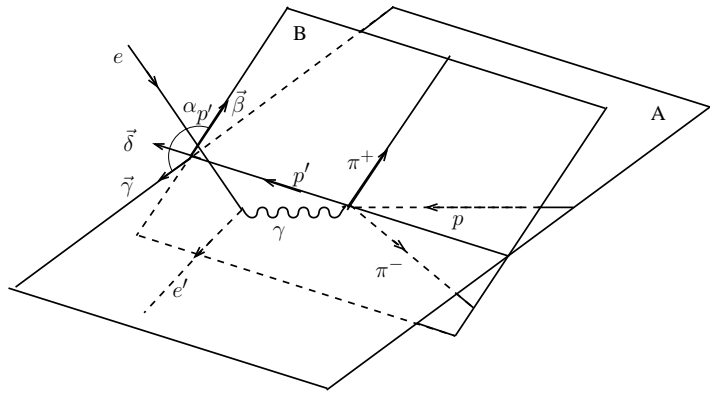


Figure 3.5: Definition of the angle $\alpha_{p'}$ between the two planes: the plane A is defined by the three-momenta of initial and scattered protons, while the plane B is defined by the three-momenta of all final hadrons.

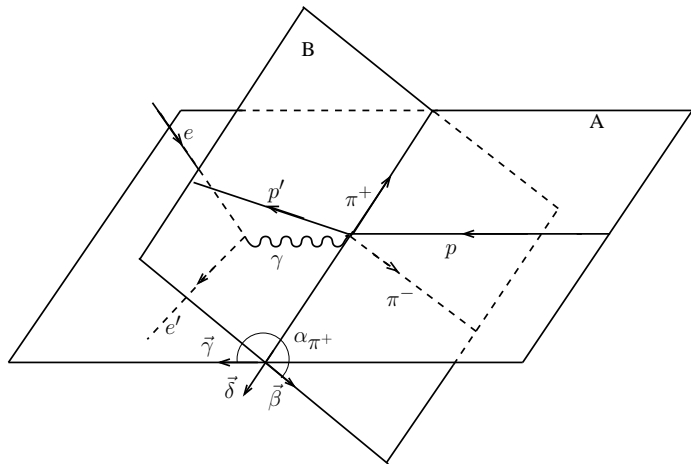


Figure 3.6: Definition of the angle α_{π^+} between the two planes: the plane A is defined by the three-momenta of the π^+ and initial proton, while the plane B is defined by the three-momenta of all final hadrons.

1138 3.4 Binning and kinematic coverage

1139 The available kinematic coverage in the initial state variables is shown by the Q^2 versus W
1140 distribution⁷ in Fig. 3.7. This distribution is filled with the double-pion events survived after
1141 the event selection described above. The blue boundary limits the analyzed kinematic area,
1142 where the double-pion cross sections are extracted. The black grid demonstrates the chosen
1143 binning in the initial state variables (25 MeV in W and 0.05 GeV² in Q^2).

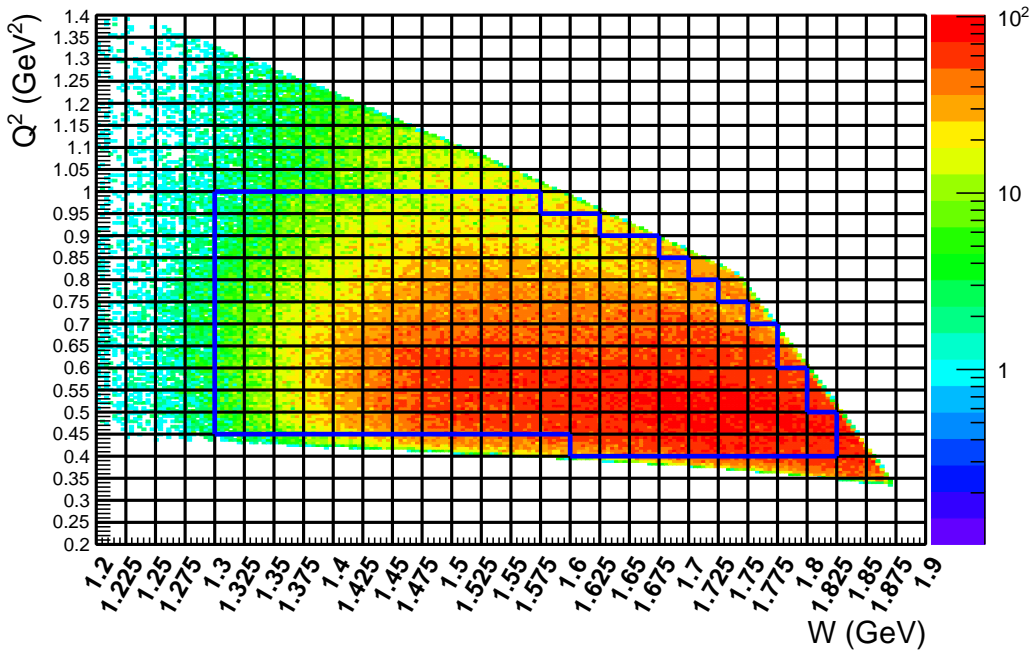


Figure 3.7: Q^2 versus W distribution⁷ populated with the selected double-pion events. The cross section is calculated in 2D cells within the blue boundaries.

1144 The kinematic coverage in the final state variables has the following reaction related
1145 features. The angular variables θ_{h_1} , φ_{h_1} , and α_{h_1} vary in the fixed ranges of $[0, \pi]$, $[0, 2\pi]$,
1146 and $[0, 2\pi]$, respectively. Meanwhile, the ranges of the invariant masses $M_{h_1 h_2}$ and $M_{h_2 h_3}$ are
1147 W dependent and broaden as W grows. More details on the specificity of the double-pion
1148 production phase-space are given in App. C.

1149 The binning in the final hadron variables used in this study is listed in Tab. 3.1. In
1150 each W and Q^2 bin the range of each final hadron variable is divided into bins of equal
1151 size. However, the number of bins differs in various W subranges, in order to take into
1152 account (i) the statistics drop near the reaction threshold, which is at ≈ 1.22 GeV and (ii)
1153 the aforementioned broadening of the reaction phase-space with increasing W . The chosen

⁷ Note that W here is W_{sm} , and therefore, the distribution boundaries are not subject to the blurring. See Sect. 3.1 for details.

amount of bins in each considered W subrange reflects the intention to maintain reasonable statistical uncertainties of the single-differential cross sections for all W and Q^2 bins.

For the binning in the polar angle note the following. The cross section, although being differential in $[-\cos \theta]$, is binned in θ . These $\Delta\theta$ bins are of equal size in the corresponding W subrange. See also Sect. 3.5 on this matter.

Table 3.1: Number of bins for hadronic variables.

		W subrange (GeV)			
Hadronic variable		[1.3, 1.35]	[1.35, 1.4]	[1.4, 1.475]	[1.475, 1.825]
$M_{h_1 h_2}$	Invariant mass	8	10	12	12
$M_{h_2 h_3}$	Invariant mass	8	10	12	12
θ_{h_1}	Polar angle	6	8	10	10
φ_{h_1}	Azimuthal angle	5	5	5	6
α_{h_1}	Angle between planes	5	6	8	8
Total number of bins in hadronic variables		9600	24000	57600	69120

The total numbers of multi-dimensional bins for the corresponding W ranges are listed in the last row of Tab. 3.1 and require some clarification. In fact the invariant masses border of the double-pion production phase-space is W -dependent and determined by the Byckling function (see App. C). Therefore, the bins located outside this border contain no double-pion events and hence do not contribute to the cross section. For a given W value, the border is distinct, however for a W bin, which corresponds to a range of W values, it is somewhat diffused. If events are binned in W_{true} (like in a free proton experiment) and the bin is small, e.g. 25 MeV, this diffusion is marginal. Then the quantity of bins involved in the cross section calculation (including both non-empty and empty cells) varies from 90% to 70% of the total numbers given in the last row of Tab. 3.1 as W increases from the threshold. However, if events are binned in W_{sm} (like in this analysis), each W_{sm} value in a bin corresponds to a sequence of W_{true} spread over 50-100 MeV. In this case a very pronounced boundary diffusion takes place, increasing the quantity of bins filled with events, i.e. the fraction of bins involved in the cross section calculation turn out to vary from 100% to 80% as W increases⁸.

⁸This estimation is based on the Monte Carlo simulation performed with TWOPEG [36] and TWOPEG-D [26] for the reactions off the proton at rest and off the moving proton, respectively.

1174 The specific organization of the double-pion production phase-space in the invariant
 1175 masses ($M_{h_1 h_2}$, $M_{h_2 h_3}$) causes the need to pay special attention to the binning in these vari-
 1176 ables. Equation (3.4.1) gives the expressions for the lower and upper boundaries of the $M_{h_1 h_2}$
 1177 distribution and demonstrates that the upper boundary depends on the value of W , while
 1178 the lower does not (see also App. C on this matter).

$$\begin{aligned} M_{lower} &= m_{h_1} + m_{h_2} \\ M_{upper}(W) &= W - m_{h_3}. \end{aligned} \tag{3.4.1}$$

1179 Here m_{h_1} , m_{h_2} , and m_{h_3} are the masses of the final hadrons.

1180 Since the cross section is calculated in a bin $W_{left} < W < W_{right}$, the boundary of M_{upper}
 1181 is not distinct. For the purpose of binning in mass, the value of M_{upper} is calculated using
 1182 W_{center} , at the center of the W bin. As a result, some events with $W > W_{center}$ turned out
 1183 to be located beyond M_{upper} . Hence it was decided to use a specific arrangement of mass
 1184 bins with the bin width ΔM determined by

$$\Delta M = \frac{M_{upper} - M_{lower}}{N_{bins} - 1}, \tag{3.4.2}$$

1185 where N_{bins} is the number of bins specified in the first row of Tab. 3.1. The left boundary
 1186 of the first bin is set to M_{lower} .

1187 The chosen arrangement of bins forces the last bin to be situated completely out of the
 1188 boundaries given by Eq. (3.4.1) using W_{center} ⁹. Therefore, the cross section in this extra bin
 1189 finally is not reported. However, this bin is kept in the analysis since its content (though
 1190 being very small) contributes to all cross sections that are obtained by integrating over the
 1191 corresponding invariant mass distribution.

1192 Note that the cross section in the next to last bin in invariant mass needs a special
 1193 correction. This correction is described in Sect. 4.4.

⁹ Note that for each W bin and for each invariant mass, ΔM given by Eq. (3.4.2) is greater than 12.5 MeV, which is the half of the W bin width.

1194 3.5 Cross section formulae

1195 3.5.1 Electron scattering cross section

1196 The experimental electron scattering cross section σ_e for the reaction $ep(n) \rightarrow e'p'(n')\pi^+\pi^-$
 1197 is seven-fold differential and calculated as¹⁰

$$\frac{d^7\sigma_e}{dWdQ^2d^5\tau} = \frac{1}{R \cdot \mathcal{F}} \cdot \frac{\left(\frac{N_{full}}{Q_{full}} - \frac{N_{empty}}{Q_{empty}}\right)}{\Delta W \cdot \Delta Q^2 \cdot \Delta^5\tau \cdot \left[\frac{l \cdot \rho \cdot N_A}{q_e \cdot \mu_d}\right] \cdot \mathcal{E}}, \text{ where} \quad (3.5.1)$$

- 1198 • $d^5\tau = dM_{h_1h_2}dM_{h_2h_3}d\Omega_{h_1}d\alpha_{h_1}$ is the differential of the five independent variables of
 1199 the $\pi^+\pi^-p$ final state, which are described in Sect. 3.3;
- 1200 • N_{full} and N_{empty} are the numbers of selected double-pion events inside the seven-
 1201 dimensional bin for runs with deuterium and empty target, respectively;
- 1202 • the quantity in the square brackets in the denominator corresponds to the luminosity
 1203 of the experiment \mathcal{L} in the units $\text{cm}^{-2} \cdot \text{C}^{-1}$ and its components are

1204 $l = 2 \text{ cm}$ the length of the target,
 1205 $\rho = 0.169 \text{ g} \cdot \text{cm}^{-3}$ the density of liquid deuterium,
 1206 $N_A = 6.022 \cdot 10^{-19} \text{ mol}^{-1}$ Avogadro's number,
 1207 $q_e = 1.602 \cdot 10^{-19} \text{ C}$ the elementary charge, and
 1208 $\mu_d = 2.014 \text{ g} \cdot \text{mol}^{-1}$ the molar mass of deuterium,

1209 which results in the luminosity value of $\mathcal{L} = 0.63 \cdot 10^{42} \text{ cm}^{-2} \cdot \text{C}^{-1} = 0.63 \cdot 10^{12} \mu\text{b}^{-1} \cdot \text{C}^{-1}$;

- 1210 • $Q_{full} = 3734.69 \mu\text{C}$ and $Q_{empty} = 464.797 \mu\text{C}$ are the values of the charge accumulated
 1211 in the Faraday Cup for deuterium and empty target runs, respectively¹¹, which results
 1212 in the corresponding values of the integrated luminosity $L = \mathcal{L} \cdot Q$ of $2.35 \cdot 10^9 \mu\text{b}^{-1}$
 1213 and $0.29 \cdot 10^9 \mu\text{b}^{-1}$;
- 1214 • $\mathcal{E} = \mathcal{E}(\Delta W, \Delta Q^2, \Delta^5\tau)$ is the detector efficiency (which includes the detector accep-
 1215 tance) for each seven-dimensional bin as determined by the Monte Carlo simulation
 1216 (see Sect. 3.6);
- 1217 • $R = R(\Delta W, \Delta Q^2)$ is the radiative correction factor described in Sec. 4.2;
- 1218 • $\mathcal{F} = \mathcal{F}(\Delta W, \Delta Q^2, \Delta^5\tau)$ is the correction factor that aims at unfolding the effects of
 1219 the target motion (see Sect. 4.3).

1220 The electron scattering cross section σ_e in the left hand side of Eq. (3.5.1) is assumed to
 1221 be obtained in the center of the finite seven-dimensional kinematic bin $\Delta W \Delta Q^2 \Delta^5\tau$.

¹⁰ To deal with the multi-differential cross section, THnSparse multi-dimensional root histograms are used.

¹¹ They are calculated by summing up the charges of all analyzed *blocks* (see Sect. 2.3.2 for details).

1222 **3.5.2 Virtual photoproduction cross section**

1223 The goal of the analysis is to extract the virtual photoproduction cross section σ_v of the
1224 reaction $\gamma_vp(n) \rightarrow p'(n')\pi^+\pi^-$. This virtual photoproduction cross section σ_v is five-fold
1225 differential and in the single-photon exchange approximation connected with the seven-fold
1226 differential electron scattering cross section¹² σ_e via

$$\frac{d^5\sigma_v}{d^5\tau} = \frac{1}{\Gamma_v} \frac{d^7\sigma_e}{dW dQ^2 d^5\tau}, \quad (3.5.2)$$

1227 where Γ_v is the virtual photon flux given by

$$\Gamma_v(W, Q^2) = \frac{\alpha}{4\pi} \frac{1}{E_{beam}^2 m_p^2} \frac{W(W^2 - m_p^2)}{(1 - \varepsilon_T)Q^2}. \quad (3.5.3)$$

1228 Here α is the fine structure constant ($1/137$), m_p the proton mass, $E_{beam} = 2.039$ GeV
1229 the laboratory energy of the incoming electron beam, and ε_T the virtual photon transverse
1230 polarization given by

$$\varepsilon_T = \left(1 + 2 \left(1 + \frac{\nu^2}{Q^2} \right) \tan^2 \left(\frac{\theta_{e'}}{2} \right) \right)^{-1}, \quad (3.5.4)$$

1231 where $\nu = E_{beam} - E_{e'}$ is the virtual photon energy, while $E_{e'}$ and $\theta_{e'}$ are the energy and the
1232 polar angle of the scattered electron in the lab frame, respectively.

1233 The value of the virtual photon flux given by Eq. (3.5.3) is calculated for the central
1234 point of the $\Delta W \Delta Q^2$ bin.

1235 The limited statistics of the experiment does not allow for estimates of the five-fold
1236 differential cross section σ_v with a reasonable accuracy. Therefore, the cross section σ_v is
1237 first obtained on the multi-dimensional grid and then is integrated over at least four hadron
1238 variables. Hence, only the sets of the single-differential and fully-integrated cross sections
1239 are obtained.

¹² Note that after the corrections introduced in Eq. (3.5.1) by the factors R and \mathcal{F} , the cross section σ_e is the true electron scattering cross section attributed to the central values of the corresponding $\Delta W \Delta Q^2 \Delta^5\tau$ bin and the distinct value of the beam energy $E_{beam} = 2.039$ GeV.

¹²⁴⁰ For each W and Q^2 bin, the following cross sections are extracted for each variable set.

$$\begin{aligned}
 \frac{d\sigma_v}{dM_{h_1 h_2}} &= \int \frac{d^5\sigma_v}{d^5\tau} dM_{h_2 h_3} d\Omega_{h_1} d\alpha_{h_1}, \\
 \frac{d\sigma_v}{dM_{h_2 h_3}} &= \int \frac{d^5\sigma_v}{d^5\tau} dM_{h_1 h_2} d\Omega_{h_1} d\alpha_{h_1}, \\
 \frac{d\sigma_v}{d[-\cos\theta_{h_1}]} &= \int \frac{d^5\sigma_v}{d^5\tau} dM_{h_1 h_2} dM_{h_2 h_3} d\varphi_{h_1} d\alpha_{h_1}, \\
 \frac{d\sigma_v}{d\alpha_{h_1}} &= \int \frac{d^5\sigma_v}{d^5\tau} dM_{h_1 h_2} dM_{h_2 h_3} d\Omega_{h_1}, \quad \text{and} \\
 \sigma_v^{int}(W, Q^2) &= \int \frac{d^5\sigma_v}{d^5\tau} dM_{h_1 h_2} dM_{h_2 h_3} d\Omega_{h_1} d\alpha_{h_1}.
 \end{aligned} \tag{3.5.5}$$

¹²⁴¹ As a final result for each W and Q^2 bin, the integral cross section σ_v^{int} , averaged over the
¹²⁴² three variable sets, is reported together with the nine single-differential cross sections given
¹²⁴³ in (3.5.6), where each column is taken from the corresponding variable set.

$$\begin{array}{ccc}
 \frac{d\sigma_v}{dM_{p'\pi^+}} & \frac{d\sigma_v}{dM_{\pi^-\pi^+}} & \frac{d\sigma_v}{dM_{\pi^-p'}} \\
 \frac{d\sigma_v}{d[-\cos\theta_{p'}]} & \frac{d\sigma_v}{d[-\cos\theta_{\pi^-}]} & \frac{d\sigma_v}{d[-\cos\theta_{\pi^+}]} \\
 \frac{d\sigma_v}{d\alpha_{p'}} & \frac{d\sigma_v}{d\alpha_{\pi^-}} & \frac{d\sigma_v}{d\alpha_{\pi^+}}
 \end{array} \tag{3.5.6}$$

¹²⁴⁴ Regarding the middle row in (3.5.6) note the following. Although being differential
¹²⁴⁵ in $[-\cos\theta]$, the cross sections are calculated in $\Delta\theta$ bins, which are of equal size in the
¹²⁴⁶ corresponding W subrange (see Sect. 3.4 for details). This is a conventional way of presenting
¹²⁴⁷ the θ -distributions in the studies of double-pion cross sections [15–19, 21–23].

1248 3.6 Efficiency evaluation

1249 For the Monte Carlo simulation the TWOPEG-D event generator was used [26]. This is
 1250 the version of TWOPEG (an event generator for double-pion electroproduction off the free
 1251 proton [36]), which is able to simulate the effects of the initial proton motion. In this version
 1252 of the event generator the Fermi motion of the initial proton is generated according to the
 1253 Bonn potential [37] and then naturally merged into the specific kinematics of double-pion
 1254 electroproduction. TWOPEG-D accounts for radiative effects according to the approach
 1255 described in Refs. [36, 39].

1256 The generated events are passed through the standard detector simulation (GSIM, GPP)
 1257 and reconstruction procedures (reccsis) with the majority of parameters kept the same as in
 1258 the studies [22, 40], which were also devoted to the “e1e” run period¹³.

1259 In the studies of double-pion production cross section it is especially important to gen-
 1260 erate enough Monte Carlo statistics in order to saturate each multi-dimensional bin of the
 1261 reaction phase-space with events (see Tab. 3.1). Insufficient Monte Carlo statistics leads to
 1262 an improper efficiency evaluation and an unnecessary rise in the empty cells contribution
 1263 (see Sect. 4.1), thus systematically affecting the accuracy of the extracted cross sections. For
 1264 this study the total of about $4 \cdot 10^{10}$ double-pion events were generated in the investigated
 1265 kinematic region, which is considered adequate.

1266 The TWOPEG-D event generator performs a weighted event generation [36], i.e. all
 1267 kinematic variables are generated randomly according to the double-pion production phase-
 1268 space, while each event generated at a particular kinematic point acquires an individual
 1269 weight, which corresponds to the cross section at this point. Therefore, the efficiency factor
 1270 \mathcal{E} from Eq. (3.5.1) is calculated in each $\Delta W \Delta Q^2 \Delta^5 \tau$ bin as

$$\mathcal{E}(\Delta W, \Delta Q^2, \Delta^5 \tau) = \frac{\mathbb{N}_{rec}}{\mathbb{N}_{gen}} = \frac{\sum_{i=1}^{N_{rec}} w_i}{\sum_{j=1}^{N_{gen}} w_j}, \quad (3.6.1)$$

1271 where N_{gen} is the number of generated double-pion events (without any cuts) inside the
 1272 multi-dimensional bin, N_{rec} is the number of reconstructed double-pion events that survived
 1273 in the bin after the event selection, while \mathbb{N}_{gen} and \mathbb{N}_{rec} are the weighted numbers of the
 1274 corresponding events and w is a weight of an individual event.

1275 The efficiency in some kinematic bins could not be reliably determined due to boundary
 1276 effects, bin to bin event migration, and limited Monte Carlo statistics. Such cells were
 1277 excluded from consideration. They can be differentiated from the cells with reliable efficiency
 1278 by a larger relative efficiency uncertainty $\delta\mathcal{E}/\mathcal{E}$.

¹³ See the beginning of Sect. 2 and also App. E for more details on the simulation/reconstruction procedure and for the information on the corresponding parameters used in this analysis.

Meanwhile, the calculation of the efficiency uncertainty $\delta\mathcal{E}$ is not straightforward and needs special attention, since (i) N_{gen} and N_{rec} in Eq. (3.6.1) are not independent and (ii) Monte Carlo events in this equation are subject to weighting. Therefore, the special approach described in Ref. [41] was used to calculate $\delta\mathcal{E}$. Neglecting the event migration between the bins, this approach gives the following expression for the absolute statistical uncertainty of the efficiency in a bin for the case of weighted Monte Carlo simulation,

$$\delta\mathcal{E} = \sqrt{\frac{N_{gen} - 2N_{rec}}{N_{gen}^3} \sum_{i=1}^{N_{rec}} w_i^2 + \frac{N_{rec}^2}{N_{gen}^4} \sum_{j=1}^{N_{gen}} w_j^2}. \quad (3.6.2)$$

Meanwhile, according to Ref. [41], in the case of unweighted Monte Carlo simulation, the formula in Eq. (7.1.3) reduces to

$$\delta\tilde{\mathcal{E}} = \sqrt{\frac{N_{rec}(N_{gen} - N_{rec})}{N_{gen}^3}}, \text{ where } \tilde{\mathcal{E}} = \frac{N_{rec}}{N_{gen}}. \quad (3.6.3)$$

Figure 3.8 (a) shows the distribution of the relative efficiency uncertainty $\delta\mathcal{E}/\mathcal{E}$ versus efficiency \mathcal{E} plotted taking the weights (see Eq. (7.1.3)) into account. In this plot the statistical effects turn out to be convoluted with the distribution of weights thus complicating the revealing of cells with unreliable efficiency. To isolate only the statistical effects, the distribution $\delta\mathcal{E}/\tilde{\mathcal{E}}$ versus $\tilde{\mathcal{E}}$, which is produced ignoring the weights (see Eq. (3.6.3)), is plotted in the panel (b). As seen in this plot, the cells with high relative efficiency uncertainty are clustered along the horizontal stripes. This clustering originates from the fact that (if the weights are ignored) the efficiency is obtained by the division of two integer numbers, which reveals the bins with small statistics of the reconstructed events. These horizontal stripes, furthermore, contain many cells with unreliable extremely small efficiency. Therefore, the following criterion for the selection of cells with reliable efficiency is used $\delta\tilde{\mathcal{E}}/\tilde{\mathcal{E}} < 0.3$. This cut is shown in Fig. 3.8 (b) by the red horizontal line. All cells above this line were excluded from the analysis. The influence of this cut on the distribution $\delta\mathcal{E}/\mathcal{E}$ (with the weights taken into account) is shown in Fig. 3.8 (c).

The number of reconstructed events in the revealed cells with unreliable efficiency is set to zero ($N_{rec} = 0$). Then such a cell is ranked as an “empty cell” and, along with other empty cells, is subject to the filling procedure, which is described in Sect. 4.1.

The described above cut on the relative efficiency uncertainty directly impacts the cross section’s uncertainties. On the one hand, it eliminates the $\Delta^5\tau$ bins with high relative efficiency uncertainty, thus reducing the total statistical uncertainty of the extracted cross sections (see Sect. 7.1). On the other hand, this cut increases the amount of empty cells, thus increasing the cross section’s model dependence and the uncertainty associated with it (see Sect. 7.2). The cut value is therefore chosen as a compromise between these two effects.

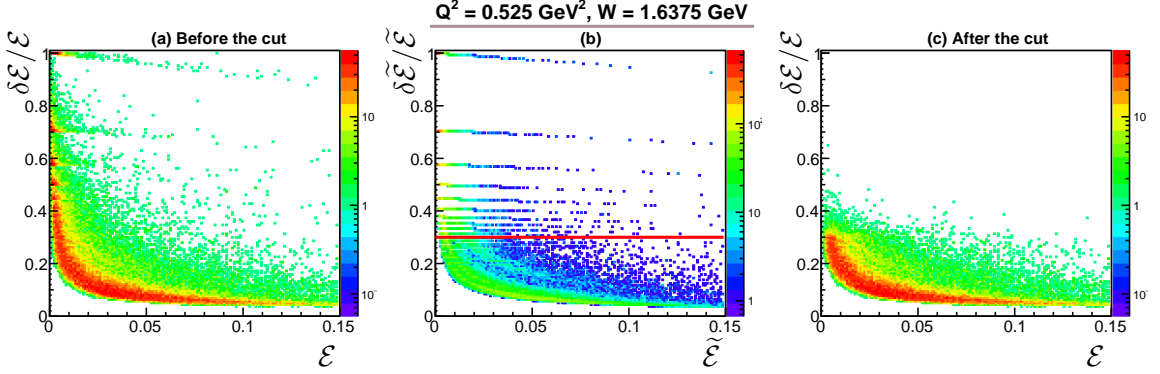


Figure 3.8: Distributions of the relative efficiency uncertainty versus efficiency (a) taking into account the weights (see Eq. (7.1.3)) and (b) ignoring them (see Eq. (3.6.3)). The cut that aims to select the cells with reliable efficiency is shown by the red horizontal line in panel (b). Panel (c) shows the influence of this cut on the distribution $\delta\mathcal{E}/\mathcal{E}$ (with the weights taken into account). The distributions are provided for one particular $\Delta W \Delta Q^2$ bin (with the central values specified in figure), and the color code represents the number of multi-dimensional cells within this bin. Note that the z-axis maximum for the plot (a) is set the same as for the plot (c).

1310 The idea of this cut is taken from the study [22, 23], which uses unweighted Monte Carlo
 1311 simulation and therefore employs Eq. (3.6.3) to calculate the efficiency uncertainty. The
 1312 study [22, 23] observed the similar cell clustering along horizontal stripes as that revealed in
 1313 this analysis in the distributions of $\delta\tilde{\mathcal{E}}/\tilde{\mathcal{E}}$ versus $\tilde{\mathcal{E}}$ (produced ignoring the weights) and also
 1314 set the cut at the position of 0.3.

1315 Note that in this particular analysis the formula (3.6.3) for the unweighted Monte Carlo
 1316 is used only for selecting the bins with reliable efficiency, since it allows the pure statistical
 1317 behavior of the efficiency uncertainty to be determined. For the estimation of the cross
 1318 section's statistical uncertainty the weights are taken into account and the formula (7.1.3)
 1319 is applied (see Sect. 7.1).

1320 **Chapter 4**

1321 **Corrections to the cross sections**

1322 This chapter gives the description of the corrections to the extracted cross sections in the
1323 order they were applied.

1324 **4.1 Filling kinematic cells with zero acceptance**

1325 Due to blind areas in the geometrical coverage of the CLAS detector, some kinematic bins
1326 of the double-pion production phase-space turned out to have zero acceptance. In such bins,
1327 which are usually called empty cells, the cross section cannot be experimentally defined.
1328 For the studies, which aim at extracting fully-differential cross sections (i.e. single-pion
1329 production analyses), this is not a problem of great importance, since the cross section in
1330 blind areas is just not reported. However, in the studies of double-pion production, where the
1331 limited experimental statistics allows only single-differential cross sections to be extracted,
1332 this issue becomes a point of special attention [17–19, 21–23]. The empty cells contribute to
1333 the integrals in Eqs. (3.5.5) along with the other kinematic bins. Ignoring the contribution
1334 from the empty cells leads to a systematic cross section underestimation and, therefore,
1335 some assumptions for the empty cells’ content are needed. This situation causes some model
1336 dependence of the final result.

1337 The map of the empty cells is determined using the Monte Carlo simulation. A cell
1338 is treated as empty, if it contains generated events ($N_{gen} > 0$), but does not contain any
1339 reconstructed events ($N_{rec} = 0$). The cells with unreliable efficiencies, revealed based on the
1340 cut on the efficiency uncertainty (see Sect. 3.6), are also treated as empty. Empty cells should
1341 not be confused with the cells that contain both generated and reconstructed events, but
1342 do not contain experimental data, i.e. they appear due to the limited experiment duration,
1343 which is taken into account via the normalization on the Faraday Cup charge, and therefore,
1344 no model assumptions for them are needed.

1345 It is conventional practice in the studies of the double-pion production to fill the empty

1346 cells by means of the Monte Carlo event generator (usually the one that is used to evaluate
 1347 the efficiency). The studies [15–19, 21] used GENEV [42] (the double-pion event generator
 1348 based on the JM05 reaction model) for this purpose. The empty cells in these studies
 1349 were filled with the generated events, which were subject to a special scaling procedure in
 1350 order to match the experimental data in the regular (non-empty) cells. Meanwhile, the
 1351 study [22, 23] used TWOPEG [36] for the empty cells filling. TWOPEG is the new double-
 1352 pion event generator, which is based on the JM15 model and up to now provides the best
 1353 cross section estimation in the kinematic region $W < 2$ GeV and $Q^2 < 1.3$ GeV 2 . Since
 1354 TWOPEG is capable of providing the absolute cross section value for a given kinematic
 1355 point, the study [22, 23] used the cross section estimated by TWOPEG as an assumption
 1356 for the empty cells content.

1357 In this particular study the empty cells are filled by means of the TWOPEG-D event
 1358 generator [26], which is the version of TWOPEG for moving protons. Although TWOPEG-D
 1359 is also capable of providing the absolute cross section value, the empty cells in this study were
 1360 nevertheless filled with the scaled generated events (as in Refs. [15–19, 21]). This method
 1361 was chosen because TWOPEG-D assumes all events to be produced in the quasi-free regime
 1362 (ignoring FSI) and therefore somewhat overestimates the quasi-free cross section.

1363 Thus, in this study empty multi-dimensional cells are filled with the Monte Carlo events
 1364 generated by TWOPEG-D (following Refs. [15–19, 21]), relying on the cross section shape
 1365 implemented in the generator. These generated events are subject to the scaling, which
 1366 leaving the shape unchanged adjusts the empty cells content to the experimental yield in
 1367 the regular (non-empty) cells. The scaling is performed individually in each $\Delta W \Delta Q^2$ bin
 1368 according to the integral yields of the experimental and simulated events in the non-empty
 1369 cells within this bin. The number of events N_{model} that is assigned as a content for the empty
 1370 $\Delta^5\tau$ cell located in the corresponding $\Delta W \Delta Q^2$ bin is then estimated as

$$N_{model}(\Delta W, \Delta Q^2, \Delta^5\tau) = \frac{\mathcal{N}_{data}^{int}}{\mathcal{N}_{rec}^{int}} \cdot \mathbb{N}_{gen}(\Delta W, \Delta Q^2, \Delta^5\tau), \quad (4.1.1)$$

1371 where \mathbb{N}_{gen} is the weighted number of generated events in the corresponding multi-
 1372 dimensional bin, while the fraction represents the integral scaling factor with \mathcal{N}_{data}^{int} and
 1373 \mathcal{N}_{rec}^{int} being the total number of experimental events (normalized by the FC charge) and
 1374 the total number of reconstructed events in all non-empty $\Delta^5\tau$ bins within the considered
 1375 $\Delta W \Delta Q^2$ bin, respectively. These quantities are given by

$$\begin{aligned} \mathcal{N}_{data}^{int}(\Delta W, \Delta Q^2) &= \sum_{\substack{\text{All } \Delta^5\tau \\ \text{with } N_{rec} > 0}} \left[\frac{N_{full}}{Q_{full}} - \frac{N_{empty}}{Q_{empty}} \right], \text{ and} \\ \mathcal{N}_{rec}^{int}(\Delta W, \Delta Q^2) &= \sum_{\substack{\text{All } \Delta^5\tau \\ \text{with } N_{rec} > 0}} \mathbb{N}_{rec}, \end{aligned} \quad (4.1.2)$$

1376 where \mathbb{N}_{rec} is the weighted number of reconstructed events in the corresponding $\Delta^5\tau$ bin.

1377 For each empty $\Delta W \Delta Q^2 \Delta^5\tau$ bin, the quantity given by Eq. (4.1.1) imitates the yield of
1378 experimental events normalized by the FC charge and corrected by the detector efficiency
1379 (see Eq. (3.5.1)). The cross section in the empty cells is then calculated as

$$\frac{d^7\sigma_e}{dW dQ^2 d^5\tau} = \frac{N_{model}}{\Delta W \cdot \Delta Q^2 \cdot \Delta^5\tau \cdot [\mathcal{L}]}, \quad (4.1.3)$$

1380 with N_{model} given by Eq. (4.1.1), and all other variables explained after Eq. (3.5.1). Note
1381 that the empty cells are filled before applying the correction factors R and \mathcal{F} .

1382 Figure 4.1 introduces the single-differential cross sections given by Eqs. (3.5.5) and
1383 (3.5.6)¹. The empty squares correspond to the case when the contribution from the empty
1384 cells was ignored, and the black circles are for the case when that was taken into account in
1385 the way described above. The figure demonstrates a satisfactory small contribution from the
1386 empty cells (and therefore a small model dependence of the results). Only the edge points
1387 in the θ distributions (middle row) reveal pronounced empty cell contributions due to the
1388 negligible/zero CLAS acceptance in the corresponding directions.

1389 Table 4.1 demonstrates the relative empty cell contribution to the integral cross sections
1390 for all reported (W, Q^2)-points¹. Different shades of red correspond to different percentage
1391 ranges, i.e. the lightest shade corresponds to the contribution $\leq 20\%$, darker shade – from
1392 21% to 30%, and the darkest one shows the contribution $> 30\%$. As seen from the table,
1393 for most of the (W, Q^2)-points the contribution from the empty cells is kept on a low
1394 level of $\sim 15\%$, having a small rise at the low Q^2 and high W boundaries, which originates
1395 from the momentum-dependent restrictions on the minimal and maximal polar angles of
1396 the scattered electron, respectively (see Sect. 2.3.1). Additionally, the rise of the empty
1397 cells contribution for small $W \sim 1.3$ GeV is thought to be related to the fact that near the
1398 production threshold the hadrons carry small momentum and hence failed to be registered
1399 since (i) they are more likely bent to the detector holes, (ii) CLAS is not designed to register
1400 hadrons with a momentum less than a certain value (see e.g. Fig. 2.10), and (iii) the smaller
1401 the hadron velocity is, the more energy it loses in materials (Bragg peak). A similar rise of
1402 the empty cells contribution near the threshold was also observed in Refs. [17, 18, 22, 23],
1403 which are devoted to the double-pion electroproduction off the free proton.

1404 To account for the model dependence, the approach established for the previous studies
1405 of double-pion production cross sections is followed [19, 20, 22], i.e. the part of the
1406 single-differential cross section that came from the empty cells is assigned a 50% relative
1407 uncertainty. The corresponding absolute uncertainty δ_{model} is then combined with the total
1408 statistical uncertainty, as was done in Refs. [19, 20, 22] (more details are in Sect. 7.1).

¹ Both Figure 4.1 and Table 4.1 are given for the cross sections, which (although being divided by the virtual photon flux) are neither corrected for the radiative effects (see Sect. 4.2) nor for the effects of the target motion (see Sect. 4.3).

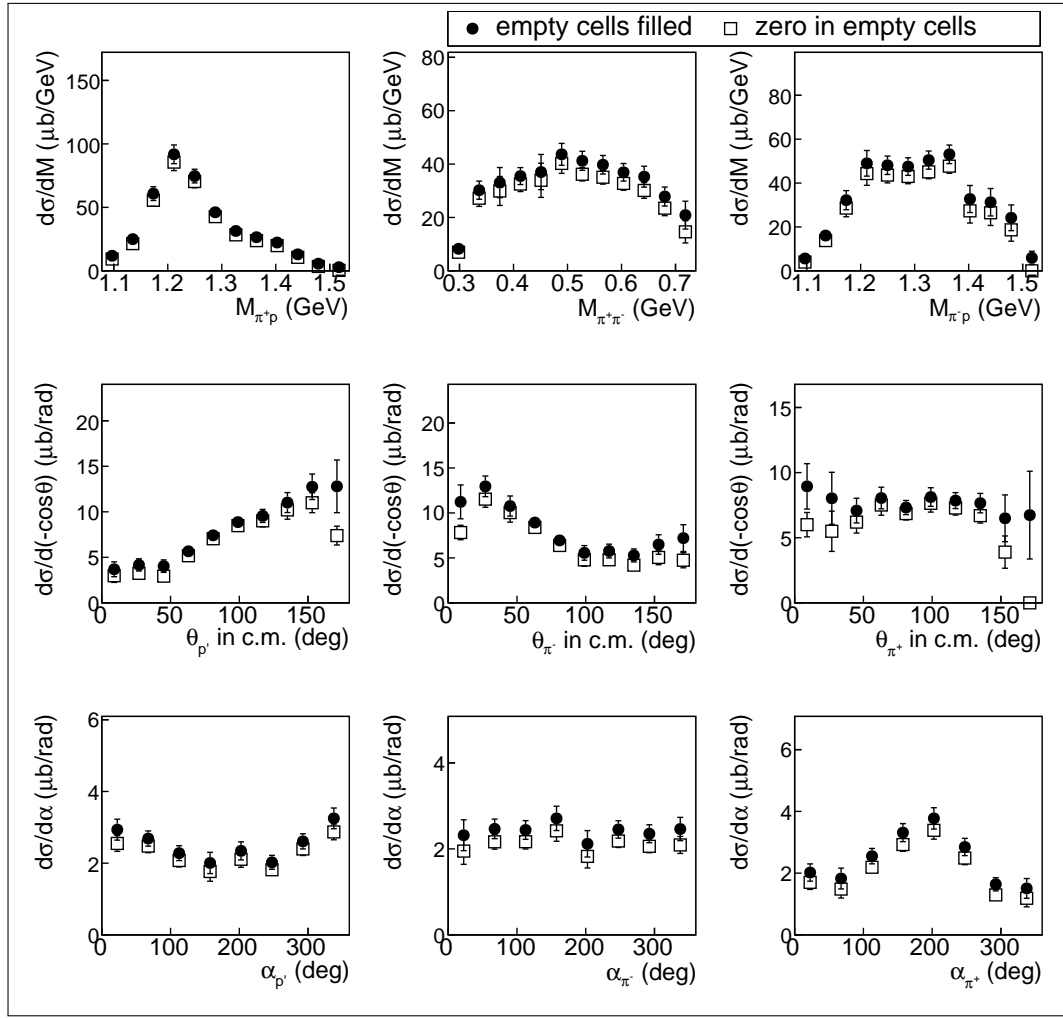


Figure 4.1: Extracted single-differential cross sections for the cases when the contribution from the empty cells was ignored (empty squares) and when it was taken into account (black circles). The former are reported with the uncertainty $\delta_{\text{stat}}^{\text{tot}}$ given by Eq. (7.1.4), while the latter are with the uncertainty $\delta_{\text{stat,mod}}^{\text{tot}}$ given by Eq. (7.4.1). All distributions are given for one particular bin in W and Q^2 ($W = 1.6375 \text{ GeV}$, $Q^2 = 0.625 \text{ GeV}^2$).

Table 4.1: Relative empty cell contribution to the integral cross sections for all reported (W , Q^2)-points. The columns correspond to the Q^2 values in GeV^2 and the rows to the W values in GeV . Different shades of red correspond to different percentage range, i.e. the lightest shade corresponds to the contribution $\leq 20\%$, darker shade – from 21% to 30%, and the darkest one shows the contribution $> 30\%$.

	0.425	0.475	0.525	0.575	0.625	0.675	0.725	0.775	0.825	0.875	0.925	0.975
1.3125	–	41	34	32	35	37	41	33	33	45	35	48
1.3375	–	28	28	27	26	28	31	32	33	35	33	35
1.3625	–	28	26	23	24	25	25	25	27	27	28	27
1.3875	–	21	19	18	17	19	19	18	18	21	23	21
1.4125	–	27	20	18	17	17	18	20	19	20	20	20
1.4375	–	23	17	17	14	14	14	17	15	15	16	18
1.4625	–	21	16	14	13	13	12	13	13	13	14	16
1.4875	–	24	18	15	14	14	13	13	15	15	15	16
1.5125	–	23	18	16	15	14	14	13	14	15	16	16
1.5375	–	23	19	16	16	14	14	14	14	17	18	15
1.5625	–	22	19	16	16	15	15	15	15	17	17	17
1.5875	–	23	18	17	20	15	15	17	16	18	17	–
1.6125	26	20	17	16	15	15	15	15	17	16	15	–
1.6375	26	19	17	16	14	16	14	16	17	16	–	–
1.6625	25	19	17	15	15	15	15	17	18	17	–	–
1.6875	24	20	17	16	15	15	16	19	18	–	–	–
1.7125	23	19	17	17	16	17	19	18	–	–	–	–
1.7375	23	20	17	17	17	18	19	–	–	–	–	–
1.7625	22	20	18	18	18	19	–	–	–	–	–	–
1.7875	21	19	18	18	–	–	–	–	–	–	–	–
1.8125	21	17	–	–	–	–	–	–	–	–	–	–

1409 **4.2 Radiative correction**

1410 The incoming and scattered electrons are subject to radiative effects, which means that
1411 they can emit photons thus reducing their energy. However, in the experiment the infor-
1412 mation on these emissions is not accessible, and one has to assume the electron energy to
1413 be unchanged. Therefore, when extracting the cross sections, one assumes the energy of
1414 the incoming/scattered electron to be greater/smaller than it actually was in the reaction.
1415 This, in turn, leads to the systematic overestimation of the virtual photon energy with the
1416 consequent overestimation of W^2 . As a result, the extracted cross section is assigned to the
1417 W value higher than the actual one. This distorts the measured W spectrum and leads to
1418 its agglomeration in the high-lying region.

1419 The common way of handling this problem is to apply the radiative correction to the
1420 extracted cross sections. In this study the radiative correction is performed using TWOPEG-
1421 D [26], which is the event generator for the double-pion electroproduction that simulates
1422 effects of the target motion. TWOPEG-D accounts for the radiative effects by means of the
1423 well-known approach of Ref. [39], which is traditionally used for the radiative corrections
1424 in the studies of double-pion electroproduction [15–19, 21–23]. In Ref. [39] the approach is
1425 applied to the inclusive case, while in TWOPEG-D, the double-pion integrated cross sections
1426 are used instead [26, 36].

1427 In the approach [26, 36, 39] the radiative photons are supposed to be emitted collinearly
1428 either to the direction of the incoming or scattered electron (the so-called “peaking approx-
1429 imation”). The calculation of the radiative cross section is split into two parts. The “soft”
1430 part assumes the energy of the emitted radiative photon to be less than a certain minimal
1431 value (10 MeV), while the “hard” part is for the photons with an energy greater than that
1432 value. The “soft” part is evaluated explicitly, while for the calculation of the “hard” part,
1433 an inclusive hadronic tensor is assumed. The latter assumption is however considered ade-
1434 quate, especially taking into account that approaches that are capable of describing radiative
1435 processes in exclusive double-pion electroproduction are not yet available.

1436 The radiative correction factor R in Eq. (3.5.1) is determined in the following way. The
1437 double-pion events either with or without radiative effects are generated with TWOPEG-
1438 D. Both radiated and non-radiated events are subjected to the smearing due to the Fermi
1439 motion of the target. Then the ratio given by Eq. (4.2.1) is taken in each $\Delta W \Delta Q^2$ bin.

$$R(\Delta W, \Delta Q^2) = \frac{N_{rad}}{N_{norad}}, \quad (4.2.1)$$

1440 where N_{rad} and N_{norad} are the weighted numbers of generated events in each $\Delta W \Delta Q^2$ bin
1441 with and without radiative effects, respectively. Note that neither N_{rad} nor N_{norad} are subject
1442 to any cuts.

2 The Q^2 value is overestimated if the incoming electron emits and underestimated if the scattered electron emits. That is why the radiative effects do not significantly impact the Q^2 -dependence of the cross section.

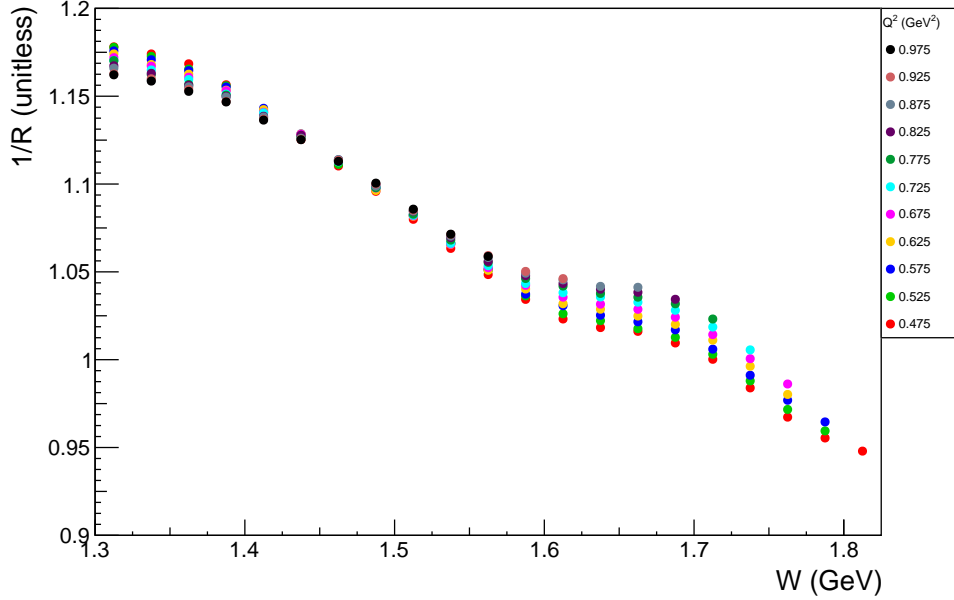


Figure 4.2: Reciprocal of the radiative correction factor ($1/R$) as a function of W for different Q^2 bins (see Eq. (4.2.1)).

This approach gives the correction factor R only as a function of W and Q^2 , disregarding its dependence on the hadronic variables. However, the need to integrate the cross section at least over four hadronic variables (see Eq. (3.5.5)) considerably reduces the influence of the final state hadron kinematics on the radiative correction factor, thus justifying the applicability of the procedure [26, 36, 39].

The quantity $1/R$ is plotted in Fig. 4.2 as a function of W for different Q^2 bins. The uncertainties associated with the statistics of generated events are very small and therefore not seen in the plot³. Note that the correction factor introduced in Fig. 4.2 is slightly different from that given in Ref. [22] for the same beam energy of the free proton experiment ($E_{beam} = 2.039$ GeV). This difference comes from the fact that generated events in Eq. (4.2.1) are subjected to the smearing due to the Fermi motion of the target proton.

Once this correction is applied, the extracted cross sections are treated as non-radiated, but Fermi-smeared.

³ The total of about $2.5 \cdot 10^9$ either radiated or non-radiated events were generated in the investigated kinematic region for the calculation of the radiative correction factor.

1456 4.3 Unfolding the effects of the target motion

1457 The motion of the target proton in a deuterium nucleus introduces into this analysis some
1458 specific issues that are not inherent for the previously conducted studies of the double-pion
1459 cross sections [15–19, 21–23]. As was described in Sects. 2.4 and 3.1, the intention to use in
1460 the analysis the π^- missing topology (that serves the purpose of the cross section extraction
1461 best) leads inevitably to working under the target-at-rest-assumption. The latter, however,
1462 not only complicates the selection of exclusive events (see Sect. 2.4), but also impacts the
1463 extracted cross sections due to the following reasons.

- 1464 • One has to use the smeared reaction invariant mass W_{sm} for the cross section binning
1465 (see Sect. 3.1). As a result, the extracted cross section is assigned to the W value
1466 different from the actual one. This makes both integral and single-differential cross
1467 sections to be distorted.
- 1468 • One has to use an approximate Lab-to-CMS transformation that ignores the target
1469 motion (see Sect. 3.2). This approximation introduces some inaccuracy to the measured
1470 angular (θ , φ , and α) distributions without having an impact on the invariant mass
1471 distributions and W and Q^2 cross section dependencies due to their Lorentz invariance.

1472 The former effect is thought to have a much greater impact on the cross section than
1473 the latter. Thus, being folded with the aforementioned effects of the target motion, the
1474 extracted cross sections are seeking the corresponding unfolding correction. This correction
1475 is performed by means of two Monte Carlo event generators TWOPEG [36] and TWOPEG-
1476 D [26]. TWOPEG is the event generator for the double-pion electroproduction off the free
1477 proton that currently provides the best cross section estimation in the investigated kinematic
1478 region. TWOPEG-D is the event generator for the same exclusive reaction but off the proton
1479 that moves in the deuterium nucleus. This event generator was especially developed to be
1480 used in the studies, where the experimental information of the target proton momentum is
1481 inaccessible, and one is forced to work under the target-at-rest-assumption. TWOPEG-D
1482 convolutes the double-pion cross section with effects of the target motion and thus imitates
1483 the conditions of the experimental cross section extraction.

1484 To calculate the correction factor, two samples of double-pion events produced either off
1485 the proton at rest and off the moving proton were generated (with TWOPEG and TWOPEG-
1486 D, respectively). Both event generators provide the particle’s four-momenta written in the
1487 Lab system and distribute events according to the corresponding electron-scattering cross
1488 section. As the reaction invariant mass both samples use the value calculated from the
1489 initial particles (see Eq. (3.1.1)), which for the “moving proton” events is calculated under
1490 the target-at-rest-assumption (as was done for the cross section calculation). The generated
1491 four-momenta are then subject to the transformation to the CMS. For both samples the
1492 transformation is performed according to the procedure given in App. B for the case of

1493 the proton at rest. For the “moving proton” sample, this approximation introduces in the
 1494 event distributions the same inaccuracy as appears in the extracted cross sections. Then the
 1495 kinematic variables are calculated and the generated events of both samples are binned in
 1496 the same way as the extracted cross sections (see Sect. 3.4).

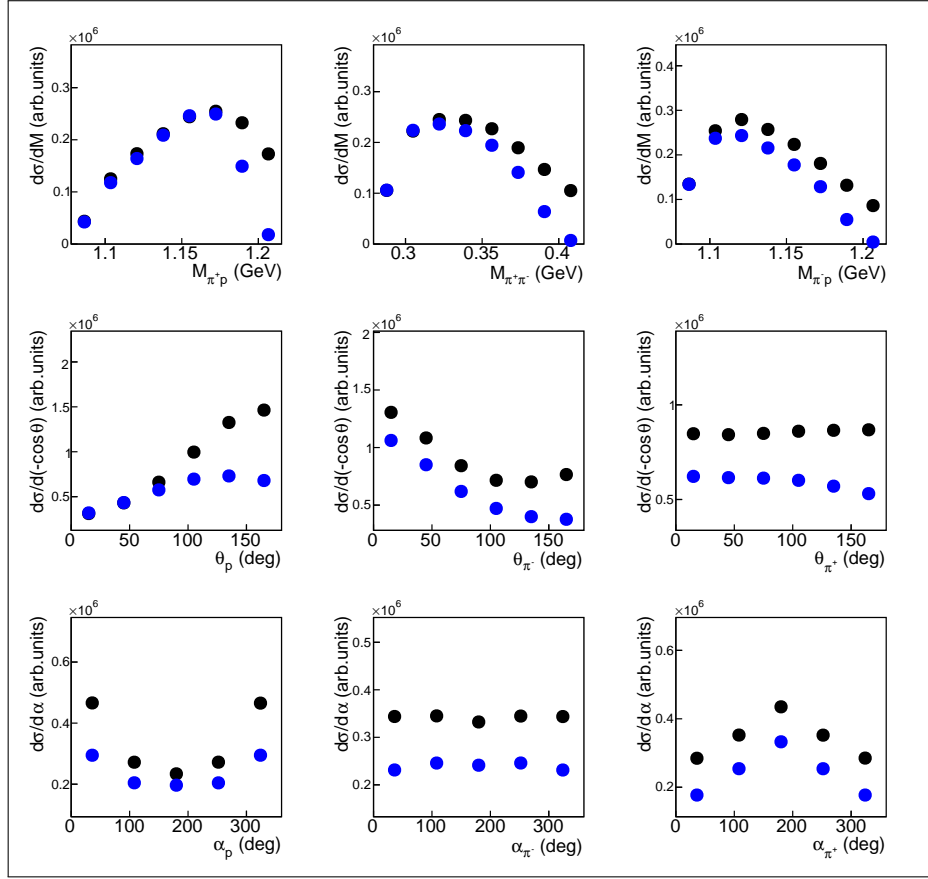


Figure 4.3: Single-differential distributions of generated double-pion events produced off the proton at rest (blue symbols) and off the moving proton (black symbols). The former were generated with TWOPEG [36] and the latter with TWOPEG-D [26]. The example is given for the particular $\Delta W \Delta Q^2$ bin with the central point at $W = 1.3375$ GeV and $Q^2 = 0.475$ GeV 2 . As this bin is located near the threshold, the moving proton distributions (black symbols) have a high relative event excess comparing with the free proton distributions (blue symbols). See text for details.

1497 Therefore, the distributions of events generated with TWOPEG-D acquire the same in-
 1498 accuracies as the extracted cross sections, i.e. the value W_{sm} is used for the binning and
 1499 the approximate Lab-to-CMS transformations are applied. The manifestation of these inac-
 1500 curacies differs depending on various final state variables and has a strong W -dependence
 1501 as Figs. 4.3 and 4.4 demonstrate. These figures show the single-differential distributions
 1502 of $N_{nofermi}$ (blue symbols) and N_{fermi} (black symbols), which are the weighted numbers of

events generated with TWOPEG and TWOPEG-D, respectively. In Fig. 4.3 these distributions are shown for a low $W = 1.3375$ GeV, while in Fig. 4.4 they are shown for a higher $W = 1.5625$ GeV. The uncertainties associated with the statistics of generated events are very small and therefore not seen in the plots⁴.

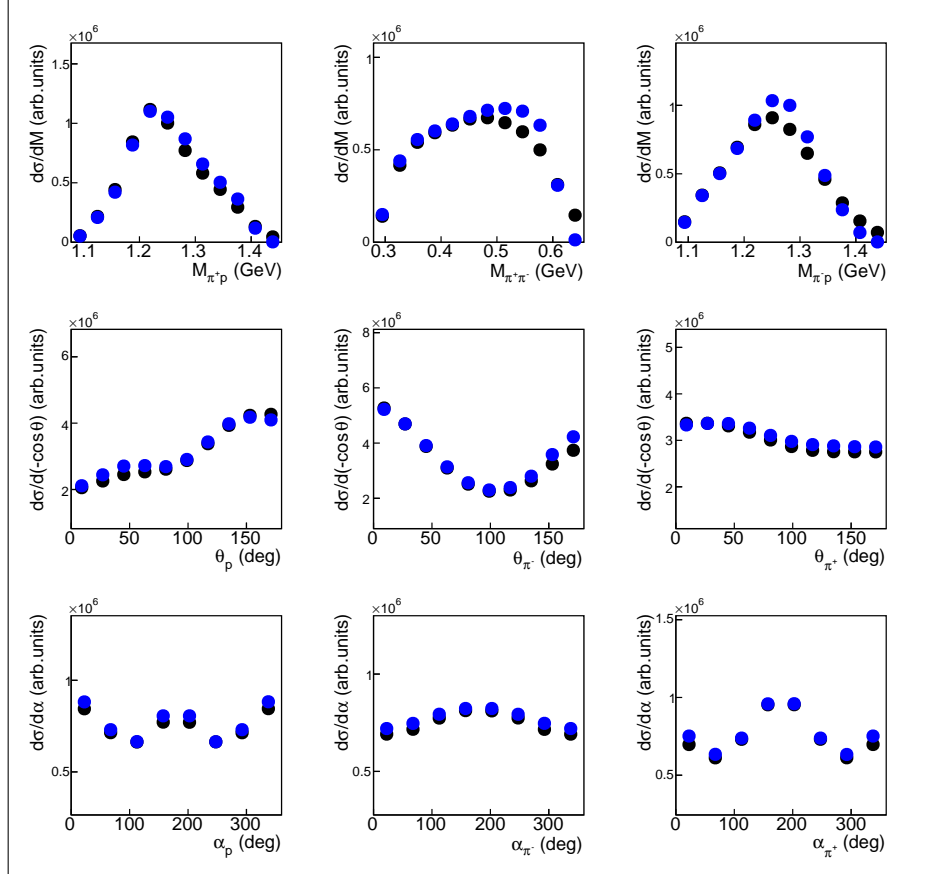


Figure 4.4: Single-differential distributions of generated double-pion events produced off the proton at rest (blue symbols) and off the moving proton (black symbols). The former were generated with TWOPEG [36] and the latter with TWOPEG-D [26]. The example is given for the particular $\Delta W \Delta Q^2$ bin with the central point at $W = 1.5625$ GeV and $Q^2 = 0.475$ GeV 2 . As the bin is located in the peak region, the moving proton distributions (black symbols) have a small relative event deficit comparing with the free proton distributions (blue symbols). See text for details.

As seen from Figs. 4.3 and 4.4, the target motion considered under the itemized conditions listed above affects mostly the cross section near the threshold, while for higher W their impact is significantly less pronounced. This happens due to the following. Let's consider a particular W_{true} bin. As shown in Ref. [26], each value of W_{true} corresponds to a sequence

⁴ For each event sample the total of about $2.5 \cdot 10^{10}$ events were generated in the investigated kinematic region for the calculation of the correction factor.

1511 of W_{sm} values, which are symmetrically scattered in the vicinity of W_{true} with a spread of
 1512 50-100 MeV. This leads to the fact that the same bin in W_{sm} has a different number of
 1513 events compared to the W_{true} bin. This difference depends on the cross section behavior in
 1514 the vicinity of 50-100 MeV of this bin. The cross section abruptly rises from the threshold
 1515 with a strong convex nonlinearity, which smooths as W grows up to 1.4 GeV, and then turns
 1516 to a concave nonlinearity forming the left slope of the resonance peak at 1.5 GeV. Then the
 1517 cross section modestly increases and decreases several times changing its nonlinearity type.
 1518 In any W_{true} subrange the cross section can be written as $a + f(W)$, where $a = const$, while
 1519 $f(W)$ evolves from zero and determines the cross section nonlinearity within the subrange.
 1520 Then the absolute variation in the event number in W_{sm} bin is determined solely by the
 1521 nonlinearity of the function $f(W)$, i.e. convex nonlinearity leads to an event excess in the
 1522 bin, while concave nonlinearity – to an event deficit. Hence, in the resonance peaks an event
 1523 deficit is observed, while the region close to the threshold and the dip between the peaks have
 1524 an event excess. However, the relative event variation depends on a and is higher for smaller
 1525 a . The smallest value of a is reached at the threshold ($a = 0$), therefore the near-to-threshold
 1526 subrange has the greatest relative variation of event number.

1527 Indeed, in Fig. 4.3, which is plotted for the W bin located close to the threshold, the
 1528 moving proton distributions (black symbols) have a high relative event excess compared to
 1529 the free proton distributions (blue symbols). Meanwhile, in Fig. 4.4, which is plotted for
 1530 the W bin located at the peak region, the moving proton distributions (black symbols) have
 1531 small relative event deficit comparing with the free proton distributions (blue symbols).

1532 For the low W region (as in Fig. 4.3) it is noteworthy that a very large relative difference
 1533 between the free proton and the moving proton cross sections is observed for the right part
 1534 of the invariant mass distributions. This happens due to the phase space broadening with W
 1535 that takes place for invariant masses (see App. C). The invariant mass distribution typically
 1536 has a maximum in the middle and gradually goes to zero on both edges. The lower the W
 1537 value is, the narrower is the distribution width. As W grows, the distribution widens to
 1538 the right and goes to zero farther away. Meanwhile, each bin in W_{sm} contains a mixture of
 1539 events with the values of W_{true} spread within 50-100 MeV near this bin. For low W this
 1540 spread is comparable with the total width of the invariant mass distribution. Therefore, the
 1541 right distribution side acquired the event excess that comes from the same bins in invariant
 1542 mass but located at higher W_{true} and hence having high cross sections.

1543 The unfolding correction is performed in each multi-dimensional bin of the double-pion
 1544 production phase-space (see Sect. 3.3 as well as App. C), i.e. in each $\Delta W \Delta Q^2 \Delta^5 \tau$ bin the
 1545 cross section is divided by the correction factor \mathcal{F} (see Eq. (3.5.1)) that is calculated as

$$\mathcal{F}(\Delta W, \Delta Q^2, \Delta^5 \tau) = \frac{\mathbb{N}_{fermi}}{\mathbb{N}_{nofermi}}, \quad (4.3.1)$$

1546 where $\mathbb{N}_{nofermi}$ and \mathbb{N}_{fermi} are the weighted numbers of generated double-pion events in the
 1547 $\Delta W \Delta Q^2 \Delta^5 \tau$ bin produced off the proton at rest and off the moving proton, respectively.

1548 Both event samples were generated without radiative effects, since the correction factor \mathcal{F} is
1549 applied to the cross sections that are already corrected for the radiative effects (see Sect. 4.2).

1550 The impact of the unfolding correction on the extracted integral cross sections is illus-
1551 trated in Fig. 4.5, where the distributions before the correction are plotted in orange, while
1552 the distributions after the correction are plotted in dark blue. The comparison is given for
1553 two Q^2 bins. As was expected, the correction causes a slight cross section increase in the
1554 resonance peaks and a decrease near the threshold and in the dip between the peaks.

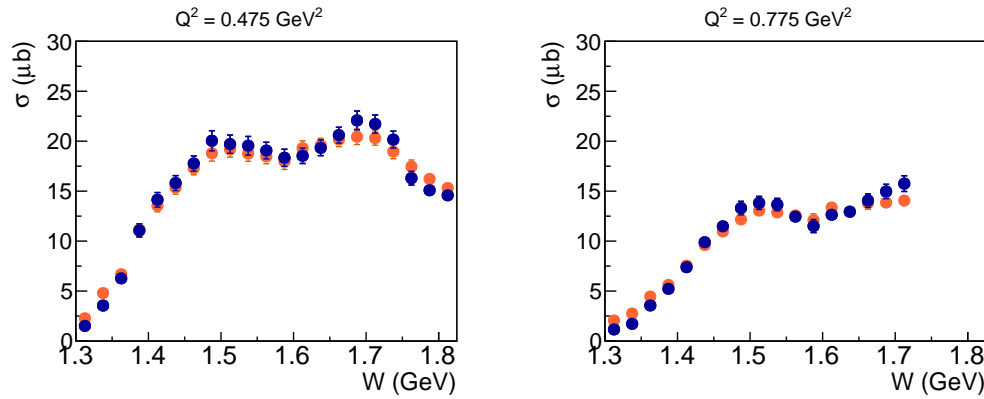


Figure 4.5: Impact of the unfolding correction on the extracted integral cross sections. The cross section before the correction is plotted in orange, while the cross section after the correction is plotted in dark blue (both are divided by the virtual photon flux). The comparison is given for two Q^2 bins as specified above the plots.

1555 The value of the correction factor in Eq. (4.3.1) depends on both the free proton cross
1556 sections and the model of the deuteron wave function that were employed in the event
1557 generators. The former relies strongly on the JM model fit of the available data on double-
1558 pion cross sections, while for the latter the Bonn model was used (see Refs. [26, 36] for
1559 more detail). Therefore, the uncertainty of the extracted cross sections that comes from this
1560 unfolding correction is attributed to the model dependence uncertainty and is discussed in
1561 Sect. 7.2.

1562 Once corrected for the effects of the target motion and then divided by the virtual
1563 photon flux, the cross section is treated as the true virtual photoproduction cross section
1564 and is attributed to the central point of the corresponding $\Delta W \Delta Q^2 \Delta^5 \tau$ bin.

1565 4.4 Correction for binning effects

1566 The cross section, extracted in bins of a finite size, is assigned to the central point of a
1567 bin. On this way the cross sections acquire binning caused distortions and, therefore, are

1568 seeking the corresponding corrections. In this section, which is devoted to the binning effects,
1569 two separate binning issues are distinguished, i.e. (i) the specific issue of affecting the cross
1570 section value in the next to last point of the invariant mass distributions and (ii) the common
1571 binning issue that impacts the cross section value in any bin of finite size.

1572 Let's address the specific binning issue in the invariant mass distributions first. As shown
1573 in Sect. 3.4, the binning in invariant mass requires special attention due to the broadening
1574 of the reaction phase-space with W (see App. C) and the corresponding W dependence of
1575 the upper boundary of the invariant mass distributions (see Eq. (3.4.1)). This effect makes
1576 the upper boundary M_{upper} to be indistinct, since the cross section is calculated in a bin
1577 $W_{left} < W < W_{right}$. To deal with this difficulty, the value of M_{upper} is calculated using
1578 W_{center} , the center of the W bin. Then a specific arrangement of mass bins is used, which
1579 forces the last bin to be situated completely out of the boundaries given by Eq. (3.4.1) using
1580 W_{center} . When integrating the cross section over the mass distribution, the events in the
1581 extra bin are included, but a cross section for this bin is not reported.

1582 Meanwhile, the cross section in the next to last bin (labeled as bin number $N_{bins} - 1$)
1583 should be treated carefully. This is best illustrated in Fig. 4.6, which shows schematically
1584 the event distribution in mass, ending in M_{upper} for three choices of W at W_{left} (dot-dashed),
1585 W_{center} (solid) and W_{right} (dashed). The black points at $M_{left}^{N_{bins}-1}$ and $M_{right}^{N_{bins}-1}$ show the left
1586 and right boundaries of the next to last bin, respectively. In the next to last bin events with
1587 $W < W_{center}$ are distributed over a range, which is less than ΔM defined by Eq. (3.4.2).
1588 However, when extracting the cross sections, the event yield was divided by the full bin
1589 width ΔM , thus leading to an underestimation of the cross section.

1590 The correction for this effect was taken from Ref. [22, 23]. It was made using the
1591 TWOPEG double-pion event generator [36]. The correction factor to the cross section in
1592 the next to last bin is the ratio of the simulated cross sections calculated with fixed ΔM
1593 defined by Eq. (3.4.2) and with $\widetilde{\Delta M} = W - m_{h_3} - M_{left}^{N_{bins}-1}$, which was different for each
1594 generated event. This factor provides the correction to the cross section in the next to last
1595 bin that varied from $\sim 5\%$ to $\sim 10\%$.

1596 Let's now address the common binning issue that impacts the cross section value in any
1597 bin of a finite size. Extracted in a finite bin, the cross section is subject to averaging within
1598 this bin. For instance, if there is a sharp peak in the middle of a bin, then the average value
1599 of the cross section in that bin will always be smaller than the peak value. Any non-linear
1600 behavior of the cross section will likely result in an offset of the obtained value. There are two
1601 methods of correcting this offset, i.e. (i) to correct the kinematic quantities associated with
1602 the bin and use the corrected values instead of the central values or (ii) to correct the cross
1603 section value in the center of the bin. Both these methods are widely used for the binning
1604 corrections. In the studies of double-pion cross sections, however, the second method has
1605 become conventional [17, 18, 22, 23]. Therefore, in this study the second method is chosen,
1606 in order to keep the initial binning over the kinematic variables and to facilitate the cross
1607 section comparison with the results obtained off the proton at rest [22, 23].

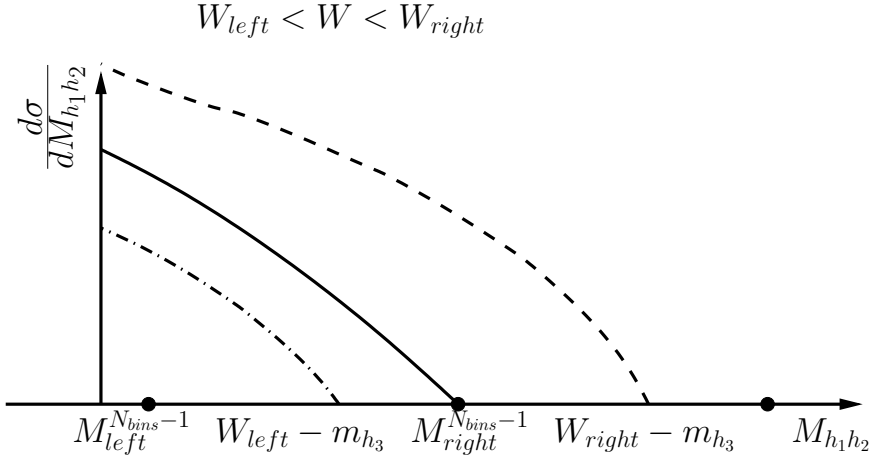


Figure 4.6: Schematic representation of the invariant mass distributions ending in M_{upper} calculated according to Eq. (3.4.1) for three choices of W at W_{left} (dot-dashed), W_{center} (solid) and W_{right} (dashed). The black points at $M_{left}^{N_{bins}-1}$ and $M_{right}^{N_{bins}-1}$ show the left and right boundaries of the next to last bin, respectively, while the remaining point marks the right boundary of the last mass bin.

1608 In this study one-dimensional binning corrections are performed, i.e., the cross section
 1609 dependence on each kinematic variable x is corrected individually (where x corresponds to
 1610 W , Q^2 , and hadron variables). In any one-dimensional bin $[x_{min}, x_{max}]$ the cross section
 1611 value is multiplied by the correction factor C_{bin} . To estimate this factor some assumptions
 1612 about the cross section behavior within the bin are needed, and hence, the cross section
 1613 shape should be described by a continuous function $f(x)$. The multiplicative correction
 1614 factor C_{bin} is then calculated in each bin $[x_{min}, x_{max}]$ as

$$C_{bin} = \frac{f(x_{center})}{\int_{x_{min}}^{x_{max}} f(x) dx} , \quad (4.4.1)$$

1615 where x_{center} is the central point of the $[x_{min}, x_{max}]$ bin.

1616 For the single-differential distributions a cubic spline approximation is chosen to contin-
 1617 uously describe the cross section shape, as shown in Fig. 4.7. The black and red points in
 1618 this figure are the cross sections before and after binning corrections, respectively, and the
 1619 curves correspond to the spline approximation. For the invariant mass and θ angular dis-
 1620 tributions the splines are forced to pass through the intermediate points that are obtained
 1621 by averaging over two neighboring cross section points. This method reduces the splines
 1622 sensitivity to accidental cross section fluctuations. Beside this, for the invariant mass dis-
 1623 tributions the splines are required to give zero at the distribution edges. For the α angular
 1624 distributions the splines are forced to pass through the points that are obtained by averaging

1625 over two cross section points symmetrical with respect to $\alpha = 180^\circ$. This approach reflects
 1626 the fact that after the integration over φ , the cross section must be symmetrical in the α
 1627 angle (meanwhile, the extracted experimental distributions are slightly asymmetrical)⁵.

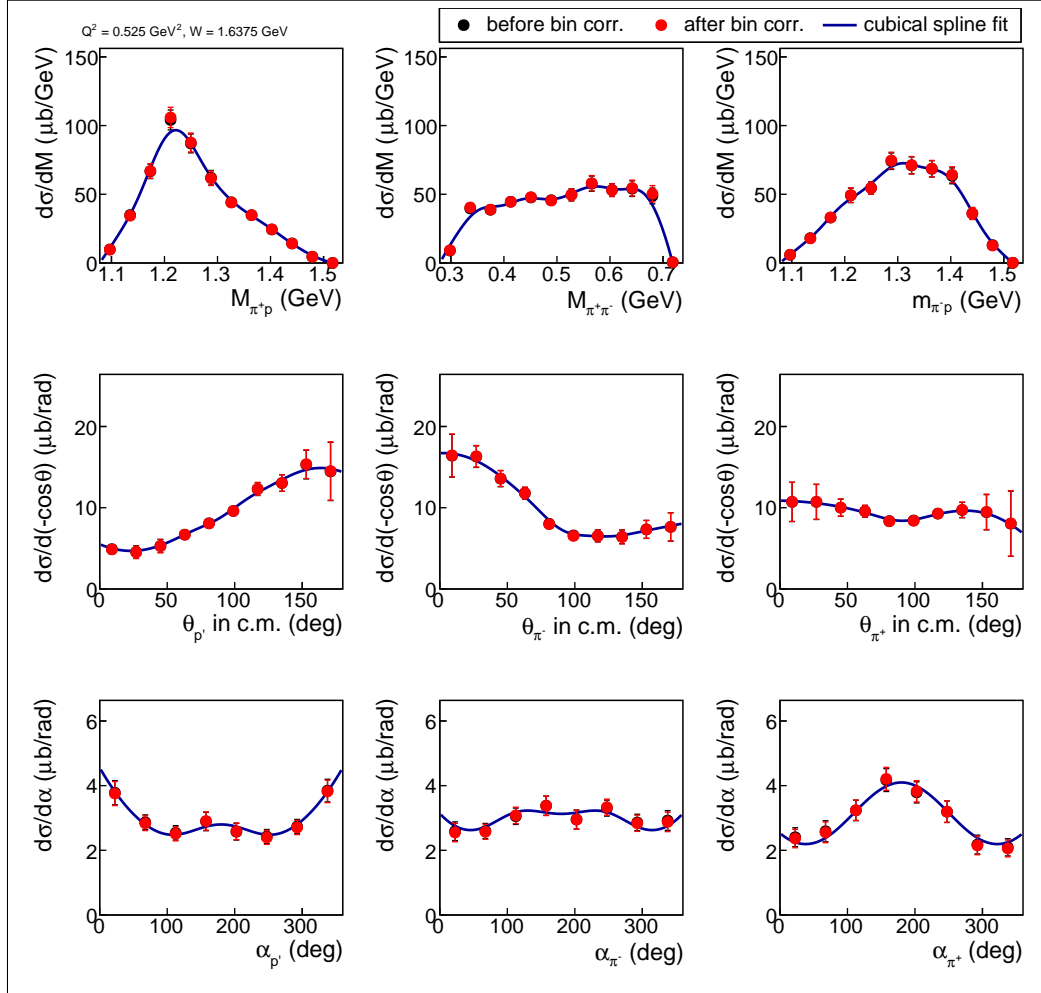


Figure 4.7: Single-differential cross sections as functions of the final hadron variables before (black points) and after (red points) the binning corrections. Curves represent a cubic spline approximation. The example is given for a particular $\Delta W \Delta Q^2$ bin with the central point $W = 1.6375$ GeV and $Q^2 = 0.525$ GeV².

1628 The integral cross sections are subjected to individual corrections of the Q^2 dependence
 1629 inside the W bins and the W dependence inside the Q^2 bins, as shown on the left and
 1630 right plots of Fig. 4.8, respectively. In this figure black and red points represent the cross

⁵ Although the φ distributions are not reported here, they were nevertheless extracted and added to the CLAS physics database [5]. The φ distributions were thus subjected to the binning correction with the same approach used for the θ distributions.

1631 section values before and after binning corrections, respectively, while the curves correspond
 1632 to the continuous cross section approximation. The latter are based on a second order
 1633 polynomial fit of the Q^2 distributions (left plot) and on a cubic spline approximation for
 1634 the W distributions (right plot). The splines are forced to pass through the intermediate
 1635 points that are obtained by averaging over two neighboring cross section points. In this way,
 1636 the integral cross section value in each $\Delta W \Delta Q^2$ bin acquires two multiplicative correction
 1637 factors. The corrections obtained for the integral distributions are then propagated to the
 1638 single-differential cross sections.

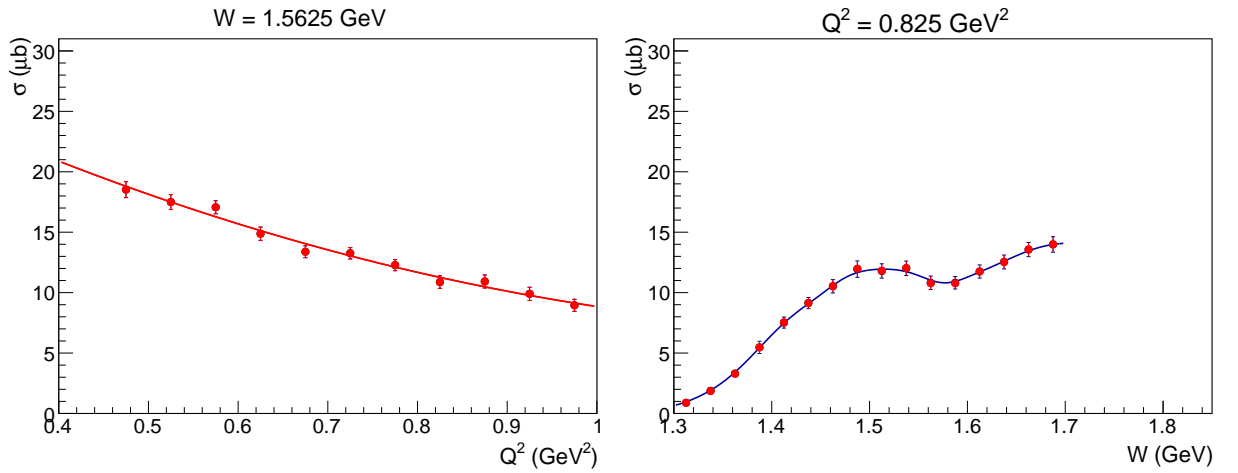


Figure 4.8: Q^2 dependence (left plot) and the W dependence (right plot) of the integral cross sections before (black points) and after (red points) the binning corrections. The curves correspond to a second order polynomial fit for the left plot and a cubic spline approximation for the right one. Each distribution is plotted for one particular bin as specified above the plots.

1639 Since in this analysis a relatively fine binning in all kinematic variables is chosen (see
 1640 Sect. 3.4), the effect of the binning corrections is almost insignificant. This is why in Figs. 4.7
 1641 and 4.8 the black points (before the correction) are almost completely covered by the red
 1642 ones (after the correction). For the Q^2 dependences the correction factors are less than 1%
 1643 in all bins, and for the W dependences they are $\sim 2\%-3\%$ for the first two low W bins and
 1644 less than 1% in all other bins. For the single-differential distributions, the corrections are on
 1645 the level of 1%-2% for the majority of bins, but rise for some points (mostly at low W) up
 1646 to 5%-6%.

¹⁶⁴⁷ Chapter 5

¹⁶⁴⁸ Other issues

¹⁶⁴⁹ 5.1 The cross section dependence on the beam energy

¹⁶⁵⁰ The phi-integrated virtual photoproduction cross section σ_v can be decomposed into the
¹⁶⁵¹ combination of the structure functions,¹

$$\sigma_v = \sigma_T + \varepsilon_L \sigma_L \quad \text{with} \quad \varepsilon_L = \frac{Q^2}{\nu^2} \varepsilon_T, \quad (5.1.1)$$

¹⁶⁵² where σ_T and σ_L are the transverse and longitudinal structure functions, respectively, while
¹⁶⁵³ ε_L is the longitudinal polarization of the virtual photon with ε_T given by Eq. (3.5.4).

¹⁶⁵⁴ Being decomposed in this way, the cross section σ_v has a specific beam energy dependence,
¹⁶⁵⁵ which is incorporated into the coefficient ε_L . The structure functions themselves, meanwhile,
¹⁶⁵⁶ do not depend on the beam energy. A single experiment conducted with a certain beam
¹⁶⁵⁷ energy allows for the extraction of σ_v as a whole without accessing the separate structure
¹⁶⁵⁸ functions. Thus, the beam energy dependence turns out to be implicitly incorporated into
¹⁶⁵⁹ the extracted cross sections.

¹⁶⁶⁰ Although the experiment is conducted with a fixed value of the laboratory beam energy,
¹⁶⁶¹ the actual energy of the incoming electron involved in the reaction turns out to alter and
¹⁶⁶² differ from the fixed laboratory value due to (i) the radiative effects that electrons undergo
¹⁶⁶³ and (ii) the Fermi motion of the target proton. As a consequence, the extracted cross
¹⁶⁶⁴ section cannot be associated with a distinct value of the electron beam energy, and this may
¹⁶⁶⁵ complicate the interpretation of the results. Let's address these issues in more detail.

¹⁶⁶⁶ (i) The incoming and scattered electrons can emit photons thus reducing their energy. Due
¹⁶⁶⁷ to the change of the incoming electron energy, the extracted cross sections correspond

¹ The full decomposition (for the case of the unpolarized electron beam) can be found e.g. in Refs. [3, 36]

1668 to the superposition of various beam energies. The correction due to this effect is
1669 included into the procedure of radiative corrections (see Sect. 4.2).

1670 (ii) The experiment off the moving proton with fixed laboratory beam energy corresponds
1671 to that off the proton at rest performed with varying effective beam energies [26].
1672 As a result, the extracted cross sections off moving protons are convoluted with the
1673 dependence of the quantity ε_L on the beam energy (see Eq. (5.1.1)). A study in
1674 Ref. [26], however, proves that this effect has an insignificant influence on the cross
1675 section. The correction due to this effect (which is negligible anyway) is automatically
1676 included into the procedure of unfolding the effects of the target motion (see Sect. 4.3)².

1677 Being corrected, the cross sections extracted in this analysis may be assigned to the
1678 distinct value of the laboratory beam energy of $E_{beam} = 2.039$ GeV.

1679 5.2 Off-shell effects

1680 The target proton is bound in the deuterium nucleus and thus undergoes nucleon-nucleon
1681 interactions. The nucleon mass, however, is thought to be an interaction-dependent quantity,
1682 i.e. the nucleon's physical mass in a nucleus is smaller than that of a free nucleon [14]. In
1683 other words, the target proton bound in the deuteron is off-shell, which means that its
1684 four-momentum squared is not equal to its mass squared.

1685 In the study [43], which aimed at π^- electroproduction off the neutron in deuterium, the
1686 impact of the off-shell effects on the measured cross sections was shown to be marginal. In
1687 this study the off-shell effects are ignored.

² Note that the radiative effects decrease the beam energy, while the Fermi motion leads to a symmetrical spread of the effective beam energy around the laboratory value.

1688

Chapter 6

1689

Normalization verification

1690 To prove the credibility of an extracted observable, some well-established quantity is com-
1691 monly used as a reference point. For this purpose one can use already published measure-
1692 ments of this observable, if they exist in the desired kinematic region, but this usually is not
1693 the case. Alternatively, one can focus on some quantity, which can be reliably approximated
1694 in this kinematic region by a theoretical model or parameterization. This auxiliary quantity
1695 is then extracted from the analyzed dataset, and the comparison of the measured value with
1696 the approximated one allows the reliability of the main result to be judged.

1697 For experiments off a free proton, the elastic cross section usually serves as such a ref-
1698 erence quantity as it can be approximated in a wide kinematic region by Peter Bosted
1699 parameterization with an excellent accuracy of a few percent, as Ref. [44] demonstrates (see
1700 App. B there). Therefore an agreement between the auxiliary measured elastic cross section
1701 with the parameterized one, if achieved indicates both the correct normalization of the main
1702 result and the trustworthy quality of the electron selection.

1703 Meanwhile, for experiments off a deuterium target, the quasi-elastic cross section off
1704 nucleons can serve as the corresponding reference quantity. However, this observable, if
1705 compared with the elastic free proton cross section, is less understood and lacking the same
1706 quality of theoretical description [44]. Nonetheless, several techniques have been developed
1707 in this matter with the Bosted parameterization of the deuteron quasi-elastic peak being the
1708 most commonly used tool.

1709 Ref. [44] gives some details on the performance of the Bosted parameterization of the
1710 deuteron quasi-elastic peak [45, 46] and tests its ability to describe experimental data by
1711 comparing the parameterized cross sections with published measurements [47–49]. This
1712 testing, being performed in the Q^2 range from $\sim 0.3 \text{ GeV}^2$ to $\sim 4 \text{ GeV}^2$, is of great importance
1713 for the current analysis as its Q^2 coverage falls within this range.

1714 As follows from Ref. [44], the Bosted parameterization in its default implementation
1715 systematically overestimates the measured integrals under the quasi-elastic peak and the

1716 overall description quality gradually decreases from several percent to almost 20% as Q^2
 1717 grows from 0.3 GeV 2 to 4 GeV 2 . The default implementation corresponds to the case when
 1718 the nuclear scaling function is estimated using a PWIA calculation and the Paris deuteron
 1719 wave function (see Refs. [45, 46] for details).

1720 Meanwhile, as also shown in Ref. [44], the Bosted parameterization in its alternative im-
 1721 plementation systematically underestimates the corresponding integrals with the description
 1722 quality gradually increasing from $\sim 15\%$ to a few percent as Q^2 grows from 0.3 GeV 2 to
 1723 4 GeV 2 . The alternative implementation corresponds to the case when the nuclear scaling
 1724 function is estimated according to the parameterization from Ref. [50] and is available with
 1725 some minor modifications of the source code.

1726 Beside this, Ref. [44] describes a useful approximation formula for the cross section at
 1727 the quasi-elastic peak, which came from Durand's theory [51]. This formula is of particular
 1728 interest for this analysis, since it describes very nicely the experimental peak values in the Q^2
 1729 range from ~ 0.3 GeV 2 to ~ 1.8 GeV 2 . As shown in Ref. [44], the normalization of the cross
 1730 section distributions of the Bosted parameterization to the values provided by this formula
 1731 improves the data description quality in this Q^2 range.

1732 Once we have acquired an impression of the performance and reliability of the param-
 1733 eterizations currently available for the deuteron quasi-elastic peak, let's now estimate the
 1734 quasi-elastic cross section from the analyzed dataset and then perform its comparison with
 1735 the cross section approximated by various implementations of the Bosted parameterization.
 1736 This investigation is carried out in the framework established in Ref. [44] and therefore, uses
 1737 the same notations and color codes.

1738 To extract the cross section in the region of the quasi-elastic peak, the only particle that
 1739 should be registered is the scattered electron. With the electron selection being exactly the
 1740 same as for the double-pion cross section extraction, the quasi-elastic cross section is defined
 1741 in each $\Delta E' \Delta \theta_{e'}$ bin by

$$\frac{d\sigma_{exp}}{d\Omega dE'} = \frac{1}{2\pi} \cdot \frac{\left(\frac{N_{full}}{Q_{full}} - \frac{N_{empty}}{Q_{empty}} \right)}{\Delta E' \Delta(-\cos \theta_{e'})[\mathcal{L}]} \cdot \frac{N_{gen}}{N_{rec}}, \quad (6.1)$$

1742 where N_{full} and N_{empty} are the numbers of selected events inside the $\Delta E' \Delta \theta_{e'}$ bin for runs
 1743 with deuterium and empty target, respectively. N_{gen} and N_{rec} come from the Monte Carlo
 1744 simulation and correspond to the numbers of generated and reconstructed quasi-elastic events
 1745 inside the $\Delta E' \Delta \theta_{e'}$ bin, respectively. The latter were subject to the same electron selection
 1746 cuts as the experimental events. For the Monte Carlo simulation an event generator based
 1747 on the measurements from Ref. [10] was used. The other variables are defined in the context
 1748 of Eq. (3.5.1).

1749 The cross section calculated according to Eq. (6.1) is shown by the black symbols in
 1750 Fig. 6.1 (note that it is the radiated cross section). The blue and green histograms in this
 1751 figure correspond to the Bosted parameterization with the default and alternative methods of

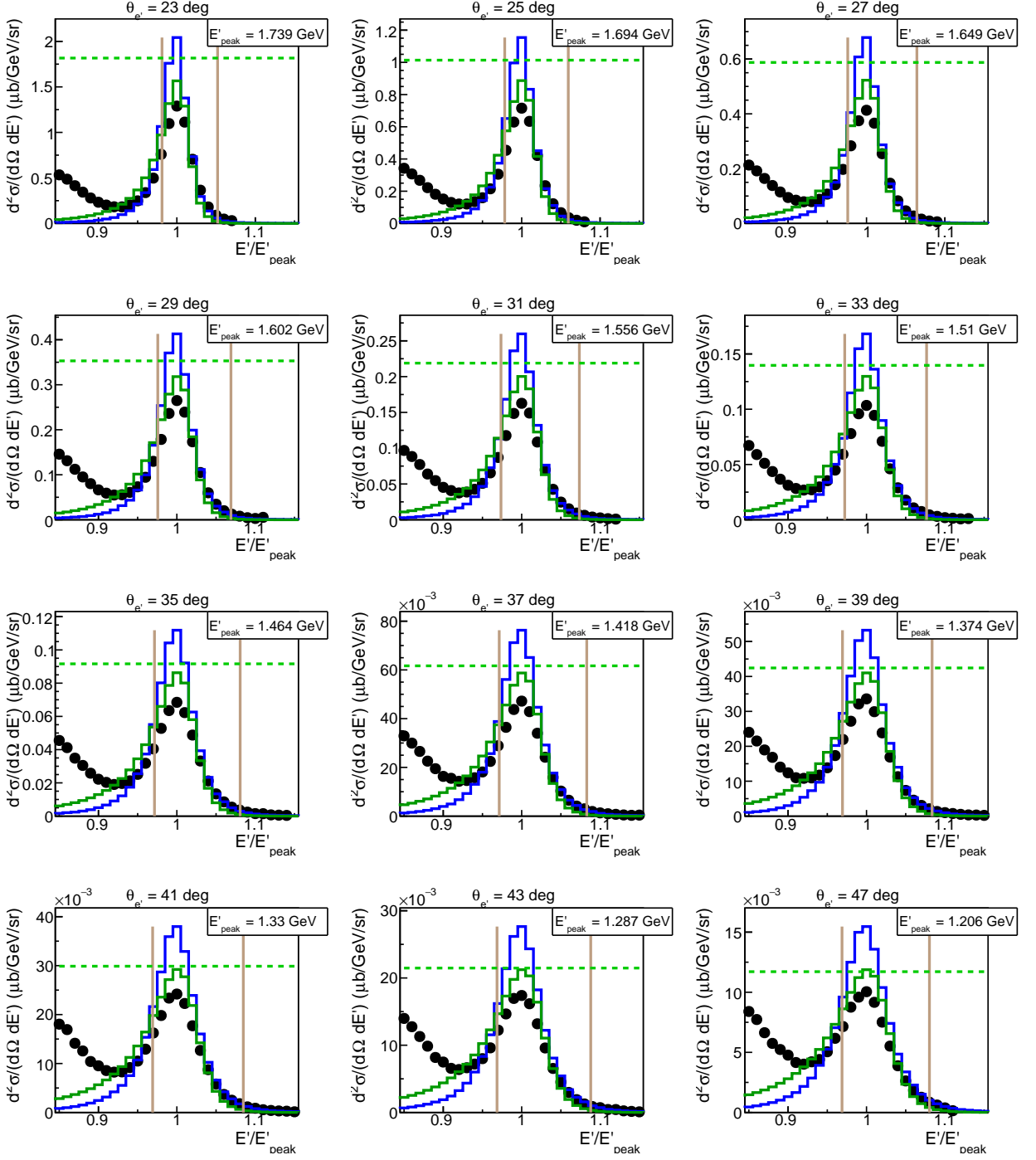


Figure 6.1: Black symbols correspond to the (radiated) cross section in the region of the quasi-elastic peak extracted from the analyzed dataset according to Eq. (6.1). The results of the Bosted parameterization [45, 46] are shown by the histograms. The blue histograms correspond to the default method to calculate the nuclear scaling function, while the green histograms to the alternative method. The green horizontal lines correspond to the peak values approximated by the formula described in Ref. [44]. The vertical lines correspond to the integration limits.

Table 6.1: Ratios of the experimental integrals under the quasi-elastic peak (σ_{exp}) obtained from the analyzed dataset to those obtained from the Bosted parameterization [45, 46] with the nuclear scaling function calculated by the default (σ_{par}^1) and alternative (σ_{par}^2) methods. The index *norm* means that the parameterization histogram was scaled in a way that its maximum was equal to the prediction of the formula described in Ref. [44]. The dark-green shade stands for deviations $\leq 5\%$, light-green for 5%-10%, and light-red for more than 10%.

$\theta_{e'}$, deg	Q^2 , GeV 2	E'_{peak} , GeV	Left cut	R	σ_{peak}^{peak} , μb	$\sigma_{exp}/\sigma_{par}^1$	$\sigma_{exp}/\sigma_{par}^1,_{norm}$	$\sigma_{exp}/\sigma_{par}^2$	$\sigma_{exp}/\sigma_{par}^2,_{norm}$
23	0.56	1.739	0.9811	0.8222	1.817E0	0.91	1.03	1.13	0.98
25	0.65	1.694	0.9784	0.8280	1.014E0	0.89	1.02	1.10	0.96
27	0.73	1.649	0.9761	0.8325	5.876E-1	0.87	1.00	1.07	0.95
29	0.82	1.602	0.9757	0.8324	3.531E-1	0.89	1.04	1.10	0.99
31	0.91	1.556	0.9736	0.8362	2.188E-1	0.87	1.03	1.07	0.98
33	0.99	1.51	0.9722	0.8384	1.397E-1	0.85	1.02	1.05	0.97
35	1.08	1.464	0.9715	0.8394	9.162E-2	0.84	1.02	1.04	0.98
37	1.17	1.418	0.9714	0.8390	6.167E-2	0.83	1.03	1.04	0.99
39	1.25	1.374	0.9694	0.8427	4.244E-2	0.83	1.04	1.04	1.00
41	1.33	1.33	0.9691	0.8428	2.988E-2	0.84	1.07	1.05	1.03
43	1.41	1.287	0.9686	0.8436	2.147E-2	0.83	1.07	1.04	1.03
45	1.49	1.246	0.9680	0.8444	1.571E-2	0.83	1.09	1.04	1.04
47	1.56	1.206	0.9688	0.8427	1.171E-2	0.83	1.10	1.04	1.05

1752 calculating the nuclear scaling function, respectively. The green horizontal lines correspond
1753 to the prediction of the peak value given by the aforementioned approximation formula.

1754 Since the experimental cross section is radiated, while the parameterized cross section is
1755 not, their visual comparison loses informativeness. To judge more definitely the agreement
1756 of the measurement with the parameterization, the corresponding integrals under the quasi-
1757 elastic peak were compared. The distributions were integrated within the limits shown by
1758 the vertical lines in Figs. 6.1. To determine the positions of these limits, the procedure
1759 suggested in Ref. [44] was used. First, the quasi-elastic peaks in the experimental spectra
1760 were fit by Gaussians with polynomial background. Then the values $\mu - \sigma$ and $\mu + 3\sigma$
1761 were set as the left and right integration limits, respectively, with μ and σ being the mean
1762 value and the standard deviation of the corresponding Gaussian function. The integration
1763 limits were chosen to be asymmetrical in order to minimize the inelastic background under
1764 the quasi-elastic peak. This procedure of obtaining the integration limits allows to achieve
1765 consistency among all plots, since the width of the quasi-elastic peak and its proximity to
1766 the inelastic part of the spectrum depend on the kinematics.

1767 The experimental integrated cross sections were divided by the radiative correction factors
1768 (R), which were calculated in each $\theta_{e'}$ bin according to the Mo&Tsai approach [39]. These
1769 correction factors are listed in Tab. 6.1 together with the positions of the corresponding left
1770 integration limits. The peak cross section values given by the approximation formula are also
1771 given there. The last four columns contain the values of the ratio of the experimental integral
1772 under the quasi-elastic peak (σ_{exp}) to that obtained from the Bosted parameterization with
1773 the nuclear scaling function calculated by the default (σ_{par}^1) and alternative (σ_{par}^2) methods.
1774 The index *norm* indicates that the parameterization histogram was scaled in a way that its
1775 maximum is equal to the prediction of the considered approximation formula. The cells'
1776 coloring is the same as for Tab. 1 in Ref. [44], i.e. the dark-green shade stands for deviations
1777 $\leq 5\%$, light-green for 5%-10%, and light-red for more than 10%.

1778 The ratios of the experimental integrals to the parameterized ones are also shown in
1779 Fig. 6.2 as a function of the polar angle of the scattered electron ($\theta_{e'}$). The left side corre-
1780 sponds to the case, when the nuclear scaling function was calculated by the default method
1781 (blue symbols), while for the right side it was calculated by the alternative method (green
1782 symbols). The top row stands for the unscaled parameterization histograms, while for the
1783 bottom row they were scaled to the peak value given by the approximation formula.

1784 As seen from both Tab. 6.1 and Fig. 6.2, the measured integrals under the quasi-elastic
1785 peak were found to be lower than the values given by the Bosted parameterization in its
1786 default implementation and their difference increases from $\sim 10\%$ to $\sim 15\%$ as Q^2 grows.
1787 The measured integrals were also found to be higher than the values given by the Bosted
1788 parameterization in its alternative implementation with the difference decreasing with Q^2
1789 from $\sim 10\%$ to $\sim 5\%$. Meanwhile, if the parameterization histograms are scaled to the peak
1790 values predicted by the formula described in Ref. [44], the corresponding ratio stays in the
1791 vicinity of unity with a reasonable deviation for both options of scaling function calculation.

1792 This result is fully consistent with the conclusion made in Ref. [44] regarding the ability
 1793 of the Bosted parameterization to describe experimental measurements in this kinematic
 1794 region. The deviations of the measured integrals from their parameterized values revealed in
 1795 this analysis and the Q^2 behavior of those deviations are almost exactly the same as those
 1796 found in Ref. [44] for already established measurements.

1797 Thus, one can conclude that the quality of agreement between the quasi-elastic cross
 1798 section estimated in this analysis with the Bosted parameterization [45, 46] is the same
 1799 as was observed for other published measurements. This, in turn, indicates that in this
 1800 particular analysis, both the electron selection and overall cross section normalization are
 1801 under control.

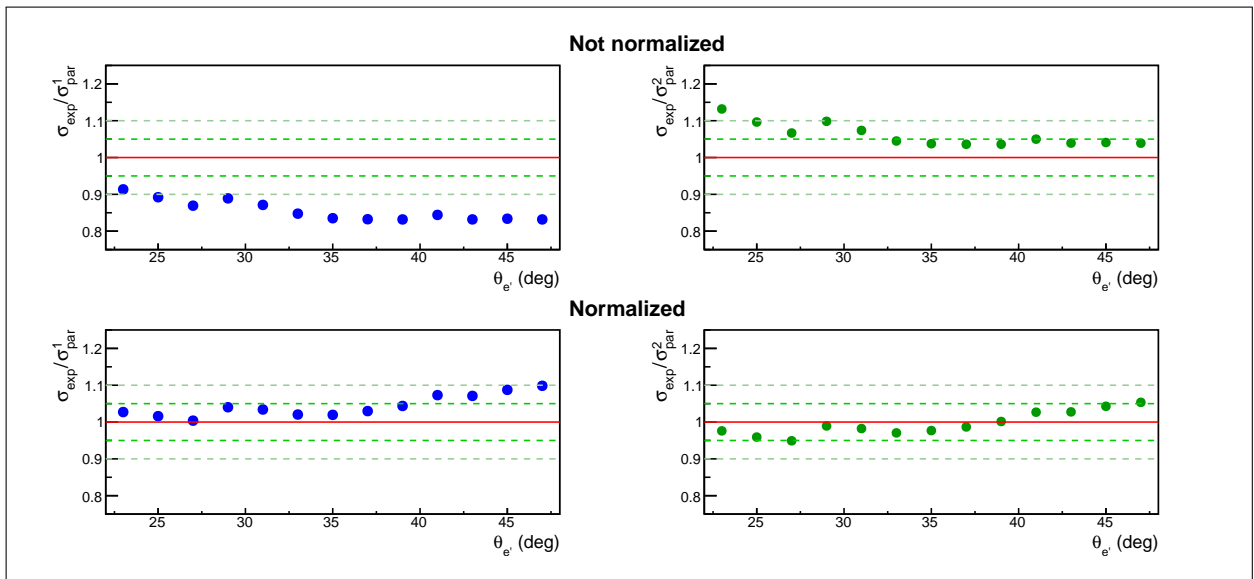


Figure 6.2: Ratios of the experimental integral under the quasi-elastic peak to the parameterized one as a function of the angle $\theta_{e'}$. The left side corresponds to the case, when the nuclear scaling function was calculated by the default method (blue symbols), while for the right side it was calculated by the alternative method (green symbols). The top row stands for the unscaled parameterized histograms, while for the bottom row, they were scaled to the peak value approximated by the formula described in Ref. [44]. The red solid line marks the position of unity. The dark-green dashed lines mark the deviation of 5%, while the light-green ones show the deviation of 10%.

1802 The value of the uncertainty due to normalization and electron identification is then
 1803 estimated considering the following arguments.

- 1804 • as shown in this Section, the quasi-elastic cross section extracted from the current
 1805 dataset have the same quality of agreement with the Bosted parameterization as other
 1806 published measurements demonstrate [44];

- 1807 • as follows from Tab. 6.1 and Fig. 6.2, one can achieve a good $\sim 5\%$ agreement between
1808 the measured and parameterized values of the quasi-elastic cross sections when the
1809 parameterized distributions are normalized to the peak values approximated by the
1810 formula that was proven to describe well the experimental peak cross sections in this
1811 kinematic region [44];
- 1812 • as shown in Refs. [22, 23], the elastic cross section off protons estimated from the
1813 same “e1e” run period (as it included both hydrogen and deuterium target runs in the
1814 same experimental configuration) agrees within $\sim 3\%$ with the corresponding Bosted
1815 parameterization. The latter, meanwhile, employs the same empirical fit of the nucleon
1816 electromagnetic form factors as the Bosted parameterization of the quasi-elastic cross
1817 section off deuteron used in the current study [52].

1818 Taking these facts into account, a 5% global uncertainty is assigned to the extracted
1819 double-pion cross sections due to potential inaccuracies in the normalization and electron
1820 selection.

₁₈₂₁ **Chapter 7**

₁₈₂₂ **Cross section uncertainties**

₁₈₂₃ In this study (like in other studies of the double-pion cross sections [15–19, 21–23]) three
₁₈₂₄ separate types of the cross section uncertainties are considered, i.e. statistical uncertainty,
₁₈₂₅ uncertainty due to the model dependence, and systematic uncertainty. The recipe for esti-
₁₈₂₆ mating the uncertainty of each type is given below.

₁₈₂₇ **7.1 Statistical uncertainties**

₁₈₂₈ The limited statistics of both the experimental data and the Monte Carlo simulation are
₁₈₂₉ the two sources of statistical fluctuations of the extracted cross sections. The cut on the
₁₈₃₀ efficiency uncertainty described in Sec. 3.6 was chosen in a way that the latter source gives
₁₈₃₁ a minor contribution to the total statistical uncertainty.

₁₈₃₂ The statistical uncertainty to the five-fold differential virtual photoproduction cross sec-
₁₈₃₃ tion is calculated individually in each non-empty multi-dimensional $\Delta^5\tau$ bin as described
₁₈₃₄ below.

₁₈₃₅ The absolute statistical uncertainty due to the limited statistics of the experimental data
₁₈₃₆ is calculated in the non-empty bins as¹

$$\delta_{\text{stat}}^{\text{exp}}(\Delta^5\tau) = \frac{1}{\mathcal{E} \cdot R \cdot \mathcal{F} \cdot \Gamma_v} \cdot \sqrt{\left(\frac{N_{\text{full}}}{Q_{\text{full}}^2} + \frac{N_{\text{empty}}}{Q_{\text{empty}}^2} \right)} \cdot \frac{\Delta W \cdot \Delta Q^2 \cdot \Delta^5\tau \cdot \mathcal{L}}, \quad (7.1.1)$$

₁₈₃₇ where Γ_v is the virtual photon flux given by Eq. (3.5.3), while the other ingredients are
₁₈₃₈ explained after Eq. (3.5.1).

₁₈₃₉ The absolute uncertainty due to the limited Monte Carlo statistics is estimated in the

¹ See Eq. (D.1) in App. D.

1840 non-empty bins as²

$$\delta_{\text{stat}}^{\text{MC}}(\Delta^5\tau) = \frac{d^5\sigma_v}{d^5\tau} \left(\frac{\delta\mathcal{E}}{\mathcal{E}} \right), \quad (7.1.2)$$

1841 where $\frac{d^5\sigma_v}{d^5\tau}$ is the virtual photoproduction cross section given by Eq. (3.5.2), \mathcal{E} is the efficiency
 1842 inside the multi-dimensional bin defined by Eq. (3.6.1), while $\delta\mathcal{E}$ is its absolute statistical
 1843 uncertainty.

1844 Meanwhile, the calculation of the efficiency uncertainty $\delta\mathcal{E}$ is not straightforward and
 1845 needs special attention, since (i) N_{gen} and N_{rec} in Eq. (3.6.1) are not independent and (ii)
 1846 Monte Carlo events in this equation are subject to weighting. Therefore, the special approach
 1847 described in Ref. [41] was used for this purpose. Neglecting the event migration between the
 1848 bins, this approach gives the following expression for the absolute statistical uncertainty of
 1849 the efficiency in a bin for the case of weighted Monte Carlo simulation,

$$\delta\mathcal{E}(\Delta^5\tau) = \sqrt{\frac{\mathbb{N}_{\text{gen}} - 2\mathbb{N}_{\text{rec}}}{\mathbb{N}_{\text{gen}}^3} \sum_{i=1}^{N_{\text{rec}}} w_i^2 + \frac{\mathbb{N}_{\text{rec}}^2}{\mathbb{N}_{\text{gen}}^4} \sum_{j=1}^{N_{\text{gen}}} w_j^2}, \quad (7.1.3)$$

1850 where N_{gen} and N_{rec} are the numbers of the generated and reconstructed Monte Carlo events
 1851 inside the multi-dimensional bin, respectively, \mathbb{N}_{gen} and \mathbb{N}_{rec} are the corresponding weighted
 1852 event numbers, while w is a weight of an individual event.

1853 The two parts of the statistical uncertainty given by Eqs. (7.1.1) and (7.1.2) are combined
 1854 quadratically into the total absolute statistical uncertainty in each non-empty $\Delta^5\tau$ bin³,

$$\delta_{\text{stat}}^{\text{tot}}(\Delta^5\tau) = \sqrt{(\delta_{\text{stat}}^{\text{exp}})^2 + (\delta_{\text{stat}}^{\text{MC}})^2}. \quad (7.1.4)$$

1855 The cross section assigned to the empty $\Delta^5\tau$ cells (see Eq. (4.1.3)) acquires zero statistical
 1856 uncertainty.

1857 For the extracted single-differential cross sections the statistical uncertainty $\delta_{\text{stat}}^{\text{tot}}(\Delta X)$
 1858 (where X is one of the final state variables, i.e. $M_{h_1 h_2}$, $M_{h_2 h_3}$, θ_{h_1} , α_{h_1}) is obtained from the
 1859 uncertainties $\delta_{\text{stat}}^{\text{tot}}(\Delta^5\tau)$ of the five-fold differential cross sections according to the standard
 1860 error propagation rules.

²See Eq. (D.2) in App. D.

³The THnSparse root histograms offer an easy way of dealing with the uncertainties. Each multi-dimensional bin of the histograms with the experimental data acquires the absolute uncertainty $\sqrt{N_{\text{full}}}$ and $\sqrt{N_{\text{empty}}}$ for full and empty target runs, respectively. The efficiency histograms get the uncertainty $\delta\mathcal{E}(\Delta^5\tau)$ given by Eq. (7.1.3). Then the uncertainty automatically propagates upon all manipulations with these histograms (addition, division, scaling).

¹⁸⁶¹ 7.2 Model dependent uncertainties

¹⁸⁶² In the studies of the double-pion cross sections off the free proton [15–19, 21–23], the un-
¹⁸⁶³ certainty of the model dependence is commonly treated as a unique uncertainty type and is
¹⁸⁶⁴ associated with the filling of the empty cells. In this analysis one more source of the cross
¹⁸⁶⁵ section model dependence had to be considered, which is unfolding the effects of the target
¹⁸⁶⁶ motion. These two sources give comparable uncertainties only for the two lowest W bins,
¹⁸⁶⁷ while for the other bins the dominant part of the model dependent uncertainty comes from
¹⁸⁶⁸ the filling of the empty cells.

¹⁸⁶⁹ Both the contribution from the empty cells and the value of the unfolding correction vary
¹⁸⁷⁰ greatly (from completely insignificant to considerable) for different final state variable bins.
¹⁸⁷¹ Therefore, it is convenient to estimate the model dependent uncertainties in each ΔX bin of
¹⁸⁷² the single-differential cross sections (where X is one of the final state variables introduced
¹⁸⁷³ in Sect. 3.3).

¹⁸⁷⁴ 7.2.1 Uncertainty due to the empty cells filling

¹⁸⁷⁵ During the empty cell filling the extracted cross sections acquire a moderate model depen-
¹⁸⁷⁶ dence (see Sect. 4.1). Once the empty cells are filled, the part of the single-differential cross
¹⁸⁷⁷ section that came from the empty cells is assigned a 50% relative uncertainty⁴ (see Sect. 4.1).
¹⁸⁷⁸ The absolute cross section uncertainty $\tilde{\delta}_{\text{model}}^{\text{cells}}(\Delta X)$ is hence given by

$$\tilde{\delta}_{\text{model}}^{\text{cells}}(\Delta X) = \frac{1}{2} \left(\left[\frac{d\sigma}{dX} \right]_{\text{filled}} - \left[\frac{d\sigma}{dX} \right]_{\text{not filled}} \right), \quad (7.2.1)$$

¹⁸⁷⁹ where the parentheses contain the difference between the cross section values calculated with
¹⁸⁸⁰ the empty cell contributions (“filled”) and without them (“not filled”).

¹⁸⁸¹ The corresponding relative uncertainty $\varepsilon_{\text{model}}^{\text{cells}}(\Delta X)$ is in turn given by

$$\varepsilon_{\text{model}}^{\text{cells}}(\Delta X) = \frac{\tilde{\delta}_{\text{model}}^{\text{cells}}}{\left[\frac{d\sigma}{dX} \right]_{\text{filled}}}. \quad (7.2.2)$$

¹⁸⁸² After the filling of the empty cells the cross section is subject to several subsequent
¹⁸⁸³ manipulations, i.e. virtual photon flux normalization, radiative correction, and unfolding
¹⁸⁸⁴ the effects of initial proton motion. Along this path the absolute uncertainty $\tilde{\delta}_{\text{model}}^{\text{cells}}(\Delta X)$ is
¹⁸⁸⁵ propagated in such a way as to keep the relative uncertainty $\varepsilon_{\text{model}}^{\text{cells}}(\Delta X)$ in each ΔX bin of
¹⁸⁸⁶ the single-differential distribution unchanged.

⁴This way to estimate this uncertainty, although being rather conservative, has become conventional for the studies of double-pion production cross sections [19, 20, 22].

1887 Therefore, the absolute uncertainty $\delta_{\text{model}}^{\text{cells}}(\Delta X)$ for the final single-differential distributions is obtained by
 1888

$$\delta_{\text{model}}^{\text{cells}}(\Delta X) = \left[\frac{d\sigma_v}{dX} \right]_{\text{final}} \cdot \varepsilon_{\text{model}}^{\text{cells}}, \quad (7.2.3)$$

1889 with the relative uncertainty $\varepsilon_{\text{model}}^{\text{cells}}$ given by Eq. (7.2.2) and the single-differential cross
 1890 section determined according to Eq. (3.5.5).

1891 7.2.2 Uncertainty due to unfolding the effects of target motion

1892 In this study the cross sections are subjected to one extra correction compared to the cross
 1893 sections extracted off the free proton [15–19, 21–23], i.e. unfolding the effects of initial proton
 1894 motion. The potential inaccuracies due to this procedure are also attributed to the model
 1895 dependent uncertainty, since the procedure is based on (i) the free proton cross sections
 1896 taken from the model JM and (ii) the model of the deuteron wave function, which was the
 1897 Bonn model (see Sect. 4.3 for more detail).

1898 For each ΔX bin of the single-differential distributions the relative uncertainty due to
 1899 the unfolding procedure was estimated by⁵

$$\varepsilon_{\text{model}}^{\text{unfold}}(\Delta X) = \frac{\left[\frac{d\sigma}{dX} \right]_{\text{folded}} - \left[\frac{d\sigma}{dX} \right]_{\text{unfolded}}}{\left[\frac{d\sigma}{dX} \right]_{\text{folded}} + \left[\frac{d\sigma}{dX} \right]_{\text{unfolded}}}. \quad (7.2.4)$$

1900 The corresponding absolute uncertainty is then given by

$$\delta_{\text{model}}^{\text{unfold}}(\Delta X) = \left[\frac{d\sigma_v}{dX} \right]_{\text{final}} \cdot \varepsilon_{\text{model}}^{\text{unfold}}. \quad (7.2.5)$$

1901 7.3 Systematic uncertainties

1902 The systematic uncertainty of the extracted cross sections is estimated in each bin in W and
 1903 Q^2 . As in the previous studies of the double-pion production cross sections [15–19, 21–23],
 1904 the dependence of the systematic uncertainty on the hadronic variables is not investigated.

1905 The following sources are considered to contribute to the total systematic uncertainty of
 1906 the extracted cross sections.

⁵ Although the relative uncertainty due to empty cell filling can also be estimated in this way, it was decided to calculate it according to Eq. (7.2.2) to observe consistency with the free proton results [22].

1907 **Normalization and electron identification**

1908 The presence of quasi-elastic events in the dataset advantages the verification of both the
1909 overall cross section normalization and the quality of the electron selection. The former
1910 may lack accuracy due to potential miscalibrations of the Faraday cup, fluctuations in the
1911 target density, deviations of the beam current and position, inaccuracies in determining
1912 the DAQ live-time as well as imprecise knowledge of other “luminosity ingredients” such as
1913 target length or the density of liquid deuterium (see Eq. (3.5.1)). Meanwhile, the quality of
1914 the electron selection may suffer from potential miscalibrations of different detector parts,
1915 inaccuracies in the electron tracking and identification as well as uncertainties of the cuts
1916 and corrections involved in the electron selection.

1917 To verify the correct cross section normalization and the quality of the electron selection,
1918 the study [22, 23] (which is the study of double-pion cross sections off the free proton in
1919 the same kinematic region) estimates the elastic cross section and then compares it with
1920 the Bosted parameterization [52]. This comparison revealed a 3% agreement between the
1921 experimental and parameterized cross sections that allowed to assign a 3% global uncertainty
1922 to the extracted double-pion cross sections due to inaccuracies in the normalization and
1923 electron selection.

1924 To achieve the same goals in the current analysis, the quasi-elastic cross section was
1925 estimated and then compared with the Bosted parameterization of the quasi-elastic cross
1926 section off the deuteron [45, 46] (see Sect. 6 for details). This comparison allows to claim a
1927 5% agreement between the experimental and parameterized cross sections and, therefore, to
1928 assign a 5% global uncertainty to the extracted double-pion cross sections due to inaccuracies
1929 in the normalization and electron selection.

1930 **Integration over three sets of final hadron variables**

1931 According to Sect. 3.3, the cross sections are extracted in three sets of the kinematic variables.
1932 The integral cross sections are found to slightly differ among the sets due to the different
1933 data and efficiency propagation to various kinematic grids. As a final result, the integral
1934 cross sections averaged (as an arithmetic mean) over these three grids are reported. The
1935 standard error of the mean is interpreted as a systematic uncertainty (which is calculated
1936 according to Eq. (D.4) in App. D). The single-differential cross sections and the uncertainty
1937 $\delta_{\text{stat,mod}}^{\text{tot}}$ are scaled to the mean integral value.

1938 Since different variable sets correspond to different registered final hadrons (and, there-
1939 fore, to different combinations of the hadron cuts), this systematic error includes the error
1940 due to the shapes of the hadron cuts that are used in the analysis. The average value of this
1941 uncertainty among all W and Q^2 bins is 1.6%. However, the error is larger in the first two
1942 W bins (with the maximum of 9.5% achieved in the first W bin at $Q^2 = 0.675 \text{ GeV}^2$), which
1943 being located near the reaction threshold, correspond to low momenta of the final hadrons.

1944 **Relative efficiency uncertainty cut**

1945 The cut on the relative efficiency uncertainty directly impacts both the cross section value
1946 and the cross section uncertainties, since it excludes entire kinematic cells from further
1947 consideration (see Sect. 3.6). This cut, therefore, reduces the total statistical uncertainty
1948 and increases the model dependent uncertainty, and a cut value $\delta\tilde{\mathcal{E}}/\tilde{\mathcal{E}} = 0.3$ is chosen as
1949 a compromise between these two effects. To estimate the systematic effect of the cut, the
1950 integral cross sections were also calculated for the cut values 0.25 and 0.35. As a final result,
1951 the arithmetic mean of the integral cross sections for these three cut values is reported, and
1952 the standard error of the mean is interpreted as a systematic uncertainty (which is calculated
1953 according to Eq. (D.4) in App. D). The single-differential cross sections and the uncertainty
1954 $\delta_{\text{stat,mod}}^{\text{tot}}$ are reported for the cut value 0.3, being scaled to the mean integral value.

1955 The systematic effect of the relative efficiency uncertainty cut is estimated for each bin
1956 in W and Q^2 individually and is found to be minor, i.e. the average uncertainty value is
1957 0.8%. Taking into account that the cut on the relative efficiency uncertainty impacts directly
1958 the amount of empty cells, the revealed small uncertainty associated with this cut indicates
1959 that the procedure of the empty cell filling is well under control and that the cross section
1960 inaccuracy caused by the corresponding model dependence is not significant.

1961 **Correction due to FSI-background admixture**

1962 One more part of the systematic uncertainties comes from the effective correction due to
1963 FSI-background admixture. This correction is performed for the experimental events in the
1964 π^- missing topology and described in Sect. 2.4.2. The fit shown in Fig. 2.33 (as well as the
1965 corresponding correction factor given by Eq. (2.4.2)) turned out to be slightly dependent on
1966 the histogram binning. To account for this uncertainty, the correction factor is estimated
1967 for five different histogram bin sizes, and the arithmetic mean of these five individual values
1968 is used for the correction (for each bin in W). The absolute uncertainty of the resulting cor-
1969 rection factor is estimated as a standard error of the mean (which is calculated according to
1970 Eq. (D.4) in App. D). The corresponding cross section uncertainty is estimated by Eq. (D.3),
1971 where the quantity a includes the number of events from the π^- missing topology, while c
1972 in the denominator includes the efficiency estimated for both topologies.

1973 The systematic effect of the FSI-background correction is estimated for each bin in W
1974 and Q^2 . The average value of the relative systematic uncertainty is 0.4%, which is rather
1975 marginal.

₁₉₇₆ **Radiative corrections**

₁₉₇₇ As a common practice in studies of the double-pion cross sections with CLAS [15–19, 21–
₁₉₇₈ 23], a 5% global uncertainty is assigned to the cross section due to the inclusive radiative
₁₉₇₉ correction procedure (see Sect. 4.2).

₁₉₈₀ **Summary of the systematic uncertainties**

₁₉₈₁ The average values of integral systematic errors with their sources are presented in Tab. 7.1.
₁₉₈₂ The uncertainties due to these sources were summed up in quadrature in each W and Q^2
₁₉₈₃ bin to obtain the total systematic uncertainty for the integral cross sections. The common
₁₉₈₄ value of the total systematic uncertainty in the bin is $\sim 7\%$ (it is, however, higher near the
₁₉₈₅ threshold).

Table 7.1: Average values of integral systematic uncertainties.

Source	Average value
Normalization and electron identification	5%
Integration over three sets of hadron variables	1.7%
Relative efficiency uncertainty cut	0.6%
Correction due to FSI-background admixture	0.4%
Radiative corrections	5%
Total	7.4%

₁₉₈₆ **7.4 Summary for the cross section uncertainties**

₁₉₈₇ Finally, the model dependent uncertainties $\delta_{\text{model}}^{\text{cells}}(\Delta X)$ and $\delta_{\text{model}}^{\text{unfold}}(\Delta X)$ defined by Eq. (7.2.3)
₁₉₈₈ and Eq. (7.2.5), respectively, are combined with the total statistical uncertainty $\delta_{\text{stat}}^{\text{tot}}(\Delta X)$
₁₉₈₉ defined in Sect. 7.1 as the following.

$$\delta_{\text{stat,mod}}^{\text{tot}}(\Delta X) = \sqrt{(\delta_{\text{stat}}^{\text{tot}})^2 + (\delta_{\text{model}}^{\text{cells}})^2 + (\delta_{\text{model}}^{\text{unfold}})^2}. \quad (7.4.1)$$

₁₉₉₀ The extracted cross sections are reported with the uncertainty $\delta_{\text{stat,mod}}^{\text{tot}}$, which for the
₁₉₉₁ single-differential distributions is given by Eq. (7.4.1), while for the integral cross sections is

1992 obtained from the uncertainty of the single-differential distributions according to the stan-
1993 dard error propagation rules⁶. For the majority of (W , Q^2) points of the integral cross
1994 sections the uncertainty $\delta_{\text{stat,mod}}^{\text{tot}}$ stays on a level of $\sim 4\%-6\%$.

1995 It should be mentioned that to combine the statistical uncertainty with the uncertainty
1996 of the model dependence and to report the final cross sections with the resulting uncer-
1997 tainty $\delta_{\text{stat,mod}}^{\text{tot}}$ have become conventional for the studies of double-pion production cross
1998 sections [15–19, 21–23].

1999 In addition to the uncertainty $\delta_{\text{stat,mod}}^{\text{tot}}$, for the integral cross sections the total systematic
2000 uncertainty is also reported as a separate quantity. If necessary, the relative systematic
2001 uncertainty in each W and Q^2 bin can be propagated as a global factor to the corresponding
2002 single-differential distributions.

2003 In this study the uncertainty $\delta_{\text{stat,mod}}^{\text{tot}}$ is less than the total systematic uncertainty for the
2004 majority of (W , Q^2) points, exceeding it only near the threshold (for $W \lesssim 1.4$ GeV). This
2005 happens because the former rises close to the threshold due to small experimental statistics,
2006 large contribution of the empty cells (see Sect. 4.1), and pronounced impact of the unfolding
2007 correction (see Sect. 4.3).

⁶ Note that for the integral cross sections the value of $\delta_{\text{stat,mod}}^{\text{tot}}$ was averaged (as arithmetic mean) among the three sets of final hadron variables.

2008 **Chapter 8**

2009 **Results and conclusion**

2010 As a result of this study, the integral and single-differential cross sections of the reaction
2011 $\gamma_v p(n) \rightarrow p'(n')\pi^+\pi^-$ in the kinematic region of invariant mass W from 1.3 GeV to 1.825 GeV
2012 and photon virtuality Q^2 from 0.4 GeV 2 to 1 GeV 2 were obtained. The cross sections
2013 were extracted in the quasi-free regime, which means that FSI-background admixture in the
2014 analyzed event sample was decreased as much as was possible and left on a level comparable
2015 with that in the free proton cross sections.

2016 Figure 8.1 shows the W dependences of the extracted integral cross sections in various
2017 bins in Q^2 , while Figure 8.3 shows their Q^2 dependences in various bins in W . The red
2018 shadowed area for each point is the total cross section uncertainty, which is the uncertainty
2019 $\delta_{\text{stat,mod}}^{\text{tot}}$ (see Sect. 7.2) summed up in quadrature with the total systematic uncertainty (see
2020 Sect. 7.3). The error bars correspond to the uncertainty $\delta_{\text{stat,mod}}^{\text{tot}}$ only, which for most of the
2021 points is smaller than the symbol size.

2022 For each integral (W, Q^2) point nine single-differential cross sections are reported¹. They
2023 are presented in App. F with the uncertainty $\delta_{\text{stat,mod}}^{\text{tot}}$ shown by error bars. Once the analysis
2024 is approved, the whole set of the extracted cross sections (both integral and single-differential)
2025 will be available in the CLAS physics database [5].

2026 After approval the cross sections will be subject to further physical interpretation, which
2027 includes as an important step the comparison with the double-pion cross sections off the
2028 free proton recently extracted from CLAS data [22, 23]. These cross sections were obtained
2029 in the same experimental configuration (including beam energy and target setup) as the
2030 cross sections of this study. Both measurements have, therefore, similar inherent systematic
2031 inaccuracies. Moreover, the cross sections of both sets, being obtained in the same kine-

1 Note that FSI-background admixture left after the exclusivity cut in the π^- -missing topology (see Sect. 2.4.2), being corrected only in integral sense, may potentially impact the shape of extracted single-differential distributions (mostly angular). However, since this admixture is present only for events from the π^- -missing topology for $W > 1.4875$ GeV and stays on the level of 3-7%, its impact is not thought to be discernible against the total cross section uncertainty.

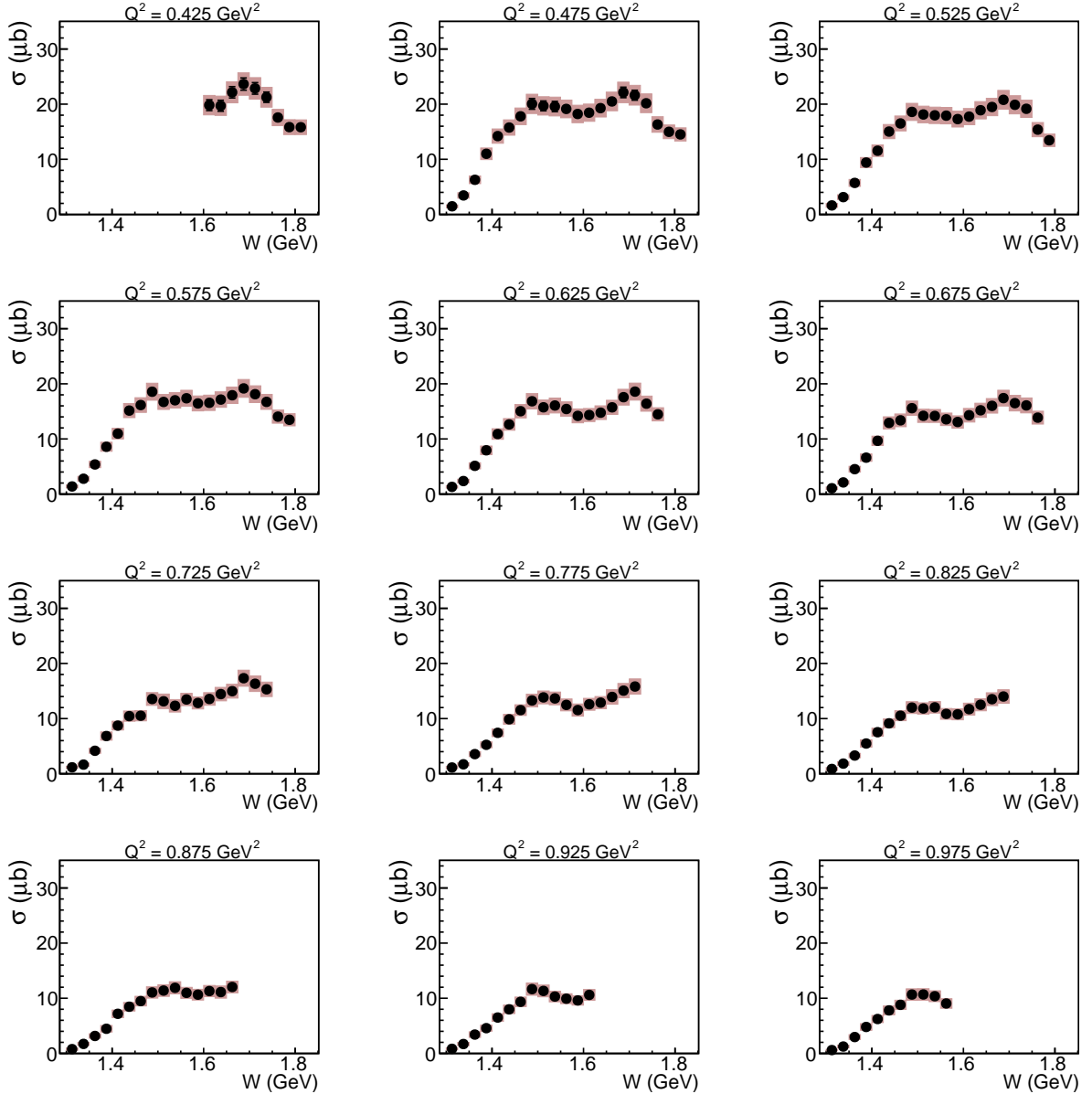


Figure 8.1: W dependences of the extracted integral cross sections in various bins in Q^2 . The pink shadowed area for each point is the total cross section uncertainty, which is the uncertainty $\delta_{\text{stat,mod}}^{\text{tot}}$ (see Sect. 7.2) summed up in quadrature with the total systematic uncertainty (see Sect. 7.3). The error bars that correspond to the uncertainty $\delta_{\text{stat,mod}}^{\text{tot}}$ only, are smaller than the symbol size.

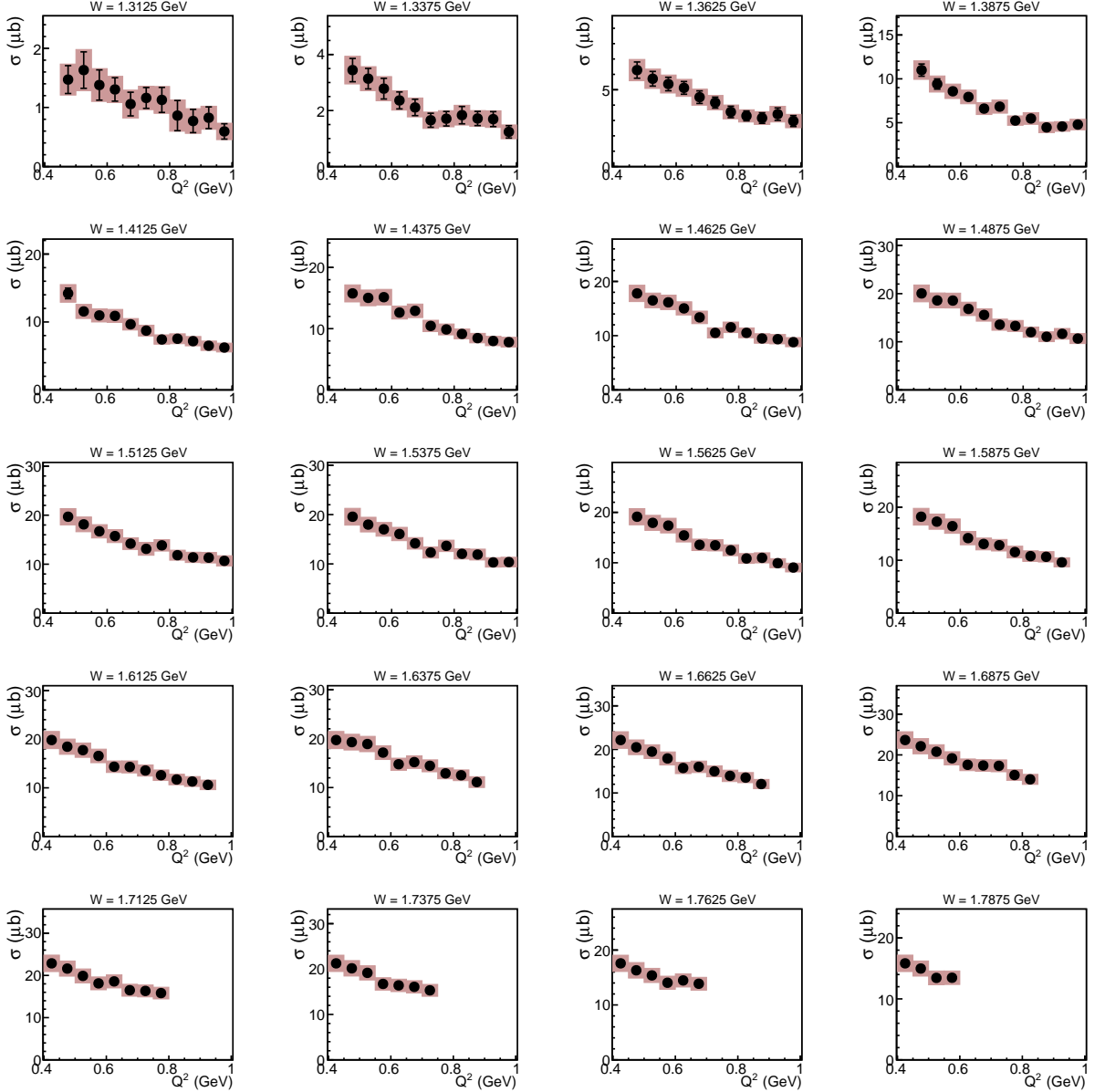


Figure 8.2: Q^2 dependences of the extracted integral cross sections in various bins in W . The pink shadowed area for each point is the total cross section uncertainty, which is the uncertainty $\delta_{\text{stat,mod}}^{\text{tot}}$ (see Sect. 7.2) summed up in quadrature with the total systematic uncertainty (see Sect. 7.3). The error bars that correspond to the uncertainty $\delta_{\text{stat,mod}}^{\text{tot}}$ only, are smaller than the symbol size.

2032 matic region, have identical binning in the kinematic variables that advantages their direct
 2033 comparison. This comparison hence provides the experimentally best possible opportunity
 2034 to investigate the differences and alterations (including possible in-medium modifications)
 2035 that occur in the exclusive reaction off the bound proton in comparison with that off the
 2036 free proton.

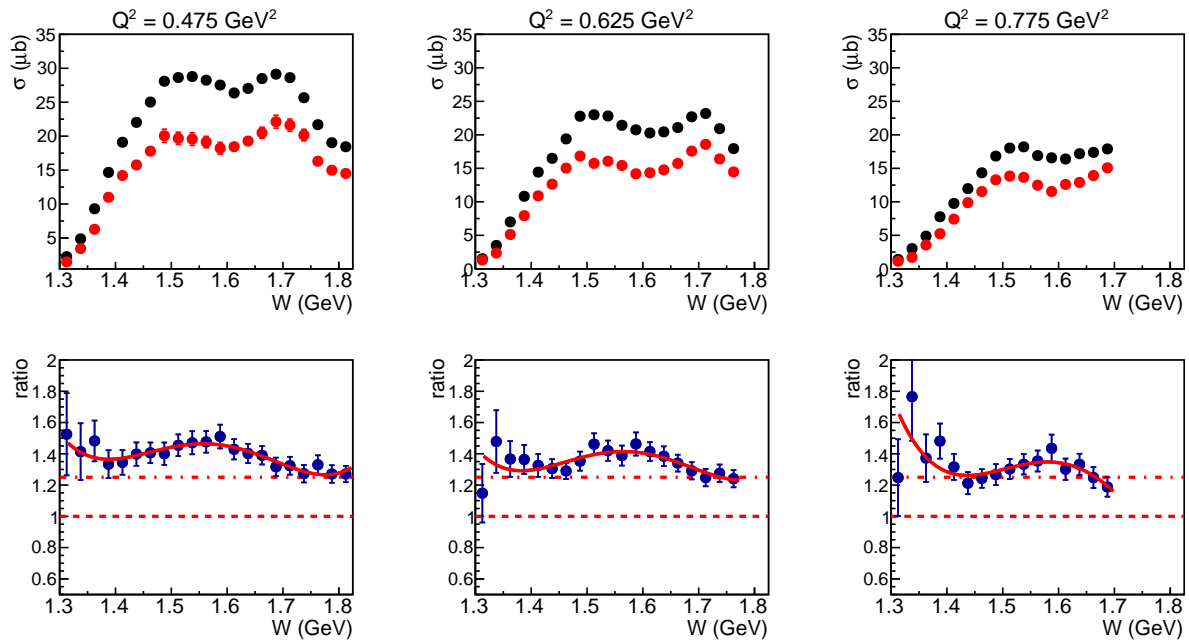


Figure 8.3: Comparison between integral cross sections obtained in this analysis (red symbols) and those obtained off the free proton [22, 23] (black symbols) shown for three typical equidistant Q^2 bins specified in the plots. The cross sections from both studies are given with the uncertainties $\delta_{\text{stat,mod}}^{\text{tot}}$ only (shown by error bars), while systematic effects are assumed to be identical and are hence ignored. The bottom row of Fig. 8.3 shows the ratio of the corresponding distributions from the top row together with its preliminary fit by the fifth order polynomial. The dashed line marks the position of unity, while the dash-dotted line shows the value of 1.25.

2037 The top row of Fig. 8.3 shows some example plots, which demonstrate the difference
 2038 between integral cross sections obtained in this analysis (red symbols) and their free proton
 2039 analogue from Ref. [22, 23] (black symbols). The comparison shown here is given for three
 2040 typical equidistant Q^2 bins specified in the plots. The cross sections from both studies are
 2041 given with the uncertainties $\delta_{\text{stat,mod}}^{\text{tot}}$ only (shown by error bars), while systematic effects are
 2042 assumed to be identical and are hence ignored. The bottom row of Fig. 8.3 shows the ratio
 2043 of the corresponding distributions from the top row together with its preliminary fit by the
 2044 fifth order polynomial.

2045 The examples shown in Fig. 8.3 indicate a pronounced difference between the free proton
 2046 cross section and its quasi-free analogue measured off the proton bound in deuterium. This

2047 difference, which is thought to be attributed mainly to the FSI effects, is seeking a detailed
2048 investigation and physical interpretation including the study of its dependence on various
2049 kinematic variables. This activity will eventually shed light on the processes that occur in
2050 the deuteron, such as FSI and in-medium effects.

2051 Further physical discussions and interpretations of the obtained results are left for the
2052 PhD thesis (which is in preparation) and a future publication on the subject.

2053 It is also noteworthy that during this study a sophisticated analysis framework was
2054 elaborated that includes the tools for data processing and cross section calculation. This
2055 framework, which is partially based on the achievements of the study [22, 23], might be
2056 of use for future studies including the upcoming analysis of new CLAS12 data. Therefore,
2057 the data analysis procedure and the links to the codes of programs and scripts are given in
2058 App. E.

2059 Appendices

2060 Appendix A: Features of missing mass distributions

2061 Let's consider the double-pion electroproduction off the free proton $ep \rightarrow e'p'\pi^+\pi^-$ and
 2062 define the following missing quantities,

$$M_{X[0]}^2 = [P_{X[0]}^\mu]^2 = [P_e^\mu + P_p^\mu - P_{e'}^\mu - P_{p'}^\mu - P_{\pi^+}^\mu - P_{\pi^-}^\mu]^2, \quad (\text{A.1})$$

$$M_{X[\pi^-]}^2 = [P_{X[\pi^-]}^\mu]^2 = [P_e^\mu + P_p^\mu - P_{e'}^\mu - P_{p'}^\mu - P_{\pi^+}^\mu]^2,$$

2063 where $P_{X[0]}^\mu$ and $P_{X[\pi^-]}^\mu$ are the corresponding missing four-vectors, while P_i^μ is the four-momentum of the particle i .

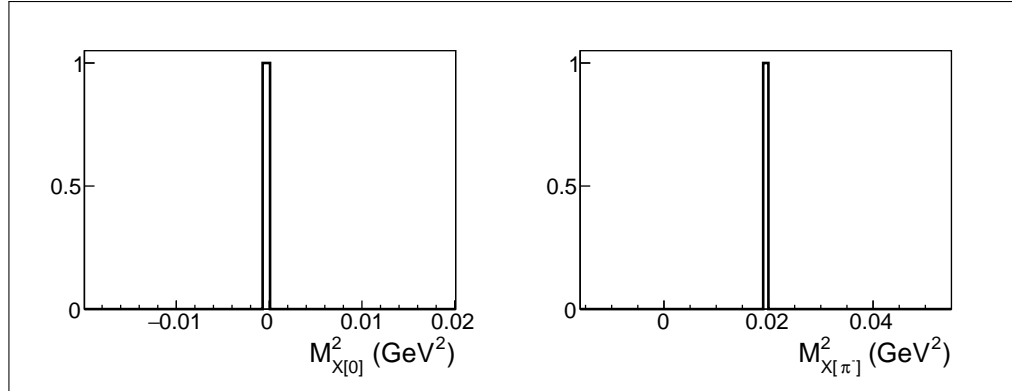


Figure A.1: Quantities $M_{X[0]}^2$ (left) and $M_{X[\pi^-]}^2$ (right).

2064 Let's firstly assume that (i) all events in the sample correspond to the reaction $ep \rightarrow$
 2065 $e'p'\pi^+\pi^-$, (ii) all four-momenta are defined exactly without any resolution uncertainty, and
 2066 (iii) neither radiative effects nor FSI occur. Then¹

$$M_{X[0]}^2 = 0 \quad \text{and} \quad M_{X[\pi^-]}^2 = [P_{\pi^-}^\mu]^2 = m_\pi^2, \quad (\text{A.2})$$

¹ Note that for the quantity $M_{X[0]}^2$ the missing four-vector in the square brackets in Eqs. (A.1) is equal to zero componentwise, which means that the energy and each momentum component are equal to zero.

which means that both $M_{X[0]}^2$ and $M_{X[\pi^-]}^2$ form a discrete narrow peak at the position of zero and m_π^2 , respectively, as Fig. A.1 demonstrates².

Now let's trace the impact of different effects on the missing mass distributions.

Radiative effects

Let's calculate the quantities $M_{X[0]}^2$ and $M_{X[\pi^-]}^2$ assuming that either the incoming or scattered electron can emit a radiative photon, and (if the emission occurs) $P_e^\mu/P_{e'}^\mu$ in Eqs. (A.1) is the four-momentum of the incoming/scattered electron determined before/after the emission, respectively. Then for events with the photon emission

$$\begin{aligned} M_{X[0]}^2 &= [P_\gamma^\mu]^2 = 0 \quad \text{and} \\ M_{X[\pi^-]}^2 &= [P_{\pi^-}^\mu + P_\gamma^\mu]^2 = [P_{\pi^-}^\mu]^2 + [P_\gamma^\mu]^2 + 2(P_{\pi^-}^\mu \cdot P_\gamma^\mu) = \\ &= m_\pi^2 + 2(E_{\pi^-} - E_\gamma - (\vec{p}_{\pi^-} \cdot \vec{p}_\gamma)) = \\ &= m_\pi^2 + 2(E_{\pi^-} - E_\gamma - |\vec{p}_{\pi^-}|E_\gamma \cos\beta) = \\ &= m_\pi^2 + 2E_\gamma(E_{\pi^-} - |\vec{p}_{\pi^-}| \cos\beta) > m_\pi^2, \end{aligned} \quad (\text{A.3})$$

where β corresponds to the angle between the π^- and the emitted radiative photon.

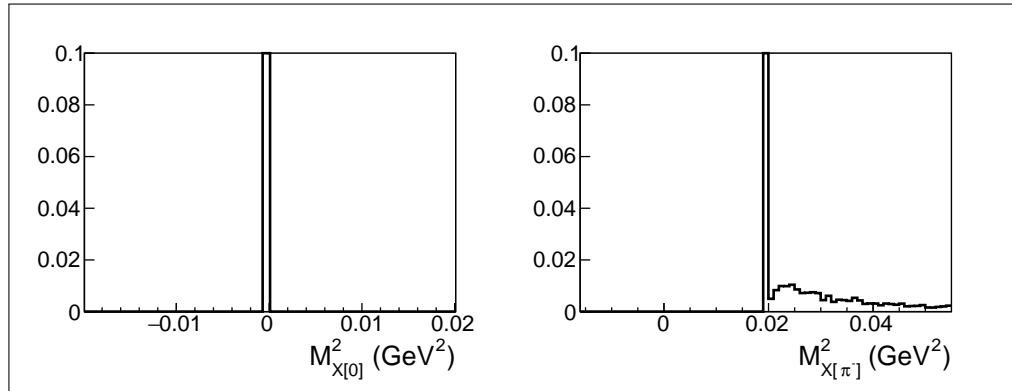


Figure A.2: Impact of radiative effects on $M_{X[0]}^2$ (left) and $M_{X[\pi^-]}^2$ (right). Both distributions are zoomed in onto small y to make the impact of the radiative effects visible.

As follows from Eqs. (A.3), the quantity $M_{X[0]}^2$ feels no impact of the radiative photon emission³, while the quantity $M_{X[\pi^-]}^2$ acquires a right-side tail, which is demonstrated in Fig. A.2.

² All histograms in this Appendix are filled with events generated with TWOPEG [36] for $E_{beam} = 2.039$ GeV, $1.4 \text{ GeV} < W < 1.8 \text{ GeV}$ and $0.4 \text{ GeV}^2 < Q^2 < 0.6 \text{ GeV}^2$ (unless specified otherwise). All distributions are normalized in a way that the maxima of the main peaks are equal to one.

³ Note that for the quantity $M_{X[0]}^2$ the missing four-vector in the square brackets in Eqs. (A.1) is the four-momentum of the radiative photon, which is not equal to zero componentwise. However, being massless, the photon has the energy equal to its momentum magnitude, which gives zero upon the calculation of $M_{X[0]}^2$. Thus the zero value of $M_{X[0]}^2$ has a different nature for events with and without radiative effects.

2080 **Admixture from other channels**

2081 Let's assume that some events in the sample correspond to the background channel with
 2082 greater amount of final state particles, i.e. $ep \rightarrow e'p'\pi^+\pi^-x$. Then for the background events
 2083

$$M_{X[0]}^2 = [P_x^\mu]^2 = m_x^2 > 0 \text{ and}$$

$$\begin{aligned} M_{X[\pi^-]}^2 &= [P_{\pi^-}^\mu + P_x^\mu]^2 = [P_{\pi^-}^\mu]^2 + [P_x^\mu]^2 + 2(P_{\pi^-}^\mu \cdot P_x^\mu) = \\ &= m_\pi^2 + m_x^2 + 2(E_{\pi^-} - E_x - (\vec{p}_{\pi^-} \cdot \vec{p}_x)) > \\ &> m_\pi^2 + m_x^2 + 2m_\pi m_x > m_\pi^2, \end{aligned} \quad (\text{A.4})$$

2084 which means that background events form an additional right-side peak well-separated from
 2085 the main one by m_x^2 and $m_x^2 + 2m_\pi m_x$ for $M_{X[0]}^2$ and $M_{X[\pi^-]}^2$, respectively.

2086 This situation is illustrated in Fig. A.3 for the case when the background channel is
 2087 $ep \rightarrow e'p'\pi^+\pi^-\pi^0$.

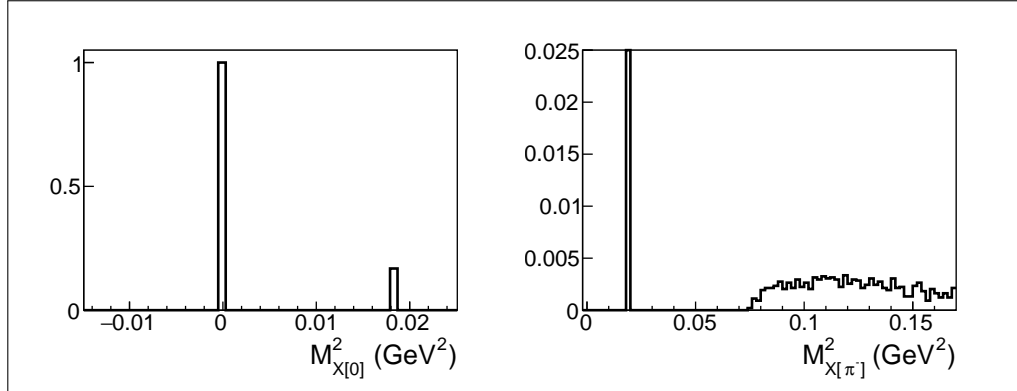


Figure A.3: Quantities $M_{X[0]}^2$ (left) and $M_{X[\pi^-]}^2$ (right) plotted for the case when the event sample has an admixture from the background channel $ep \rightarrow e'p'\pi^+\pi^-\pi^0$. The discrete right peak (in the left plot) and the right-side structure (in the right plot), both well-separated from the main peak, correspond to the background events. The right plot is zoomed in onto small y . The plots are produced by means of the GENEV event generator [42] for $E_{beam} = 2.039$ GeV, $1.4 \text{ GeV} < W < 1.8 \text{ GeV}$ and $0.4 \text{ GeV}^2 < Q^2 < 0.6 \text{ GeV}^2$.

2088 **Detector resolution**

2089 Let's now assume that for all events in the sample the particle four-momenta P_i^μ in Eqs. (A.1)
 2090 are determined with the uncertainty of the detector resolution and then estimate the resulting
 2091 uncertainties of the missing mass distributions.

2092 The missing quantity M_X^2 can be written in the following way,

$$\begin{aligned} M_X^2 &= (E_X)^2 - (p_X^x)^2 - (p_X^y)^2 - (p_X^z)^2 = \\ &= \left(\sum_i \pm \sqrt{m_i^2 + p_i^2} \right)^2 - \left(\sum_i \pm p_i^x \right)^2 - \left(\sum_i \pm p_i^y \right)^2 - \left(\sum_i \pm p_i^z \right)^2, \end{aligned} \quad (\text{A.5})$$

where E_X and p_X^j ($j = x, y, z$) are the energy and momentum components of the missing four-vector, while m_i , E_i , and p_i^j are the mass, energy, and momentum components of the individual particles with the index i running over all particles involved in the missing mass calculation (see Eqs. (A.1)). For the \pm sign the plus is taken for the initial particles (e and p) and the minus for the final particles.

Then let's estimate the uncertainties of the quantities E_X and p_X^j through the corresponding uncertainties for the individual particles. The absolute uncertainties for the energy components E_X are given by

$$\begin{aligned}\Delta E_{X[0]} &= \sqrt{(\Delta E_{e'})^2 + (\Delta E_{p'})^2 + (\Delta E_{\pi^+})^2 + (\Delta E_{\pi^-})^2} = \\ &= \sqrt{(\Delta p_{e'})^2 + (p_{p'}/E_{p'})^2 (\Delta p_{p'})^2 + (p_{\pi^+}/E_{\pi^+})^2 (\Delta p_{\pi^+})^2 + (p_{\pi^-}/E_{\pi^-})^2 (\Delta p_{\pi^-})^2}, \\ \Delta E_{X[\pi^-]} &= \sqrt{(\Delta E_{e'})^2 + (\Delta E_{p'})^2 + (\Delta E_{\pi^+})^2} = \\ &= \sqrt{(\Delta p_{e'})^2 + (p_{p'}/E_{p'})^2 (\Delta p_{p'})^2 + (p_{\pi^+}/E_{\pi^+})^2 (\Delta p_{\pi^+})^2},\end{aligned}\quad (\text{A.6})$$

where Δp_i is the uncertainty of the momentum magnitude for the particle i , which comes from the momentum resolution of Drift Chambers (where the momentum magnitude is supposed to be measured).

The absolute uncertainties for the momentum components p_X^j are in turn

$$\begin{aligned}\Delta p_{X[0]}^j &= \sqrt{(\Delta p_{e'}^j)^2 + (\Delta p_{p'}^j)^2 + (\Delta p_{\pi^+}^j)^2 + (\Delta p_{\pi^-}^j)^2}, \\ \Delta p_{X[\pi^-]}^j &= \sqrt{(\Delta p_{e'}^j)^2 + (\Delta p_{p'}^j)^2 + (\Delta p_{\pi^+}^j)^2},\end{aligned}\quad (\text{A.7})$$

where Δp_i^j are the uncertainties of the j -components of the particle's three-momenta ($j = x, y, z$), which come from both the momentum magnitude resolution and the spatial angular resolution of Drift Chambers.

As follows from Eqs. (A.6) and (A.7), $p_{X[0]}^j$ and $E_{X[0]}$ acquire larger absolute uncertainties than $p_{X[\pi^-]}^j$ and $E_{X[\pi^-]}$, respectively, as they include extra terms associated with uncertainties of the registration of an additional particle (the π^- in this case).

Now let's estimate the absolute uncertainties of the corresponding missing masses.

$$\begin{aligned}\Delta M_{X[0]}^2 &= \sqrt{(2E_{X[0]}\Delta E_{X[0]})^2 + \sum_{j=x, y, z} \left(2p_{X[0]}^j\Delta p_{X[0]}^j\right)^2} \\ \Delta M_{X[\pi^-]}^2 &= \sqrt{(2E_{X[\pi^-]}\Delta E_{X[\pi^-]})^2 + \sum_{j=x, y, z} \left(2p_{X[\pi^-]}^j\Delta p_{X[\pi^-]}^j\right)^2}\end{aligned}\quad (\text{A.8})$$

In Eqs. (A.8) the quantities $\Delta E_{X[0]}$, $\Delta p_{X[0]}^j$ and $\Delta E_{X[\pi^-]}$, $\Delta p_{X[\pi^-]}^j$ are respectively com-

parable, though (as was shown above) the former is systematically large than the latter. Meanwhile, both $E_{X[0]}$ and $p_{X[0]}^j$ are very close to zero, while both $E_{X[\pi^-]}$ and $p_{X[\pi^-]}$ are non-zero. As a consequence, the quantity $\Delta M_{X[0]}^2$ acquires smaller absolute uncertainty value than $\Delta M_{X[\pi^-]}^2$. This is, however, not the case for their relative uncertainties, since (in contrast with $M_{X[\pi^-]}^2$) the quantity $M_{X[0]}^2$ is extremely close to zero.

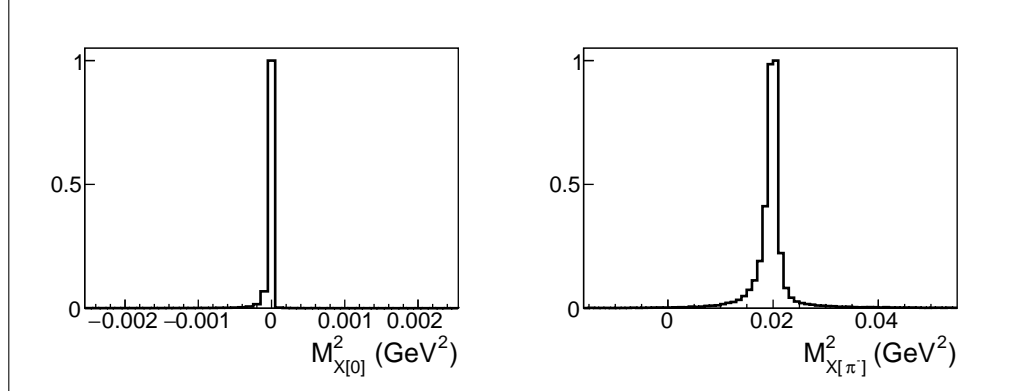


Figure A.4: Impact of the detector resolution on $M_{X[0]}^2$ (left) and $M_{X[\pi^-]}^2$ (right). The distribution of $M_{X[0]}^2$ is zoomed in on x to demonstrate the disturbances.

This impact of the detector resolution⁴ on $M_{X[0]}^2$ and $M_{X[\pi^-]}^2$ is demonstrated in Fig. A.4, where $M_{X[0]}^2$ is shown to be visually very narrow with slight disturbances, while $M_{X[\pi^-]}^2$ acquires perceptible smearing.

Final state interactions

Let's estimate the quantities $M_{X[0]}^2$ and $M_{X[\pi^-]}^2$ considering the change of the final hadron momenta as in the case of FSI. To simplify the estimation, let's assume the following: (i) for each event only one final state hadron is affected⁵, (ii) the type of the affected hadron is the same among all events in the sample, (iii) FSI are limited to the change of the momentum magnitude of the affected hadron as $p'_h = \varepsilon p_h$, and (iv) such momentum modification occurs in all events in the sample. Then

$$\begin{aligned} M_{X[0]}^2 &= [P_h^\mu - P_h'^\mu]^2 = [P_h^\mu]^2 + [P_h'^\mu]^2 - 2(P_h^\mu \cdot P_h'^\mu) = \\ &= 2m^2 - 2(EE' - (\vec{p} \cdot \vec{p}')) = \\ &= 2m^2 - 2(\sqrt{m^2 + p^2}\sqrt{m^2 + \varepsilon^2 p^2} - \varepsilon p^2), \end{aligned} \quad (\text{A.9})$$

where m and p are the mass and the momentum magnitude of the affected hadron.

The final expression in Eq. (A.9) is always less than zero regardless of both the value of ε and hadron kinematics, as the comparison below demonstrates.

⁴ To produce this plot, generated events were reconstructed via CLAS reconstruction software.

⁵ This imitates the interaction with the remaining neutron for the case of deuteron target.

$$\begin{aligned}
& 2m^2 - 2(\sqrt{m^2 + p^2}\sqrt{m^2 + \varepsilon^2 p^2} - \varepsilon p^2) \wedge 0 \\
& m^2 - \sqrt{m^2 + p^2}\sqrt{m^2 + \varepsilon^2 p^2} + \varepsilon p^2 \wedge 0 \\
& \quad m^2 + \varepsilon p^2 \wedge \sqrt{m^2 + p^2}\sqrt{m^2 + \varepsilon^2 p^2} \\
& \quad m^4 + \varepsilon^2 p^4 + 2m^2 \varepsilon p^2 \wedge m^4 + p^2 m^2 + m^2 \varepsilon^2 p^2 + \varepsilon^2 p^4 \\
& \quad 2m^2 \varepsilon p^2 \wedge p^2 m^2 + m^2 \varepsilon^2 p^2 \\
& \quad 0 \wedge p^2 m^2 (\varepsilon^2 - 2\varepsilon + 1) \\
& \quad 0 < p^2 m^2 (\varepsilon - 1)^2
\end{aligned} \tag{A.10}$$

2131 The quantity $M_{X[\pi^-]}^2$ in turn can be written as

$$\begin{aligned}
M_{X[\pi^-]}^2 &= [P_{\pi^-}^\mu + P_h^\mu - P'_h]{}^2 = \\
&= [P_{\pi^-}^\mu]^2 + [P_h^\mu - P'_h]{}^2 + 2P_{\pi^-}^\mu(P_h^\mu - P'_h) = \\
&= m_\pi^2 + M_{X[0]}^2 + 2\{E_{\pi^-}(E_h - E'_h) - (\vec{p}_{\pi^-} \cdot \vec{p}_h)(1 - \varepsilon)\},
\end{aligned} \tag{A.11}$$

2132 which can be either greater or smaller than zero depending on the value of ε and kinematics.

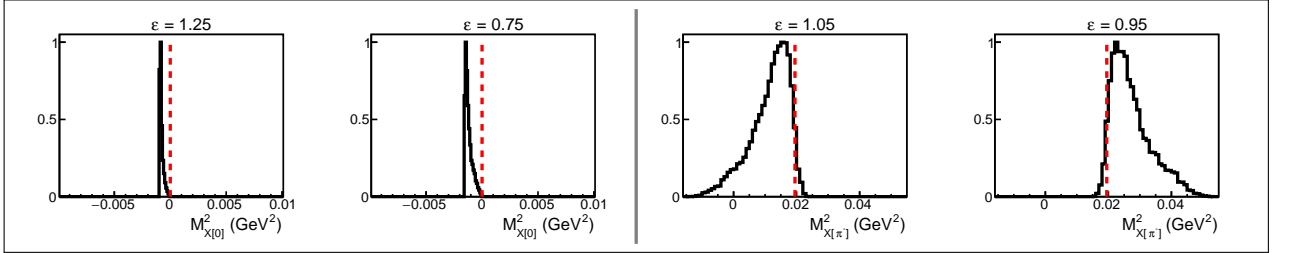


Figure A.5: Quantities $M_{X[0]}^2$ (left side) and $M_{X[\pi^-]}^2$ (right side) plotted assuming the change of the π^+ momentum magnitude as $p'_{\pi^+} = \varepsilon p_{\pi^+}$. Red dashed lines mark the position of zero and pion mass squared, respectively.

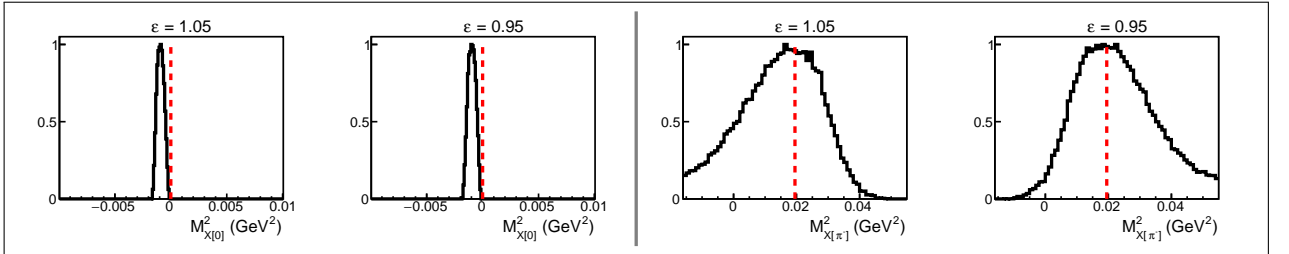


Figure A.6: Quantities $M_{X[0]}^2$ (left side) and $M_{X[\pi^-]}^2$ (right side) plotted assuming the change of the momentum magnitude of the final proton as $p'_{p'} = \varepsilon p_{p'}$. Red dashed lines mark the position of zero and pion mass squared, respectively.

2133 Figure A.5 shows the distributions of $M_{X[0]}^2$ and $M_{X[\pi^-]}^2$ for the case, when all positive
2134 pions change their momenta as $p'_{\pi^+} = \varepsilon p_{\pi^+}$. The quantity $M_{X[0]}^2$ (left side) is plotted for
2135 the sizable values of ε ($\varepsilon = 1.25$ and $\varepsilon = 0.75$), since it turns out to be rather insensitive

2136 to the change of pion momenta. The quantity $M_{X[\pi^-]}^2$ (right side), being in contrast rather
 2137 sensitive to the π^+ momentum change, is plotted for $\varepsilon = 1.05$ and $\varepsilon = 0.95$.

2138 Figure A.6 shows the distributions of $M_{X[0]}^2$ and $M_{X[\pi^-]}^2$ for the case, when all final protons
 2139 change their momenta as $p'_{p'} = \varepsilon p_{p'}$. Both $M_{X[0]}^2$ (left side) and $M_{X[\pi^-]}^2$ (right side) turn out
 2140 to be sensitive to the proton momentum change and therefore are plotted for $\varepsilon = 1.05$ and
 2141 $\varepsilon = 0.95$.

2142 **Appendix B: Lab to CMS transformation for the proton 2143 at rest case**

2144 Here the procedure of the Lab-to-CMS transformation for an electroproduction experiment
 2145 off the proton at rest (bottom left illustration in Fig. 3.2) is described [22]. In this case the
 2146 CMS axis orientation is different for each reaction event and is specified by the direction of
 2147 the scattered electron. The transformation from Lab to CMS includes the following steps¹:

2148 A. The xy -plane of the Lab system is rotated around the z -axis (given by the incom-
 2149 ing electron direction) to make the x -axis lying in the electron scattering plane (see
 2150 Fig. A.7). This rotation transforms the four-momentum as $P' = P \cdot R_1(\varphi_{e'})$, with

$$R_1(\varphi_{e'}) = \begin{pmatrix} \cos \varphi_{e'} & -\sin \varphi_{e'} & 0 & 0 \\ \sin \varphi_{e'} & \cos \varphi_{e'} & 0 & 0 \\ 0 & 0 & 1 & 0 \\ 0 & 0 & 0 & 1 \end{pmatrix}, \quad (\text{B.1})$$

2151 where $\varphi_{e'}$ is the azimuthal angle of the scattered electron.

2152 After this rotation $\varphi_{e'} = 0$, while $\varphi_{\gamma_v} = \pi$ with respect to the intermediate reference
 2153 frame.

2154 B. The Lab system is then rotated to align the z -axis with the virtual photon direction.
 2155 The four-momentum transformation for this rotation is given by $P'' = P' \cdot R_2(\theta_{\gamma_v})$,
 2156 with

$$R_2(\theta_{\gamma_v}) = \begin{pmatrix} \cos \theta_{\gamma_v} & 0 & -\sin \theta_{\gamma_v} & 0 \\ 0 & 1 & 0 & 0 \\ \sin \theta_{\gamma_v} & 0 & \cos \theta_{\gamma_v} & 0 \\ 0 & 0 & 0 & 1 \end{pmatrix}, \quad (\text{B.2})$$

¹ In all derivations the energy is assumed to be the last component of the four-momentum and the four-momentum to be a row vector.

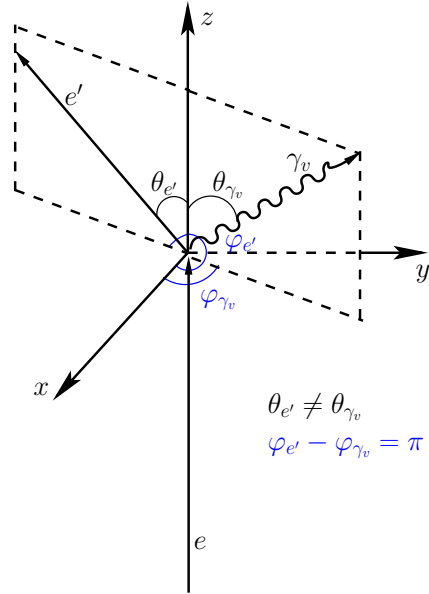


Figure A.7: Virtual photon and scattered electron angles θ and φ in the Lab frame for the proton at rest experiment.

2157 where θ_{γ_v} is the polar angle of the virtual photon.²

2158 C. Finally, a boost into the CM frame of the *virtual photon – initial proton* system is
2159 performed. It is given by the formula $P''' = P'' \cdot R_3(\beta)$, with

$$R_3(\beta) = \begin{pmatrix} 1 & 0 & 0 & 0 \\ 0 & 1 & 0 & 0 \\ 0 & 0 & \gamma & -\gamma\beta \\ 0 & 0 & -\gamma\beta & \gamma \end{pmatrix}, \quad \beta = \frac{|\vec{q}|}{E_\gamma + m_{proton}} = \frac{\sqrt{E_\gamma^2 + Q^2}}{E_\gamma + m_{proton}}, \quad \gamma = \frac{1}{\sqrt{1 - \beta^2}}, \quad (\text{B.3})$$

2160 where $|\vec{q}|$ is the magnitude of the three-vector of the virtual photon and β the mag-
2161 nitude and z -component of the three-vector $\vec{\beta} = (0, 0, \beta)$.³

² Using embedded ROOT functions, both rotations can be coded using the unit vectors TVector3 $uz = P4_gamma.Vect().Unit()$ and TVector3 $ux = (P4_EL.Vect().Cross(P4_ELP.Vect())).Unit()$, where P4_gamma, P4_EL, and P4_ELP are the four-momenta of the virtual photon, initial and final electrons, respectively. The axis vector ux needs to be rotated according to $ux.Rotate(3.*M_PI/2,uz)$. Finally the rotation is defined as $rot.SetZAxis(uz,ux).Invert()$ and needs to be applied to the four-momentum (P4) of each particle: $P4.Transform(rot)$.

³ Note: if you use the ROOT function .Boost, you should change the sign of the z -component of β -vector as $.Boost(0,0,-\beta)$.

²¹⁶² **Appendix C: The reaction phase-space**

²¹⁶³ The phase-space of the reaction $ep \rightarrow e'p'\pi^+\pi^-$ is determined by seven kinematic variables,
²¹⁶⁴ i.e. W , Q^2 , $M_{h_1h_2}$, $M_{h_2h_3}$, θ_{h_1} , φ_{h_1} , and α_{h_1} (see Sect. 3.3 for details). The kinematic coverage
²¹⁶⁵ for various variables has the following specificities.

- ²¹⁶⁶ • In the W and Q^2 variables it depends on the electron beam energy and experimental
²¹⁶⁷ conditions and is fixed for a particular experiment.
- ²¹⁶⁸ • The angular variables θ_{h_1} , φ_{h_1} , and α_{h_1} vary in the fixed limits of $[0, \pi]$, $[0, 2\pi]$, and
²¹⁶⁹ $[0, 2\pi]$, respectively.
- ²¹⁷⁰ • In the invariant masses $M_{h_1h_2}$ and $M_{h_2h_3}$ the coverage depends on W and broadens as
²¹⁷¹ W grows.

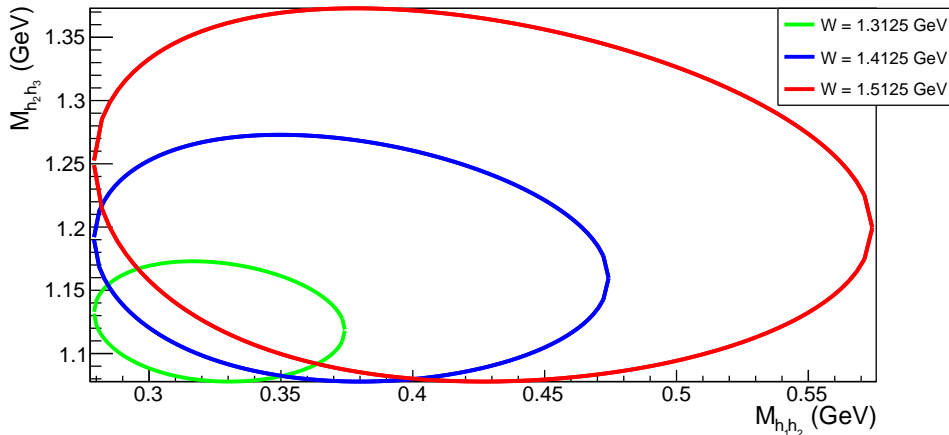


Figure A.8: Boundary of the $M_{h_2h_3}$ versus $M_{h_1h_2}$ distribution for several distinct values of W specified in the plot.

²¹⁷² The shape of the reaction phase-space in the invariant masses is determined by the
²¹⁷³ condition $B(M_{h_1h_2}^2, M_{h_2h_3}^2, W^2, m_{h_2}^2, m_{h_1}^2, m_{h_3}^2) = 0$, where $B(x, y, z, u, v, w)$ is the Byckling
²¹⁷⁴ function [38] given by

$$\begin{aligned} B(x, y, z, u, v, w) = & x^2y + xy^2 + z^2u + zu^2 + v^2w + vw^2 + \\ & xzw + xuv + yzv + yuw - xy(z + u + v + w) - \\ & zu(x + y + v + w) - vw(x + y + z + u). \end{aligned} \quad (\text{C.1})$$

²¹⁷⁵ Figure A.8 shows the boundary of the $M_{h_2h_3}$ versus $M_{h_1h_2}$ distribution for several values
²¹⁷⁶ of W specified in the plot and visually demonstrates the effect of the phase-space broadening
²¹⁷⁷ with the increase of W .

2178 Appendix D: Uncertainties for indirect measurements

2179 Some useful examples of the error propagation for indirect measurements are described here.
 2180 In these examples one assumes that $a > 0$, $b > 0$, and $c > 0$.

- 2181 • If independent variables x_1 and x_2 have absolute uncertainties Δx_1 and Δx_2 , respectively,
 2182 then the absolute uncertainty of the variable $y = c\left(\frac{x_1}{a} - \frac{x_2}{b}\right)$ is

$$\Delta y = c \sqrt{\left(\frac{\Delta x_1}{a}\right)^2 + \left(\frac{\Delta x_2}{b}\right)^2}. \quad (\text{D.1})$$

- 2183 • If the variable x has an absolute uncertainty Δx , then the absolute uncertainty of the
 2184 variable $y = \frac{a}{x}$ is

$$\Delta y = \frac{a}{x^2} \cdot \Delta x = y \cdot \frac{\Delta x}{x}. \quad (\text{D.2})$$

- 2185 • If the variable x has an absolute uncertainty Δx , then the absolute uncertainty of the
 2186 variable $y = \frac{ax+b}{c}$ is

$$\Delta y = \frac{a \cdot \Delta x}{c}. \quad (\text{D.3})$$

- 2187 • If there is a set of measurements x_1, x_2, \dots, x_n with the arithmetic mean \bar{x} , then the
 2188 absolute standard error of the arithmetic mean is

$$\Delta \bar{x} = \sqrt{\frac{\sum_{i=1}^n (x_i - \bar{x})^2}{n \cdot (n - 1)}}. \quad (\text{D.4})$$

2189 Appendix E: Analysis procedure and code availability

2190 The following files are used as an input for the analysis.

- 2191 • 1989 files with full target runs stored at
2192 /mss/clas/e1e/production/pass1/h10/
- 2193 • 14 files with empty target runs stored at
2194 /mss/clas/e1e/production/pass1/h10emptarg_d/
- 2195 • 165625 files with the Monte Carlo simulation. They are stored at
2196 /mss/clas/e1e/production/simulation_2pi/sim_skorodum_Aug2016/nt10*

2197 All these files contain “h10” ROOT ntuples. They were converted from HBOOK outputs
2198 of nt10maker (which is a part of CLAS software) using the “h2root” utility.

2199 The scripts used for performing the Monte Carlo simulation, which incorporate the in-
2200 formation on the simulation/reconstruction parameters used in this analysis, can be found
2201 here https://github.com/skorodumina/CLAS6_sim_rec_sequence.

2202 To speed up the analysis process, the specified above files are converted to reduced “t21”
2203 ROOT ntuples, which contain only those variables that are used in the analysis (the conver-
2204 sion program is available at https://github.com/skorodumina/converter_clas6.git).
2205 After the conversion one is left with

- 2206 • 284 files with full target runs stored at
2207 /mss/home/skorodum/e1e/data_2pi_conv_2July2018/
- 2208 • 1 file with empty target runs, i.e.
2209 /mss/home/skorodum/e1e/out_conv_empty_2pi_2July2018.root
- 2210 • 33125 files with the simulation. They are stored at /mss/clas/e1e/production/
2211 simulation_2pi/sim_skorodum_Aug2016/converted_July2018_cc_ok/

2212 For further calculations the double-pion analysis program is used (it is available at
2213 https://github.com/skorodumina/two_pi_analysis_code.git). This program outputs
2214 the root file with multi-dimensional histograms.

2215 For the experimental data this process is rather simple:

- 2216 • 284 full target files are fed to the double-pion analysis program at once.
- 2217 • 1 empty target file is fed to the same program.
- 2218 • Both outputs for full and empty target runs are processed with the corresponding
2219 script to combine the topologies. This results in the output file *out_data.root*.

2220 For the Monte Carlo simulation the process is more complicated.

- 2221 • 33125 files with the simulation are processed on batch farms with the double-pion
2222 analysis program to produce 1325 output files with multi-dimensional histograms.
- 2223 • These 1325 files are then processed with the corresponding scripts. As a result one has
2224 three sets of 53 files each. Files within each set contain multi-dimensional histograms
2225 filled with σ , σ^2 , or 1.

- 2226 ● Then 53 files within each set are combined by the ROOT utility “hadd” into three
2227 resulting files.
2228 ● The three files are processed with the corresponding scripts (which either combine
2229 topologies and/or calculate efficiency) with the three resulting outputs.
2230 ● These three outputs are combined (with “hadd”) to form the output *out_sim.root*.

2231 Then the script that performs the cross section calculation is used. This script is located
2232 at https://github.com/skorodumina/twopi_crsect_calc.git together with the afore-
2233 mentioned scripts. The program for unfolding the effects of the target motion is also located
2234 there (it is needed to produce the root file with the Fermi correction factor).

2235 The script for the cross section calculation uses as inputs the files *out_data.root*,
2236 *out_sim.root* and the file with the Fermi correction factor (all of them are introduced above).
2237 The script processes the multi-dimensional histograms from the input files and performs the
2238 cross section calculation that includes the empty target subtraction, normalization to the
2239 luminosity and the virtual photon flux, filling the empty cells, radiative corrections, and
2240 unfolding the effects of the initial proton motion. Beside this, the script also calculates
2241 the cross section uncertainty $\delta_{\text{stat,mod}}^{\text{tot}}$. The single-differential and integral cross sections are
2242 finally output to the root file.

2243 Once the cross section is extracted, it is then subject to several final manipula-
2244 tions (i.e. binning corrections, averaging, and estimating the systematic uncertainties),
2245 which are performed by means of the corresponding scripts. They are also available at
2246 https://github.com/skorodumina/twopi_crsect_calc.git.

2247 The majority of codes introduced here are provided with their own README files, which
2248 are intended to clarify other details of the code performance.

2249 Appendix F: Measured single-differential cross sections

2250 This Appendix contains the full set of single-differential cross sections measured in the current
2251 analysis. The cross sections are reported with the uncertainty $\delta_{\text{stat,mod}}^{\text{tot}}$ shown by error
2252 bars (see Sect. 7.2.2). The central point of the corresponding W and Q^2 bin is specified
2253 in each figure together with the value of the relative integral systematic uncertainty (see
2254 Sect. 7.3) that can be propagated as a global factor to the corresponding single-differential
2255 cross sections.

2256 Note that the invariant mass distributions are shown in the range from M_{lower} to M_{upper} ,
2257 both given by Eq. (3.4.1) with the latter calculated using the central value of the W bin.
2258 One, therefore, should take into consideration that the cross section in invariant mass is
2259 equal to zero on both sides of the range. Also note that the invariant mass distributions
2260 contain one bin less than specified in Tab. 3.1, since the cross section in the last mass bins is
2261 not reported. This happens due to the special arrangement of mass bins used in the analysis,
2262 which forces the last bin to be situated out of the specified range (see Sect. 3.4 for details).

2263 It is also noteworthy that α angular distributions of the double-pion cross sections should
2264 be symmetrical with respect to $\alpha = 180^\circ$, when integrated over φ . However, the experimen-
2265 tally measured α distributions acquire some asymmetry. To judge more quantitatively the
2266 asymmetry degree, the average asymmetry factor was estimated for each extracted α distri-
2267 bution as

$$\text{asym} = \frac{1}{\text{int}[n/2]} \sum_{i=1}^{\text{int}[n/2]} \left| 1 - \frac{2\sigma_i}{\sigma_i + \sigma_{n-i}} \right|, \quad (\text{F.1})$$

2268 where n is the number of bins in the distribution and σ_i the cross section value in the bin i .

2269 The average asymmetry factor estimated by Eq. (F.1) is specified in the plots for each
2270 α distribution to facilitate visual judgement of the distribution's shape and its inherent
2271 systematic inaccuracy.

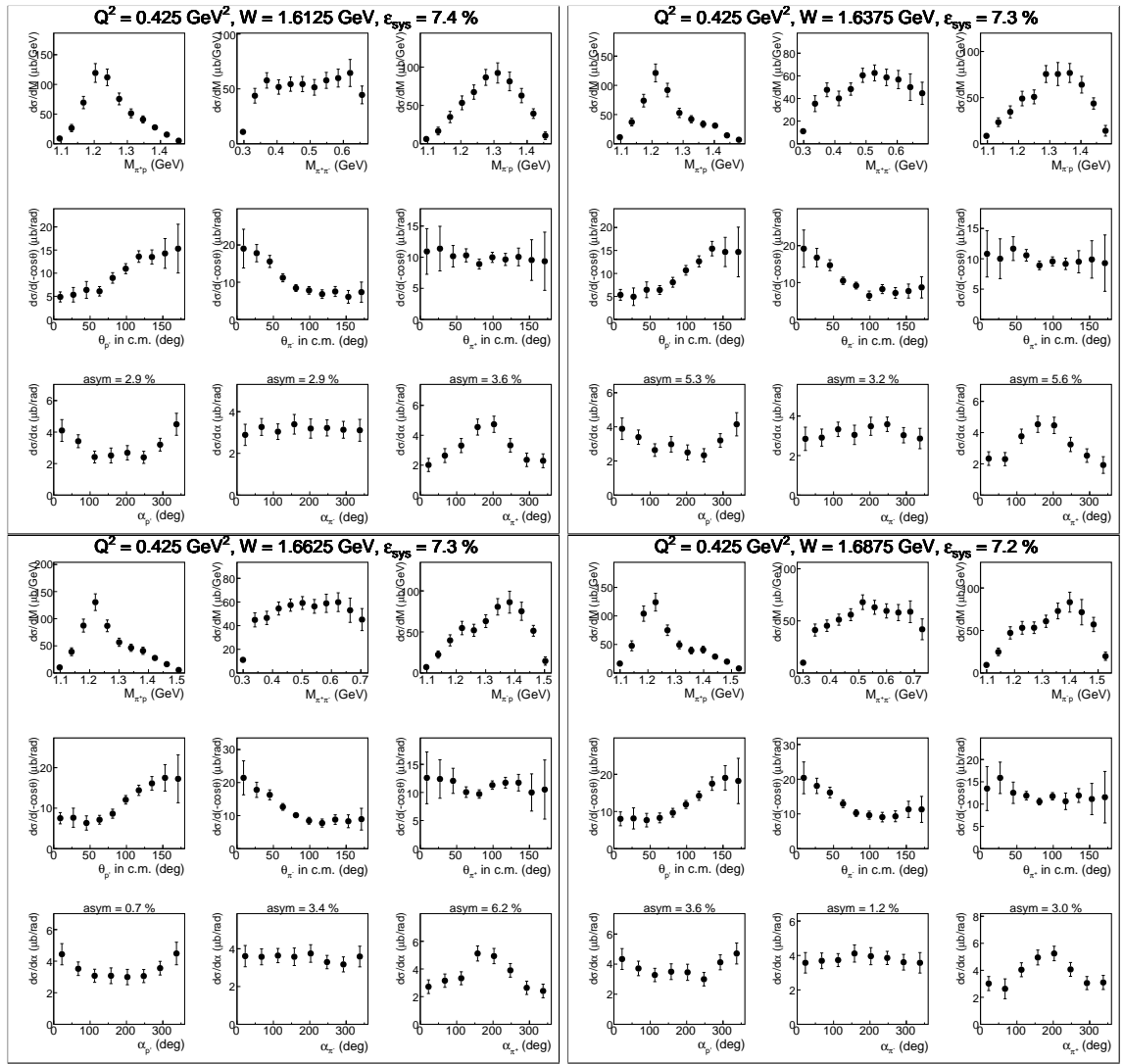


Figure A.9:

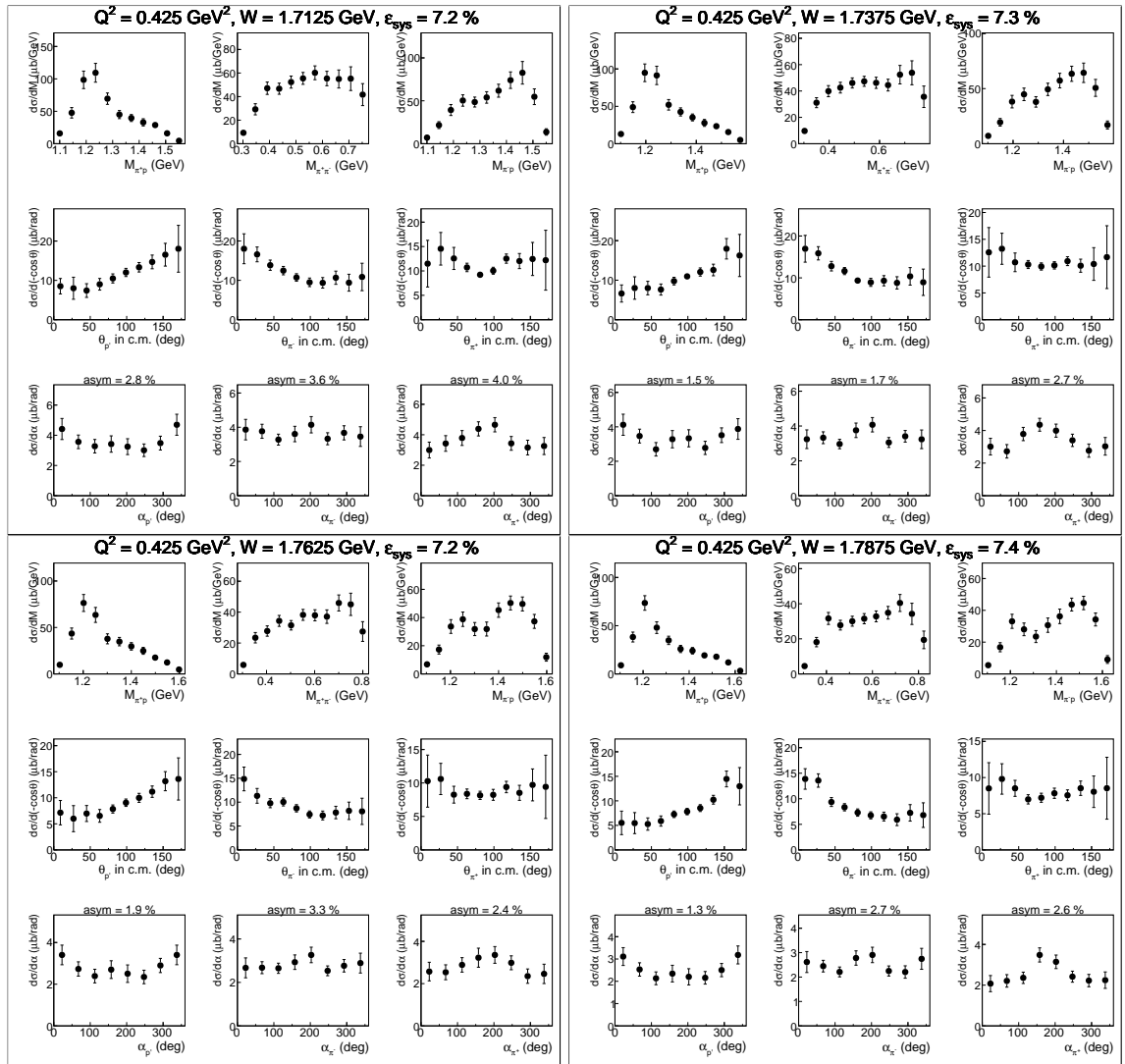


Figure A.10:

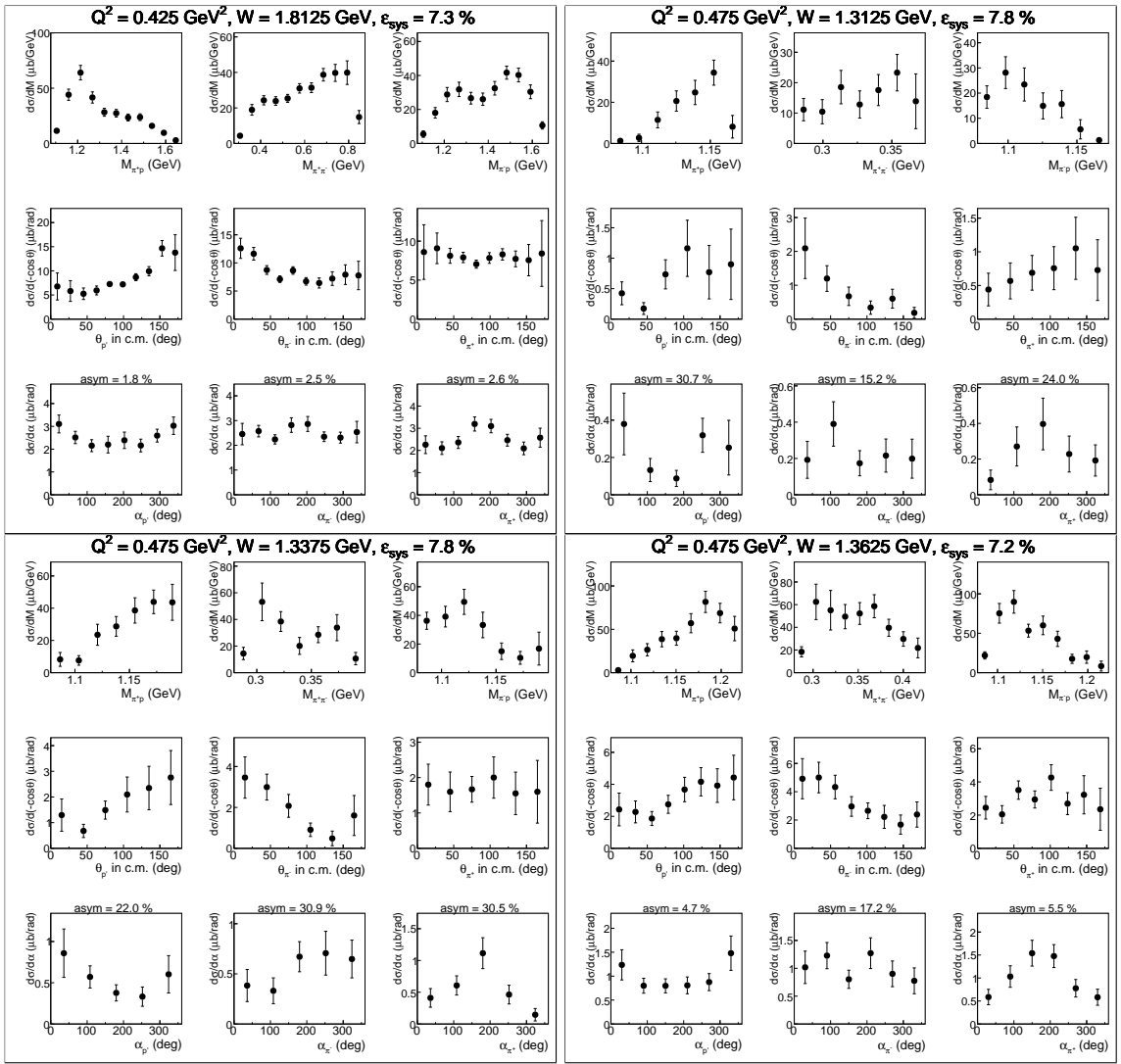


Figure A.11:

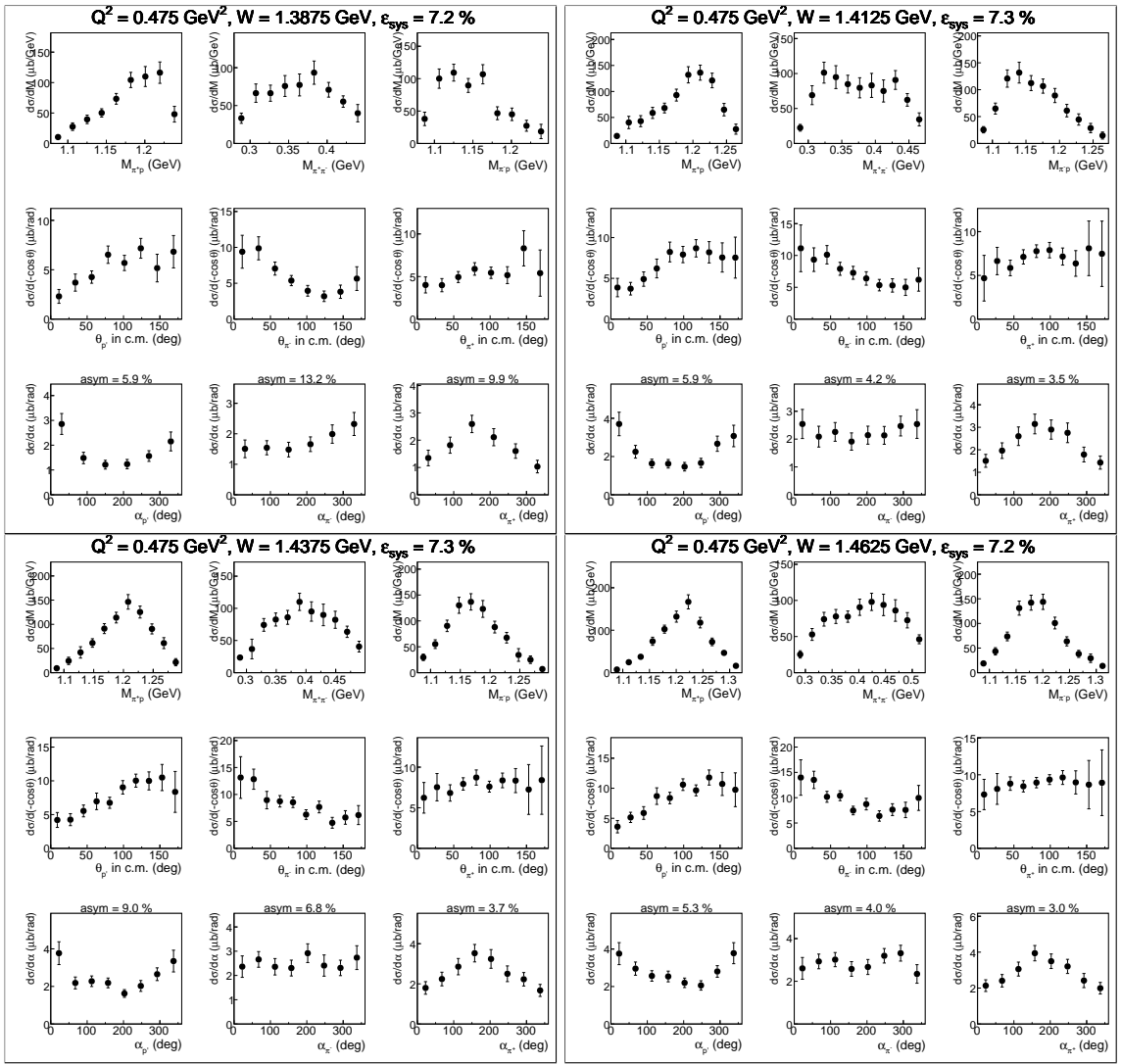


Figure A.12:

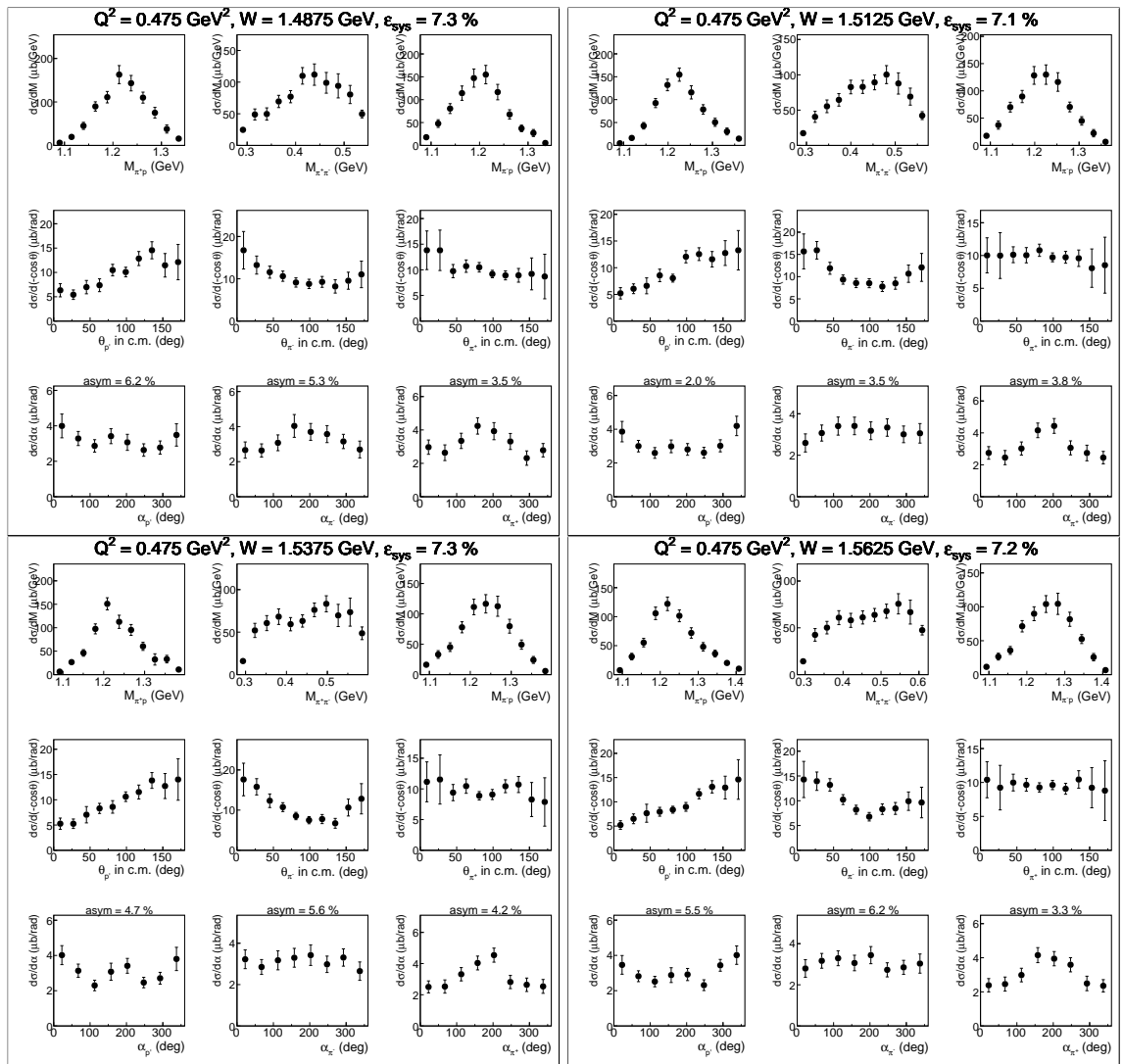


Figure A.13:

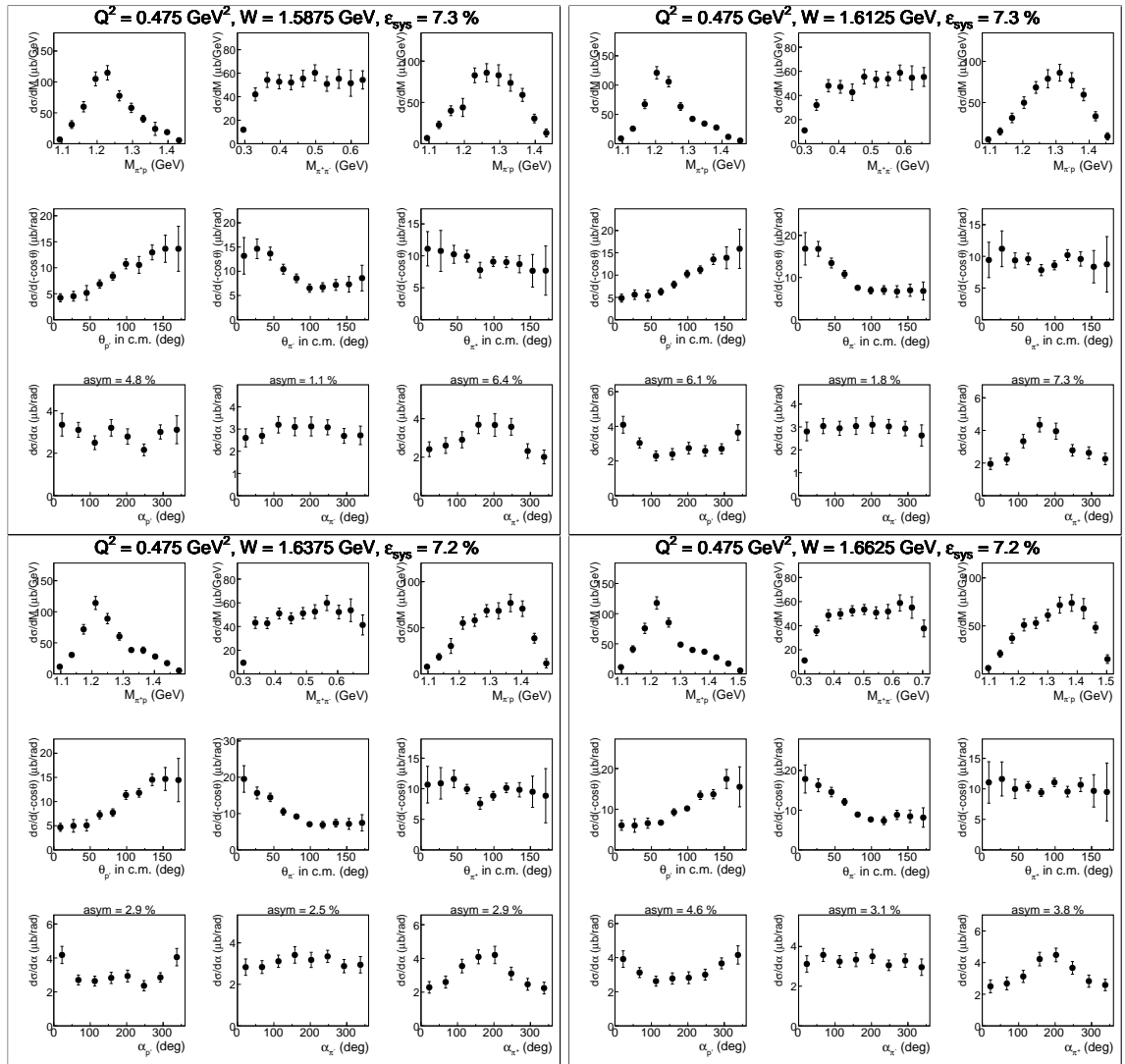


Figure A.14:

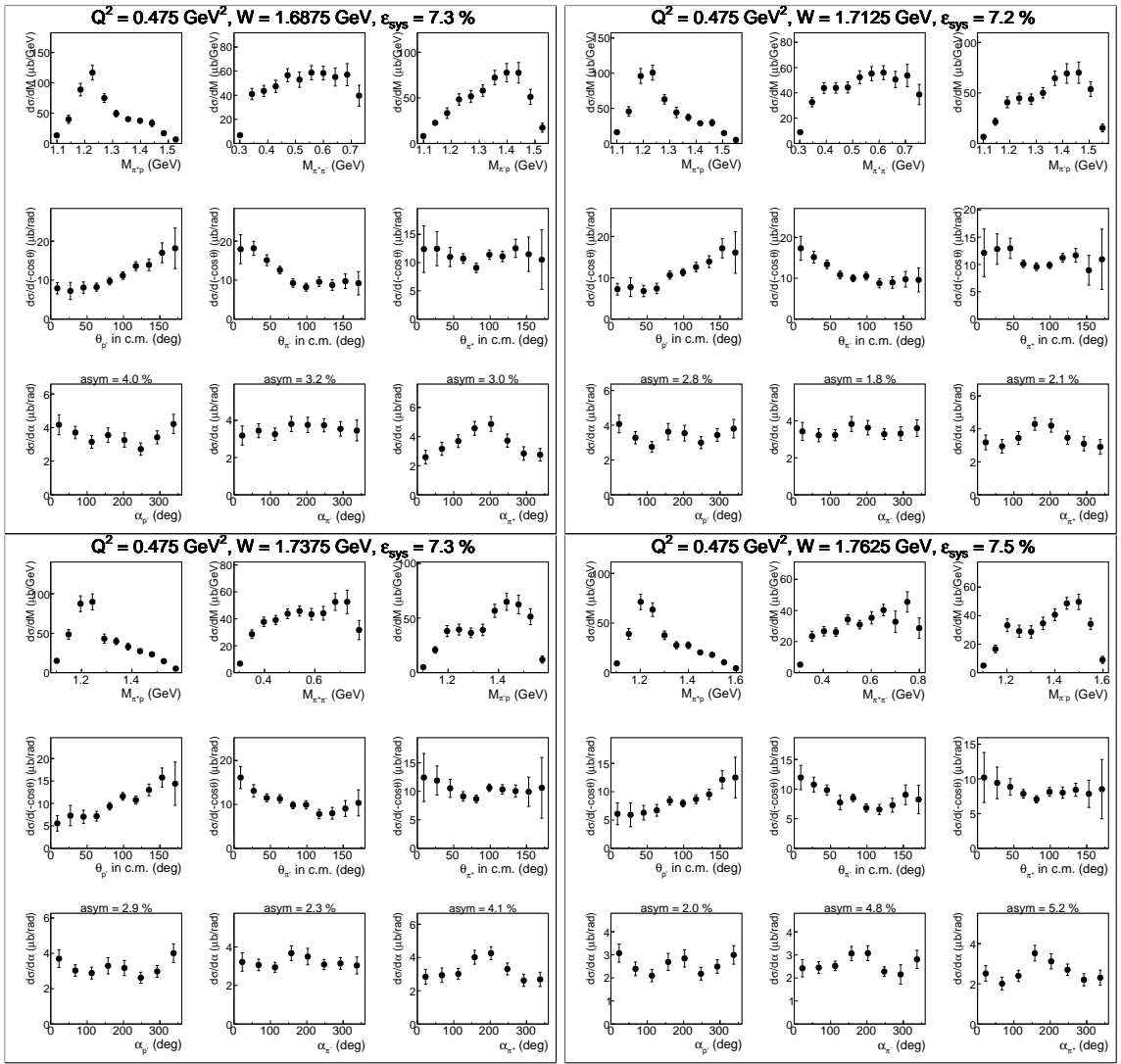


Figure A.15:

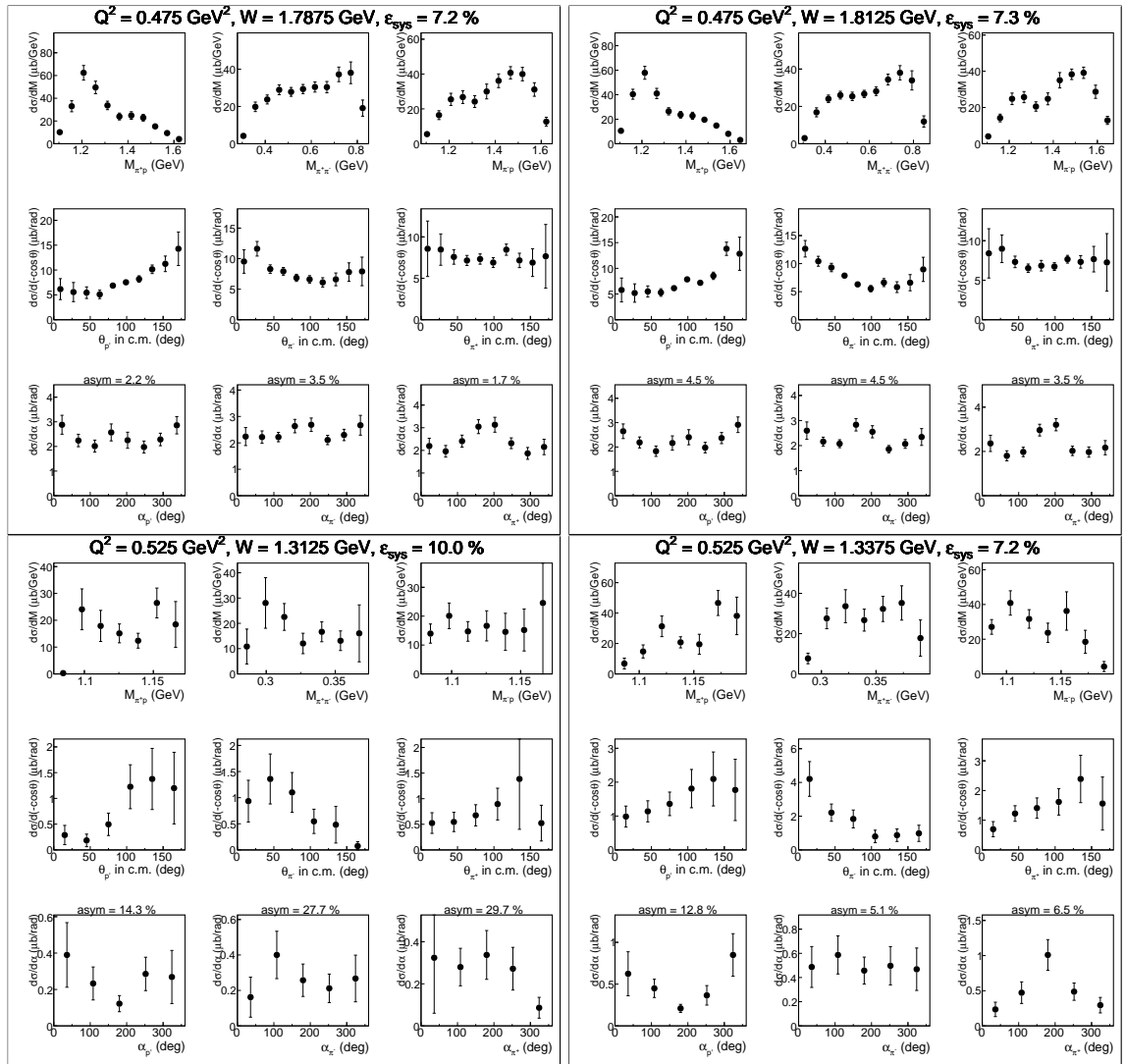


Figure A.16:

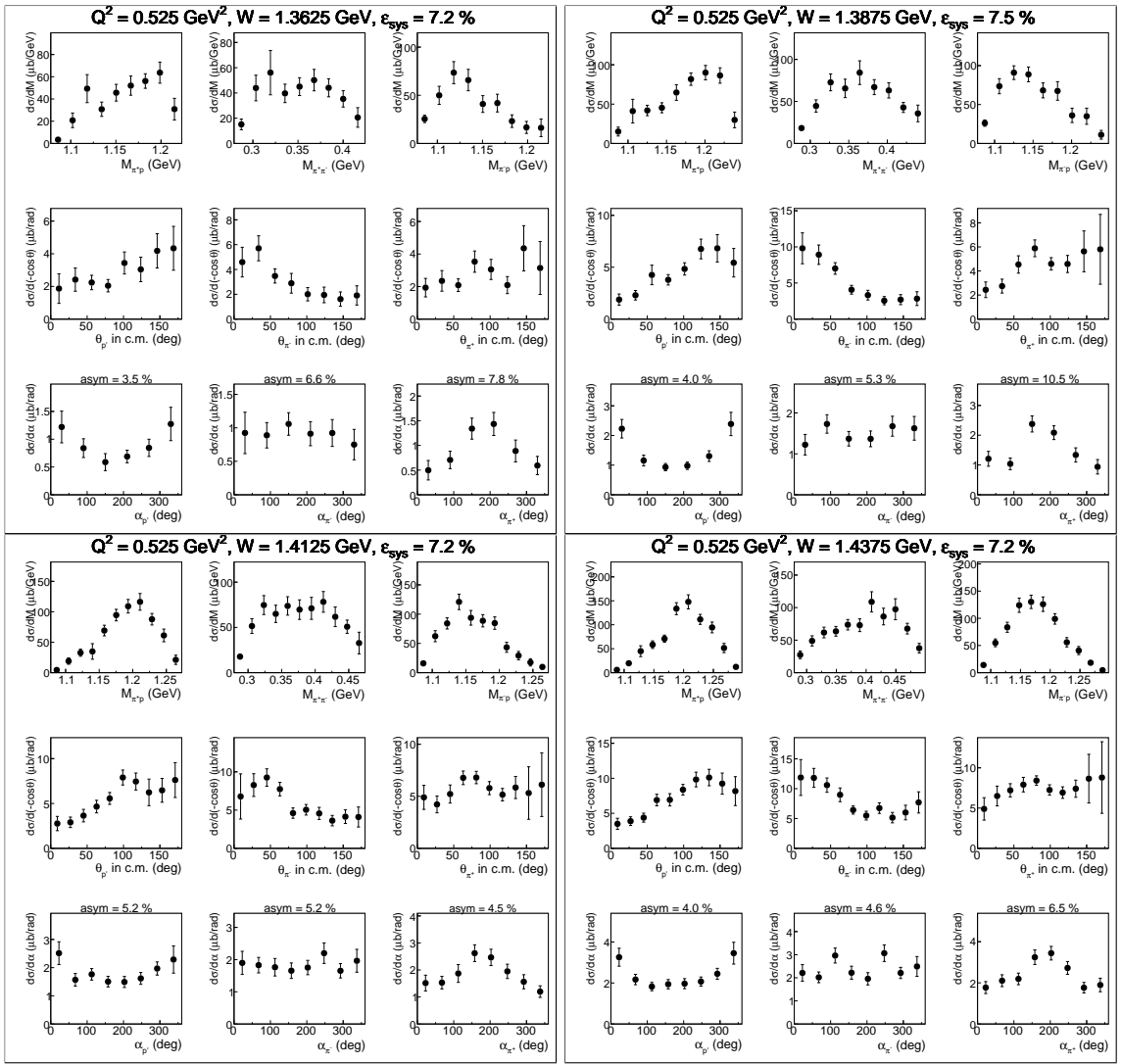


Figure A.17:

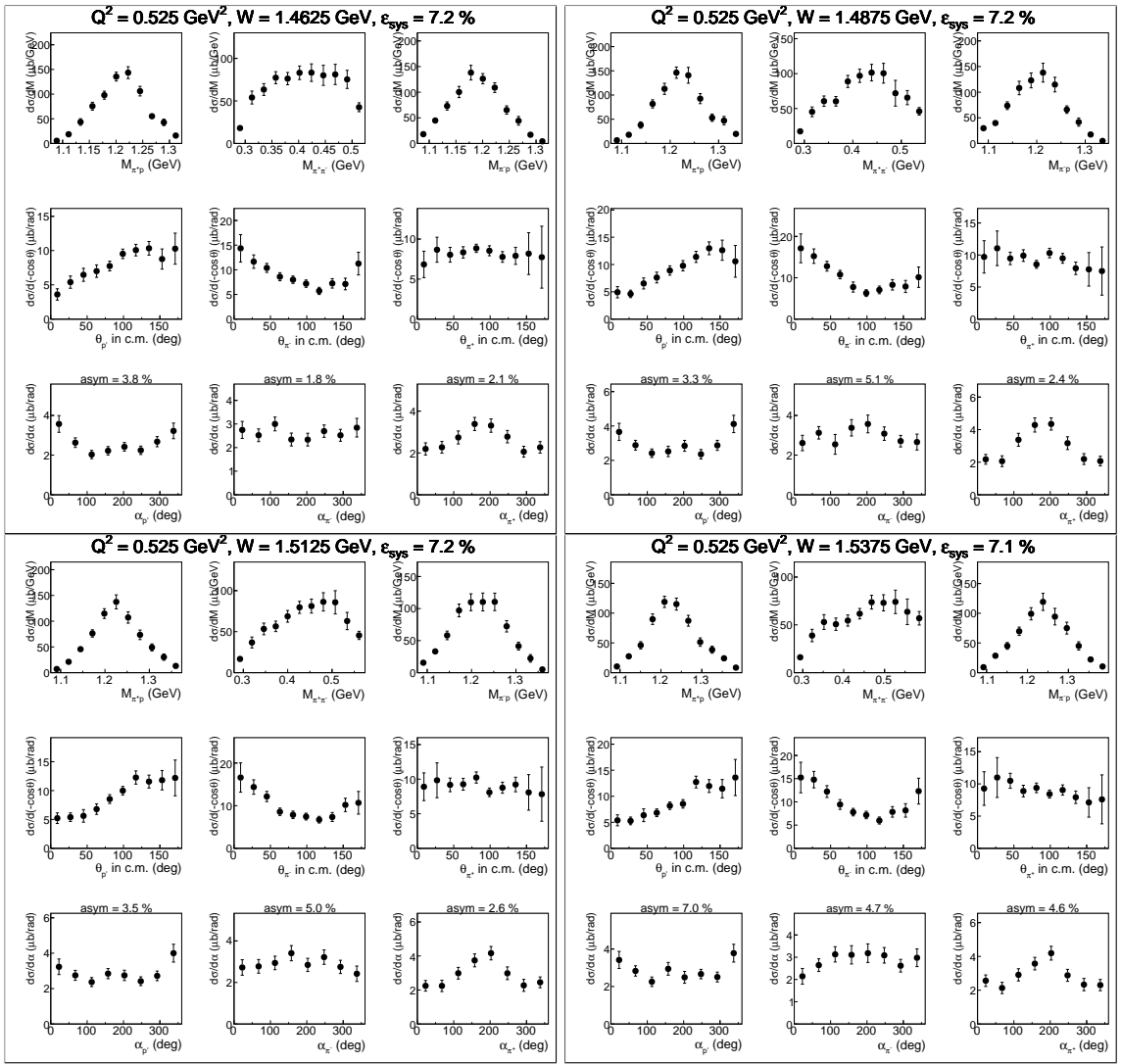


Figure A.18:

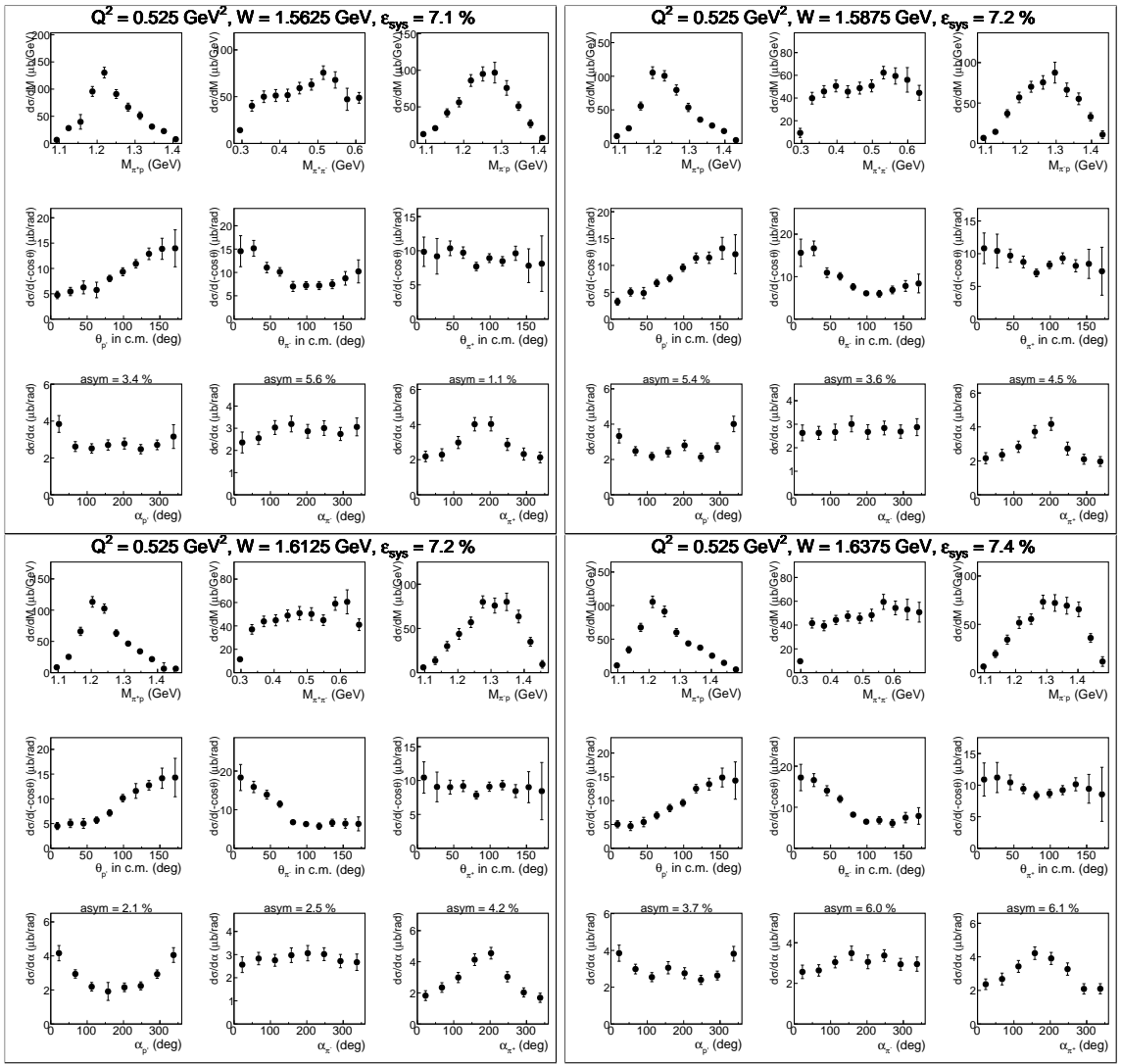


Figure A.19:

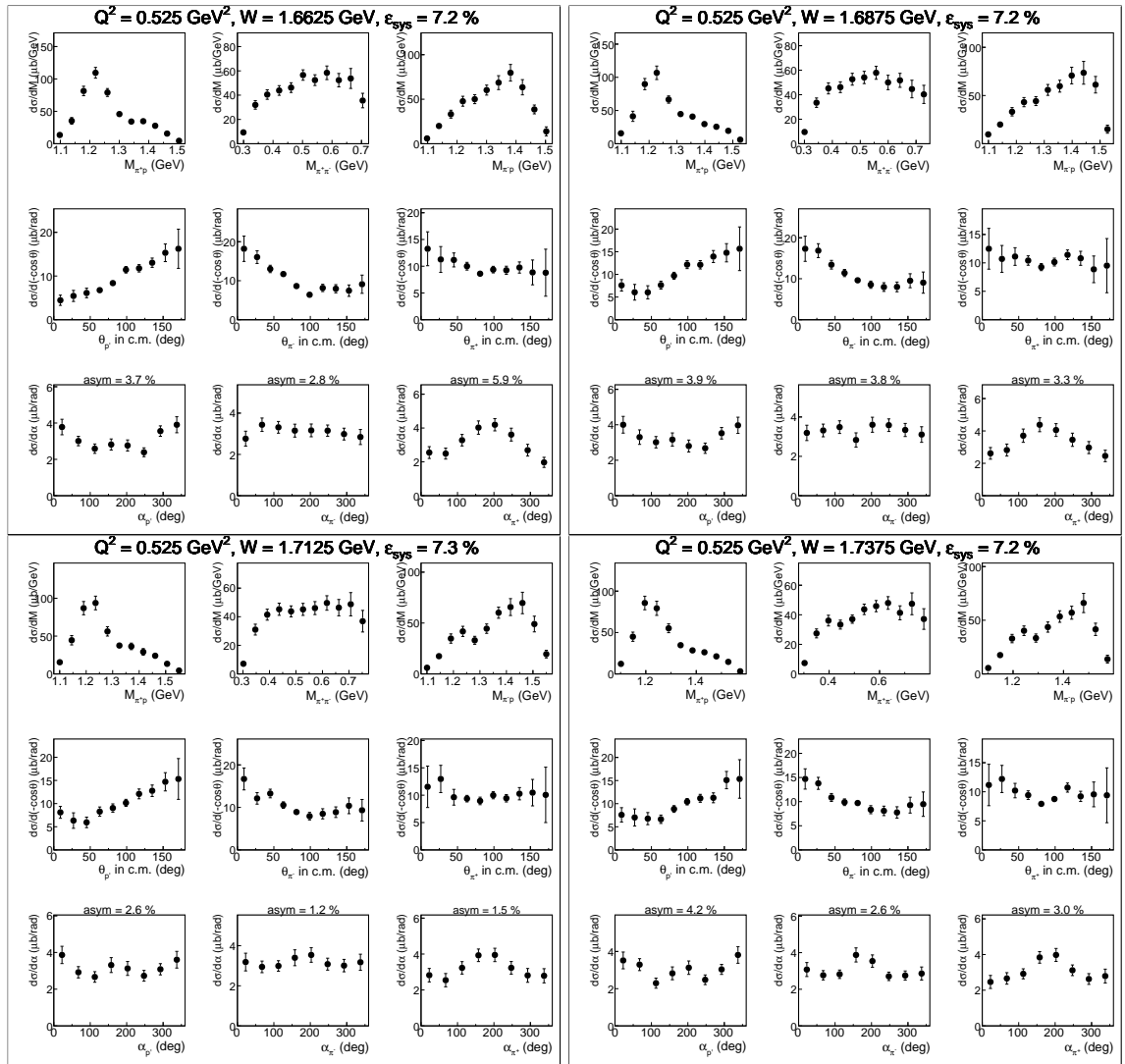


Figure A.20:

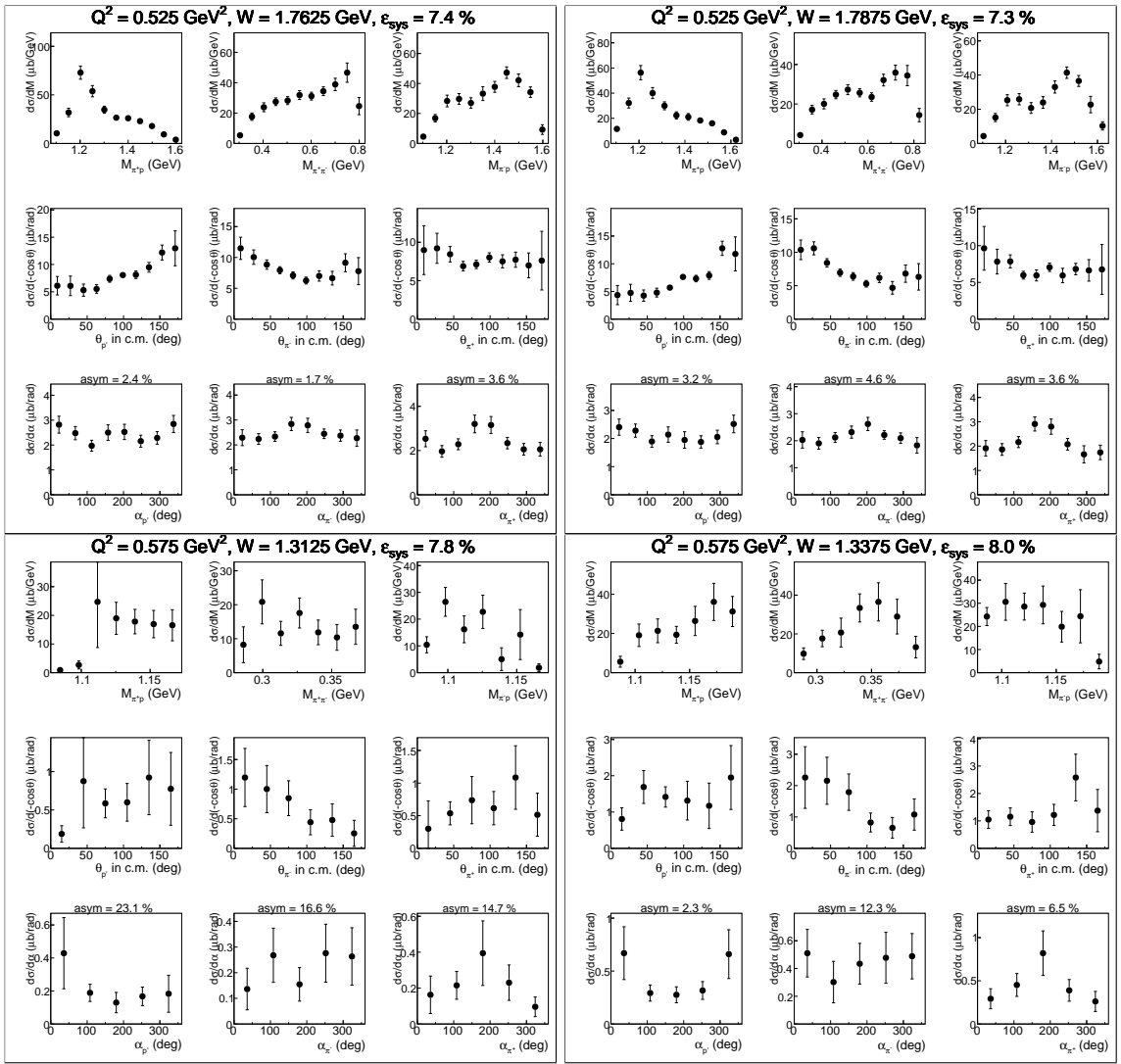


Figure A.21:

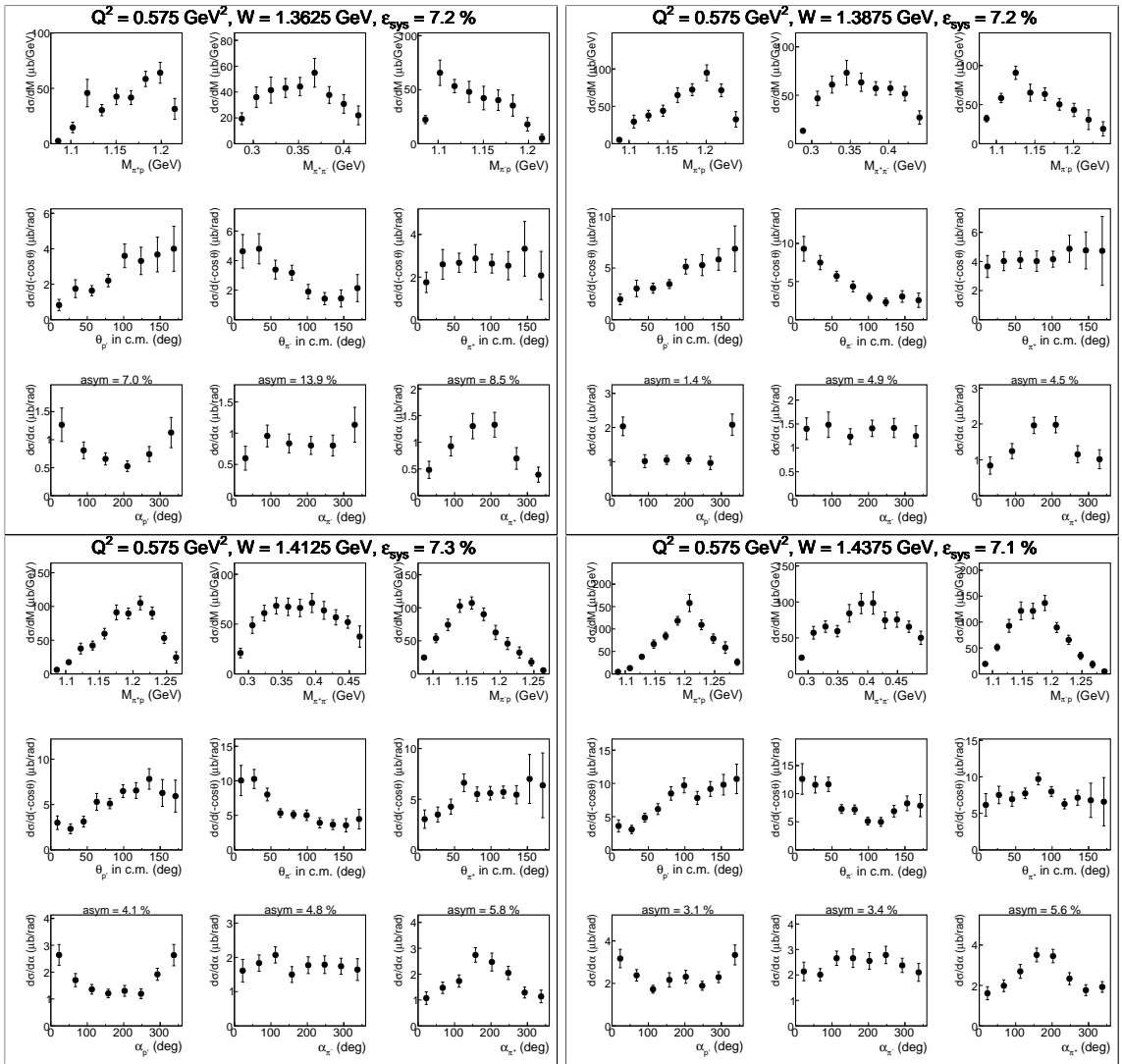


Figure A.22:

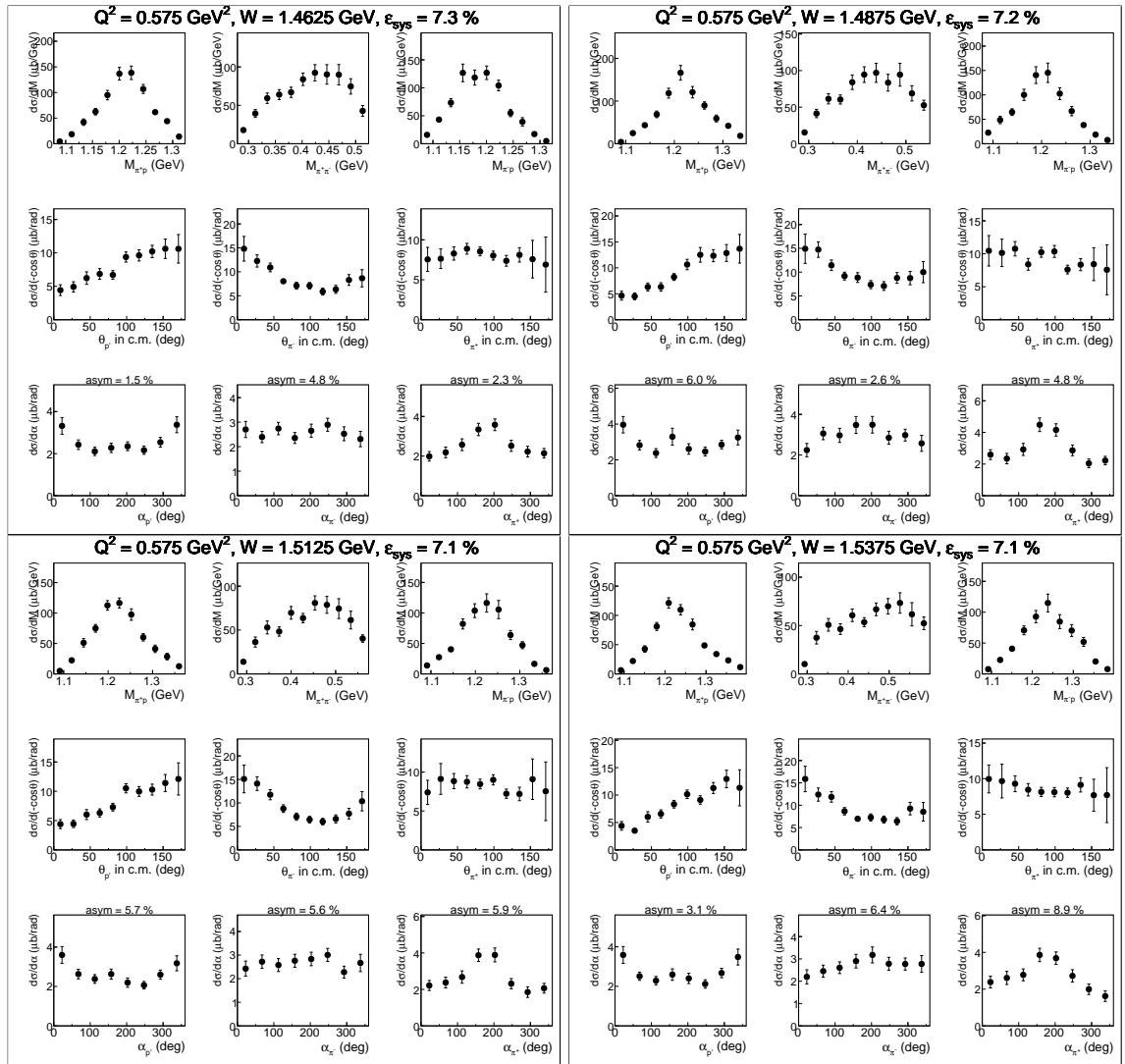


Figure A.23:

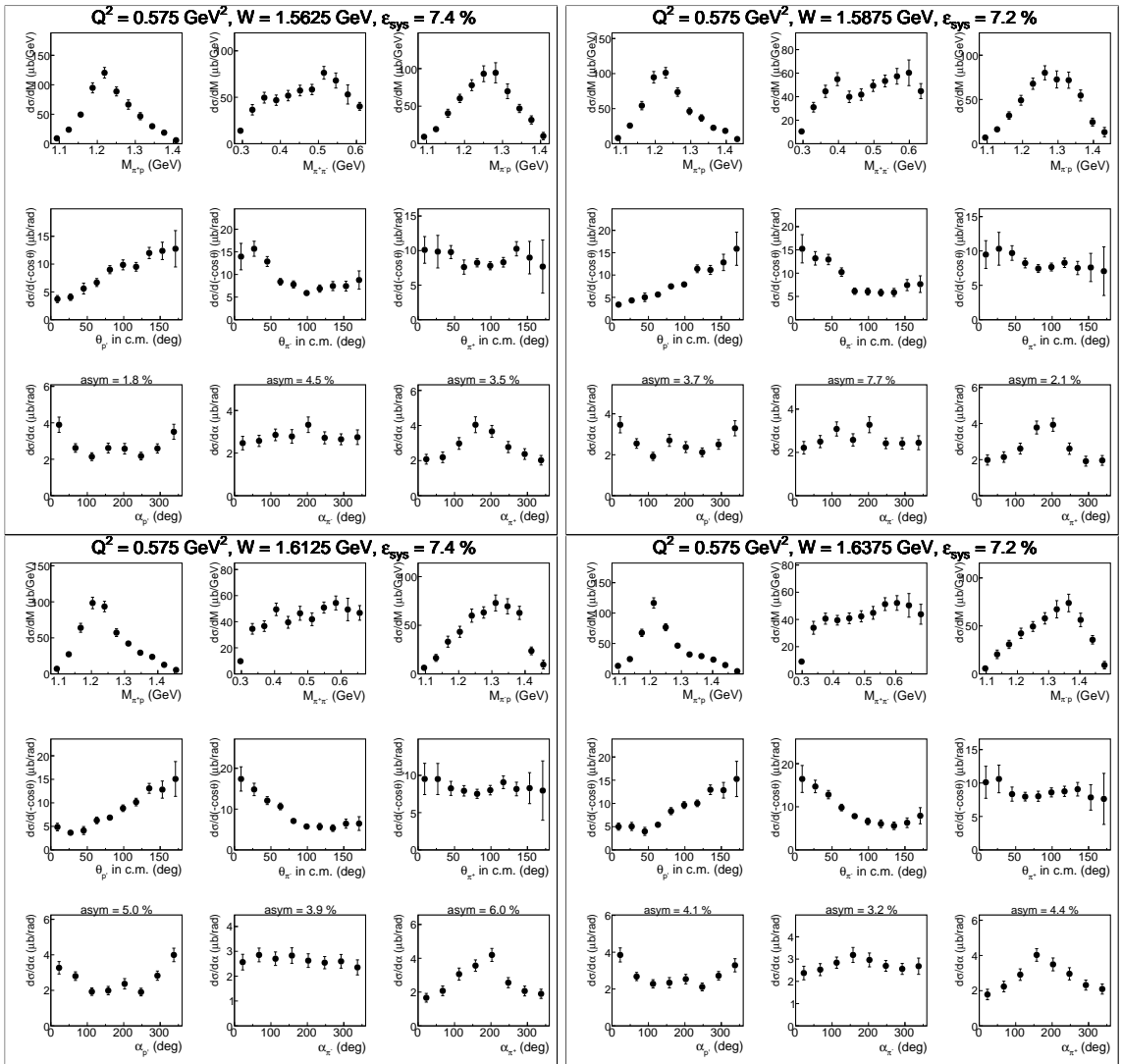


Figure A.24:

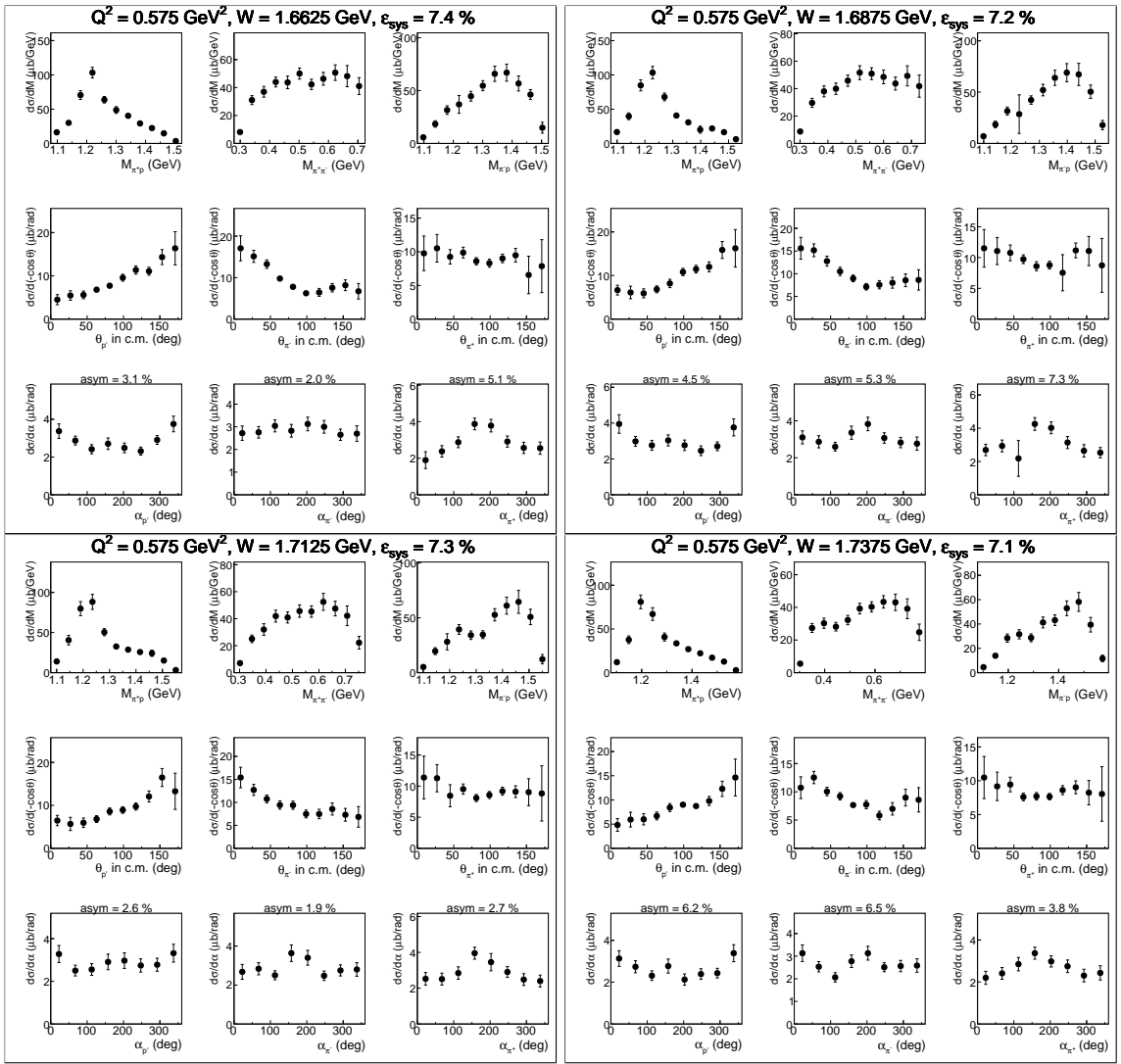


Figure A.25:

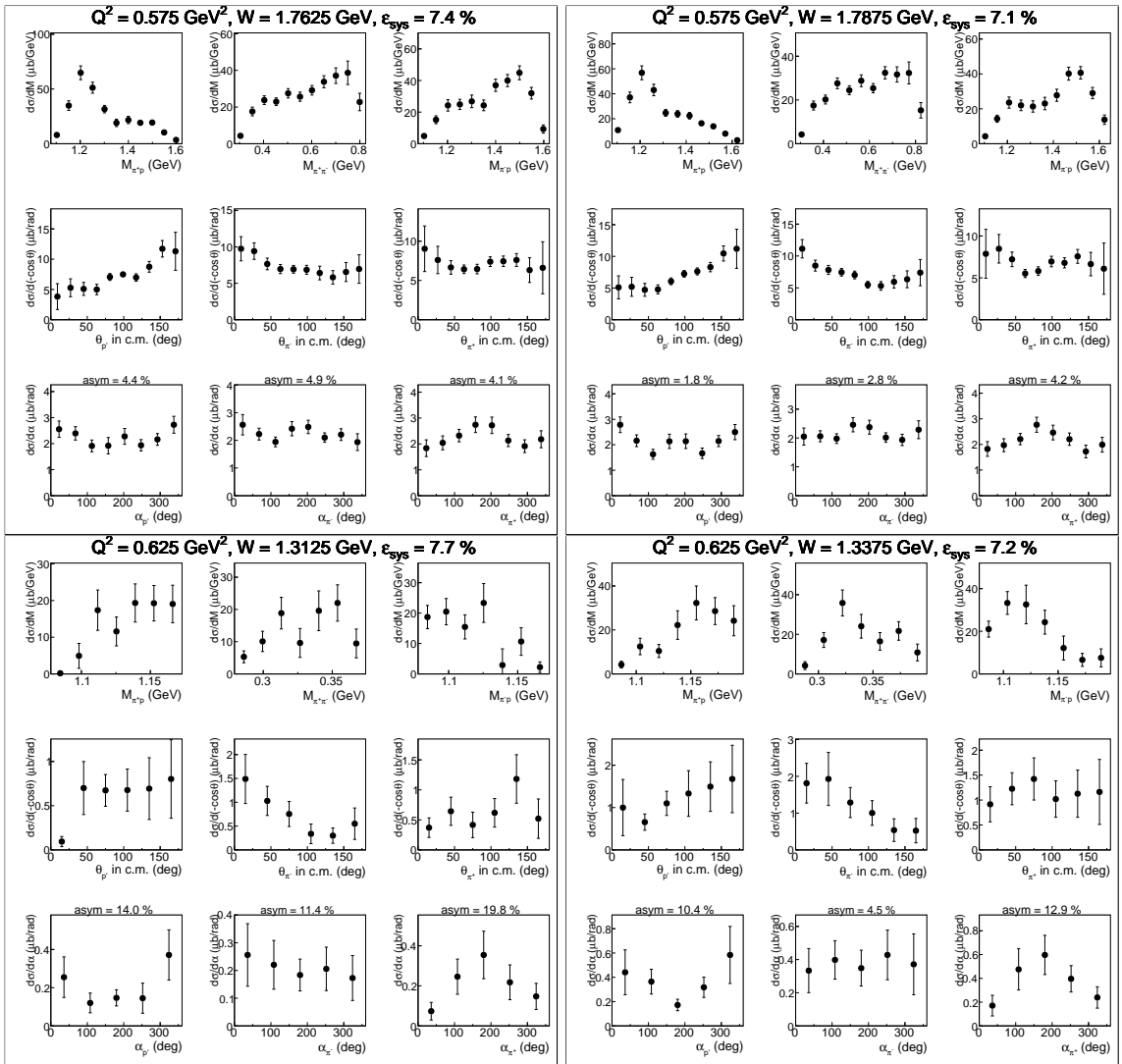


Figure A.26:

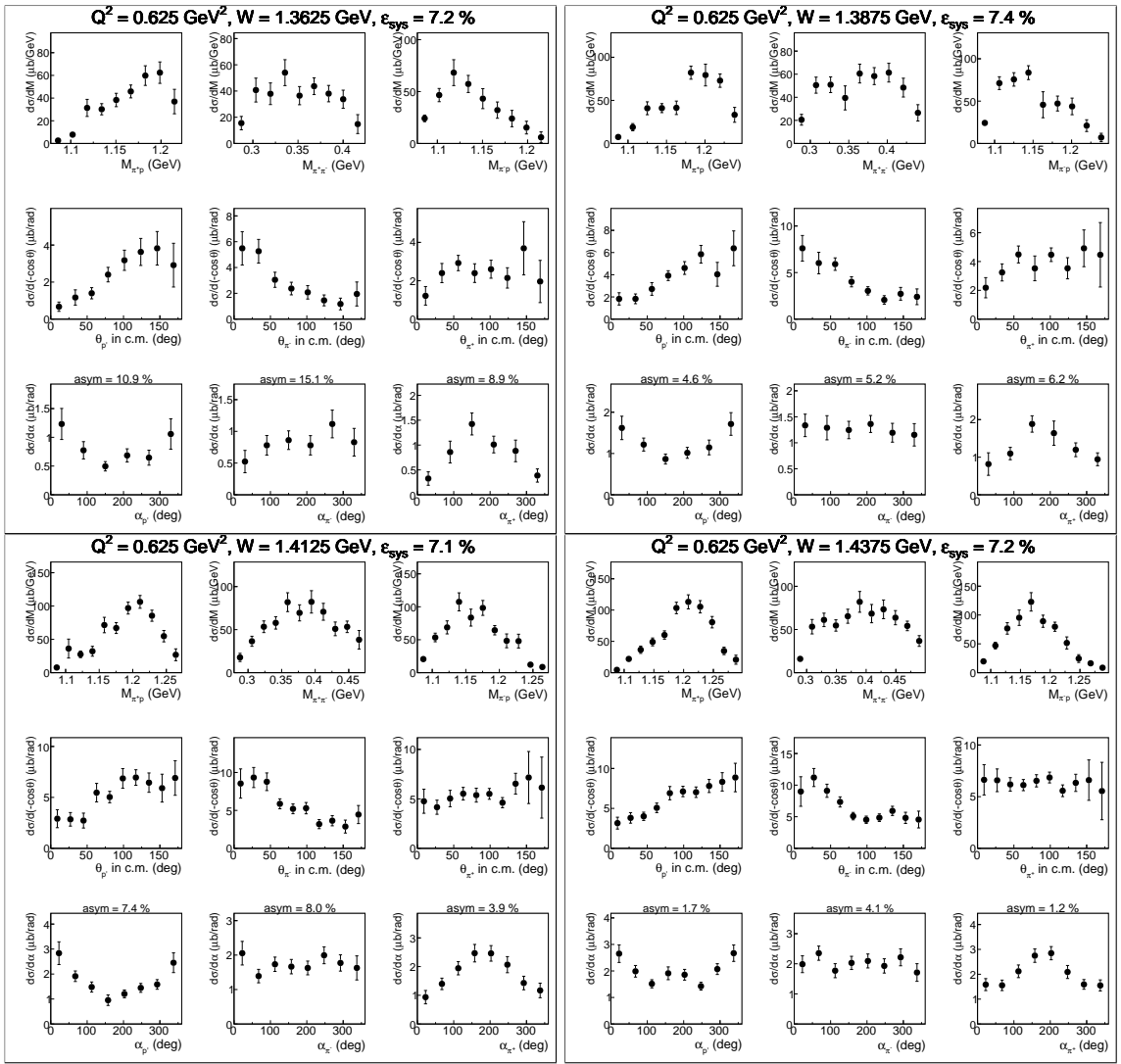


Figure A.27:

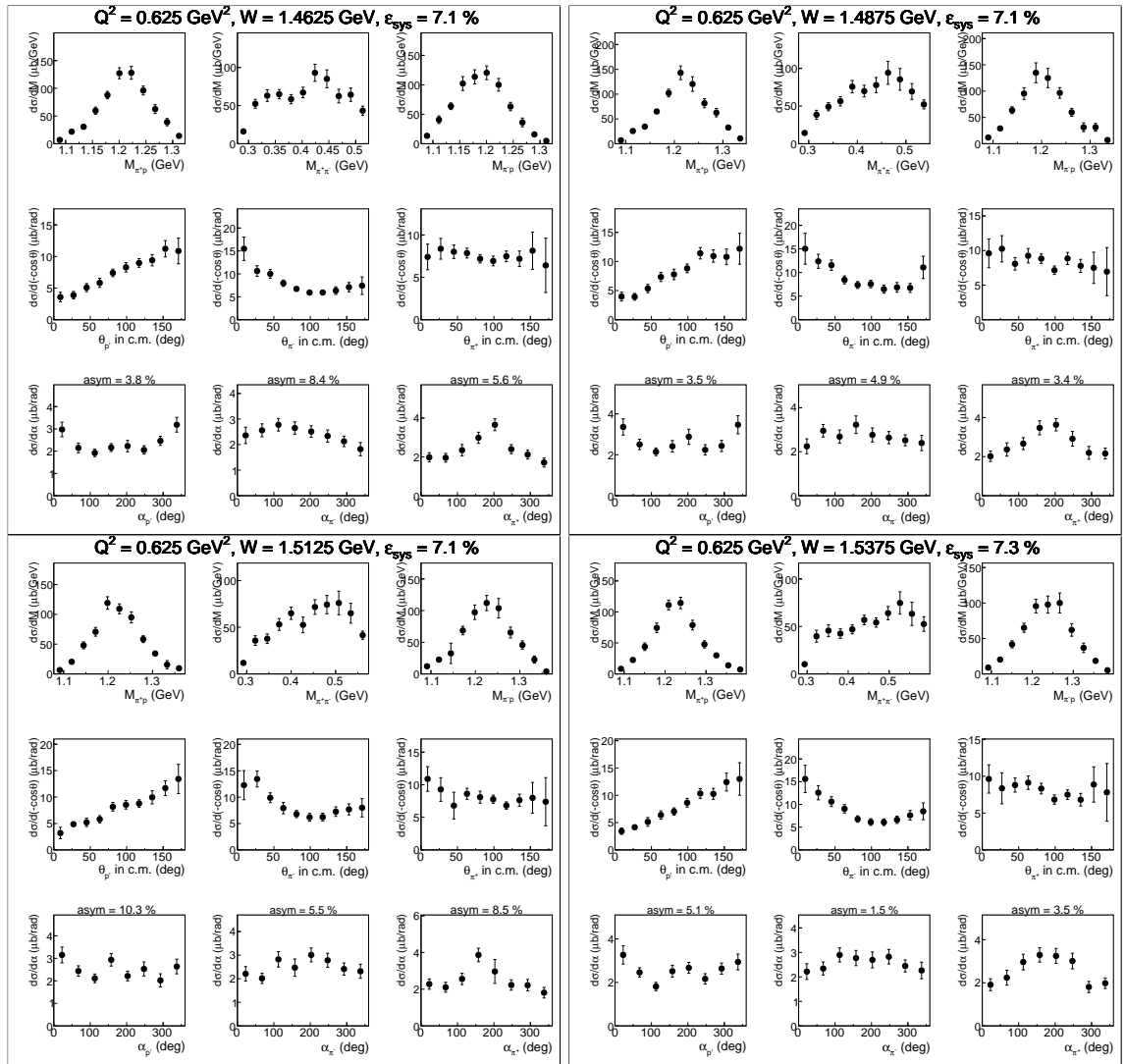


Figure A.28:

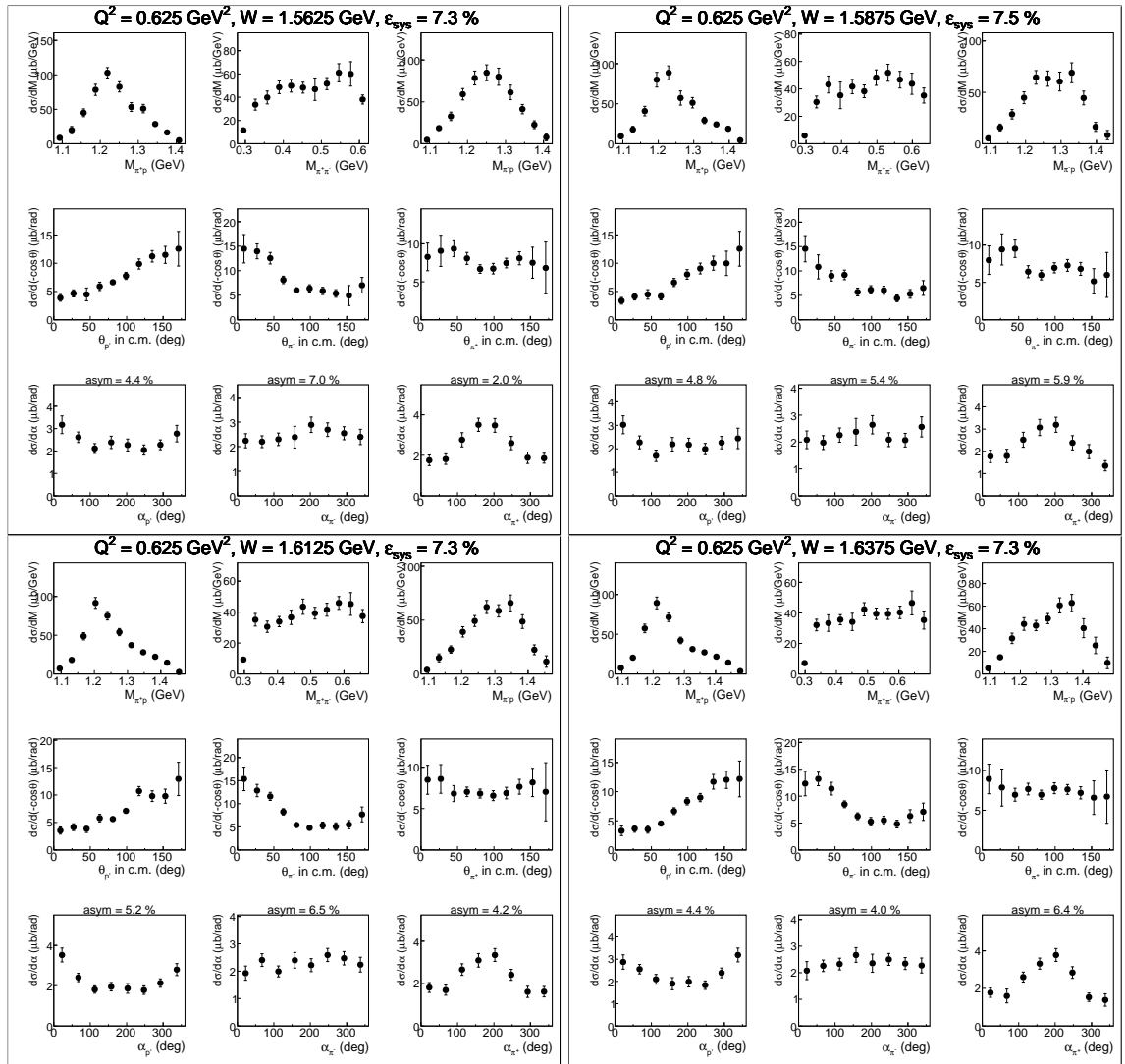


Figure A.29:

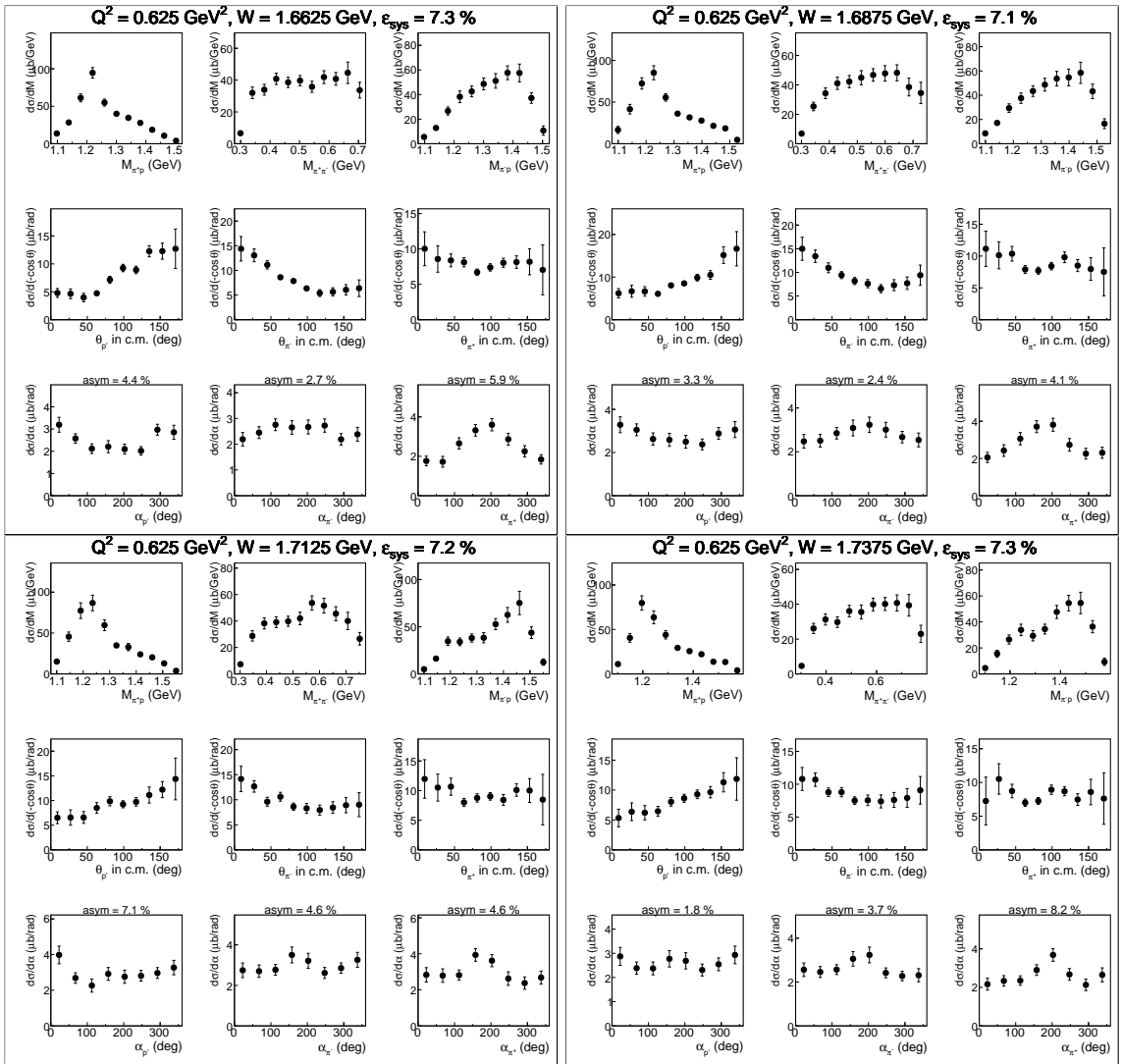


Figure A.30:

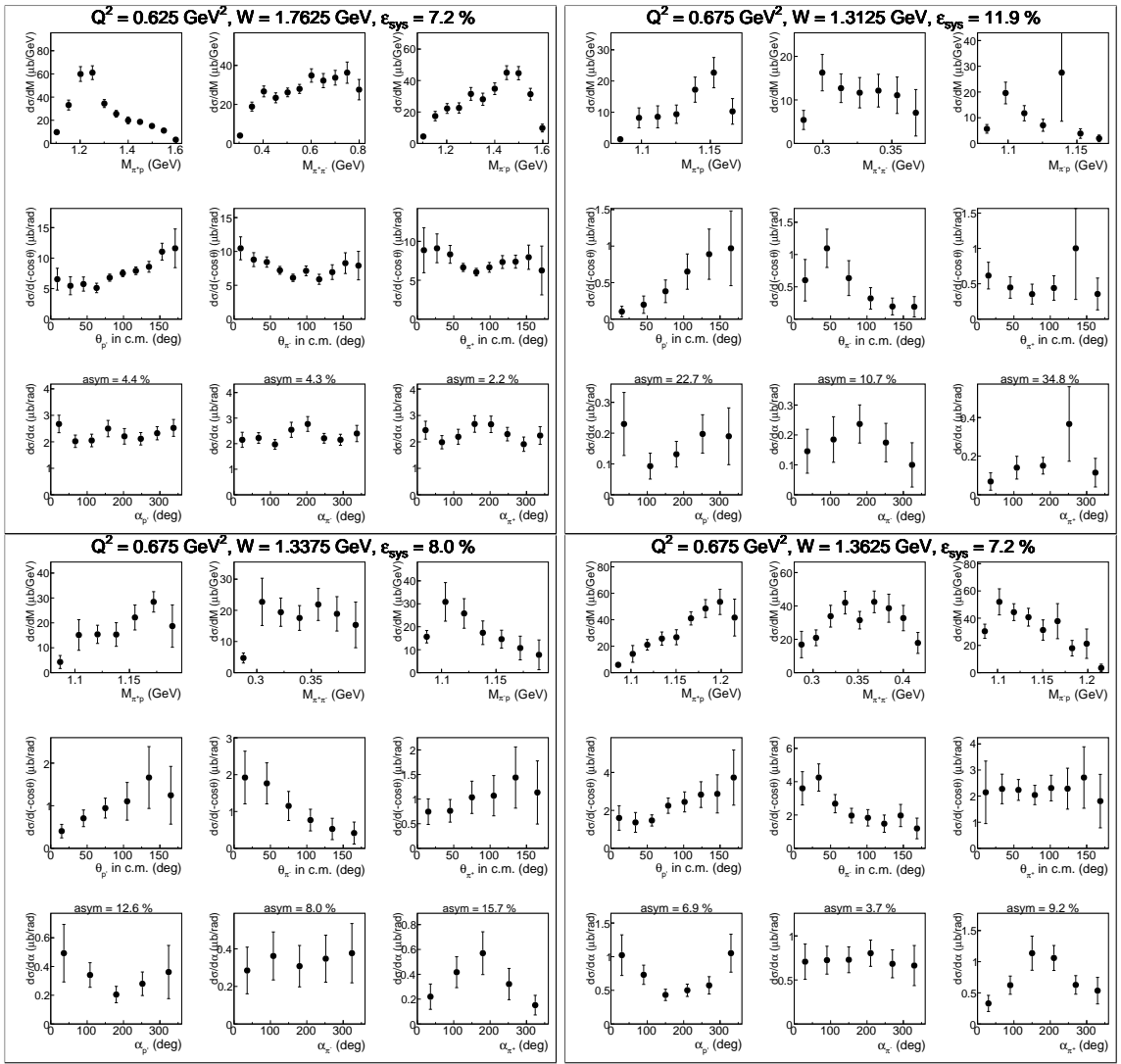


Figure A.31:

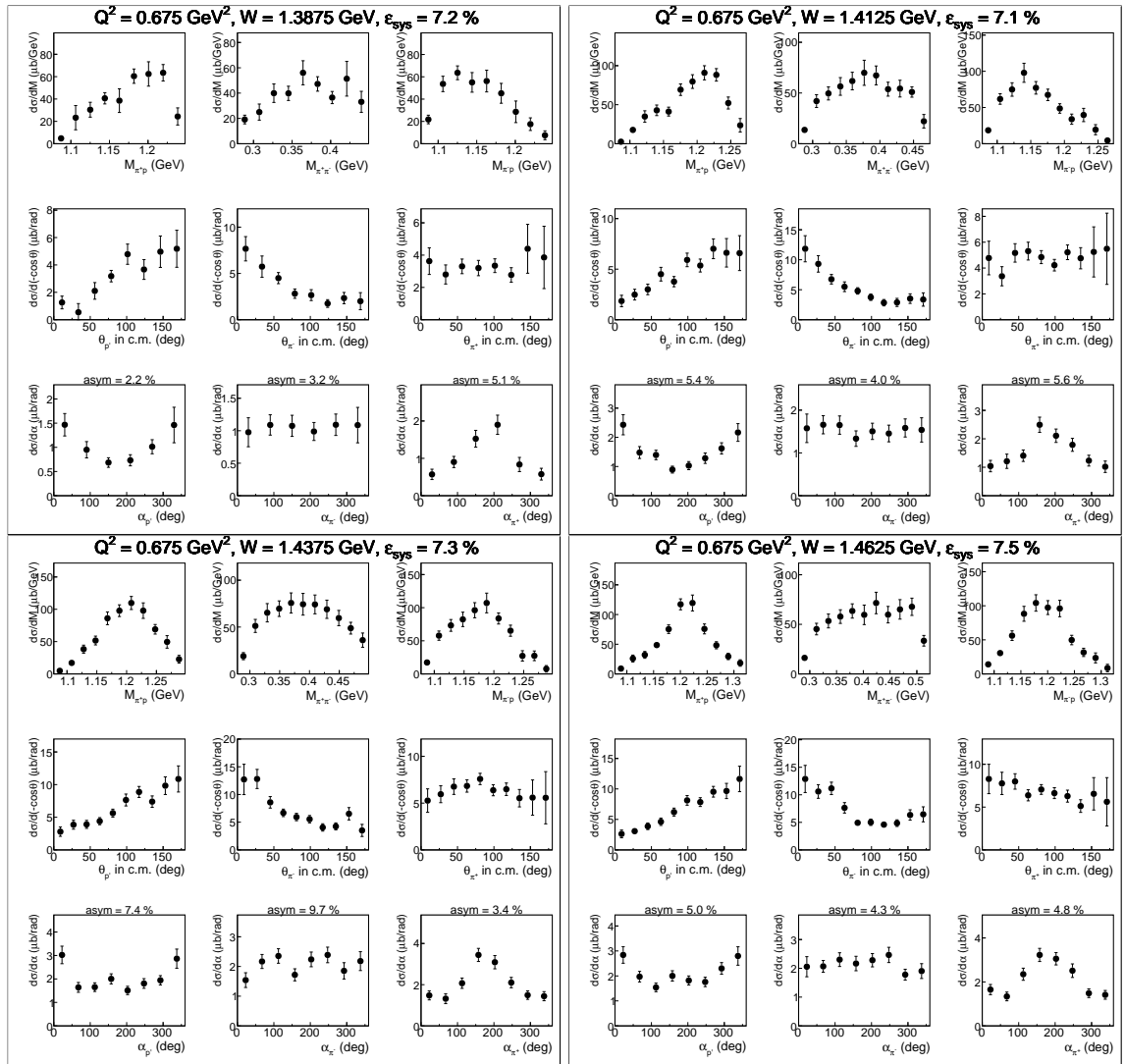


Figure A.32:

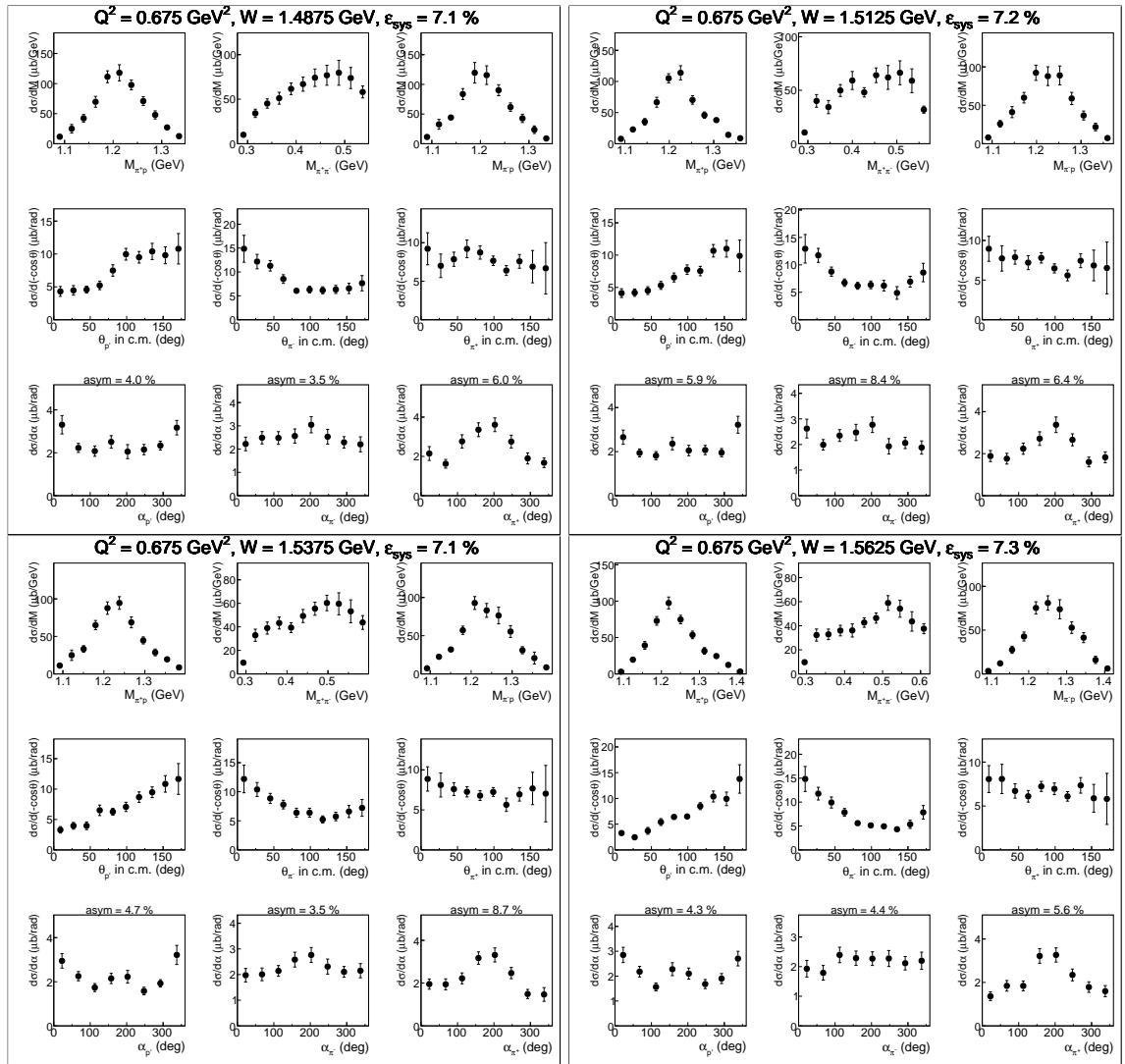


Figure A.33:

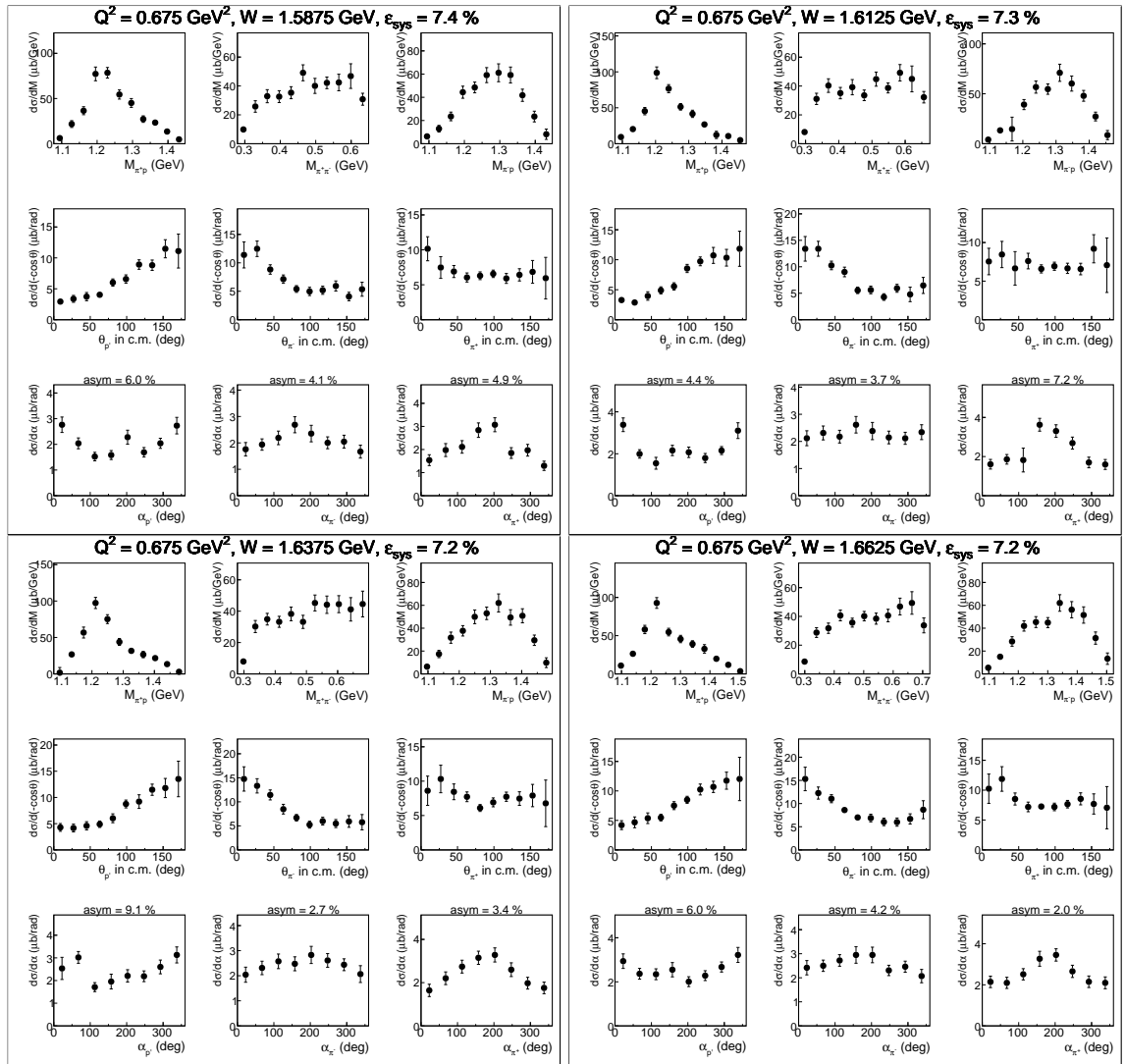


Figure A.34:

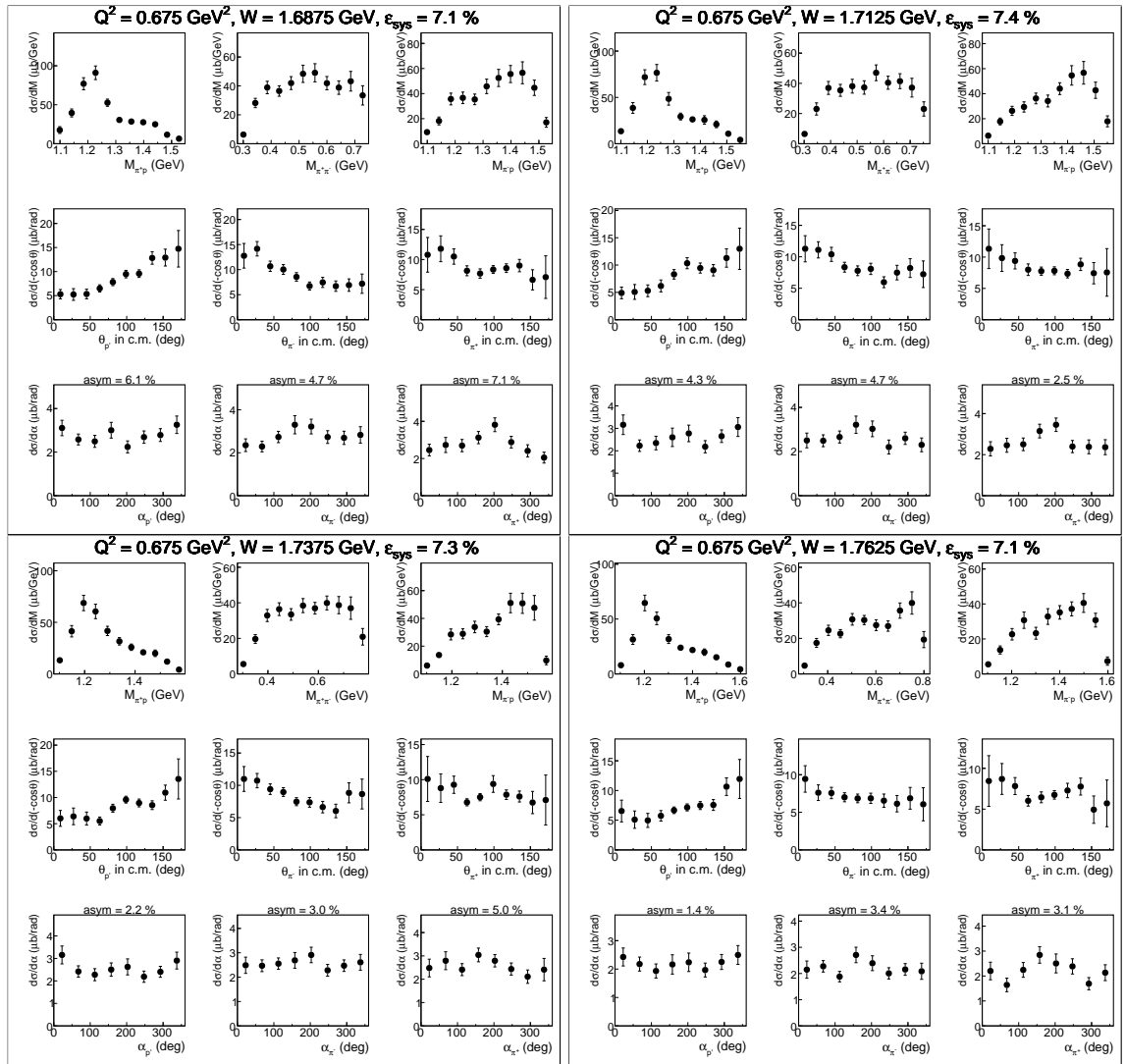


Figure A.35:

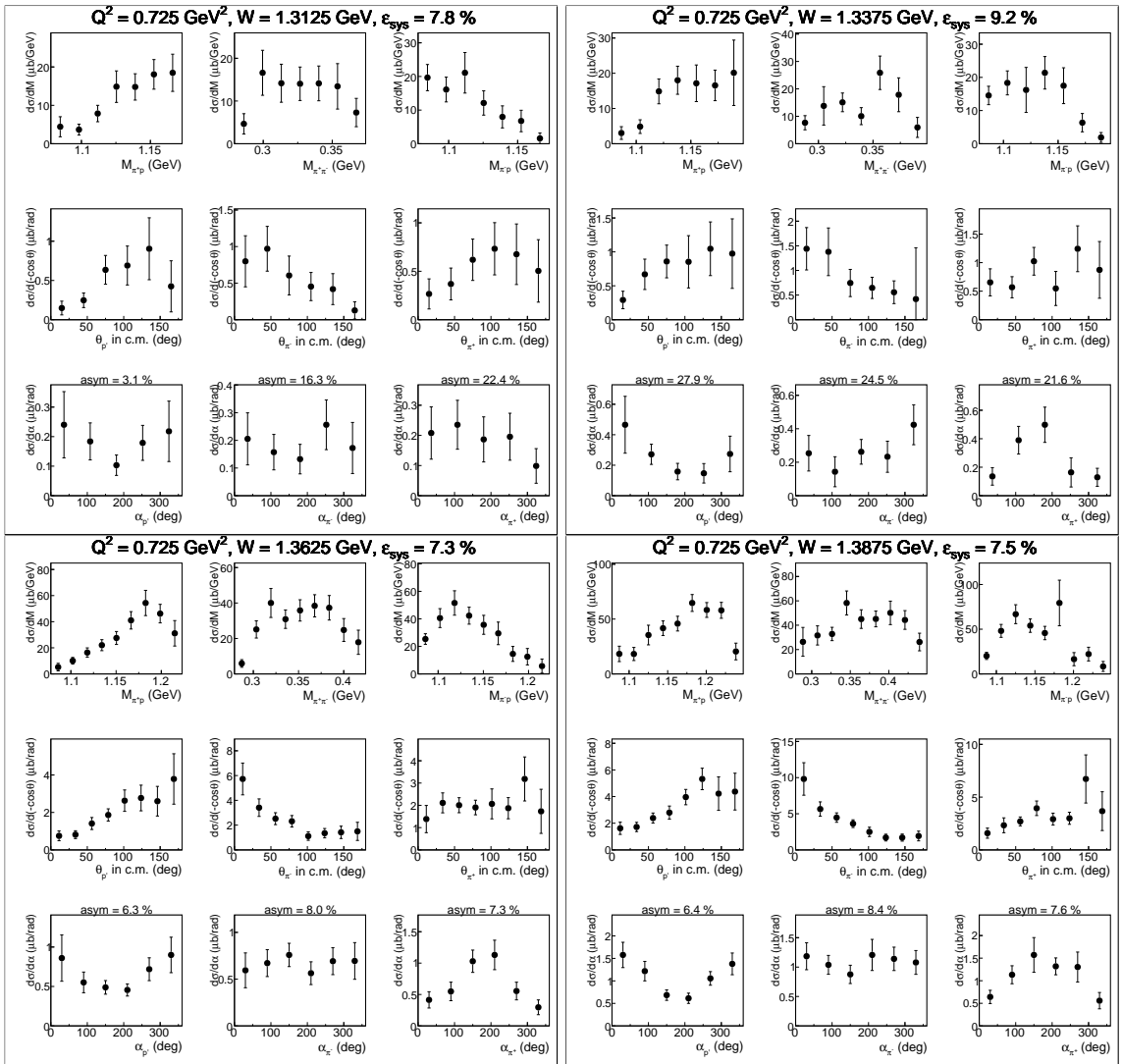


Figure A.36:

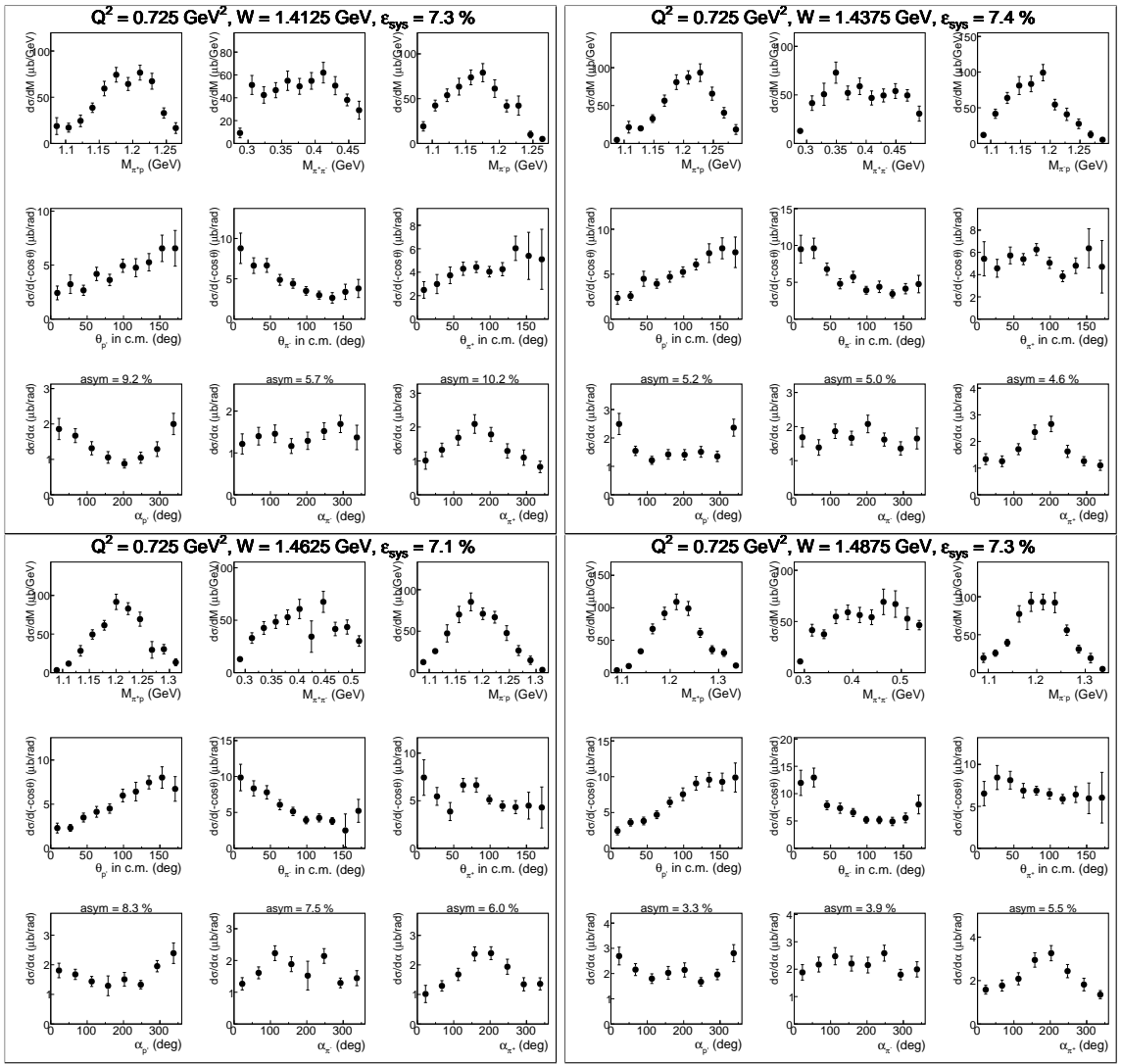


Figure A.37:

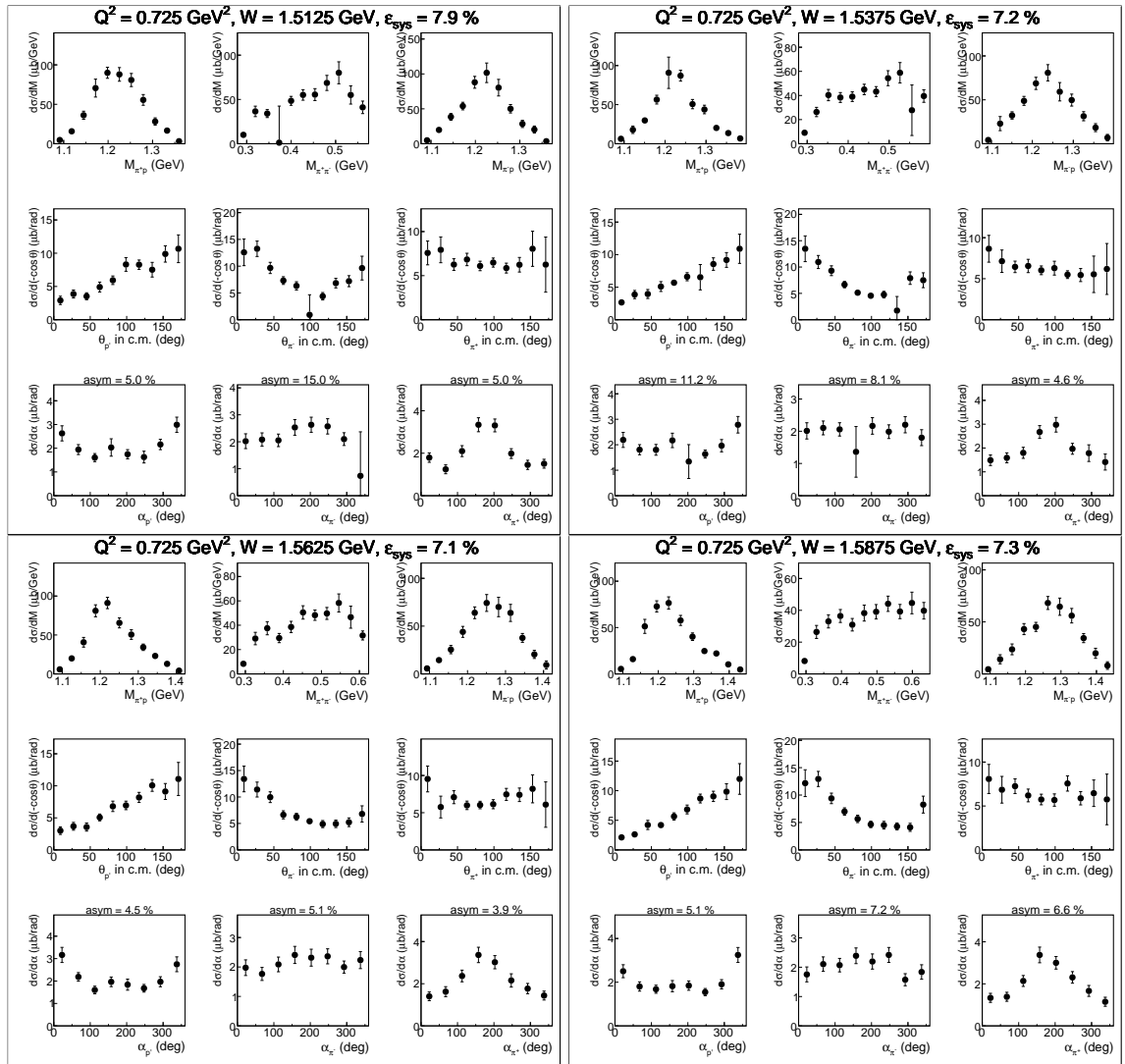


Figure A.38:

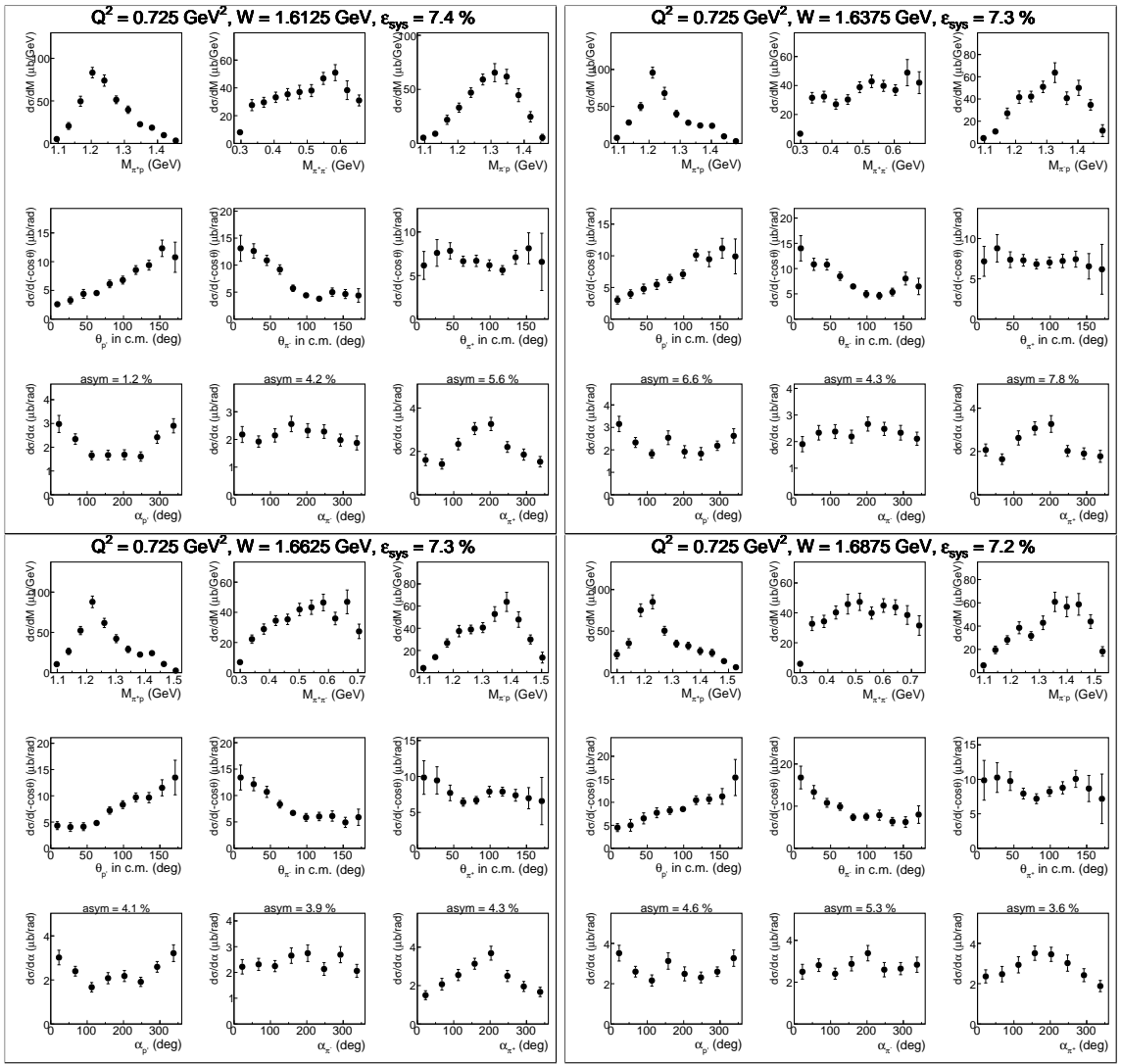


Figure A.39:

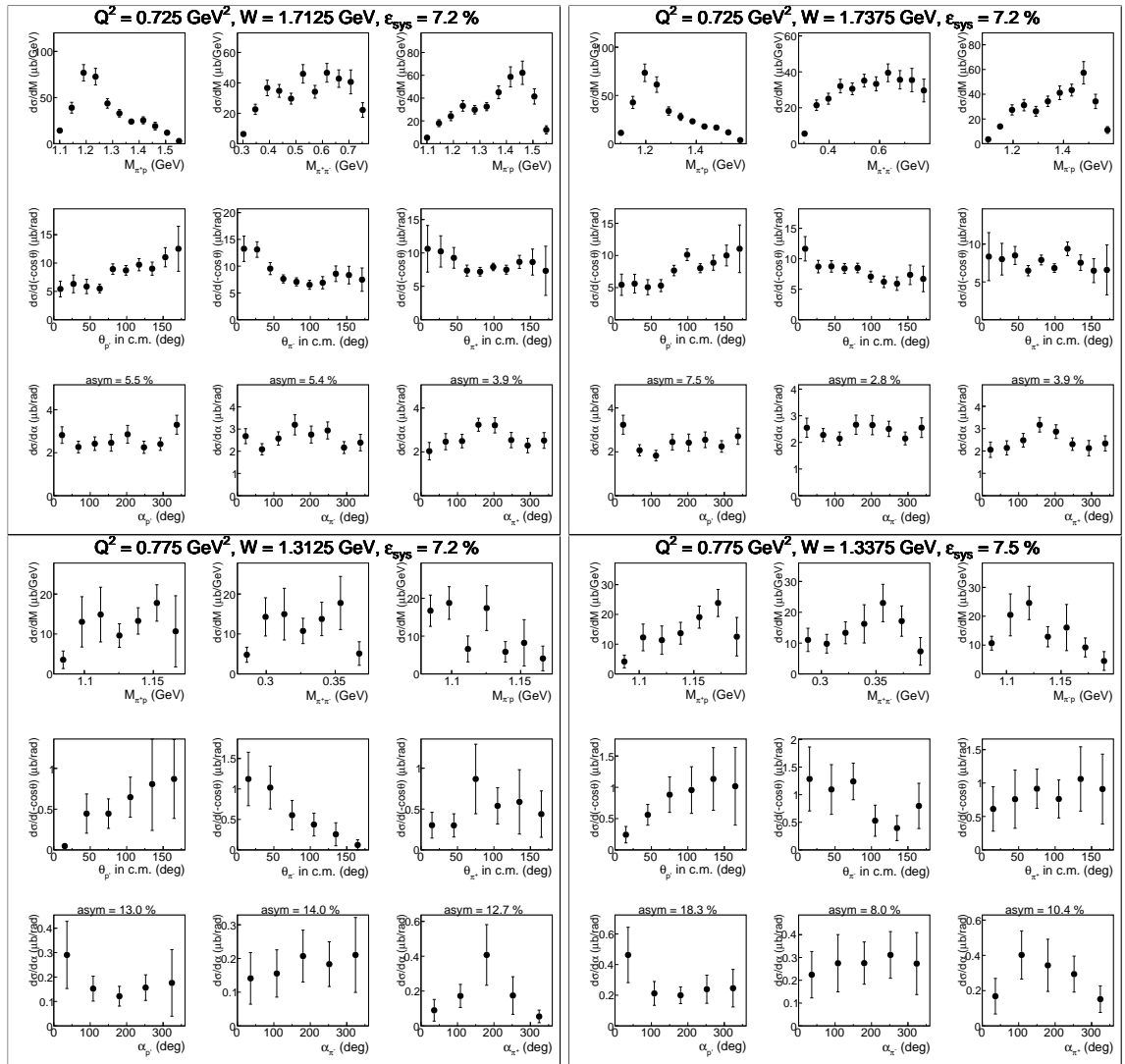


Figure A.40:

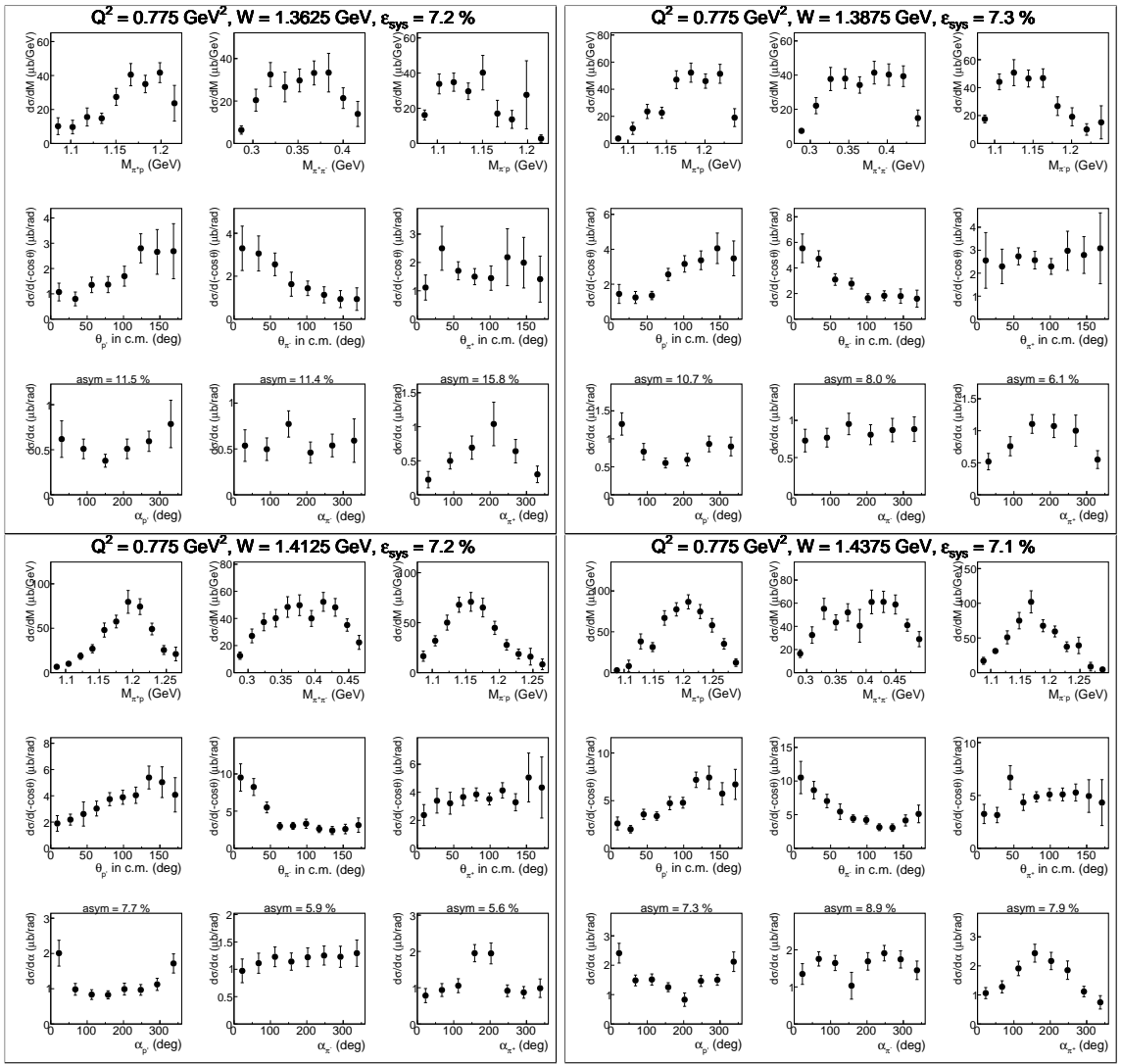


Figure A.41:

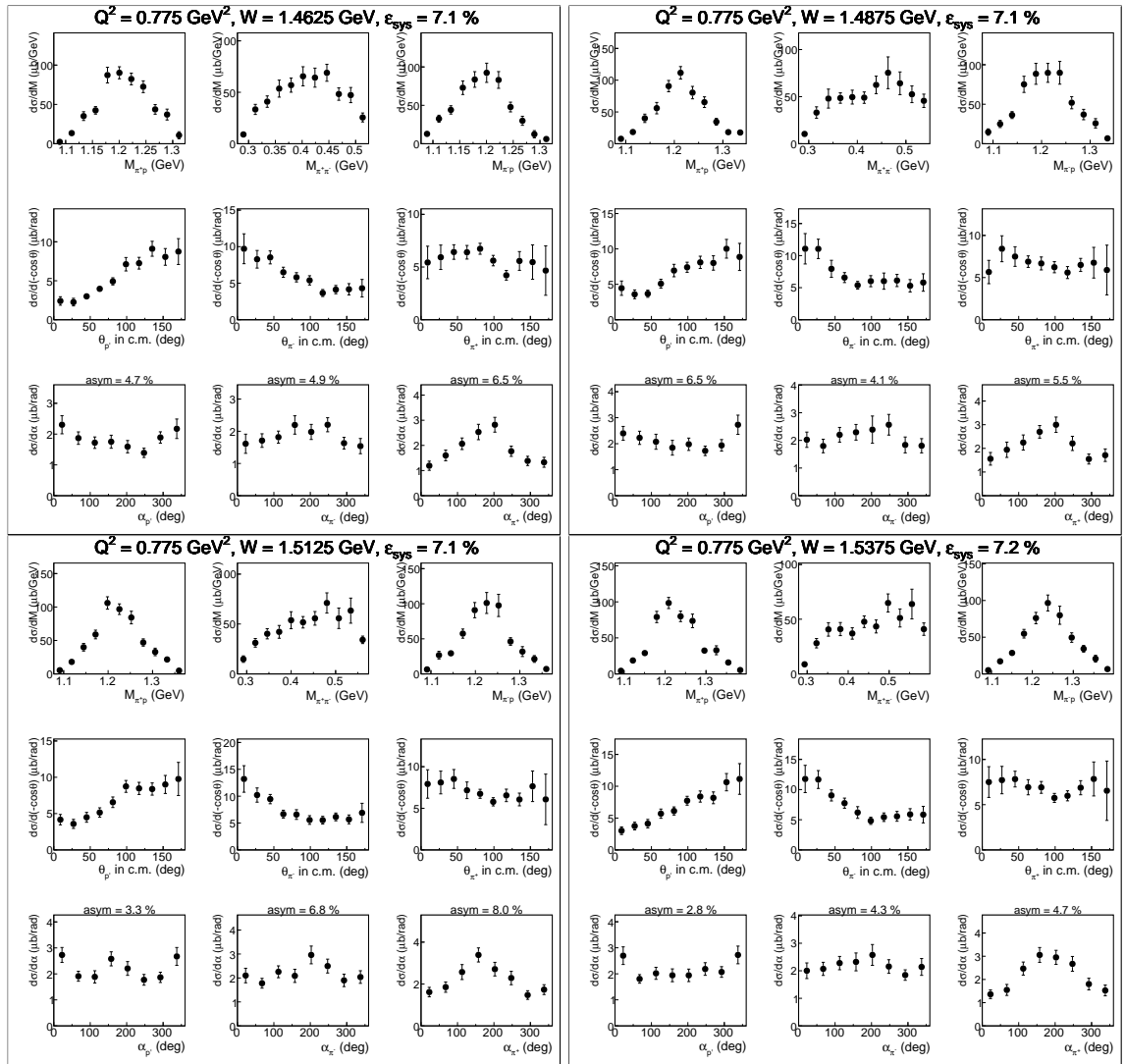


Figure A.42:

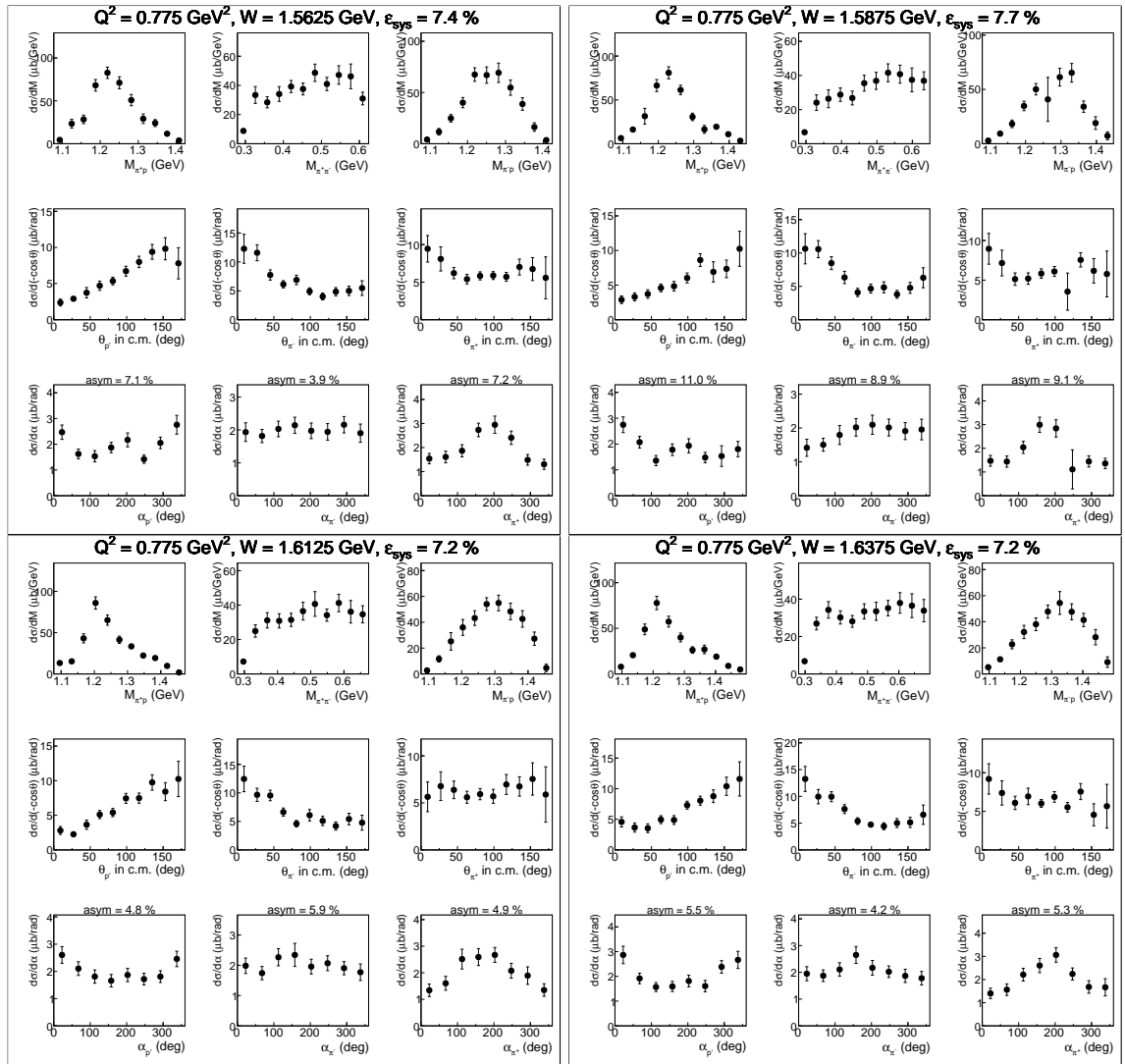


Figure A.43:

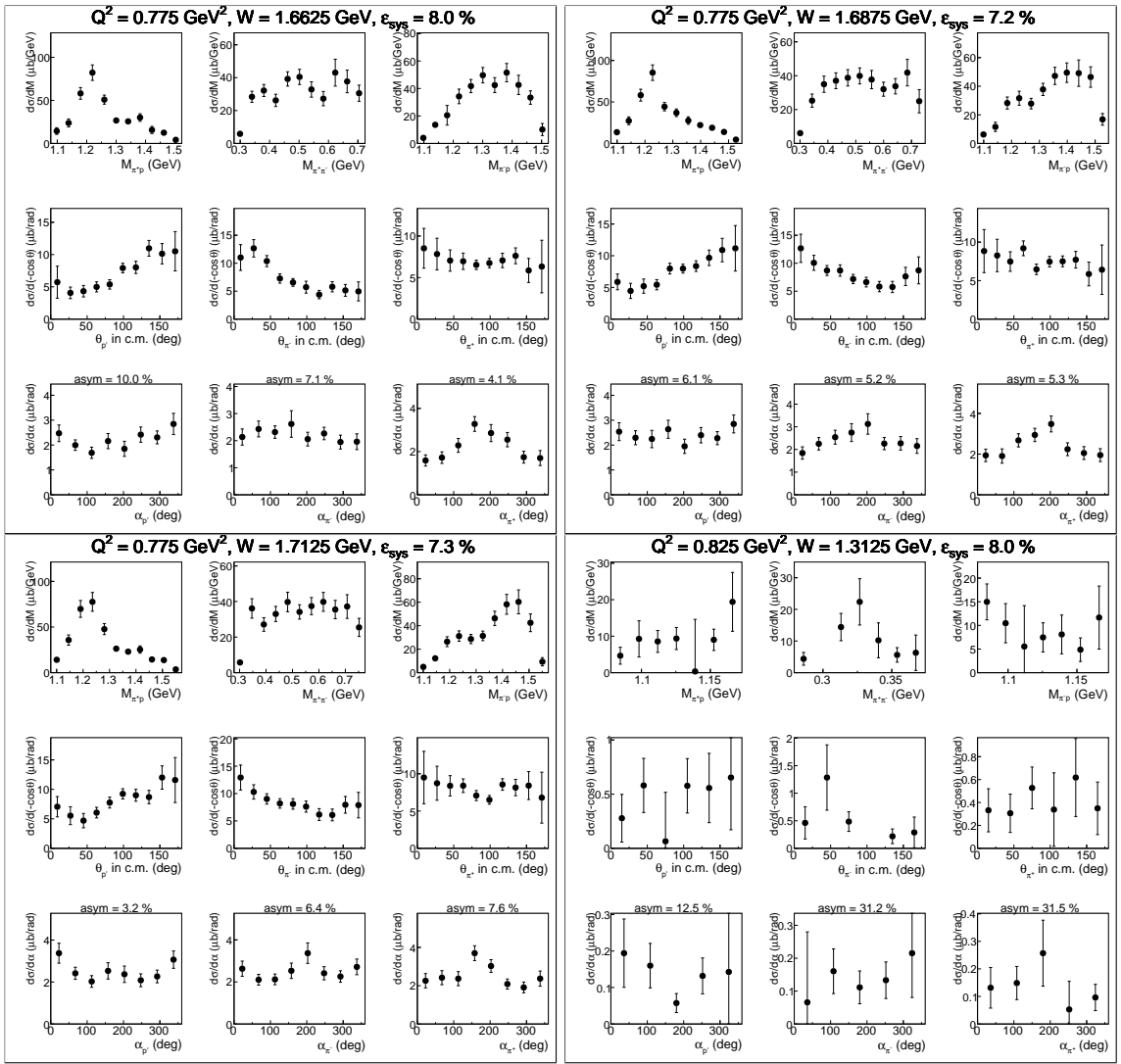


Figure A.44:

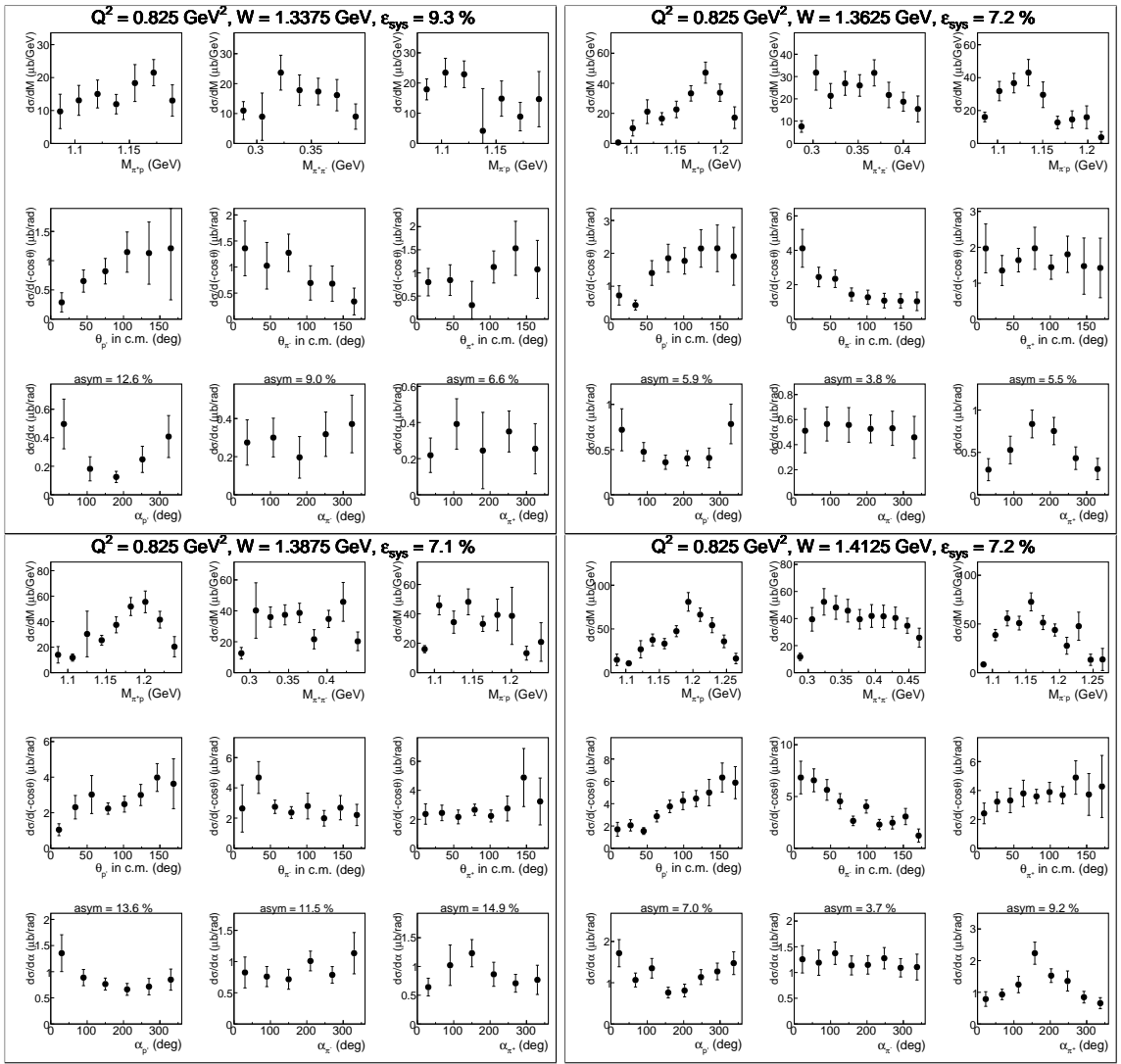


Figure A.45:

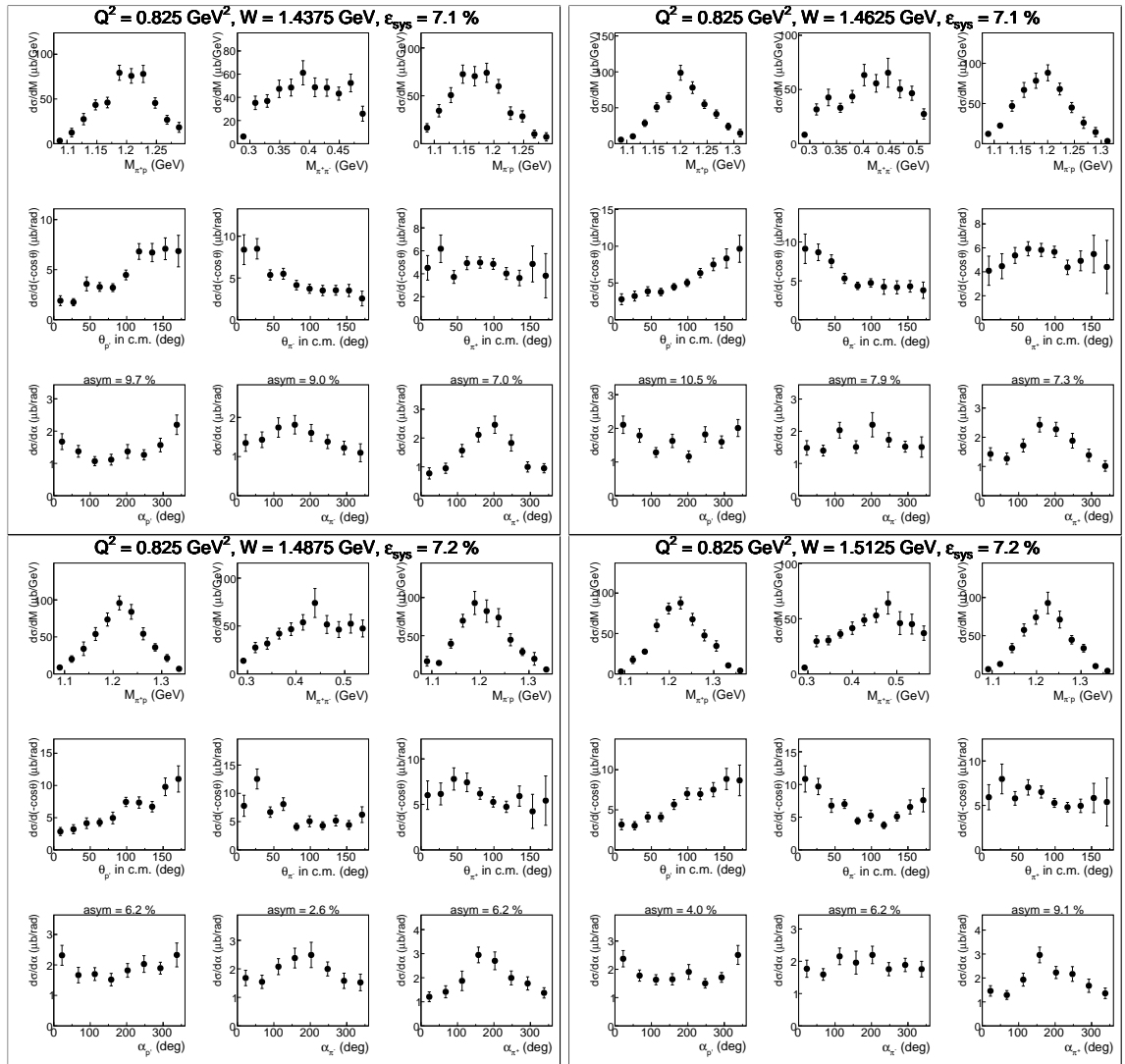


Figure A.46:

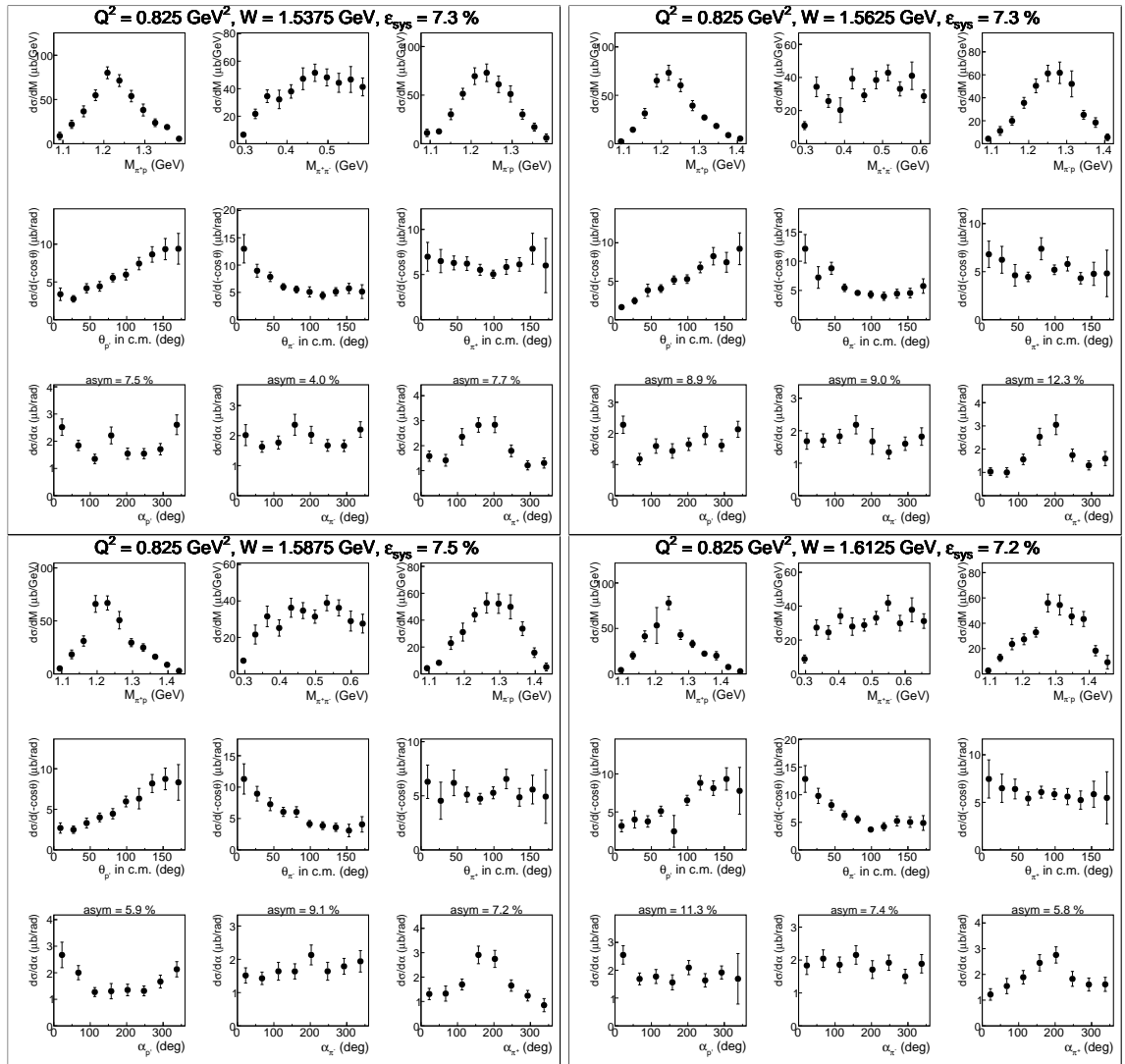


Figure A.47:

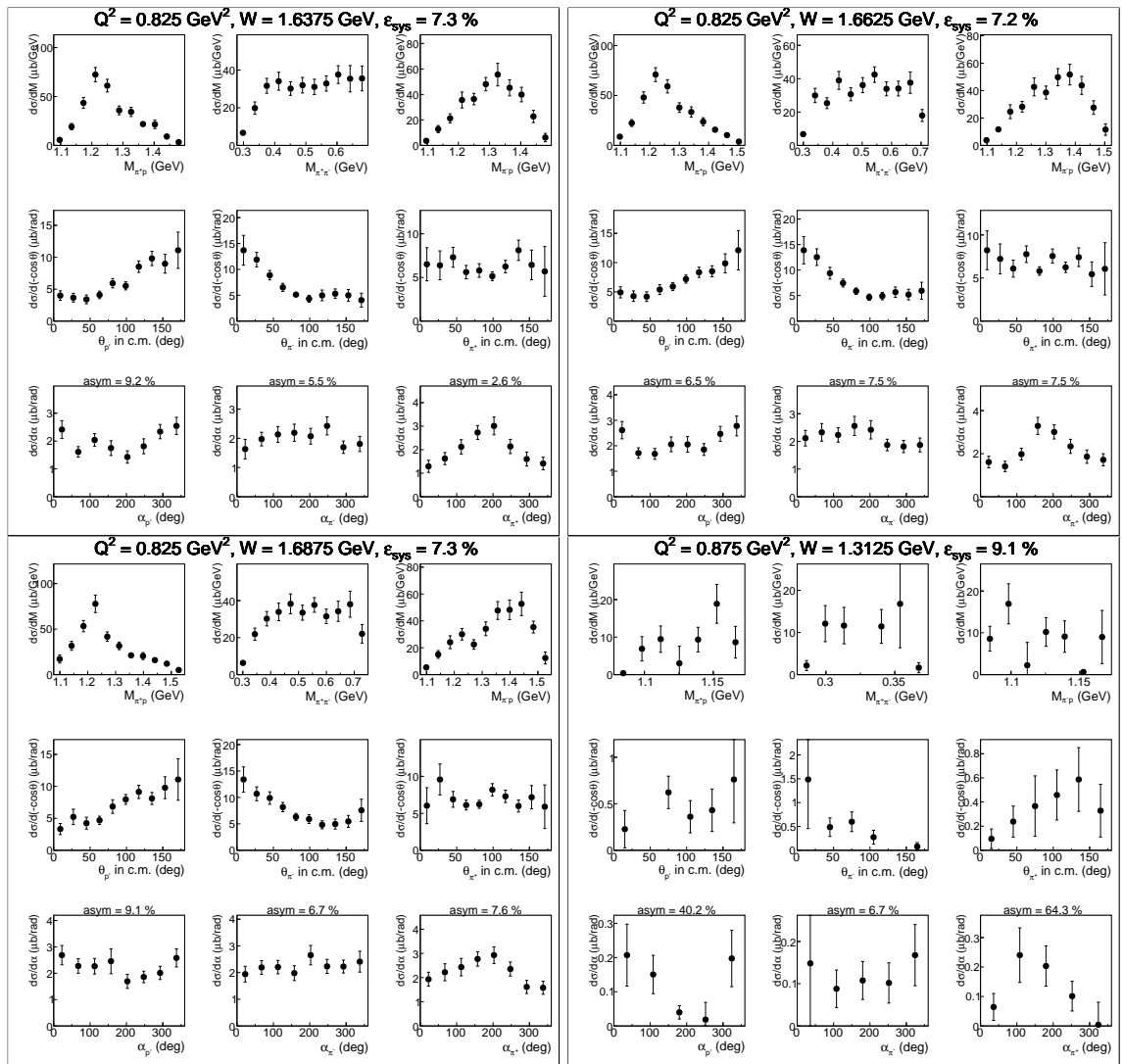


Figure A.48:

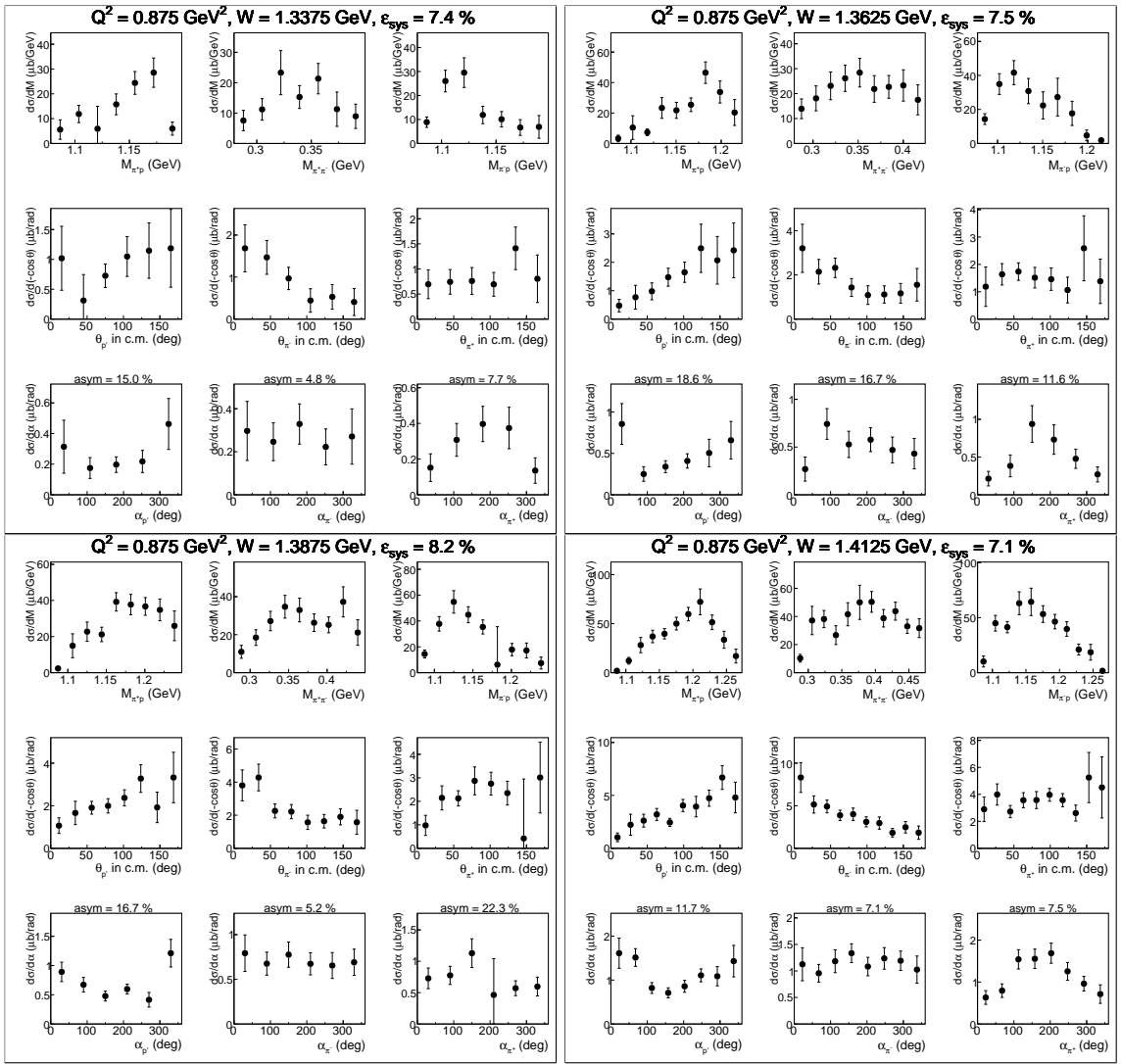


Figure A.49:

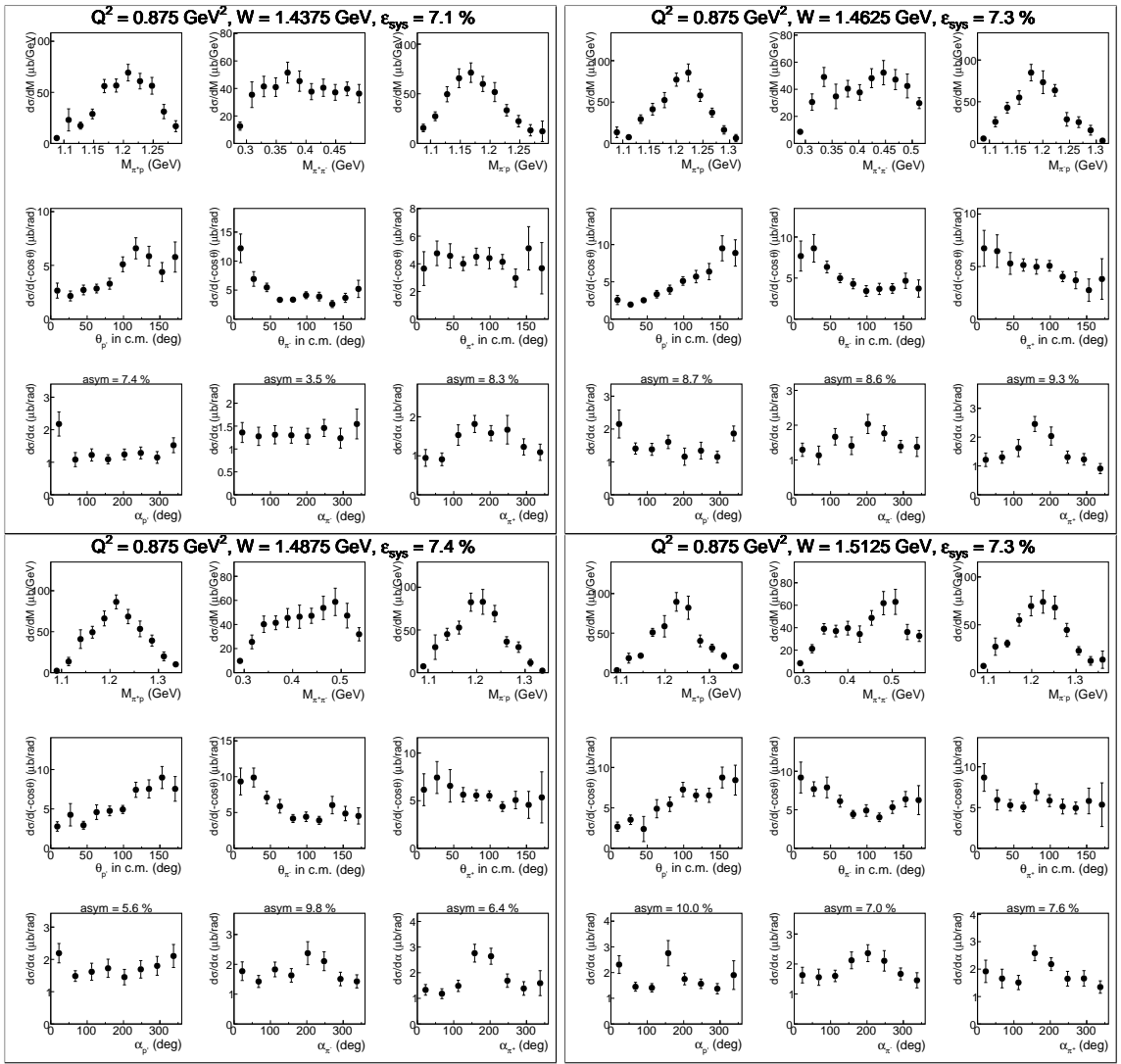


Figure A.50:

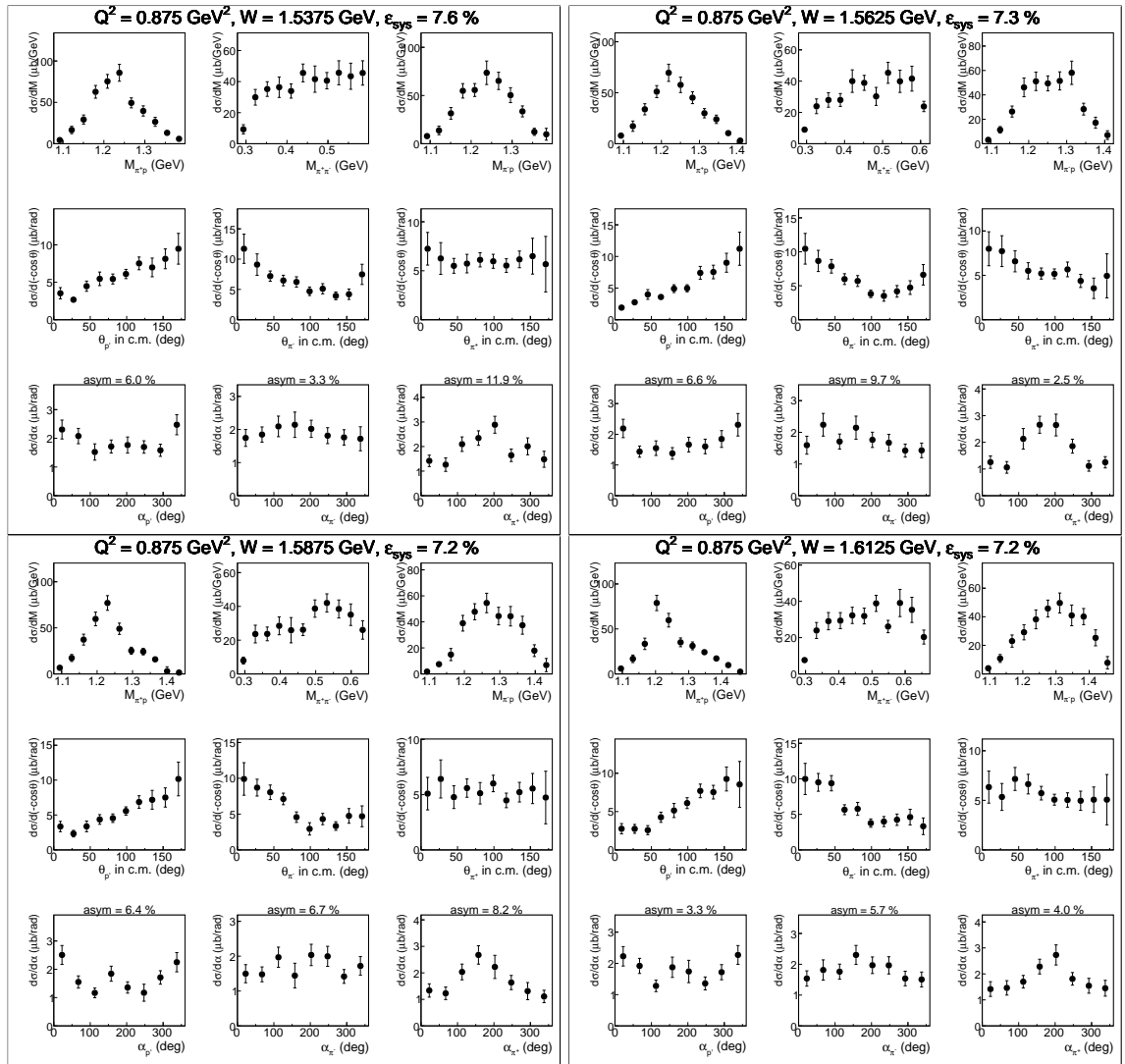


Figure A.51:

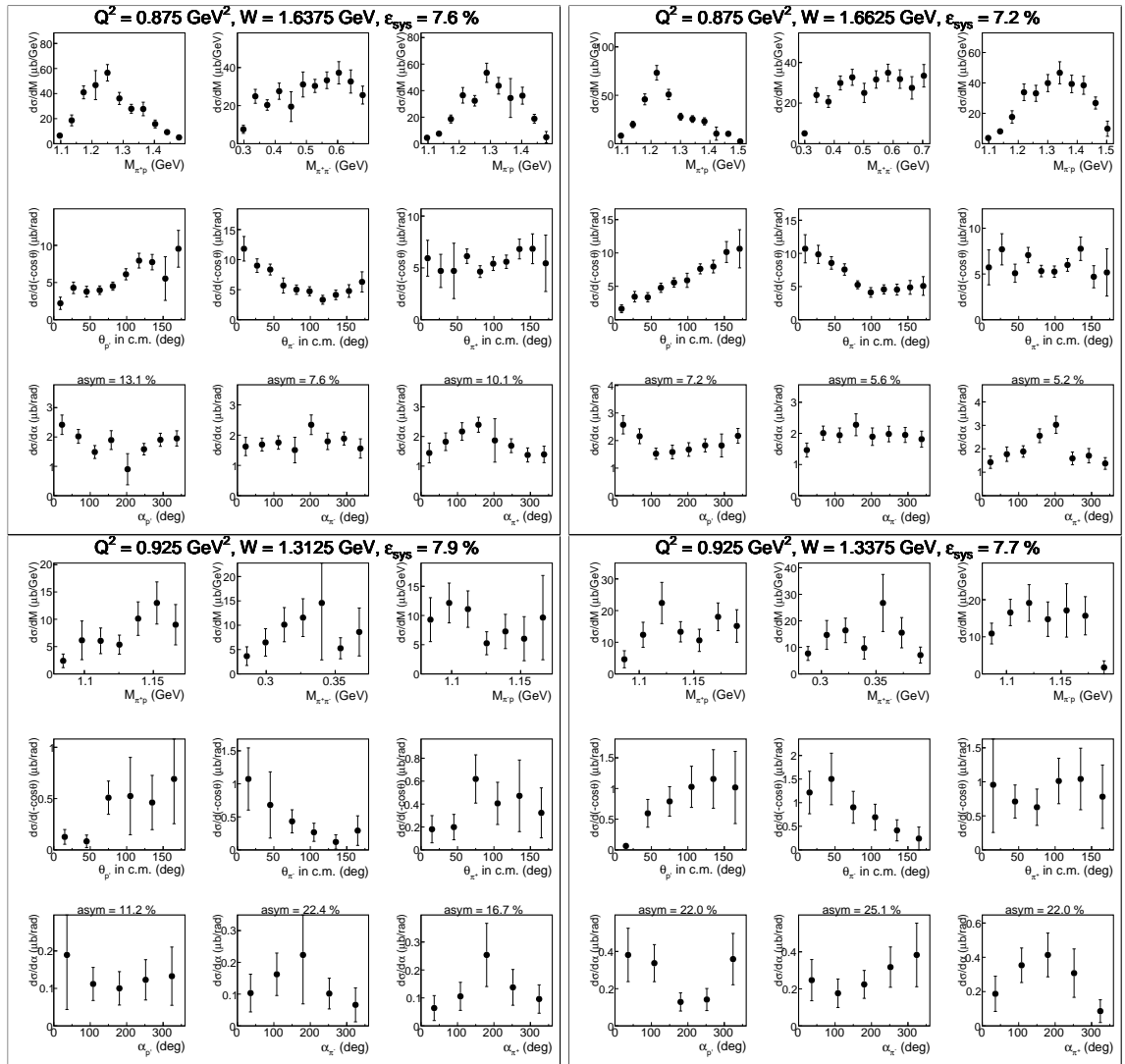


Figure A.52:

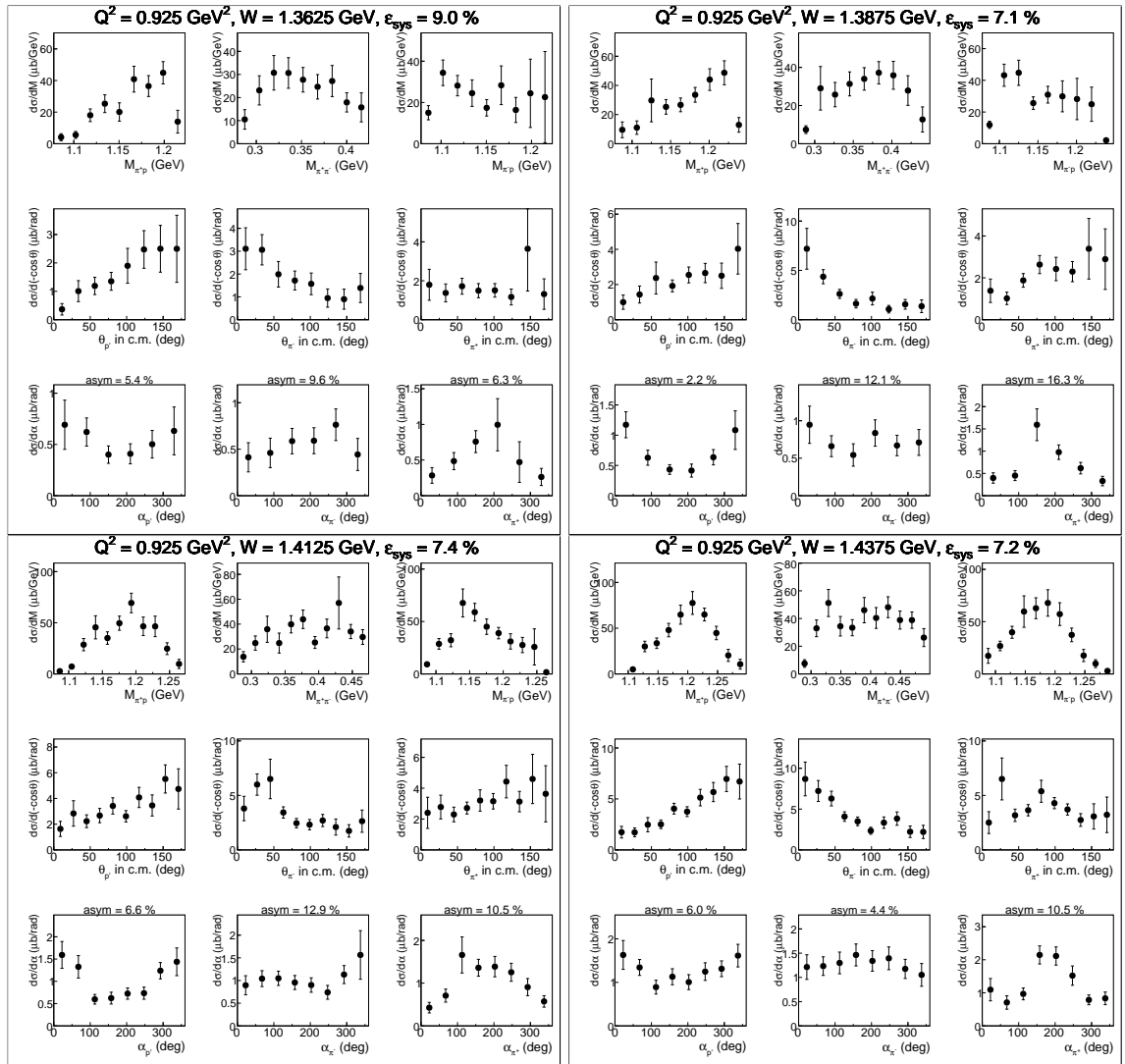


Figure A.53:

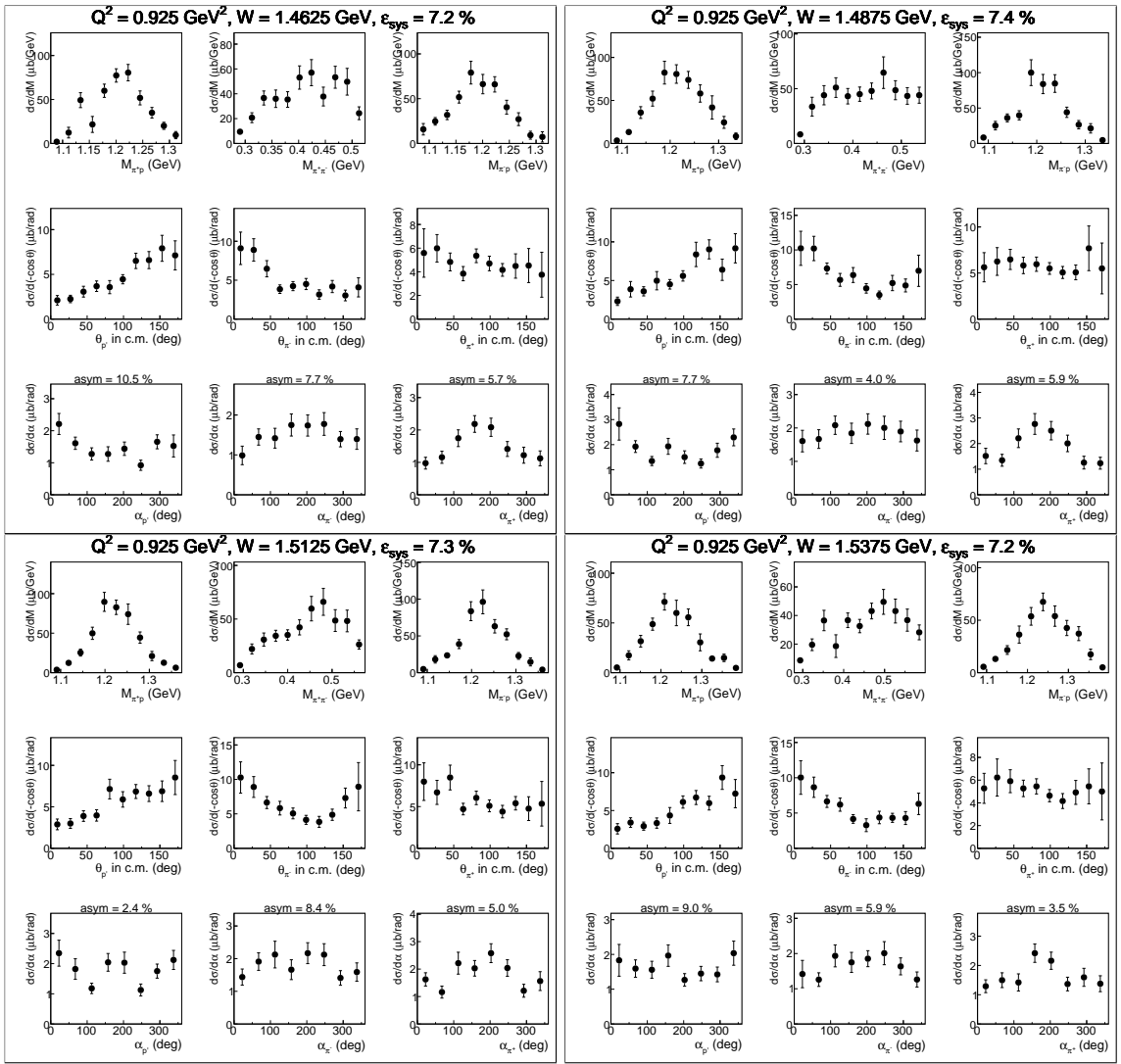


Figure A.54:

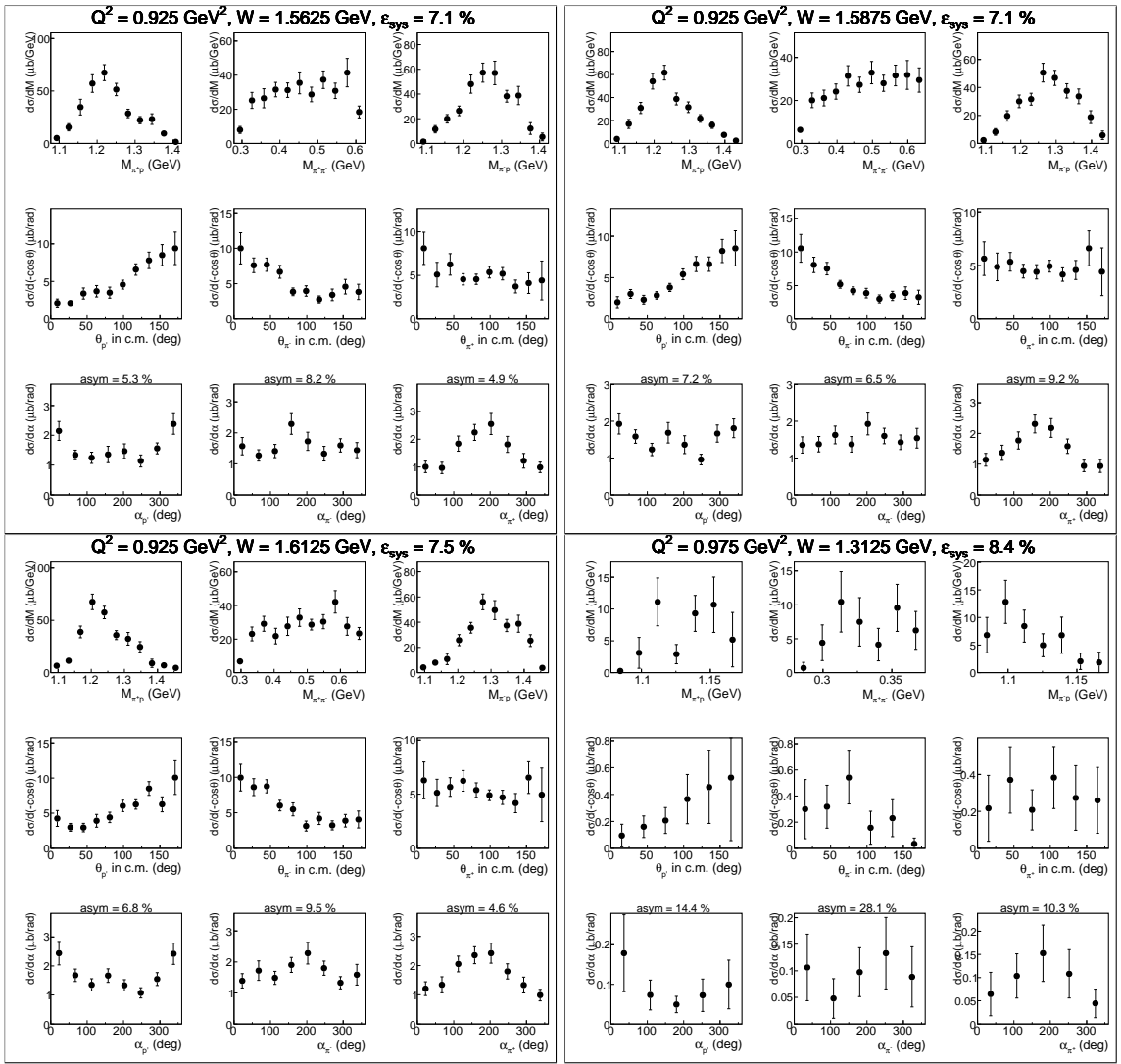


Figure A.55:

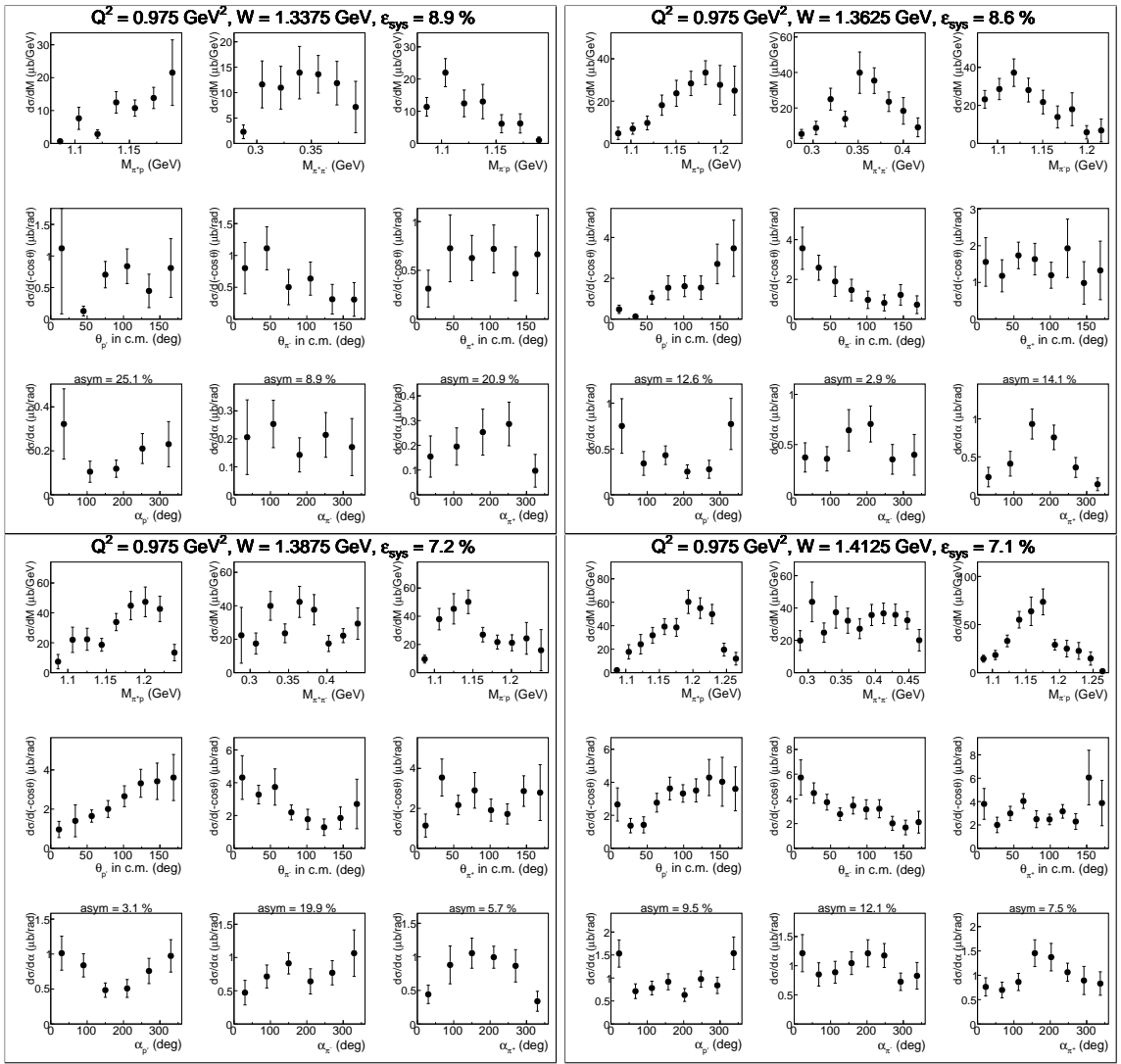


Figure A.56:

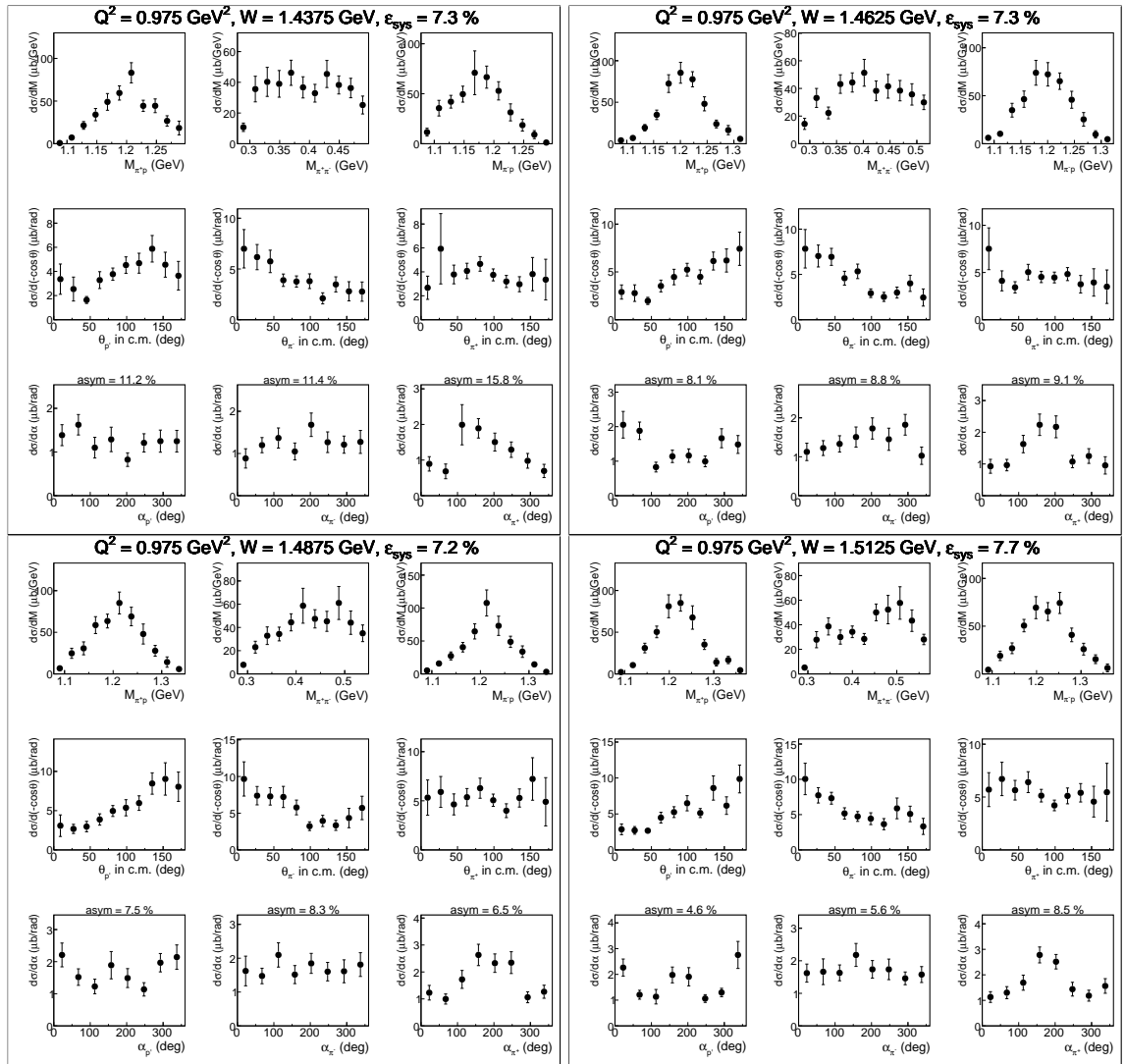


Figure A.57:

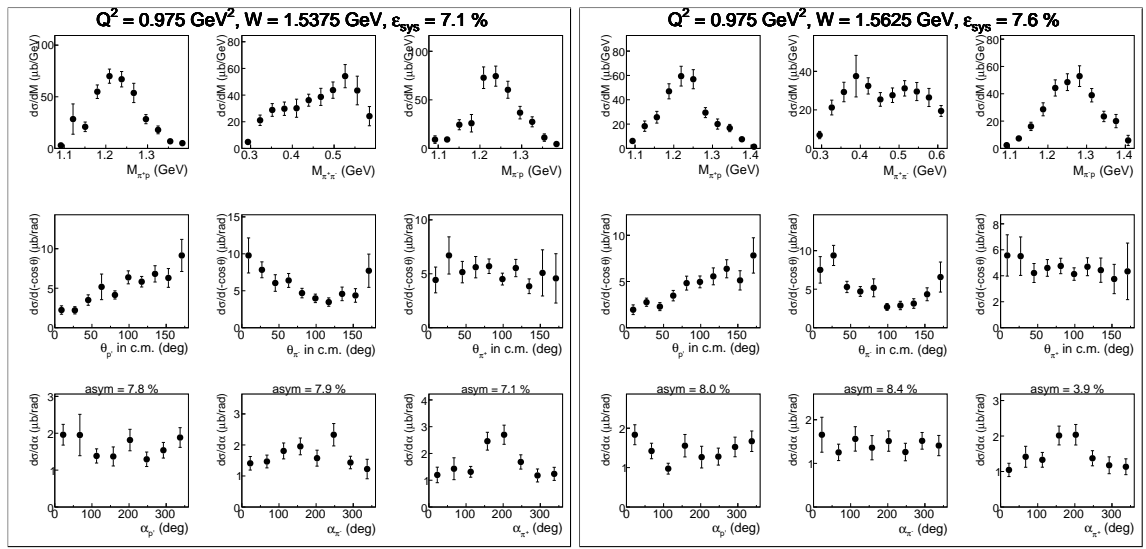


Figure A.58:

Bibliography

- [1] B. Krusche and S. Schadmand, “Study of nonstrange baryon resonances with meson photoproduction,” *Prog. Part. Nucl. Phys.*, vol. 51, pp. 399–485, 2003.
- [2] I. G. Aznauryan and V. D. Burkert, “Electroexcitation of nucleon resonances,” *Prog. Part. Nucl. Phys.*, vol. 67, pp. 1–54, 2012.
- [3] Iu. A. Skorodumina *et al.*, “Nucleon resonances in exclusive reactions of photo- and electroproduction of mesons,” *Moscow Univ. Phys. Bull.*, vol. 70, no. 6, pp. 429–447, 2015. [Vestn. Mosk. Univ.,no.6,3(2015)].
- [4] B. A. Mecking *et al.*, “The CEBAF Large Acceptance Spectrometer (CLAS),” *Nucl. Instrum. Meth.*, vol. A503, pp. 513–553, 2003.
- [5] “CLAS physics database.” <http://clas.sinp.msu.ru/cgi-bin/jlab/db.cgi>.
- [6] V. I. Mokeev, E. Santopinto, M. M. Giannini, and G. Ricco, “The Influence of the nuclear medium on the baryon resonance excitation,” *Int. J. Mod. Phys.*, vol. E4, pp. 607–624, 1995
[see also Refs.[1-5] there].
- [7] N. Bianchi *et al.*, “Absolute total photoabsorption cross-sections on nuclei in the nucleon resonance region,” *Phys. Lett.*, vol. B325, pp. 333–336, 1994.
- [8] J. Ahrens, “The Total Absorption of Photons by Nuclei,” *Nucl. Phys.*, vol. A446, pp. 229C–239C, 1985.
- [9] M. Osipenko *et al.*, “The deuteron structure function F2 with CLAS,” CLAS-NOTE-2005-013, arXiv:hep-ex/0507098, 2005.
- [10] M. Osipenko *et al.*, “Measurement of the deuteron structure function F(2) in the resonance region and evaluation of its moments,” *Phys. Rev.*, vol. C73, p. 045205, 2006.
- [11] M. Osipenko *et al.*, “Measurement of the Nucleon Structure Function F2 in the Nuclear Medium and Evaluation of its Moments,” *Nucl. Phys.*, vol. A845, pp. 1–32, 2010.

- [12] M. Osipenko *et al.*, “A Kinematically complete measurement of the proton structure function $F(2)$ in the resonance region and evaluation of its moments,” *Phys. Rev.*, vol. D67, p. 092001, 2003.
- [13] B. Krusche, “Photoproduction of mesons from nuclei: In-medium properties of hadrons,” *Prog. Part. Nucl. Phys.*, vol. 55, pp. 46–70, 2005.
- [14] J. V. Noble, “Modification of the nucleon’s properties in nuclear matter,” *Phys. Rev. Lett.*, vol. 46, pp. 412–415, 1981.
- [15] M. Ripani *et al.*, “Measurement of Two Pion Decay of Electroproduced Light Quark Baryon States with CLAS,” *CLAS-Analysis-2002-109*, 2002.
- [16] M. Ripani *et al.*, “Measurement of $ep \rightarrow e'p\pi^+\pi^-$ and baryon resonance analysis,” *Phys. Rev. Lett.*, vol. 91, p. 022002, 2003.
- [17] G. V. Fedotov *et al.*, “Analysis report on the $ep \rightarrow e'p\pi^+\pi^-$ reaction in the CLAS detector with a 1.515 GeV beam for $0.2 < Q^2 < 0.6$ GeV 2 and $1.3 < W < 1.6$ GeV,” *CLAS-Analysis-2007-117*, 2007.
- [18] G. V. Fedotov *et al.*, “Electroproduction of $p\pi^+\pi^-$ off protons at $0.2 < Q^2 < 0.6$ GeV 2 and $1.3 < W < 1.57$ GeV with CLAS,” *Phys. Rev.*, vol. C79, p. 015204, 2009.
- [19] E. L. Isupov *et al.*, “Measurements of $ep \rightarrow e'\pi^+\pi^-p'$ Cross Sections with CLAS at 1.40 Gev $< W < 2.0$ GeV and 2.0 GeV $^2 < Q^2 < 5.0$ GeV 2 ,” *Phys. Rev.*, vol. C96, no. 2, p. 025209, 2017.
- [20] E. Golovatch *et al.*, “First results on nucleon resonance photocouplings from the $\gamma p \rightarrow \pi^+\pi^-p$ reaction,” *Phys. Lett.*, vol. B788, pp. 371–379, 2019.
- [21] A. Trivedi and R. W. Gothe, “Measurement of New Observables from the $p\pi^+\pi^-$ Electroproduction off the Proton,” *CLAS-Analysis-2019-102*, 2018.
- [22] G. V. Fedotov *et al.*, “Analysis report on the $ep \rightarrow e'p\pi^+\pi^-$ reaction in the CLAS detector with a 2.039 GeV,” *CLAS-Analysis-2017-101 (CLAS-NOTE-2018-001)*, 2017.
- [23] G. V. Fedotov *et al.*, “Measurements of the $\gamma_vp \rightarrow p'\pi^+\pi^-$ cross section with the CLAS detector for 0.4 GeV $^2 < Q^2 < 1.0$ GeV 2 and 1.3 GeV $< W < 1.825$ GeV,” *Phys. Rev.*, vol. C98, no. 2, p. 025203, 2018.
- [24] <http://clasweb.jlab.org/bos/browsebos.php>.
- [25] S. Stepanyan, “Proposal for the Production of the DST’s to Distribute CLAS Data,” *CLAS-NOTE-99-002*, 1999.

- [26] Iu. Skorodumina, G. V. Fedotov, and R. W. Gothe, “TWOPEG-D: An Extension of TWOPEG for the Case of a Moving Proton Target,” *CLAS12-NOTE-2017-014*, 2017, arXiv:1712.07712.
- [27] K. Egiyan *et al.*, “Determination of electron energy cut due to the CLAS EC threshold,” *CLAS-NOTE-99-007*, 1999.
- [28] G. Adams *et al.*, “The CLAS Cherenkov detector,” *Nucl. Instrum. Meth.*, vol. A465, pp. 414–427, 2001.
- [29] M. Osipenko, A. Vlassov, and M. Taiuti, “Matching between the electron candidate track and Cherenkov counter hit,” *CLAS-NOTE-2004-020*, 2004.
- [30] P. K. Khetarpal, *NEAR THRESHOLD NEUTRAL PION ELECTROPRODUCTION AT HIGH MOMENTUM TRANSFERS*. Ph. D. Thesis: https://www.jlab.org/Hall-B/general/thesis/Khetarpal_thesis.pdf.
- [31] M. Ungaro and K. Joo, *e1-6 Electron Identification*. CLAS web page: https://userweb.jlab.org/~ungaro/maureepage/proj/pi0/e_pid/e_pid.html.
- [32] S. T. G. Mutcler and E. Smith, “CLAS TOF Scintillator Positions,” *CLAS-NOTE-1998-008*, 1998.
- [33] K. Park *et al.*, “Kinematics Corrections for CLAS,” *CLAS-Note-2003-012*, 2003.
- [34] “e1e target assembly.” https://userweb.jlab.org/~christo/tar_e1e_web.pdf.
- [35] Yu. Skorodumina *et al.*, “Investigating of the exclusive reaction of $\pi^+\pi^-$ pair electroproduction on a proton bound in a deuteron,” *Bull. Russ. Acad. Sci. Phys.*, vol. 79, no. 4, pp. 532–536, 2015. [Izv. Ross. Akad. Nauk Ser. Fiz. 79, no. 4, 575 (2015)].
- [36] Iu. Skorodumina, G. V. Fedotov, *et al.*, “TWOPEG: An Event Generator for Charged Double Pion Electroproduction off Proton,” *CLAS12-NOTE-2017-001*, 2017, arXiv/1703.08081[physics.data-an].
- [37] R. Machleidt, K. Holinde, and C. Elster, “The Bonn Meson Exchange Model for the Nucleon Nucleon Interaction,” *Phys. Rept.*, vol. 149, pp. 1–89, 1987.
- [38] E. Byckling and K. Kajantie, *Particle Kinematics*. Jyvaskyla, Finland: University of Jyvaskyla, 1971.
- [39] L. W. Mo and Y.-S. Tsai, “Radiative Corrections to Elastic and Inelastic ep and μp Scattering,” *Rev. Mod. Phys.*, vol. 41, pp. 205–235, 1969.
- [40] N. Markov *et al.*, “Single π^0 Electroproduction off the Proton in the Resonance region,” *CLAS-Analysis-2014-106*, 2014.

- [41] B. Laforge and L. Schoeffel, “Elements of statistical methods in high-energy physics analyses,” *Nucl. Instrum. Meth.*, vol. A394, pp. 115–120, 1997.
- [42] E. N. Golovach *et al.* <http://depni.sinp.msu.ru/~golovach/EG/>.
- [43] Y. Tian and R. W. Gothe, “Exclusive π^- Electroproduction off the Neutron in Deuterium in the Resonance Region,” *CLAS-Analysis-201?-???*, 201?
- [44] Iu. Skorodumina, G. V. Fedotov, and R. W. Gothe, “Testing Parameterizations of the Deuteron Quasi-Elastic Peak,” *CLAS12-NOTE-2019-003*, 2019, arXiv:???
- [45] P. Bosted *et al.* <https://userweb.jlab.org/~bosted/fits.html>.
- [46] P. E. Bosted and M. E. Christy, “Empirical fit to inelastic electron-deuteron and electron-neutron resonance region transverse cross-sections,” *Phys. Rev.*, vol. C77, p. 065206, 2008.
- [47] K. M. Hanson, J. R. Dunning, M. Goitein, T. Kirk, L. E. Price, and R. Wilson, “Large angle quasielastic electron-deuteron scattering,” *Phys. Rev.*, vol. D8, pp. 753–778, 1973.
- [48] S. Rock, R. G. Arnold, P. E. Bosted, B. T. Chertok, B. A. Mecking, I. A. Schmidt, Z. M. Szalata, R. York, and R. Zdarko, “Measurement of elastic electron - neutron scattering and inelastic electron - deuteron scattering cross-sections at high momentum transfer,” *Phys. Rev.*, vol. D46, pp. 24–44, 1992.
- [49] S. Rock *et al.*, “Measurement of elastic electron - neutron scattering and inelastic electron - deuteron scattering cross-sections at high momentum transfer,” *SLAC-PUB-5239*, 1991.
- [50] A. Bodek, M. E. Christy, and B. Coopersmith, “Effective Spectral Function for Quasielastic Scattering on Nuclei,” *Eur. Phys. J.*, vol. C74, no. 10, p. 3091, 2014.
- [51] L. Durand, “Inelastic Electron-Deuteron Scattering Cross Sections at High Energies. 2. Final-State Interactions and Relativistic Corrections,” *Phys. Rev.*, vol. 123, pp. 1393–1422, 1961.
- [52] P. E. Bosted, “An Empirical fit to the nucleon electromagnetic form-factors,” *Phys. Rev.*, vol. C51, pp. 409–411, 1995.